Abstract

Reservoir properties are mainly determined based on well log information. However, wells in most reservoirs are sparse and widely spread compared to the size of the reservoir. Seismic data is thus one of the most important complementary sources of information used to build 3D models of hydrocarbon reservoirs. The need for a high quality reservoir description starts as soon as a discovery is made. In the appraisal phase, hydrocarbons in place and the amount of recoverable reserves are estimated based on the reservoir model. Improved structural models are also needed in optimal well placement during the production and development phase of a reservoir. Knowledge about saturation and pressure distributions in a reservoir are valuable both in the exploration and development phase of a reservoir. This knowledge is used to evaluate the size of a field, determine an optimal drainage pattern, and decide on optimal well design to reduce risks for blow-outs and damage on production equipment. Reducing uncertainty in reservoir property estimates from seismic data have large economic impact on the development of a hydrocarbon reservoir.

Quantitative reservoir property information can be obtained either through direct estimates of reservoir properties from seismic data or through estimates of elastic properties (velocities and densities) that are related to reservoir properties. The relationship between physical properties of rocks and fluids and P-wave seismic data are often empirical and non-unique. This leads to large uncertainties in reservoir models derived from pressure wave seismic data alone. Since shear waves do not propagate through fluids, combined use of pressure wave seismic data and shear wave seismic data might increase our ability to derive fluid and lithology properties from seismic data. One way to obtain information about shear wave velocities over a large area is to acquire multicomponent seismic data (for instance x, y, and z component geophone data). Parts of this thesis focus on methods to combine the information from multicomponent seismic data with pressure wave (hydrophone) seismic data. In this way we improve the accuracy in the estimates of pressure wave velocity, shear wave velocity and density in the subsurface.

To obtain information about changes in reservoir parameters like fluid saturation and pore pressure during production, comparisons between different vintages of seismic data acquired over the field can be performed. Differences in the seismic signal from the same area over a time period (time-lapse seismic data) can be interpreted as changes in reservoir properties. Benefits of improved reservoir characterization include ability to locate bypassed oil and mapping of fluid fronts. This leads to saved costs due to reduced number of misplaced wells, and increased production because of optimized well placement. In the early days of seismic reservoir monitoring, the analyses were qualitative, e.g. to identify undrained areas, analyzing the sealing capacity of faults, and detect drainage patterns. Today, time-lapse seismic analysis is still mainly qualitative. To be able to obtain more quantitative estimates of changes in reservoir properties from the time-lapse seismic data, we need to establish links between the rock parameters and the seismic data. I have used both time-lapse surface seismic data and time-lapse multicomponent seismic data to estimate production related changes in fluid saturation and pressure.

Finally, to be able to utilize rock physical information obtained from seismic reservoir characterization in reservoir modelling, information about uncertainties in the estimates are essential. One way to do this is to use deterministic models (rock physics models) that relates reservoir properties to seismic data, and assume that the model parameters are independent. However, the variables in these estimations are inherently dependent and should be treated as such. By formulating the problem in a Bayesian framework, dependencies between the different variables and spatial dependencies can easily be included. I have used both deterministic uncertainty analysis and Bayesian estimation methods to quantify uncertainties in the estimates.

Preface

This dissertation is submitted in partial fulfillment of the requirements for the degree of Doktor Ingeniør at the Department of Petroleum Engineering and Applied Geophysics, the Norwegian University of Science and Technology. Professor Martin Landrø at the Department of Petroleum Engineering and Applied Geophysics, the Norwegian University of Science and Technology, has been my supervisor. I am grateful for all his help and encouragement during this period.

The general topic of the thesis is fluid and lithology prediction from seismic data. I have focused on two seismic data types that are only recently becoming widespread, i.e. time lapse seismic data and multicomponent seismic data. I have investigated how these new data types can improve the prediction of elastic properties and reservoir parameters. In addition, I have investigated the uncertainty in the estimation techniques, using both deterministic and stochastic methods. Chapter 4 is published in Geophysics, an international journal published by the Society of Exploration Geophysicists. Chapters 1 and 5 have been submitted for publication in Geophysics. Chapters 2 and 6 have been submitted for publication in Geophysical Prospecting, an international journal published by the European Association of Geoscientists and Engineers. Chapter 3 is an unpublished report.

The work, including compulsory courses corresponding to full-time studies in two semesters, has taken place in the period from August 2000 to December 2004. This includes two maternity leaves; from November 2001 to October 2002, and May 2004 to September 2004. The research was carried out at NTNU, Statoil Research Centre in Trondheim, Norway, at Statoil's Statfjord division in Stavanger, Norway, and in Statoil's research group on Fluid and Lithology Prediction, also in Stavanger. I am obliged to Statoil for providing computer facilities and seismic data. In addition, I would like to thank all employees in Statoil who have contributed to my work with this thesis, both in Stavanger and Trondheim. Special thanks to Hege Rognø, to Mark Thompson, Tage Røsten, Are Osen, Kenneth Duffaut at the Statoil Research Center in Trondheim, to Roy Sørbel, Inger Kloster Osmundsen, and Iren Måløy in the Statfjord division, and to Kari Nesbø and all the people in the GFT-group in Stavanger, especially my "office mates" Francois Renard and Ola Petter Munkvoll.

Parts of the work were performed at Schlumberger Stavanger Research Center (SSR), in cooperation with Hilde Grude Borgos. I would like to thank Lars Sønneland and Schlumberger for providing computer facilities and seismic data, and for granting me leave of absence during this period. I have had many interesting discussions with Hilde Grude Borgos, Geir Våland Dahl, Kristian Gjerding and all the rest of the people at SSR.

The work was funded by a scholarship from VISTA. VISTA is a research cooperation between the Norwegian Academy of Science and Letters (Det Norske Videnskaps-Akademi) and Statoil. Thanks to Anna Charlotte Larsen at the VISTA office for all help.

Special thanks go to my parents for teaching me to be curious and ask questions through Sunday morning discussions on everything between nuclear fission and the path of the river Moldau. My deepest gratitude goes to my husband Gunnar and my three sons, Eivind, Erlend, and Emil. I thank Gunnar for supporting me and standing by through my pre-exam-nerves. My three boys have helped motivating me and forced me to be effective by causing natural and unnatural breaks in my working day.

Contents

Introduction

Seismic data is one of the most important sources of information used to build geological models of hydrocarbon reservoirs. When the rock physic parameters of the reservoir change, seismic properties, like wave velocities and densities, will also change. Seismic data thus contains information both about the geometry of the reservoir, and about the rock physics of the reservoir.

Ideally, a geological model shows the geometrical structure of the reservoir, including fault and fracture patterns, hydrocarbon trap geometry, and shape of depositional bodies. Previously, seismic data were mainly used for structural interpretation to help in the geological modelling. The first seismic datasets used in structural modelling was two-dimensional (2D) lines shot over interesting exploration areas. The purpose was to identify potential reservoir structures. Seismic waves propagate in three dimensions, and by analyzing them in two dimensions only we loose part of the information. Three-dimensional (3D) seismic data was introduced by among others Walton (1972) to increase accuracy in structural model building. The introduction of 3D seismic data required more advanced processing, for instance new migration and dip-moveout (DMO) algorithms were developed. However, the increased accuracy in structural models by far compensated for the increased costs in acquisition and processing. When the accuracy of seismic data increased, information about depositional patterns and lateral facies variations could also be extracted from seismic data, by performing seismic stratigraphic analysis. The need for a high quality reservoir description starts as soon as a discovery is made. In the appraisal phase, estimates of hydrocarbons in place and of recoverable reserves are needed. The improved structural models also helps in optimal well placement during the production and development phase of a reservoir.

In addition to improved structural models, the enhanced processing methods also made it possible to use information about seismic amplitudes to estimate reservoir properties. This was because the new processing methods were designed to preserve the true amplitude of the seismic data. Gardner et al. (1974) showed that gas filled reservoirs should be possible to detect on seismic reflection data by differences in seismic amplitudes (bright spots). Water-filled reservoir rocks will have different pressure wave (P-wave) velocities and densities than gas-filled reservoir rocks, and this will affect reflection coefficients. Taner et al. (1979) showed how the seismic trace could be expressed in complex form, thus separating the amplitude and phase information of the data. They also showed how these new seismic attributes could be used in reservoir characterization. Another example on the use of seismic amplitudes in reservoir characterization is the work by Sønneland and Barkved (1990). Ostrander (1984), and later Rutherford and Williams (1989), introduced the concept of using changes in seismic amplitude response as a function of offset between source and receivers as hydrocarbon indicators for gas reservoirs. Rutherford and Williams (1989) suggested separating possible amplitude versus offset (AVO) responses into 3 different AVO classes or types to describe different fluid and lithology combinations. Castagna et al. (1998) separated the third AVO class into two classes, giving 4 typical AVO classes. This type of AVO analysis is normally only qualitative in nature. However, to be able to obtain reservoir property information (i.e. saturation, pressure, and porosity) that could be used in reservoir model building, quantitative information is required. The necessary information could be obtained either through direct estimates of reservoir properties from seismic data, or through estimates of elastic properties (velocities and densities) that later could be related to reservoir properties.

Elastic parameters can be related to lithology and fluid content of the reservoirs through empirical relationships, such as velocity - porosity relations, and velocity - density relations. However, these empirical relationships are highly non-unique, and uncertainties in the estimates are large. Several authors (e.g. Tjåland and Ursin (1992), and de Nicolao et al. (1993)) have shown that it is difficult to extract information of P-wave velocity, shear wave (S-wave) velocity and density from PP seismic data alone. PP seismic data is defined as a downgoing pressure wave field reflected at a lithologic boundary, and recorded as pressure waves. Because of this non-uniqueness, inversion to acoustic impedance (AI) and elastic impedance (EI) (Connolly, 1999, VerWest et al., 2000, Mallick, S., 2001, Whitcombe et al., 2002) from PP seismic data has often been used. However, the ability to estimate velocities and densities separately would be very valuable in for instance gas filled reservoirs. A small amount of gas will have large impact on the P-wave velocity, making it difficult to estimate gas saturation from impedances only. Density changes are proportional to saturation changes, making density alone a better quantitative saturation indicator than P-wave velocity. Information about the density distribution would thus be of great value in the reservoir characterization process. In addition, since S-waves do not propagate through fluids, combining S-wave seismic data with P-wave seismic data might increase our ability to extract fluid- and lithology information from the seismic data. One way to obtain information about S-waves over a large area is to acquire multicomponent seismic data. By using multicomponent sensor systems (measuring x, y, and z particle displacement) it is possible to record energy converted from P-waves to S-waves, called PS seismic data or converted wave seismic data. Duffaut et al. (2000) introduced shear elastic impedance by inverting PS seismic data. Parts of this thesis concentrate on methods to combine the information from multicomponent seismic data with P-wave seismic data. In this way we enhance the estimates of P-wave, S-wave and density changes across lithologic boundaries, and the estimates of saturation and pressure changes from time lapse multicomponent seismic data. A short introduction on multicomponent seismic data is given below.

Reservoir properties obtained from seismic data are valuable knowledge both in the exploration phase and the production phase of the reservoir. In the exploration phase of a reservoir, information about the saturation distribution in the reservoir could be used to evaluate field size, and to determine optimal placement of wells. The distribution of effective pressure could be used to evaluate seal capacity of the reservoir, and to map possible hydrocarbon migration pathways, thus increasing general knowledge of the reservoir. In the production phase, knowledge about changes in saturation over time will help determining optimal drainage patterns. Information about effective pressure could be used to determine e.g. well design to reduce risk for blowout and damage on production equipment. Reducing uncertainty in reservoir property estimates from seismic data have potentially large economic impact on the development of a hydrocarbon reservoir.

Traditionally, overpressured zones can be mapped by detecting deviation in seismic propagation velocities from normal compaction trends. Dutta (2002) gives an excellent overview of the history and current state of the art in pressure estimation from seismic data. Direct estimation of water saturation from seismic data have been introduced by e.g. calibrating seismic data to well log data through neural networks (e.g. Oldenziel et al, 2000) or through geostatistical estimation e.g. similar to the porosity mapping presented by Doyen (1988). In some cases, it is impossible to separate effects of saturation from effects of pressure using one set of stacked seismic data, since these effects can be of the same order of magnitude. However, by analyzing changes in seismic data from two PP seismic surveys acquired over the same area at different times in the life of a reservoir (time lapse seismic), it is possible to estimate the production related effects on saturation and pressure (Tura and Lumley, 1999, Landrø, 2001). By analyzing time lapse multicomponent seismic data, Landrø et al. (2003) presented estimates of production related saturation and pressure changes with higher accuracy than the ones from time lapse seismic data alone. A short introduction on time lapse seismic data analysis is given below.

Relationships between rock physics and acoustic properties need to be established to analyze time-lapse seismic changes related to saturation and pressure changes. This can be done both in a deterministic framework and a stochastic framework. Tura and Lumley (1999), Landrø (2001), and Landrø et al. (2003) presented deterministic time-lapse analysis. To be able to incorporate the information from time-lapse seismic analysis of saturation and pressure changes in reservoir modelling, quantification of the uncertainties in the estimates are necessary. When calculating uncertainties in deterministic estimations, assumptions about independent variables often have to be made (Landrø, 2002). One advantage of using a stochastic framework for estimating pressure and saturation changes is to gain immediate information about uncertainty in the estimates without making assumptions of independent variables. Theoretical rock physical relationships will be used to set up a prior model of depedencies between different variables (e.g. Haas and Dubrule, 1994, Mosegaard and Tarantola, 1995, Eide et al.,1997, and Bosch 1999, Buland and Omre, 2003). In addition, general field information obtained from regional geologic trends and field analogs can also be introduced in the prior model. Reservoir variables are then linked to measured time lapse seismic data by a likelihood model. The posterior probability can then be found by applying Bayes rule. The solution of the problem will thereby be represented by a probability density function (pdf), providing information about uncertainty in the estimations, as well as estimates of the parameters themselves. The stochastic framework is well suited to combine data from different sources (e.g. well logs, seismic data, field analogs) while keeping track of the uncertainties in the data. In addition, it is easy to include spatial dependencies in the estimations. This framework also makes it possible to identify conflicts between prior model and measured seismic data, and to evaluate the advantage of introducing new data.

Time-lapse seismic

As mentioned above, seismic data were traditionally used to generate structural interpretation models. These seismic data were shot before production started, or in the first years of production for most fields. Properties of the geologic reservoir model was extracted from well log data, and later updated with new information from producing wells. However, in most cases the reservoir model was incomplete, with little knowledge of how the reservoir would behave during production. Information about reservoir flow properties (e.g. connectivity and sealing capacities of faults) mainly came from flow simulations in the reservoir model, from new well logging information in the wells, and production data (e.g. volumes of produced hydrocarbon, pore pressure measurements). However, wells in most reservoirs are sparse and widely spread compared to the size of the reservoir. By comparing different vintages of seismic data, it is possible to obtain field wide information about changes in reservoir parameters. Differences in the seismic signal from the same area over a time period (time-lapse seismic data) can be interpreted as changes in reservoir properties, e.g. saturation changes (e.g. the Oseberg Field, Johnstad et al., 1993, Rutledal et al., 2001, the Gullfaks Field, Sønneland et al, 1997, and Landrø et al., 1999b, and the Draugen Field, Gabriels et al., 1999), pressure changes (the Magnus Field, Watts et al., 1996), and temperatures (the Duri steam flood, Jenkins et al., 1997). Benefits of improved reservoir characterization include ability to locate bypassed oil and mapping of fluid fronts. This leads to saved costs due to a reduced number of misplaced wells, and increased production because of optimized well placement.

The possible success of a time-lapse seismic study will depend on the strength of the time lapse signal difference compared to the background noise. This relationship is governed by - among others - the quality of the seismic data (noise level, repeatability), properties of the reservoir rocks and fluids (compressibility of reservoir fluids and reservoir rocks, saturation and pressure), and the nature of the recovery process (Wang, 1997). The physical basis for time lapse seismic reservoir monitoring is changes in acoustic parameters caused by changes in reservoir properties (Jack, 1997). If the changes in acoustic parameters are smaller than changes due to background noise in the seismic, time lapse seismic monitoring will fail.

Sedimentary rocks can be considered as grains that are packed together. The space between the grains is called the pore space (Figure 1). This pore space is filled with a pore fluid, for instance water, oil or gas. Pore pressure is defined as the fluid pressure in the pore space. When the communication between the pores in a rock is perfect, the pore pressure P_f is equal to the hydrostatic pressure caused by the weight of the fluid:

$$P_f(z) = \int_{z_0}^{z} \rho_f(z) g z dz + P_0, \quad (1)$$

where $\rho_f(z)$ is density of pore fluid at the depth z, g is the gravitational constant. P_0 is a reference pressure at depth z_0, usually the atmospheric pressure. The hydrostatic pressure is referred to as normal pressure conditions. Rocks with deviations from this normal pressure is called overpressured when the pore pressure is larger than the normal pressure, and underpressured when the pore pressure is smaller than the normal pressure. The differences between the pore fluid pressure and the overburden pressure is called the effective pressure:

$$P_{eff} = P_{overburden} - \eta P_f. \quad (2)$$

Here, η is the Biot coefficient, defined as (Mavko et al., 1998)

$$\eta = 1 - \frac{K_{fr}}{K_s}, \quad (3)$$

where K_{fr} is the bulk modulus of the dry, porous rock (the rock frame), and K_s is the bulk modulus of the mineral material. $P_{overburden}$ is the overburden pressure defined as

$$P_{overburden} = \int_{z_0}^{z} \rho(z) g dz, \quad (4)$$

where $\rho(z)$ is the density of the fluid filled rock, and g and z is defined as above.

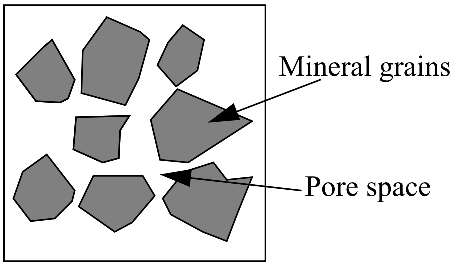

FIGURE 1. Mineral grains are building blocks of sedimentary rocks. The space between the grains are called pore space.

Depletion of the reservoir due to production will cause reduction in pore pressure which will change seismic velocities (Figure 2 and Landrø, 1999b). However, the velocity change might not be as pronounced as previously assumed. Holt et al. (2000) showed that the relationship between pressure and P-wave velocity measured on cores changes dramatically in the unloading - reloading process during coring. When changing pressure on virgin cores, only small changes in P-wave velocity are observed, making this relationship less suitable in pressure predictions from seismic data. Large increases in pressure due to injection can also introduce new fractures in the reservoir zone. These fractures might be possible to map using time-lapse seismic reservoir characterization. In carbonate reservoirs (especially chalk), pressure changes can cause compaction of the reservoir zone, and thus changes in porosity and density will occur (e.g. the Ekofisk Field, Guilbot and Smith, 2002). Because of compaction in the reservoir zone, layers above the reservoir will subside, and the seismic data will be affected in both overburden (meaning layers above the reservoir) and reservoir zone. This will complicate the time-lapse seismic analysis.

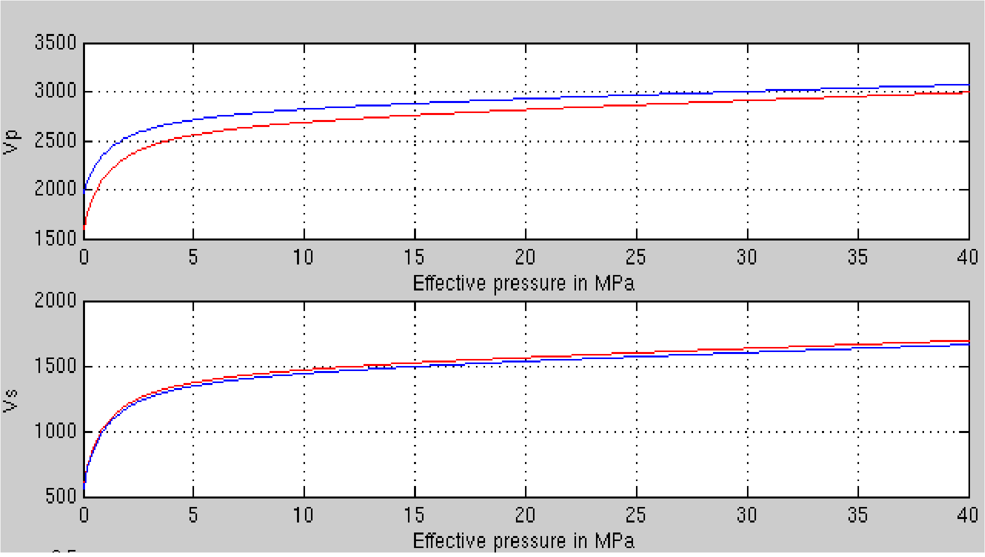

FIGURE 2. Plot of Vp (top) and Vs (bottom) against effective pressure for a rock physics model based on Gullfaks well logs.

Reservoir temperatures usually vary little during conventional production of oil. However, changes in temperature during production can occur e.g. when steam (temperature of 300 C) is injected in a shallow reservoir (temperatures of 10 – 30 C) (e.g. the Duri Field, Jenkins et al., 1997), or when cold sea water (4 – 15 C) is injected into deeper reservoirs (temperature 70 – 90 C) (Jack, 1997). These temperature changes can change both velocity and density (Mavko et al, 1998, Batzle and Wang, 1992). One of the earliest examples of time lapse seismic was a pilot study on the Holt Field in North-Central Texas (Greaves and Fulp, 1987). Here, a steam injection process was monitored by analyzing three seismic surveys, one before injection, one during injection, and one after injection had finished.

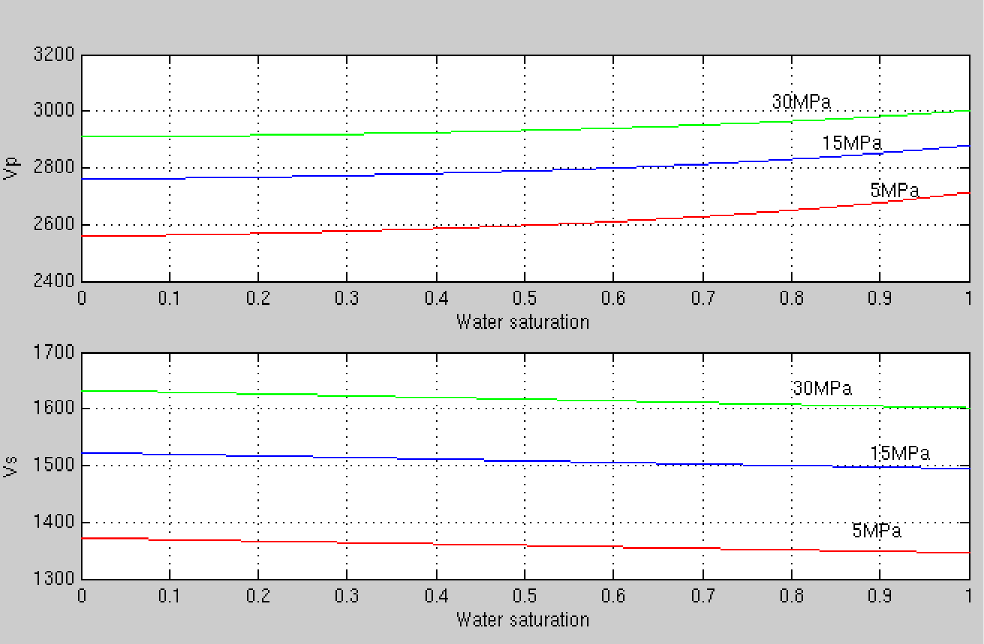

FIGURE 3. Plot of Vp (top) and Vs (bottom) against water saturation for a rock physics model based on Gullfaks well logs. The red curves are for effective pressure 5 MPa, the blue curves are for effective pressure 15 MPa, and the green curves are for effective pressure of 30 MPa.

Changes in hydrocarbon saturation and water saturation of a reservoir will also change both density and P- and S-wave velocity (Figure 3 and Batzle and Wang, 1992). When water injection is used to mechanically displace the reservoir fluid, the oil needs to be light to make the pore fluid compressibility contrast large enough for time lapse seismic monitoring. Water injection in a reservoir with live oil (oil with dissolved gas) will cause the compressibility to decrease (Wang, 1997). Further, hydrocarbon gas or CO_2 can be injected to displace the pore fluid and reduce pore fluid viscosity. In most cases, the injection gas is more compressible than the oil in the reservoir, and this compressibility contrast can be observed on time-lapse seismic differences.

There will always be some non-repeatable noise present in time-lapse seismic data. This non-repeatable noise can be caused by e.g. differences in survey geometry and acquisition parameters, and processing differences if the seismic data were not processed with time-lapse seismic analysis in mind. Rennie et al. (1997) give an overview of how processing of time-lapse seismic data can compensate for differences in acquisition geometry and acquisition parameters. Thompson and Najjar (2002) show how the repeatability between two seismic time-lapse surveys at the Statfjord Field increased when the data was reprocessed with emphasis on repeatability. In general, it is recommended to process the different vintages of seismic data in parallel to compensate for non-repeatable noise (Beasley et al., 1997). In addition, it is possible to perform some kind of cross equalization of the time-lapse seismic dataset to compensate for differences in bandwidth and amplitudes (Rickett and Lumley, 2001). Ensuring good repeatability is even more demanding when trying to compare surface seismic data with the P-component of multicomponent seismic data acquired along the sea floor (the Alba Field, Hanson et al., 2003). In cases like this it can be possible to detect fluid changes, and to use this information to place new production wells and injector wells. However, due to the low repeatability, it will be difficult to extract quantitative information from this type of time lapse seismic analysis.

Previously, seismic data were not acquired for reservoir monitoring purposes (e.g. the Magnus Field, Watts et al., 1996, the Fulmar Field, Johnston et al., 1998), but today time-lapse seismic monitoring can be considered an integral part of field management in many fields (Najjar et al., 2003, De Waal and Calvert, 2003). In the early days of seismic reservoir monitoring, the analyses were mainly qualitative, e.g. to identify undrained areas, analyzing the sealing capacity of faults, and detect drainage patterns. To be able to obtain more quantitative estimates of changes in reservoir properties from the time-lapse seismic data, we need to establish links between the rock physical parameters and the seismic data. Tura and Lumley (1998, 1999), Oldenziel et al. (2000), Landrø (2001), Landrø et al. (2003), Stovas et al. (2003), Cole et al. (2003), Lumley et al. (2003) all showed different methods to obtain quantitative estimates in saturation and pressure from time-lapse seismic data. In addition, Landa and Horne (1997) estimated the distribution of porosity and permeability from well test measurements, production history, and time lapse seismic data. The resulting equation system was solved by non-linear parameter estimation. Inspired by Landa and Horne (1997), Lygren et al. (2003) showed how time lapse seismic data could be used to update flow properties in reservoir flow models by a history matching procedure.

Fluid substitution and pressure change analysis using rock physic relationships like Gassmann’s equation (Gassmann, 1951) and the Hertz-Mindlin relationship (Mavko et al., 1998) should be performed to investigate the possibility of observing changes in the seismic data. Lumley et al (1997) gives a thorough overview of how to analyze technical success factors of a seismic reservoir monitoring study. Time lapse seismic is considered a proven technique in thick clastic oil reservoirs offshore. Other good candidates for time lapse seismic reservoir monitoring includes weak rock reservoirs with unconsolidated or poorly consolidated sands, reservoirs with large contrasts in compressibility between in situ and injected pore fluids, and reservoirs exposed to large changes in temperature and pressure. We now begin to see results on more demanding projects like carbonate field with pressure changes (e.g. the Ekofisk Field, Guilbot and Smith, 2002).

The most recent advances in time lapse seismic analysis are the use of permanent sensors, and the development of so-called instrumented oil fields. Permanent geophysical sensors are placed at or near the surface, and in boreholes to monitor the production of hydrocarbon. In addition, wells (both injectors and producers) can be equipped with downhole sensors monitoring e.g. pressure and temperature. If the wells are completed in several reservoir zones, the information from time lapse monitoring can be used to continuously control e.g. flow rates. The time lapse monitoring will then be a dynamic tool to optimize production. In the Valhall Field in the North Sea, permanent seabed cables have been installed (Barkved et al., 2004). New data are acquired every few months as necessary. The goal is primarily to optimize placement of infill wells. The data quality has become better, and the seismic data are used actively in the well placement process. Another example is the Tyrihans Field in the North Sea, operated by Statoil. Statoil has deployed permanent seismic cables at the sea floor, permanent sensors in wells, and automatic surveillance of subsea equipment. Other examples include time lapse monitoring of the Céré-la-Ronde gas storage reservoir in France, using vertical multicomponent receivers and low energy stationary seismic sources operating continuously (Meunier et al. 2001), and the Foinaven Field in the North Sea (Cooper et al., 1999).

Marine multicomponent seismic data

In conventional marine seismic data acquisition, the seismic source is an air gun array towed behind a seismic vessel. The air gun generates pressure (P) wave seismic data, and only the P-wave seismic data (PP seismic data) are recorded by hydrophones towed behind the seismic vessel. This is due to the fact that S-waves do not travel through seawater, since the shear modulus governing S-wave velocity is almost zero in water. However, knowledge about S-waves could give additional information in seismic reservoir characterization. Before towed streamers were implemented, ocen-bottom cables were the only means to aqcuire marine seismic data. However, the method was only applicable in shallow waters, and the quality was not optimal. In the late 1980s, Western Geophysical introduced Dual-sensor ocean-bottom cables with geophones acquiring the vertical particle motion in addition to hydrophones (Barr, et al., 1996, Barr, 1997). The additional information from the geophones were e.g. used to in the processing of the seismic data to reduce water layer reverberations (Barr, et al., 1996, Barr, 1997). A few years later, in the early 1990s, the first marine multicomponent seismic data were gathered by sensors (geophones and hydrophones) placed on the seafloor, using the SUMIC (Subsea Seismic) system, developed by Statoil (Berg et. al., 1994). By placing multicomponent sensor systems at the seafloor, it is possible to record the full vector wave field of passing stress waves. This includes energy converted from P-waves to S-waves, called PS seismic data or converted wave seismic data. S-wave have two possible polarizations; horizontal S-waves (SH-waves) and vertical S-waves (SV-waves). This refers to the particle motion in the waves relative to the propagation of the wave field (Figure 4). A downgoing P-wave can be converted to SV-waves, but not SH-waves. Downgoing SV-waves can generate reflected and refracted SV- and P-waves, but not SH-waves. SH-waves can only reflect and refract SH-waves. This implies that with a P-wave source and a hydrophone, and two orthogonal S-wave sources and two orthogonal geophones available, the total number of possible acquired wave components is 9 (Table 1).

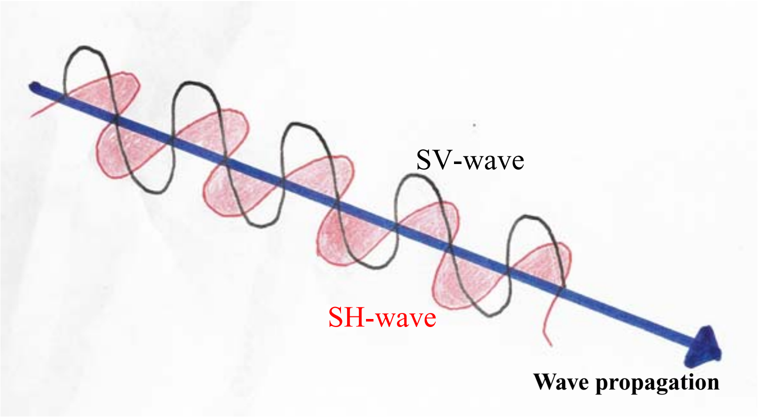

FIGURE 4. Polarization of S-waves.

P down - P up	P down - SV_y up	SV_y down - P-up
SV_y down - SV_y-up	SV_y down - SV_x up	SH_y down - SH_y up
SH_y down - SH_x up	SH_x down - SH_y up	SH_x down - SH_x up

Table 1: Possible wave components in 9-component seismic data

In multicomponent seismic reservoir characterization, the main focus is down-going P-waves converted to S-waves at the lithological boundaries. All lithological boundaries can see conversions, but due to the loss of energy in each conversion, only the first converted mode is strong enough to be recorded. The exception here is very large velocity contrast like salt or basalt contrasts, or conversion at the seabed. Here, conversion of P-waves to S-waves can take place in the down-going wave field, and then converted back to P-waves when going up again. In this thesis, I will assume that the recorded multicomponent seismic data contains the first conversion mode only.

Some of the earliest commercial multicomponent seismic data were acquired in the 1970’s, as 2D 9-component surveys on land. These cases showed that the complementary information obtained from the S-wave data could be valuable in seismic reservoir characterization. However, acquisition of multicomponent seismic data was expensive compared to acquisition of 3D seismic P-wave data, which were gaining popularity at that time. In addition, data quality was lower, and there was unsolved problems in the processing of the multicomponent data. Around 1980, the first 3D 9-component land seismic surveys were acquired, and recently extensive amount of work has been done in the area of processing and analysis of multicomponent seismic data. The industry standard for multicomponent acquisition on land is 3-component seismic acquisition, with dedicated vertically and horizontally polarized sources generating down-going P- and S-waves.

For marine multicomponent acquisition the common practice today is 4-component ocean bottom seismic (OBS), with one hydrophone receiver and 3 geophone receivers (x, y, and z component). Since S-waves are created by conversion of P-waves at the reflection boundary, conventional marine airgun sources towed in the water can be used. It is possible to use S-wave sources both for land and marine seismic surveys, but only converted wave seismic data will be treated in this thesis. Information from PP and PS reflection coefficients will be used extensively in this thesis. I have mainly used Aki and Richards' (1980) approximation to Zoeppritz's equation:

$$R_{PP}(\theta_p) = \frac{1}{2}(1 - 4\,\gamma^2 \sin^2\theta_p)\,\frac{\Delta\rho}{\rho} + \frac{1}{2(\cos\theta_p)^2}\,\frac{\Delta V_p}{V_p} - 4\,\gamma^2 \sin^2\theta_p\,\frac{\Delta V_s}{V_s}\,, \quad (5)$$

$$\begin{aligned} R_{PS}(\theta_p, \theta_s) \;=\; & 2\frac{\sin\theta_p}{\cos\theta_s}[\gamma^2 \sin^2\theta_p - \gamma\cos\theta_s\cos\theta_p]\frac{\Delta V_s}{V_s} \\ & - \frac{\sin\theta_p}{2\cos\theta_s}[1 - 2\gamma^2 \sin^2\theta_p + 2\gamma\cos\theta_p\cos\theta_s]\frac{\Delta\rho}{\rho} \end{aligned}\,, \quad (6)$$

where $\Delta V_p = V_{p2} - V_{p1}$, $V_p = (V_{p1} + V_{p2})/2$ (similar for V_s and ρ), $\gamma = V_s/V_p$, θ_p is the P-wave incidence angle, and θ_s is the S-wave incidence angle. An example of PP and PS reflection coefficients are given in Figure 5. Note that the PS reflection coefficient has no explicit dependence of the P-wave velocity contrast.

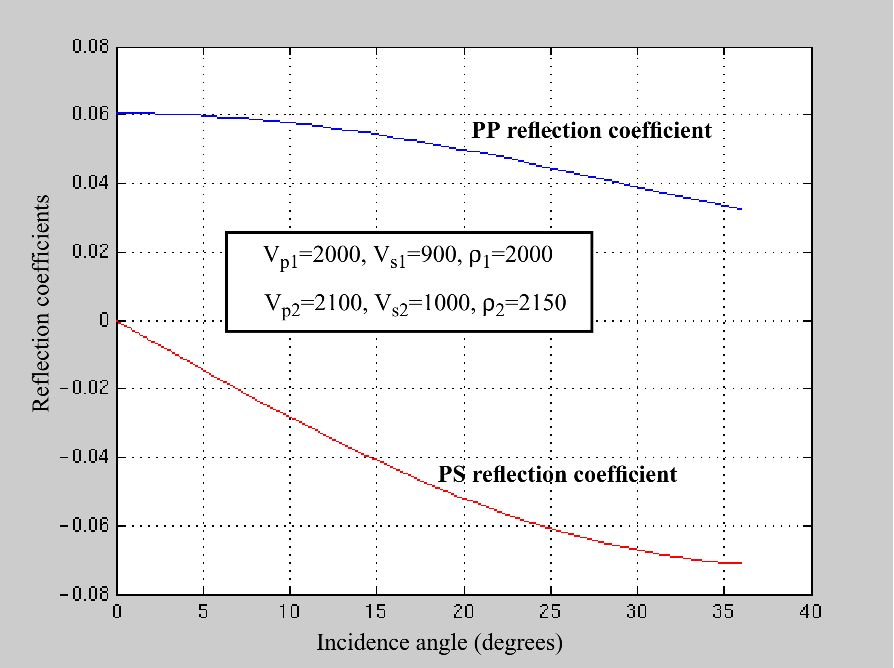

FIGURE 5. PP and PS reflection coefficients using Eqn. 5 and 6.

The main application of marine multicomponent seismic data used to be imaging through gas clouds (e.g. the Tommeliten Field, Berg et al., 1994, and the Valhall Field, Thomsen et al., 1997). Since P-waves are scattered and attenuated in gas filled rocks, the imaging in and below gas zones are poor. S-waves do not suffer the same attenuation and scattering, as the gas mainly affects the compressibility and not the rigidity of the material.

Converted waves can also be used to validate bright spots. Bright spots are defined as an increase of seismic amplitude assumed to be caused by the presence of hydrocarbons (Sheriff, 1999). Since fluids do not affect S-waves, bright spots should not show up on S-wave seismic data if they are caused by fluid fill and not lithology (Engelmark, 2001). When P-wave reflectivity contrasts are small, converted waves might provide better reflections (Engelmark, 2000). One example is the Alba Field in the North Sea (McHugo et al., 1999). Here, the lithologic boundaries of the sand channels embedded in shales are not visible on P-wave seismic data. However, the fluid contacts are clearly visible. On converted wave seismic, the fluid contacts do not show up since S-waves are not sensitive to fluids, but the lithologic boundaries are clearly visible (e.g. Caldwell, 1999, Figure 7). The multicomponent seismic survey on the Alba Field helped in imaging the complex geometry of the turbidite channel. A more recent example of reservoir characterization using converted wave seismic data is the Grane Field in the North Sea (Carrillat et al., 2003, and Fjellanger et al., 2003). Here, the PS seismic data is used for improved imaging of geologic structures such as injections, slumping and some types of faults. In addition, a fluid contact response is visible on the PP seismic data in certain areas, where the PS data in the same area show only lithologic features.

Other important applications of converted wave seismic data include imaging below salt (e.g. the Mahogany Field, Caldwell et al., 1998) and basalt (e.g. Hanssen et al., 2003), and characterization of fractures by analysis of S-wave splitting (e.g. Venezuela, Ata and Michelena, 1995, the Wayburn Field, Davis et al, 2003). Converted waves can also have increased near-surface resolution compared to PP seismic data (Berteussen et al., 1999). One of the reasons for this is the greater relative changes in S-wave velocities compared to P-wave velocities.

Processing of multicomponent seismic data requires special considerations. Stewart et al. (2002, 2003) give a thorough overview of processing and application of converted wave seismic data. I will mention only a few issues. Normally, converted wave seismic data are produced by a projection and summation of the x- and y component of the geophone data. One major difference between conventional processing and processing of mode converted data is the estimation of common conversion points (CCP). P-wave incidence angles differ from S-wave reflection angles (Figure 6), causing asymmetric ray paths and variation of PS reflection points with depth (Tessmer and Behle, 1988). S-wave reflection angles can easily be calculated by Snell’s law. Since the S-wave velocity is smaller than the P-wave velocity, the S-wave reflection angle will be smaller than the P-wave incidence angle. In conventional seismic processing, the reflection point is assumed to be positioned midway between the source and the receiver (Common Mid Point, CMP). To increase the accuracy of converted wave seismic data, the correct reflection point needs to be located (Frasier and Winterstein, 1990). The introduction of common conversion points will also influence the binning process.

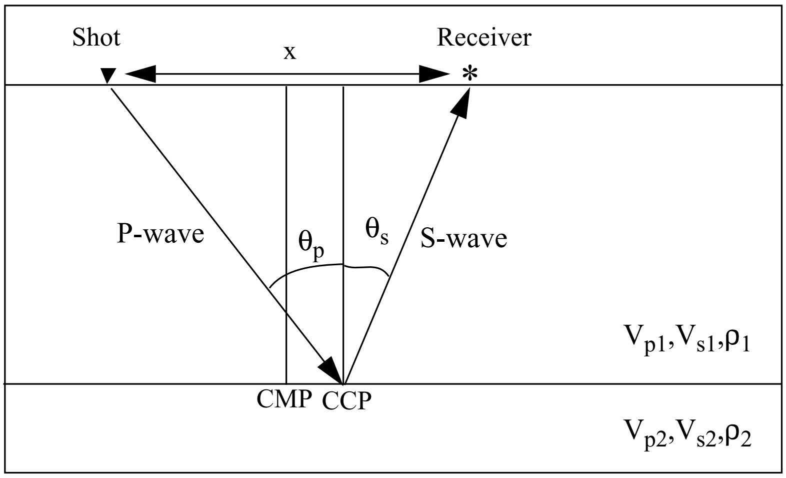

FIGURE 6. Definition of P-wave incidence angle, S-wave reflection angle and Common Conversion Point (CCP).

In addition, when lateral velocity variations or dipping subsurface layers are present, reflections from the positive and negative offsets differ and need to be treated separately. Estimation of S-wave velocities for moveout correction and stacking is more complicated than for P-wave velocities. Converted waves do not follow an hyperbolic move-out, other types of move-out correction need to be performed, e.g. Tessmer and Behle (1988) and Slotboom (1990). In prestack migration of converted wave seismic data, two velocity fields need to be handled. Another complicating factor in prestack migration is that the downgoing wave field is different from the up-going wave field (two different wave types). Finally, to be able to interpret converted wave seismic data together with pressure wave seismic data, event correlation needs to be performed. In event correlation, corresponding reflection events are identified in pressure wave seismic data and converted wave, e.g.Gaiser (1996), and Grechka et al. (2002).

Thesis overview

This project was sponsored financially by VISTA – a cooperation between Det Norske Vitenskaps-Akademi (the Norwegian Academy of Science and Letters) and Statoil. Parts of the project were done at NTNU and Statoil's research center in Trondheim, and parts at Statoil's offices and Schlumberger's in Stavanger.

The thesis contains a set of partly independent papers describing different techniques to estimate reservoir properties from multicomponent seismic data and from time lapse seismic data. The papers should be self-contained. A comprehensive reference list is attached at the end of the thesis. Most of the work has been published at conferences and later submitted to scientific journals.

The first chapter describes a methodology to perform simultaneous prestack inversion of multicomponent PP and PS seismic data using least squares estimation. The resulting equation system is solved using singular value decomposition. The output of the inversion is relative changes in P-wave velocity, relative changes in S-wave velocity, and relative changes in density. The methodology has been tested on synthetic seismic data and field multicomponent seismic data from the North Sea. The results show that the joint inversion is more stable than separate inversion of PP and PS seismic data when the data contains noise. This work was presented at the annual conference and exhibition of the Society of Explorational Geophysicists (SEG) in 2001, and submitted to Geophysics for publication in 2003.

To be able to assess the quality of simultaneous multicomponent inversion, uncertainty in the inversion had to be investigated. Chapter 2 describes a deterministic uncertainty analysis, assuming independent variables. The results are compared to uncertainty in separate inversion of PP AVO seismic data. In addition, the effect of simplifying the inversion by using different relationships between porosity, density and velocity have been analyzed. The deterministic uncertainty analysis was first presented at the annual conference and exhibition of the European Association of

Geoscientists and Engineers (EAGE) in 2003, before it was submitted for publication in Geophysical Prospecting in 2004.

The simultaneous inversion method described in Chapter 1 and 2 is developed for isotropic earth models. However, the earth is inherently anisotropic in nature, and an isotropic earth model is a simplification. Chapter 3 describes an extension of the simultaneous inversion methodology to an anisotropic earth model. Output of the inversion is relative changes in P-wave velocity, relative changes in S-wave velocity, and relative changes in density, and changes in the anisotropic parameters epsilon and delta across an interface. The method has been tested on synthetic data including anisotropy. The results are compared to isotropic inversion of the same dataset, to analyze what is gained by performing an anisotropic inversion. The results show that anisotropic inversion produces slightly better results compared to isotropic inversion of seismic data with anisotropy, but there are still instabilities in the system. The results of the anisotropic inversion have not been published.

The effects of pressure and fluid saturation can have the same degree of impact on seismic data, thus they are often inseparable by analysis of a single seismic data set. By analyzing stacked time lapse multicomponent data our ability to predict saturation and pressure effects associated with production of hydrocarbons should increase. Chapter 4 describes a multicomponent extension of Landrø's method to estimate saturation and pressure changes from time lapse PP AVO seismic data. The methodology has been tested on synthetic seismic data. This work was presented at the annual conference and exhibition of the Society of Explorational Geophysicists (SEG) in 2001, and later published in Geophysics (Landrø et al, 2003).

To be able to utilize the estimates of pressure and saturation changes in reservoir modelling and simulation, information about the uncertainty in the estimation is essential. Direct evaluation of the uncertainty in the estimations can be obtained by formulating the problem in a Bayesian framework. Here, the solution of the problem will be represented by a probability density function, giving us estimations of the uncertainties as well as direct estimations of the properties. Chapter 5 describes a stochastic approach using a Bayesian formulation for estimating saturation and pressure changes from time lapse PP AVO seismic data. Well-known rock physical relationships have been used to set up a prior stochastic model. The likelihood model establishes the link between reservoir variables and time-lapse seismic data. The methodology incorporates dependencies between different variables of the model, as well as spatial dependencies. The methodology has been tested on synthetic seismic data and field seismic data from the Gullfaks Field in the North Sea. The work was done partly at Schlumberger Stavanger Research. This work was presented at the annual conference and exhibition of the Society of Explorational Geophysicists (SEG) in 2003, and later submitted for publication in Geophysics (2004).

In Chapter 6, the methodology for stochastic estimation of saturation and pressure changes has been extended to include time lapse multicomponent seismic data. In addition, a more general matrix formulation of the posterior model is presented. This general formulation makes it easier to change both the prior model and the likelihood model. The time lapse PP AVO study presented in Chapter 5 showed a large correlation between pressure changes and changes in S-wave velocity. The PS seismic data introduce more direct information about time lapse changes in S-wave velocities. The results from synthetic tests indeed show that estimated saturation and pressure changes are improved, and that uncertainties in the estimates are lower. The paper has been submitted for publication in Geophysical Prospecting (2004).

Simultaneous inversion of PP- and PS seismic data

Helene Hafslund Veire* and Martin Landrø*.
****Department of Petroleum Engineering and Applied Geophysics, Norwegian University of Science and Technology, N-7491 Trondheim, Norway.***

Presented at the 71st Ann. Mtg., Soc. Expl. Geophys., San Antonio 2001. Submitted to Geophysics.

Abstract

Elastic parameters derived from seismic data are valuable input to reservoir characterization since these can be related to lithology and fluid content of the reservoir through empirical relationships. The relationship between physical properties of rocks and fluids and P-wave seismic data are non-unique. This leads to large uncertainties in reservoir models derived from P-wave seismic data. Since S-waves do not propagate through fluids, combined use of P- and S-wave seismic data might increase our ability to derive fluid and lithology effects from seismic data. This will reduce the uncertainty in reservoir characterization, and therefore improve 3D reservoir model building.

We present a joint inversion method for PP- and PS seismic data by solving approximated linear expressions of PP- and PS-reflection coefficients simultaneously using a least square estimation algorithm. The resulting system of equations is solved by Singular Value Decomposition (SVD). By combining the two independent measurements (PP and PS seismic data), we make the system of equations more stable than

the ones for PP- and PS seismic data separately. This leads to more robust parameter estimation. The method does not require any knowledge of PP- and PS wavelets.

We tested the stability of this joint inversion method on a 1D synthetic data set. We also applied the methodology to North Sea multi-component field data to identify sand layers in a shallow formation. The identified sand layers from our inverted sections are consistent with observations from nearby well logs.

Introduction

Elastic parameters derived from seismic data can be related to lithology and fluid content of the reservoir through empirical relationships, such as velocity - porosity relations, and velocity - density relations. However, empirical relationships between physical properties of rocks, fluids, and P-wave seismic data are highly non-unique. This leads to large uncertainties in reservoir models built from P-wave seismic data. Since shear waves do not propagate through fluids, combining P- and S-wave seismic data might increase our ability to extract fluid and lithology effects from seismic data.

A significant amount of work has been done in the area of AVO-analysis (Amplitude versus Offset) and direct hydrocarbon indicators, e.g. Rutherford et al. (1989), Helgesen and Landrø (1993), and Castagna et al, (1994), to understand how elastic parameters can be extracted from seismic data. Traditionally, this analysis was done for PP-seismic data. In the last few years; however, AVO-analysis and inversion using PS-data have also been developed using e.g. elastic impedance and elastic S-wave impedance (Connolly, 1999, Landrø et al.,1999, and Duffaut et al., 2000). The use of multicomponent seismic data has increased over the past few years, but it has not yet become part of routine seismic analysis. One obstacle is the high acquisition cost of marine multicomponent seismic data, compared to conventional marine seismic data. Another drawback is processing of multicomponent data, especially challenges related to S-wave velocity (V_s) estimation. In contrast to P-wave velocity (V_p) analysis, we hardly observe pure S-waves in multicomponent seismic data. Therefore, S-wave velocity information must be extracted from converted wave (PS) events. The mixture of P and S information leads to higher uncertainties in estimated S-velocities. This is in contrast to velocity analysis performed on SS seismic data. Shear wave statics is another hurdle to pass on the way to obtain good PS converted stacked images. challenge is the interpretation of multicomponent data. However, this is changing. With the new S-wave impedance methods (e.g. Connolly, 1999, Landrø et al.,1999, and Duffaut et al., 2000), multicomponent seismic data can easily be integrated in the seismic reservoir characterization workflow. Thus we can justify the added cost of acquiring multicomponent data by providing more reliable reservoir characteristics.

Several authors like Tjåland and Ursin (1992), and de Nicolao et al. (1993), have studied the reflection coefficient matrix. For inversions using either the exact system of equations (Tjåland and Ursin, 1992) or using linearized Zoeppritz equations, it is difficult to get reliable estimates for three parameters (P-wave velocity contrast, $\Delta V_p/V_p$, S-wave velocity contrast, $\Delta V_s/V_s$, and density (ρ) contrast, $\Delta\rho/\rho$) from a single set of seismic data (e.g. PP-data only). Nicolao et al. studied the stability of the linearized equation for PP reflection coefficients through eigenvalue and eigenvector analysis. The problem of instability is less pronounced for linearized inversion of PS-data (Jin, 1999, and Jin et al. 2000), since PS-reflection coefficients only depend on S-wave velocity contrasts and density contrasts. Jin et al. (2000) also used singular value decomposition (SVD) to stabilize the linearized PS system of equations, and obtained good results for both synthetic and field data.

Kelly and Skidmore (2001) presented three-parameter inversion of PP seismic data using non-linear AVO-equations. By including second order terms for velocity and density contrasts they obtained more accurate and stable results for large incidence angles and for large rock property contrasts. However, Mallick (2001) showed that at large incidence angles effects of multiples and mode conversions contaminates the AVO approximations and that inversion methods using convolutional assumptions will produce incorrect results. Downton et al. (2004) showed how incorporation of NMO stretch an offset dependent tuning in the forward modelling combined with a Bayesian formalism improved the three term AVO inversion.

Margrave et al. (1999) presented a joint inversion for PP- and PS seismic data using a weighted stacking technique, to produce estimates of $\Delta(\rho V_p)/(\rho V_p)$ and $\Delta(\rho V_s)/(\rho V_s)$, and pseudo Poisson's ratio fluctuations. Garotta et al. (2002) extracted V_p/V_s sections from multicomponent seismic data by combining time correlation of PP- and PS seismic data with AVO information. These V_p/V_s sections can be used to find P-wave velocity contrasts, S-wave velocity contrasts and density contrasts.

In this paper, we perform a simultaneous inversion of PP- and PS data using simple least squares estimation. The output of the inversion is P-wave velocity contrasts, S-wave velocity contrasts and density contrasts. By combining two independent measurements (PP and PS seismic data), we introduce a more stable the system of equations than the ones for PP- and PS seismic data separately. Some of the most common inversion methods are based on iterative updates of an impedance model, by maximizing the fit of recorded PP seismic data with synthetic seismic data generated from the impedance sections. These methods require a known wavelet. Our methodology does not require knowledge of wavelets from the two data sets. However, PP and PS datasets need to be aligned unambiguously in time by event correlation, in such a way that the same reflections occur at the same traveltime in both data sets. By event correlation we mean interpretation of the same seismic events in the PP and PS stacked sections. This procedure is not straightforward, especially without well control. A calibration of seismic amplitudes to reflection coefficients is also necessary. Both these tasks require careful processing of the PP and PS seismic data.

We have tested the methodology both on synthetic seismic data and field multicomponent seismic data. The results are encouraging. This method is able to produce reliable results when noise is added to the synthetic seismic data, and when the accuracy in the V_p/V_s model and the angle of incidence varies. The inverted sections from the field multicomponent data are compared to well log contrasts from the same formation, and the sand layers identified from the gamma log in a well from the same area are also identified in the inverted sections.

Methodology

Aki and Richard's approximations of the Zoeppritz's equations for PP reflection coefficients and PS reflection coefficients are given by:

$$R_{PP} = \frac{1}{2} 1 - 4\gamma^2 \sin\theta_p{}^2 \frac{\Delta\rho}{\rho} + \frac{1}{2\cos\theta_p{}^2} \frac{\Delta V_p}{V_p} - 4\gamma^2 \sin\theta_p{}^2 \frac{\Delta V_s}{V_s} \quad , (1)$$

$$\begin{aligned} R_{PS} = {} & 2\frac{\sin\theta_p}{\cos\theta_s}[\gamma^2 \sin^2\theta_p - \gamma\cos\theta_s\cos\theta_p]\frac{\Delta V_s}{V_s} \\ & -\frac{\sin\theta_p}{2\cos\theta_s}[1 - 2\gamma^2\sin^2\theta_p + 2\gamma\cos\theta_p\cos\theta_s]\frac{\Delta\rho}{\rho} \end{aligned} \quad , (2)$$

where $\Delta V_p = V_{p2} - V_{p1}$, $V_p = (V_{p1} + V_{p2})/2$ (similar for V_s and ρ), $\gamma = V_s/V_p$, θ_p is the P-wave incidence angle, and θ_s is the S-wave incidence angle. By combining PP- and PS reflection coefficients using least square estimation, we want to solve the system of equations for P-wave velocity contrast, $\Delta V_p/V_p$, S-wave velocity contrast, $\Delta V_s/V_s$, and density contrast, $\Delta\rho/\rho$. The least square system is defined as

$$LS = (1 - w)\sum_{i=1}^{n}[R^*_{PS}(\theta_{p,i}, \theta_{s,i}) - R_{PS}(\theta_{p,i}, \theta_{s,i})]^2 + w\sum_{j=1}^{m}[R^*_{PP}(\theta_{p,j}) - R_{PP}(\theta_{p,j})]^2 \quad . (3)$$

Here, R_{Px} is the linearized PP and PS reflection coefficients defined above, where x is either P or S. R^*_{Px} indicates measured seismic data (PP and PS) where the amplitudes are calibrated to represent reflection coefficients. The summation is done over all incidence angles for the PP ($j = 1 \ldots m$)and the PS reflection coefficients ($i = 1 \ldots n$). The factor $w, 0 \le w \le 1$ is a weight factor that can be used to reflect varying quality of the two datasets, e.g. if PP data are assumed to contain less noise than

PS seismic data, w should be larger than 0.5. In the field data example presented in this paper, the weight factor is set to 0.5, i.e the two data sets are assumed to have equal quality. To find the least square solution, we differentiate Eqn. 3 with respect to $\Delta\rho/\rho$, $\Delta V_p/V_p$, and $\Delta V_s/V_s$, and find the minimum values. This yields a system of equations:

$$\mathbf{A} \cdot \left[\frac{\Delta V_p}{V_p}\ \frac{\Delta V_s}{V_s}\ \frac{\Delta\rho}{\rho}\right]^T = \mathbf{b} \quad , \qquad (4)$$

where $\mathbf{A}$ is a 3x3 matrix, and $\mathbf{b}$ is a vector. $\mathbf{A}$ is symmetrical, and depends only on the angle of incidence and background models of P-wave velocity and S-wave velocity**,** whilst the vector $\mathbf{b}$ also depends on measured information about PP- and PS reflection coefficients as a function of angle in the seismic data. Detailed expressions for $\mathbf{A}$ and $\mathbf{b}$ are given in .

The system of equations is solved by singular value decomposition (SVD) to ensure stability of the solution. The stability of a system of equations can be analyzed using the condition number of the system. The condition number is calculated as the ratio between the largest and the smallest eigenvalue of the matrix A, and should preferably be as small as possible. Singular value decomposition is well-suited for solving unstable systems of linear equations (e.g. Jin et al. 2000). The matrix $\mathbf{A}$ is factored into $\mathbf{A} = \mathbf{Q}\Sigma\mathbf{Q}^T$, where $\mathbf{Q}$ is an orthogonal matrix that consists of the eigenvectors of A^TA, and Σ is a diagonal matrix with the singular values (the square roots of the non-zero eigenvalues of A^TA). The SVD can be stabilized by adding a small positive number to the diagonal of the original matrix A (called SVD damping). Singular values for the resulting least square system of equations are better balanced (have a lower condition number) than singular values for inversion of PP-data alone. Inversion of PS-data alone has a lower condition number than both PP-inversion and joint inversion for the first reflector of the synthetic example given in Figure 1. This is probably because PS-inversion only involves two unknown variables, S-wave velocity and density, and is less underdetermined than PP-inversion and joint inversion. The singular values for the joint inversion and the separate inversion of PP and PS for this example are given in Table 1.

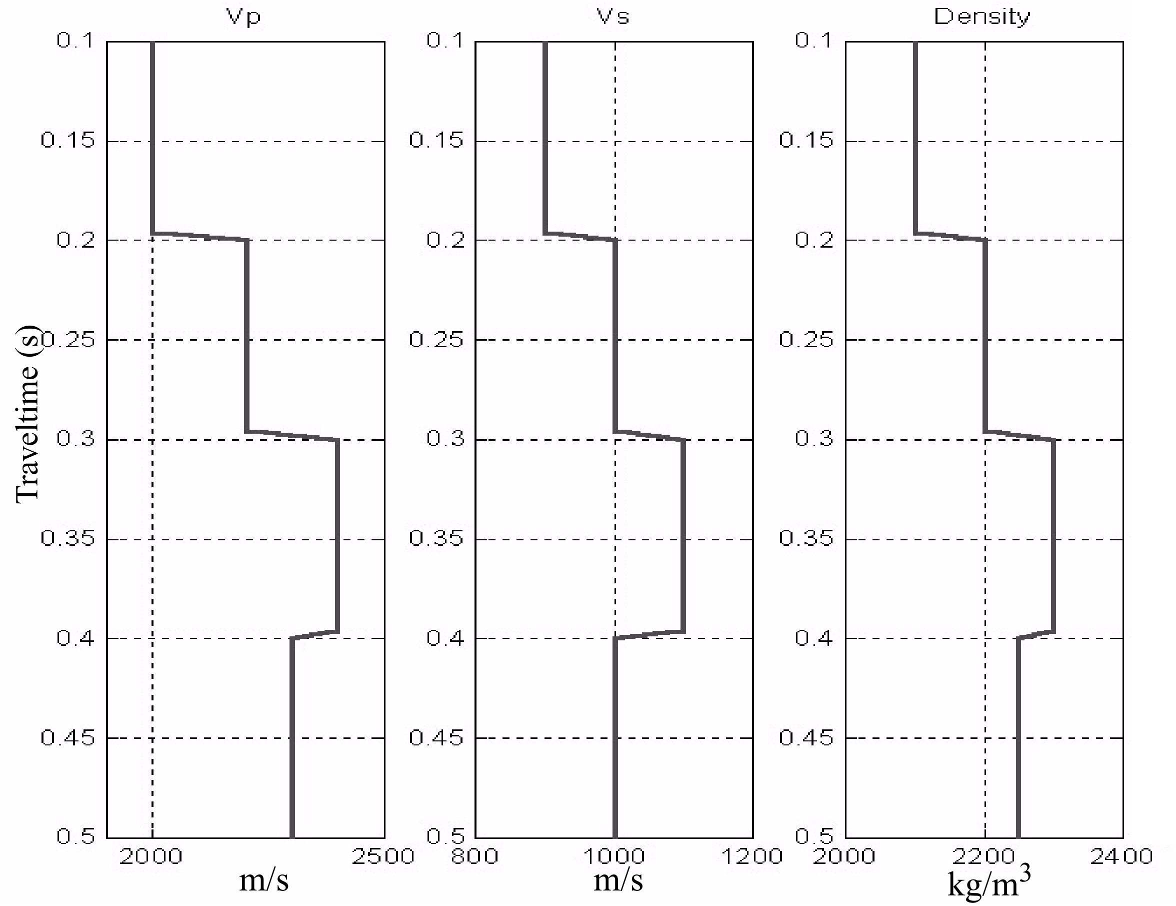

FIGURE 1. Synthetic Vp, Vs, and density models.

Inversion method	1st singular value	2nd singular value	3rd singular value
Joint inversion	18.6556	3.2481	0.0020
PP inversion	17.8065	0.2127	0.0001
PS inversion	3.8843	0.0020	-

Table 1: Singular values for the first reflection

Traveltime scaling of PS-data to PP data is a crucial point in the inversion process. If this is not done properly, non-corresponding events in the two data sets will be viewed together in the least square system of equations, and resulting velocity- and density contrasts will be inaccurate. This traveltime scaling requires an estimate of the depth varying V_p/V_s relationship. This depth varying V_p/V_s model is also needed as an input parameter in the inversion. The simple synthetic example below shows good results when the inversion is run with varying accuracy in the V_p/V_s model. An estimate of the V_p/V_s ratio can be produced by identification of corresponding reflection interfaces (event correlation) in PP and PS seismic data (Gaiser (1996), and Grechka et al. (2002)). In addition, the method requires that seismic amplitudes are calibrated such that they represent reflection coefficients. From V_p, V_S and density well logs, PP and PS reflection coefficients can be calculated for a significant reflection. The seismic amplitudes for this reflection should be extracted from PP and PS prestack seismic data. A calibration factor can be calculated by comparing seismic amplitudes with modeled reflection coefficients for this reflection. Seismic amplitudes are then scaled to represent reflection coefficients, using this calibration factor for all offsets.

The methodology has also been tested for varying degree of accuracy in the incidence angles. The conversion from offset distributions to incidence angles can be done by ray tracing. This requires a velocity model that is often not available with high accuracy in the first processing sequence, thus potential large errors in the incidence angles can occur. The inversion seems to be stable for unsystematic errors and for small systematic errors in the incidence angles.

An analysis of how the weight factor w should reflect uncertainty (or noise) in PP and PS seismic data was performed. The total uncertainty of a function $S(x, y, \ldots)$, where parameters $x, y, \ldots$ are independent, is given by

$$\delta S = \sqrt{\left(\frac{\partial S}{\partial x} \cdot \delta x\right)^2 + \left(\frac{\partial S}{\partial y} \cdot \delta y\right)^2 + \ldots} \quad , \tag{5}$$

where δx and δy indicate uncertainties in the parameters x and y, $\partial S/\partial x$ and $\partial S/\partial y$ are partial derivatives of the function $S(x, y, \ldots)$ with respect to x and y. Using this formulation, total uncertainty in the least square system as a function of uncertainty in the seismic data is given by

$$\Delta LS = \sqrt{\left(2(1-w)\delta R^*_{PS} \cdot \sum_{i=1}^{n} [R^*_{PS} - R_{PS}]\right)^2 + \left(2w\delta R^*_{PP} \cdot \sum_{j=1}^{m} [R^*_{PP} - R_{PP}]\right)^2} \tag{6}$$

Here, δR^*_{PS} and δR^*_{PP} denote uncertainties in measured PS and PP seismic amplitudes, respectively. By differentiating this expression with respect to the weight factor w, an expression for the optimal weight factor as a function of uncertainty in PP- and PS seismic data is found as

$$w_{opt} = \frac{\left(\delta R^*_{PS} \cdot \sum_{i=1}^{n} [R^*_{PS} - R_{PS}]\right)^2}{\left(\delta R^*_{PS} \cdot \sum_{i=1}^{n} [R^*_{PS} - R_{PS}]\right)^2 + \left(\delta R^*_{PP} \cdot \sum_{j=1}^{m} [R^*_{PP} - R_{PP}]\right)^2} \quad . \tag{7}$$

This means that when uncertainty of PP- and PS seismic data is equal, i.e. the noise levels are the same, and assuming PP- and PS reflection coefficients are of the same magnitude, the two data sets should be given the same weight. Looking at two synthetic seismograms from a two-layer model, one without noise and one with a small amount of noise (SNR = 0.98), we calculate the optimal weight factor as a function of uncertainty in PP- and PS-seismic data (Figure 2). Here SNR denotes Signal to Noise Ratio. The signal to noise ratio is defined as the ratio of rms-amplitudes of noise free seismic data and seismic data with noise over a time window. Assuming an uncertainty in PP amplitudes of 20%, and an uncertainty in PS amplitudes of 20%, the optimal weight factor calculated from Eqn. 7 is 0.68 in the current example. If the uncertainty in PP amplitudes increase to 30%, and PS uncertainty is kept constant, the weight factor is found to be 0.49. If PS uncertainty is increased to 30%, and PP uncertainty is kept at 20%, the optimal weight factor is 0.83. These results show that even with small uncertainties in the PS seismic data the PP seismic data will dominate the results, when PP reflection coefficients are larger than PS reflection coefficients as is the case here. When the uncertainty in PP seismic data is larger, the two data sets will be of equal importance in the inversion.

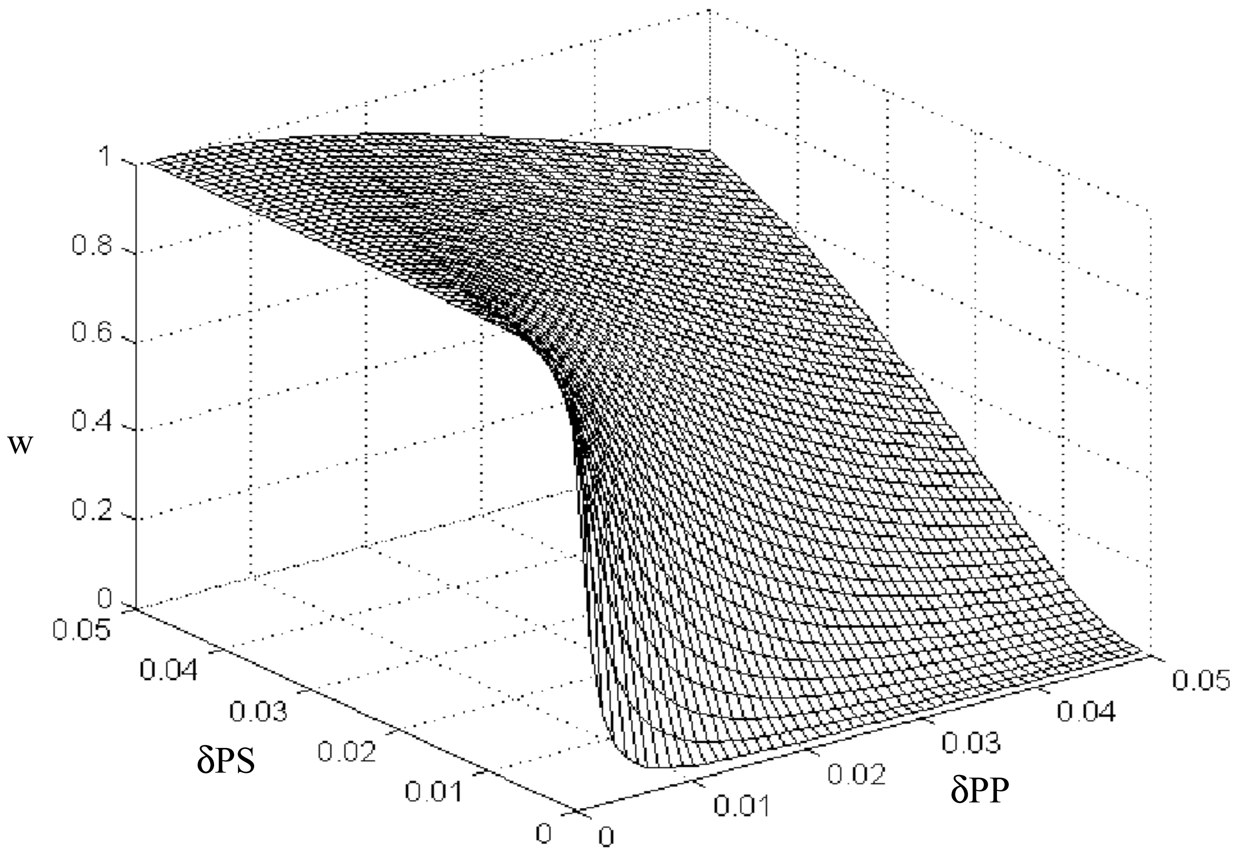

FIGURE 2. Plot of the weight factor w as a function of uncertainty in PS seismic data (δPS) and PP seismic data (δPP), with uncertainty varying from 0 to 0.05.

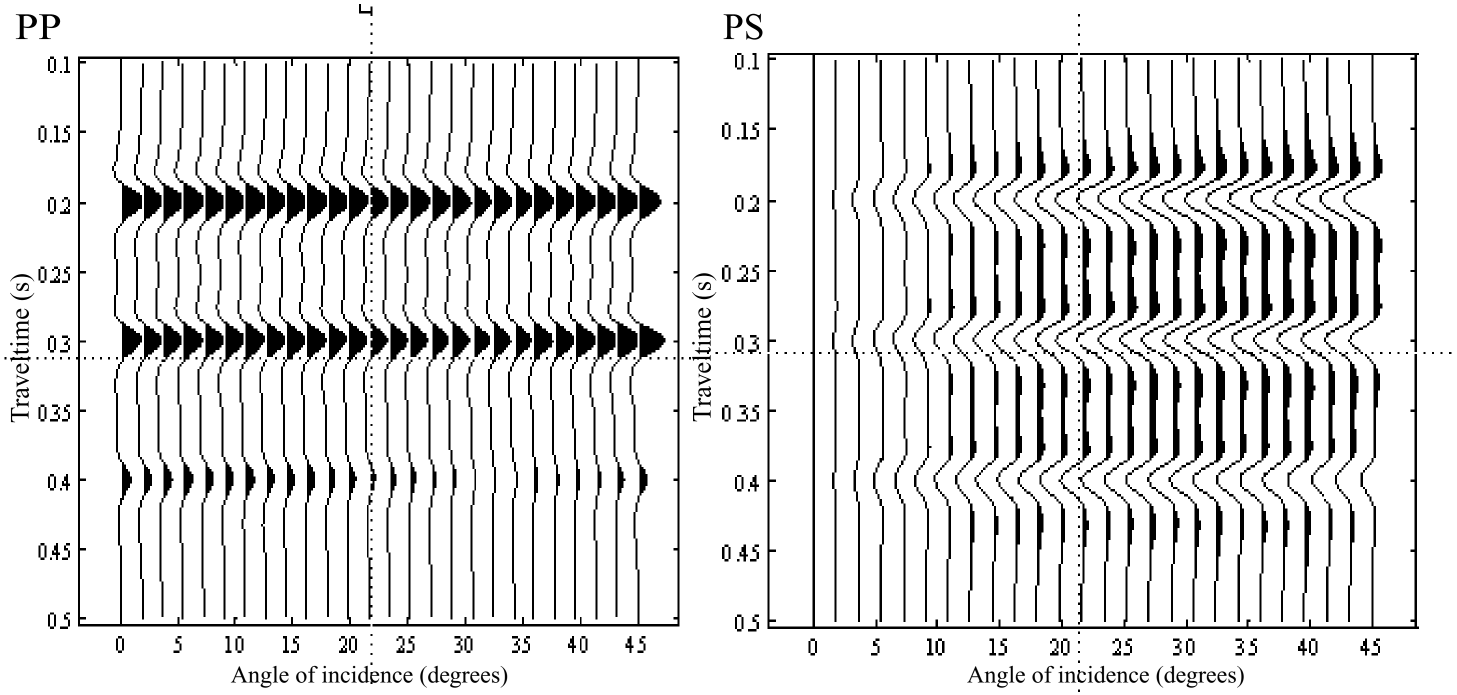

FIGURE 3. Synthetic PP (left) and PS (right) seismograms without noise.

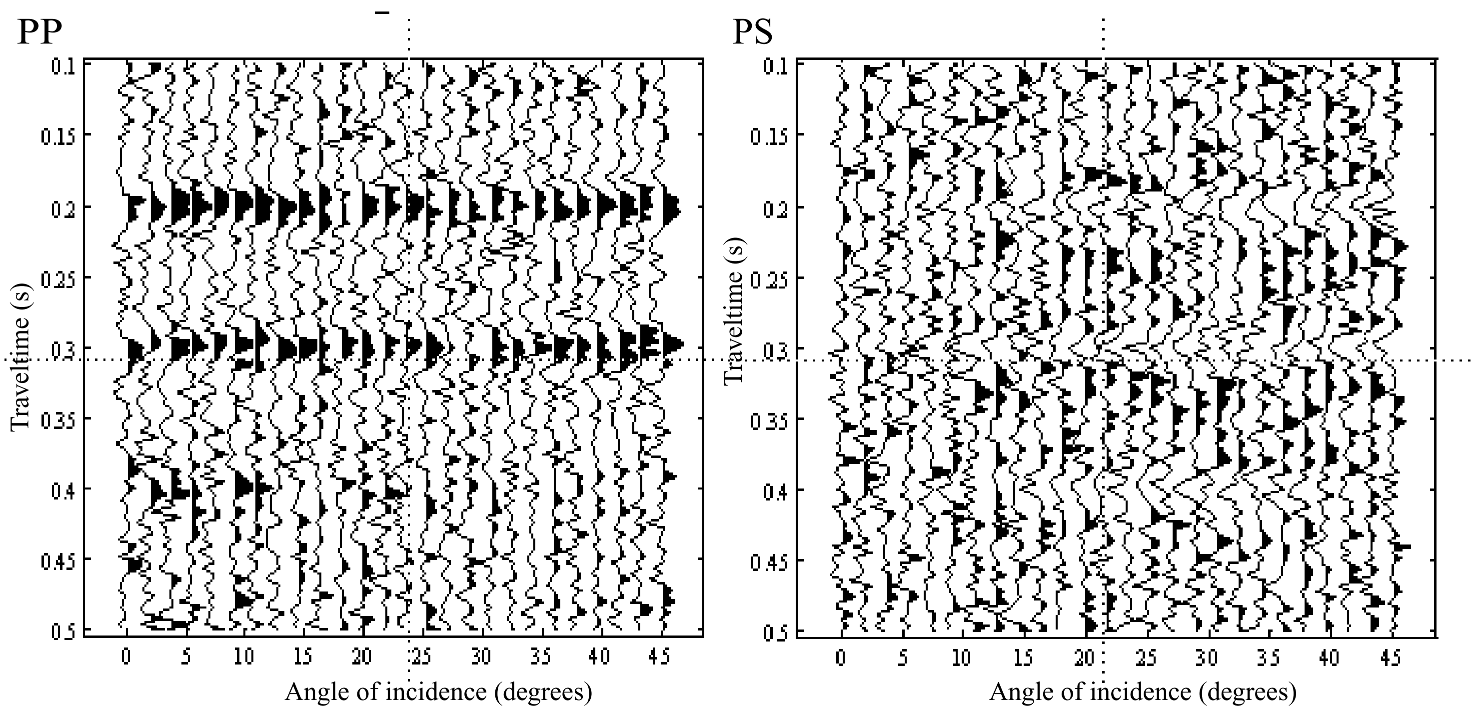

FIGURE 4. Synthetic PP (left) and PS (right) seismograms with random noise (SNR=1.0).

Synthetic data example

A synthetic 1D model with three reflection boundaries was chosen (Figure 1), and synthetic seismograms were generated from both PP- and PS-reflection coefficients for incidence angles between 0 - 30 degrees, with and without noise (Figures 3 and 4). Large angles were avoided since the accuracy of Aki and Richard's approximation to the Zoeppritz equations is poor for angles above 30 degrees. The seismograms contain no multiples and no geometrical spreading, and they are generated without normal moveout. The seismic amplitudes were calibrated to represent reflection coefficients, using one calibration factor for all angles. No deconvolution type processing was done prior to the inversion. The least square system of equations (Eqn. 4) representing changes in velocities and density was solved using singular value decomposition.

Figure 5 shows estimated P-wave velocity contrasts, S-wave velocity contrasts and density contrasts from noise-free seismic data and from noise added data, overlay with the true values. In both cases the correct depth varying V_p/V_s model was used as the required V_p/V_s trend model (solid line in Figure 6). The inversion method produces stable results with a noise level of approximately 7% added to the synthetic data. Due to limited frequency content in the wavelet, estimated values have a lower frequency content than real contrasts.

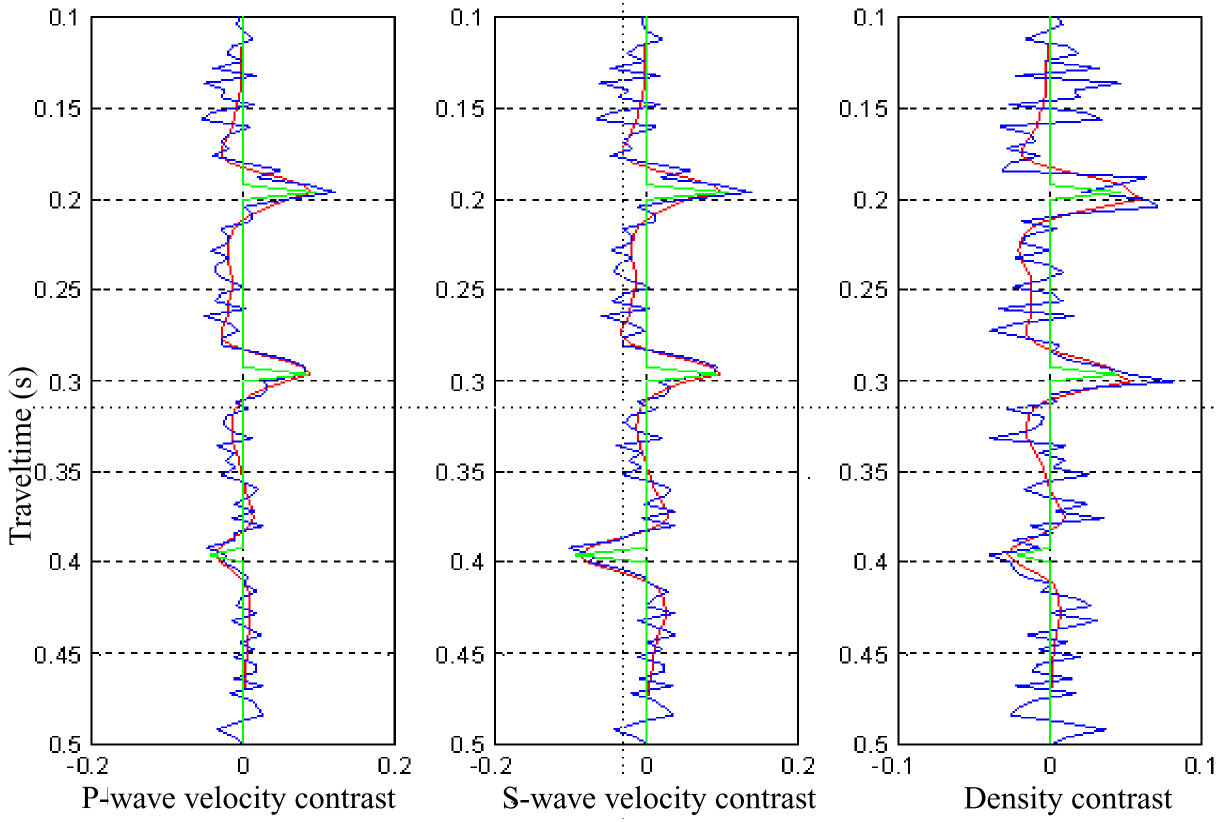

FIGURE 5. **P-wave velocity contrast (left), S-wave velocity contrast (middle), and density contrast (right), where the green curve is real changes, the red curve is estimated changes from noise-free seismic data, and the blue curve is estimated changes on seismic data with noise.**

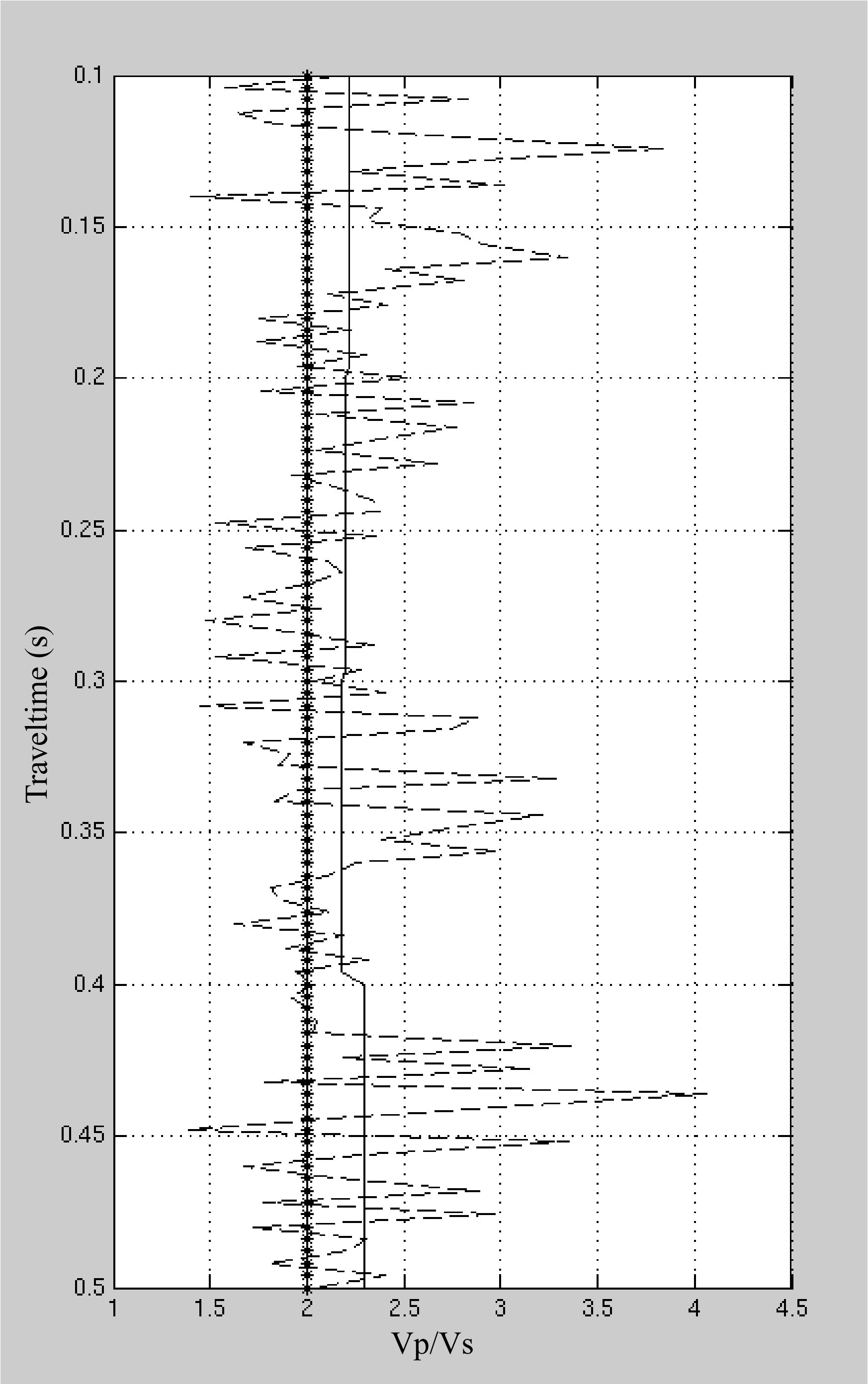

FIGURE 6. Vp/Vs models: Correct Vp/Vs model (solid line), constant Vp/Vs model (Vp/Vs=2) (***), Vp/Vs model with Gaussian noise (dashed line).

The inversion method requires an estimate of incidence angles for PP- and PS seismic data, in addition to a model of the V_p/V_s ratio. Incidence angles can be obtained from offset distributions by using Snell's law and assuming hyperbolic moveout. The V_p/V_s ratio can be estimated from interpretation of corresponding reflection events in the PP- and PS seismic data, calibrated by well log data. However, these estimates may be ambiguous, introducing errors in the inversion. To investigate the stability of the inversion to errors in input parameters, the inversion method was tested with errors in incidence angles and errors in the V_p/V_s model. Figure 7 shows results of the inversion with a varying degree of accuracy in the V_p/V_s model. The V_p/V_s model is depth (time) dependent. Especially shallow sections might have very high V_p/V_s ratios compared to typical values for reservoir rocks, and this might cause problems in the inversion when not using a depth dependent V_p/V_s model. Both a constant, noise-free V_p/V_s model and a depth dependent model with Gaussian white noise added were tested and compared to inversion with the correct noise-free and depth dependent V_p/V_s model. The correct V_p/V_s ratio varies between 2.08 and 2.2 (solid line in Figure 6). For the results with Gaussian noise in the V_p/V_s model, the V_p/V_s ratio varied between 1.38 and 4.05 (dotted line in Figure 6). There is almost no difference in the inversion results with different V_p/V_s models, indicating that the inversion is not sensitive to variations in the V_p/V_s model. Figure 8 shows the results of the inversion with errors in the incidence angles. The inversion was tested with a systematic error in the angles of incidences (approximately 2 degrees too large) and with Gaussian noise added to the incidence angles. For unsystematic errors (Gaussian noise) in the incidence angles, high frequency differences are visible (Figure 8), e.g. around the first reflector at 0.2 s. However, the main trends remain undistorted. For systematic errors, the accuracy of the results is reduced. The system becomes unstable for systematic errors above 4 degrees. Deterministic uncertainty analysis assuming independent variables (Veire and Landrø, 2004) also shows that uncertainty in incidence angles is one of the major contributors to uncertainty in inverted velocity and density contrasts.

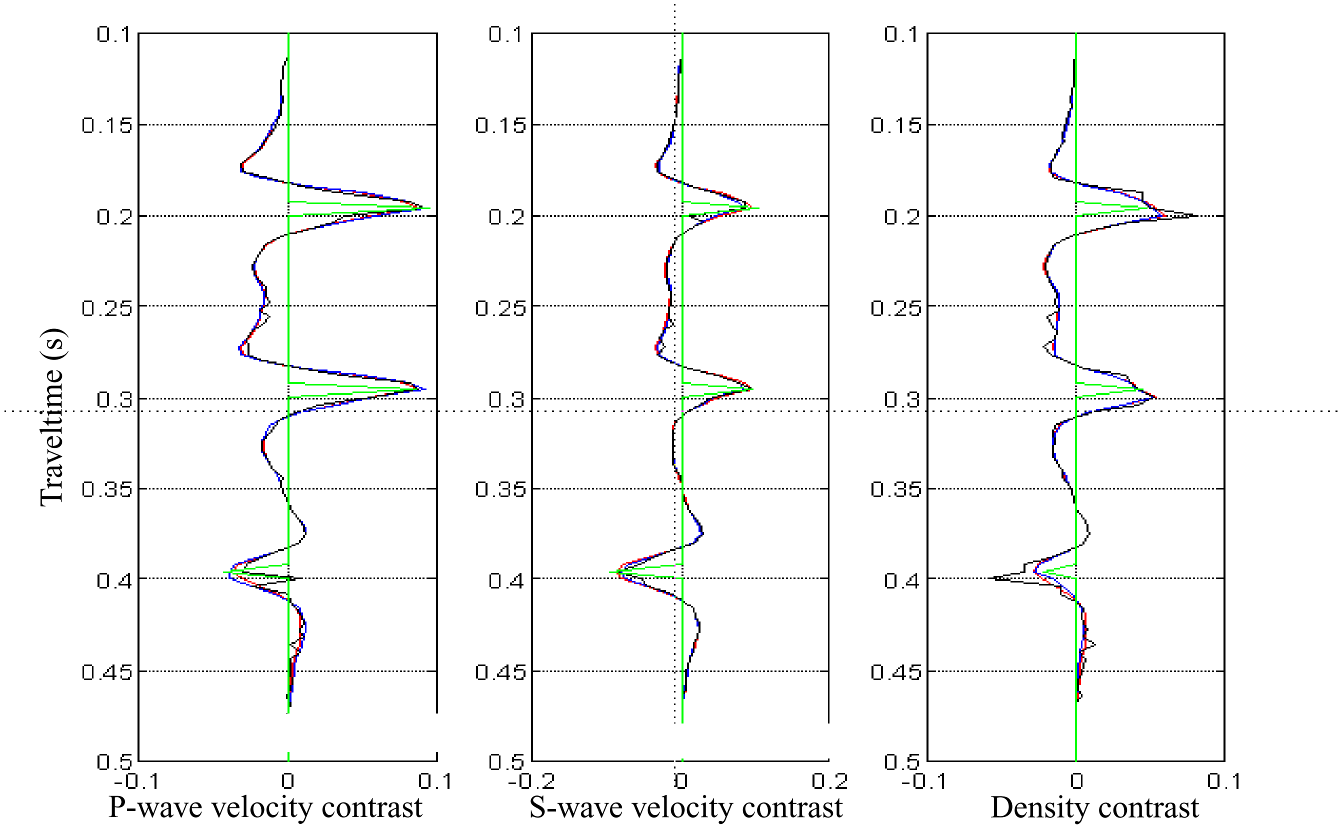

FIGURE 7. P-wave velocity contrast (left), S-wave velocity contrast (middle), and density contrast (right), where the green curve is real changes, the red curve is estimated changes with correct Vp/Vs model, the blue curve is estimated changes with a constant Vp/Vs model, and the black curve is estimated changes when the Vp/Vs model was randomly perturbed.

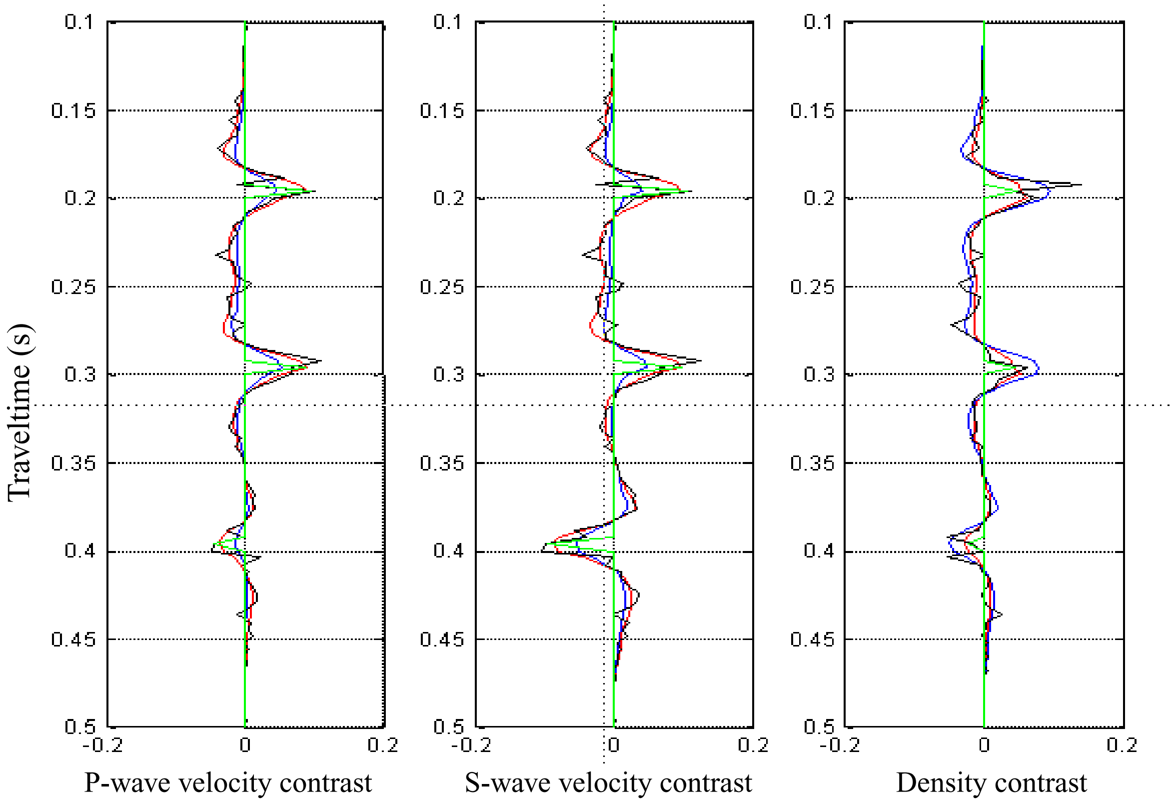

FIGURE 8. **P-wave velocity contrast (left), S-wave velocity contrast (middle), and density contrast (right), where the green curve is real changes, the red curve is estimated changes with correct incidence angles, the blue curve is estimated changes with a systematic error in incidence angles, and the black curve is estimated changes when incidence angles were randomly perturbed.**

Estimated contrasts for the synthetic model without noise in the seismic data from joint inversion were compared to results of separate PP- and PS inversions (Figure 9). The SVD damping was set separately for each method. Joint inversion and PP inversion give almost the same results for synthetic seismic data without noise. However, when noise is added (Figure 10), joint inversion is more stable than separate PP inversion. Results from PS inversion are of lower quality than both PP inversion and joint inversion for noise free data. When noise is added to the seismic data, PS inversion is more stable than PP inversion. This is because the PS equation system is better conditioned than the PP equation system, making PP inversion more sensitive to noise in the seismic data than PS inversion. This is most likely linked to the fact that PS inversion involves 2 unknown variables and PP inversion involves 3 unknown variables. The joint inversion is better than both PP and PS inversion with noise in the seismic data, and this indicates that the combination of the two data sets indeed stabilizes the inversion for field data.

Figure 11 shows the inversion results using different weighting factors. The synthetic models and results will be presented in more detail below. For this test the SNR in PP seismic data was 1.05 and the SNR in PS seismic data was 0.96. This gives an optimal weight factor of 0.9. The inversion was run without weighting (red curve), with most weight on PS seismic data (blue curve), w=0.1, and with most weight on PP seismic data (yellow curve), w=0.9. We observe that the results from no weighting and most weight on PS data both give noisy results, while the inversion with the optimal weighting factor gives a better result. For real data purposes, the variance of the amplitude data along a given interface might serve as an initial estimate of the uncertainty in the data. Another approach is to estimate the background noise directly from the field data.

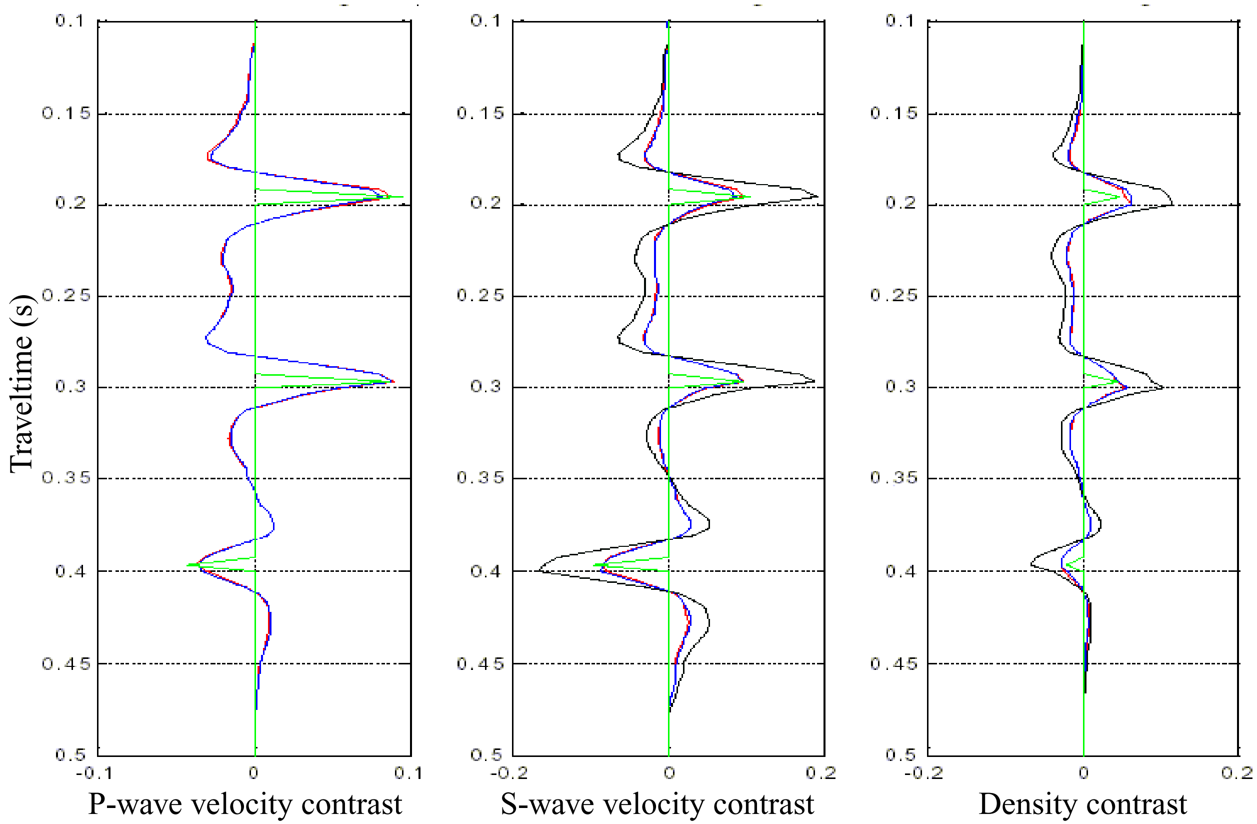

FIGURE 9. P-wave velocity contrast (left), S-wave velocity contrast (middle), and density contrast (right). The green curve is real changes, the blue curve is changes estimated from PP-data alone, the black curve is changes estimated from PS-data alone, whilst the red curve is changes estimated with joint PP- and PS-inversion.

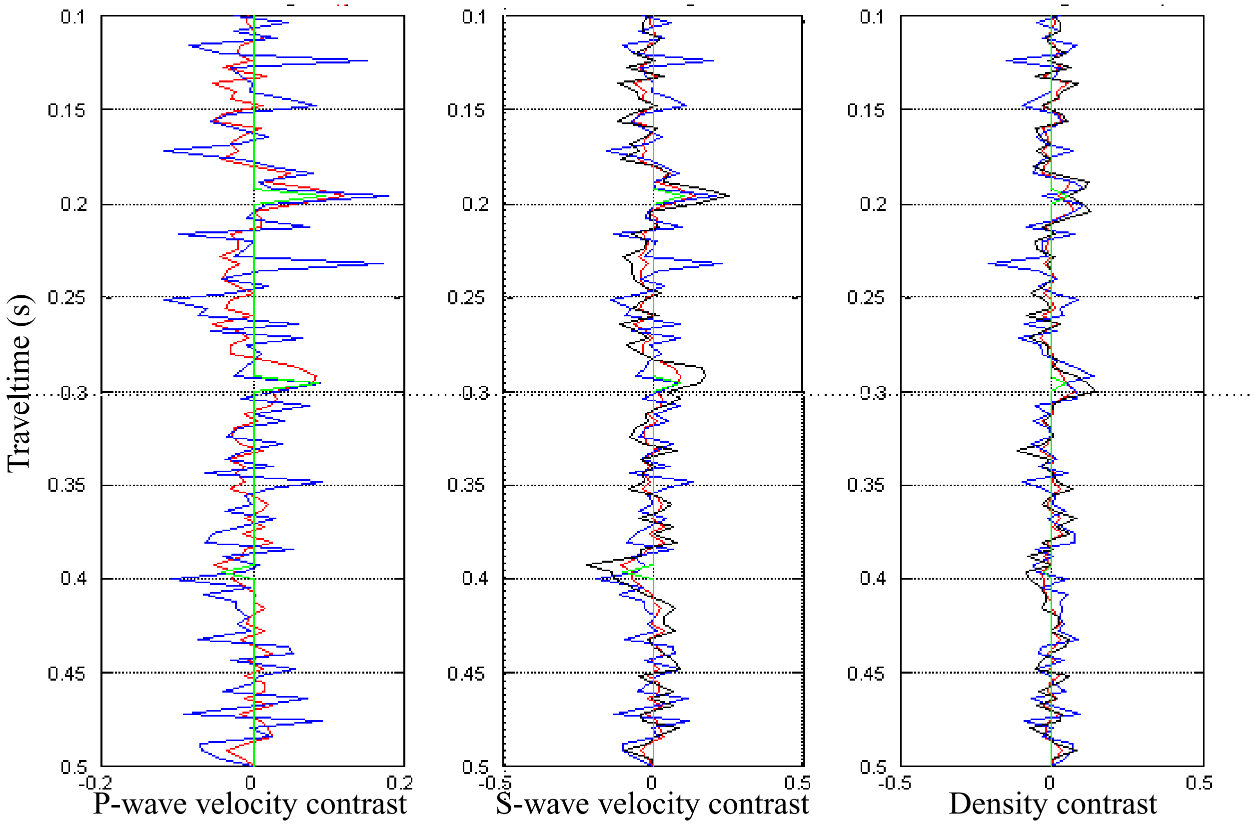

FIGURE 10. P-wave velocity contrast (left), S-wave velocity contrast (middle), and density contrast (right). The green curve is real changes, the blue curve is changes estimated from PP-data with noise, the black curve is changes estimated from PS-data with noise, whilst the red curve is changes estimated with joint PP- and PS-inversion on noisy data.

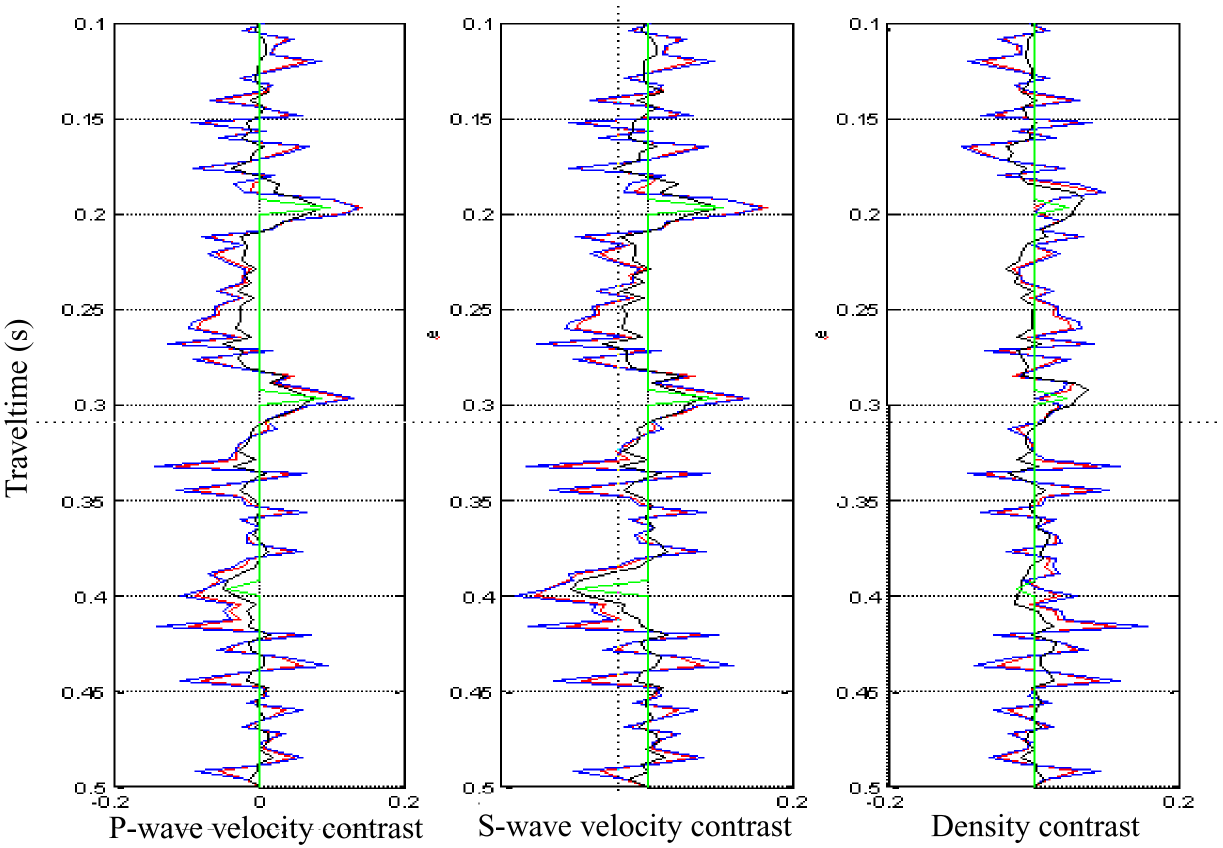

FIGURE 11. Inversion results using different weighting factors. The green curves are the real velocity and density contrasts, the red curves are results with no weighting, the blue curves represent results with most weight on PS seismic data (w=0.1), and the black curves represent results with most weight on PP seismic data (w=0.9).

Inversion of field 4C data

The inversion methodology has also been tested on a field multicomponent data set (Figure 12). The multicomponent survey consisted of 2 cables with a lateral separation of 300 m. The number of groups per receiver line was 800, and both x, y, z and a pressure component were acquired. Two sources with a separation of 50 m were used, and the depth of the sources was 6 m. The shot point interval was 25 m.

The seismic data was filtered with an anti-alias Butterworth filter before PP- (hydrophone) and Z-component (geophone) data were calibrated and summed (P/Z data) on a shot by shot basis. The PS reflections in the P/Z data are assumed to be negligible, thus P/Z data can be regarded as equivalent to PP seismic data. Static correction of receivers to surface was performed on PS data. The PS data is the radial component of the geophone data. The x- and y-component are rotated to identify the orientation that maximizes the radial component. The preprocessing was done by a seismic contractor. Spherical divergence correction and deconvolution was then applied. The P/Z dataset was DMO corrected, and the PS data was first NMO corrected before PS DMO was performed. Figure 13 shows move-out corrected gathers of prestack P/Z- and PS seismic data.

A depth varying V_p/V_s model was estimated from stacking velocities for P/Z- and PS data using Dix' formula, combined with interval velocities from a well log. Estimated V_p/V_s ratios were used to scale PS data from PS time to P/Z time by using the basic relationship between PS traveltime and PP traveltime together with a sinc interpolator. The PS traveltime (t_{PS}) is given by

$$t_{PS} = \frac{t_{PP}}{2}\left(1 + \frac{V_p}{V_s}\right) , \tag{8}$$

where t_{PP} is the two-way PP traveltime. The estimated V_p/V_s model was also used as background trend model in the inversion. The V_p/V_s model can alternatively be estimated by identification of corresponding reflection interfaces (event correlation) in PP and PS seismic data (Gaiser (1996), and Grechka et al. (2002)). If strong, characteristic reflections are present, event correlation does not require well logs to succeed. However, the confidence of the results benefits from correlation with well log data or well seismic data.

To convert from offset to angle domain we use

$$\theta \approx \arcsin\left(\frac{x \cdot V_{int}}{t \cdot V_{NMO}^2}\right) \quad , \tag{9}$$

from Snell's law and assuming hyperbolic moveout (Bale et al., 2001). Here, θ is the angle of incidence, x is the offset, t is the traveltime, V_{int} is the interval velocity, and V_{NMO} is the NMO-velocity (assumed to be equal to the RMS-velocity). A more precise method to compute angle distributions from offset distributions would be to use ray tracing.

Finally, seismic amplitudes were calibrated such that they represent reflection coefficients. From a set of given Vp, Vs and densities, a model of reflection coefficients for calibration was generated for one major reflection, and seismic amplitudes were scaled to the level of reflection coefficients. For velocities, the Vp and Vs trend models described above were used. Densities were estimated from Gardner's relation:

$$\rho = 1.741 \cdot Vp^{0.252} \quad , \tag{10}$$

where Vp is given in km/s and the density is given in g/cm^3 (Mavko et al. 1998) and compared with the available density log. Assuming that the AVO response of seismic data have been preserved during processing, only one calibration factor was used for all offsets.

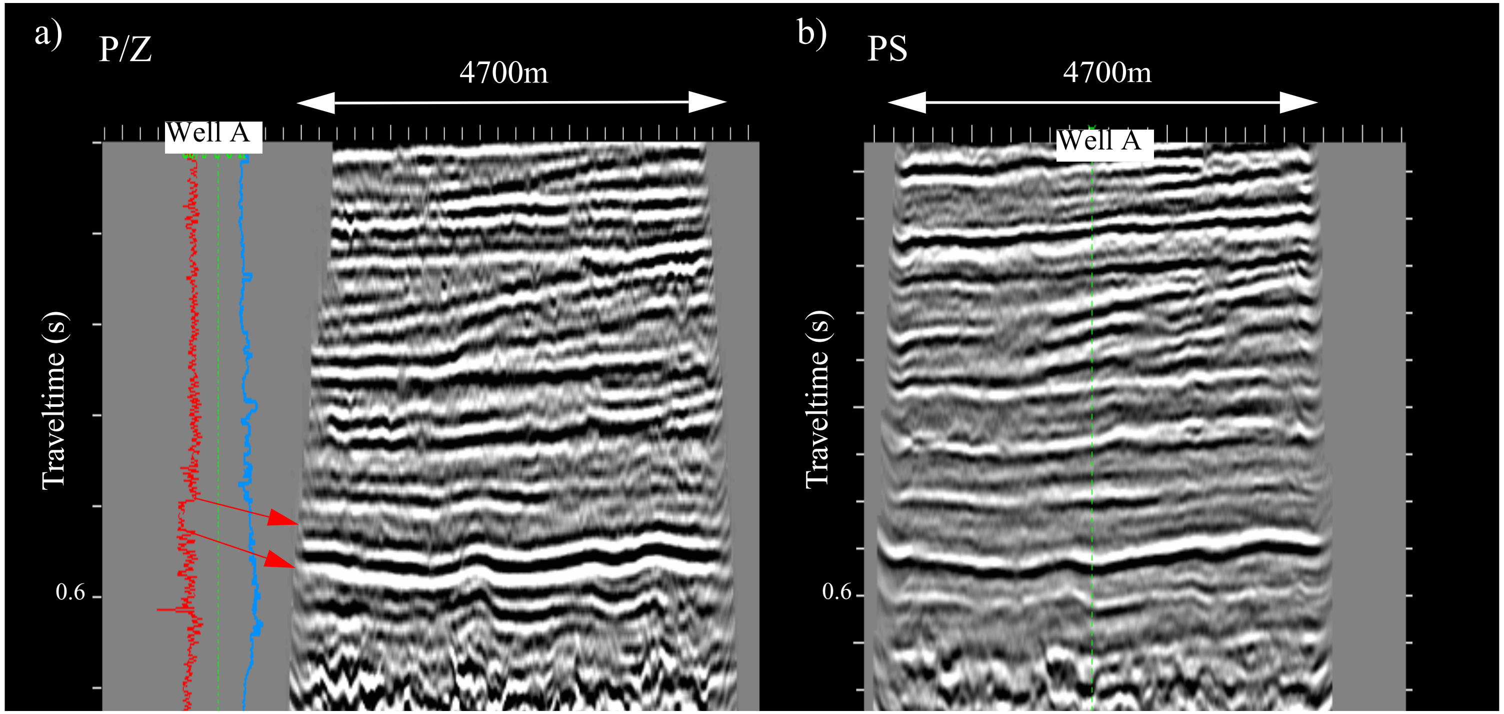

FIGURE 12. (a) P/Z-section with gamma-log (red curve) and density log (blue curve) from a well in the vicinity of the seismic line, and (b) PS-section in the shallow formation.

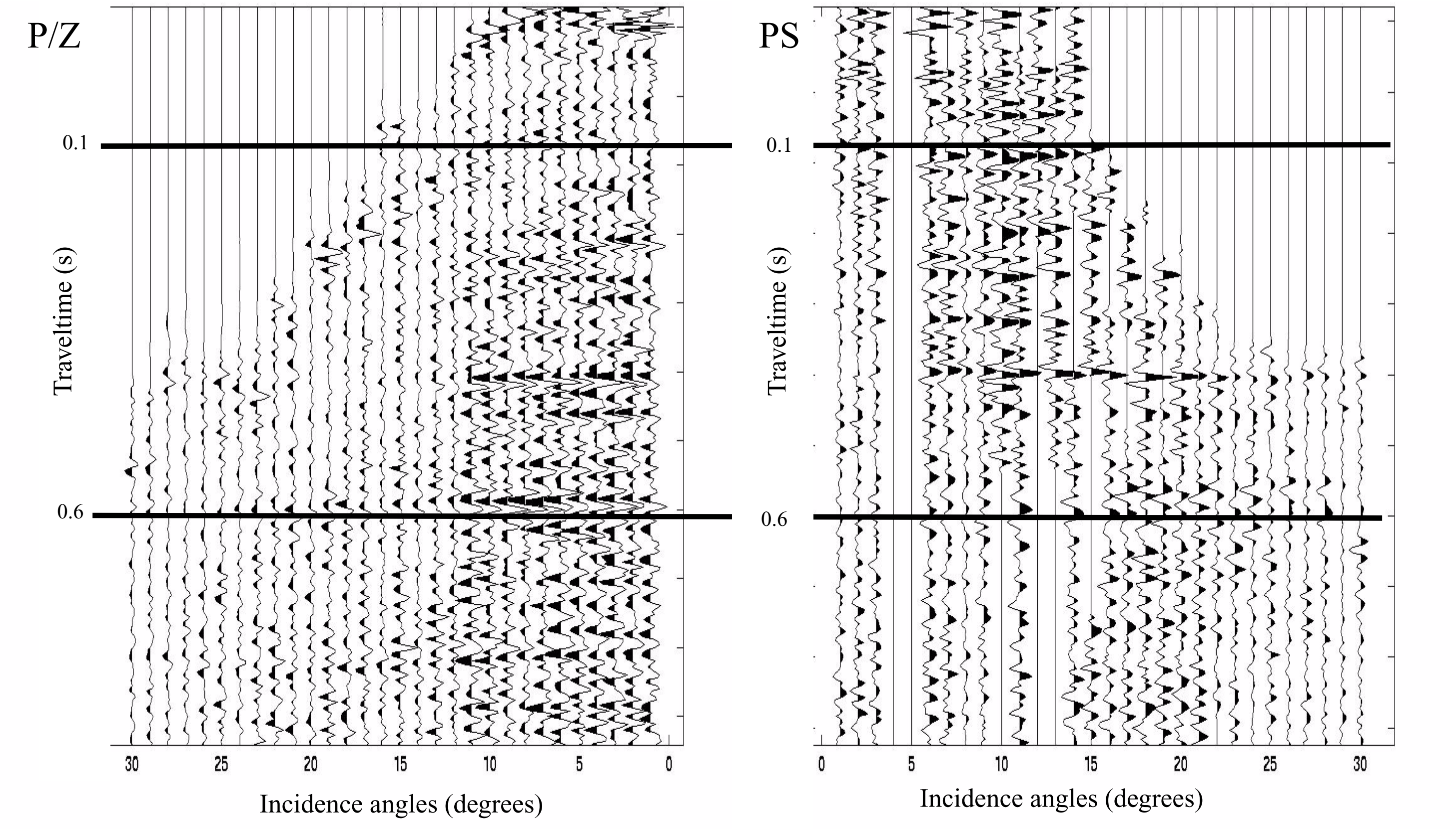

FIGURE 13. P/Z (left) and PS (right) NMO corrected prestack gathers after scaling the PS time to PP time. The inversion has been performed in the time window 0.1 - 0.6 s as indicated by the horizontal lines.

The inversion was performed in a time window containing sand layers in a shallow formation (Figure 12). The SVD damping was set with the same parameter for all traces, and the weighting factor was set to 0.5, meaning equal weight to PP and PS seismic data. The inversion was run point by point - one inversion run for each time and common depth point (cdp) location. Estimated P-velocity contrasts, S-velocity contrasts, density contrasts and the V_p/V_s contrasts are shown in Figures 14 and 15. The V_p/V_s contrast has been generated using $\Delta\left(\frac{Vp}{Vs}\right)/\left(\frac{Vp}{Vs}\right) \approx \frac{\Delta Vp}{Vp} - \frac{\Delta Vs}{Vs}$. Low-pass filtered well log contrasts are shown together with the inverted results. The log contrasts are generated by calculating $2 \cdot (a_{i+1} - a_i)/(a_{i+1} + a_i)$, where a_i are samples from the P-wave velocity log, the S-wave velocity log, the density log and the V_p/V_s contrast log, respectively. The well logs are taken from a well nearby where the thickness of the shallow formation is slightly smaller than the one along the seismic line. To compensate for this thickness difference, the well logs were stretched.

In this shallow formation, sand layers have been identified from seismic data and well logs. Around 0.6 s (figures 14 and 15) a strong contrast can be observed on inverted P-wave velocity, S-wave velocity and density contrasts, as well as on the V_p/V_s contrast. This contrast corresponds to the top of a sand layer located above the base reflector for the shallow formation. This strong event is also observed on the log contrasts. Weaker contrasts exist between 0.2s and 0.3s, corresponding to known thinner sand layers. These contrasts can also be observed on all inverted contrasts and on the log contrast for S-wave velocity and P-wave velocity. The density contrast generated from the well log is more noisy for the smaller layers, and the layers are also less pronounced on the inverted density section. The V_p/V_s contrast generated from logs show very distinct responses for all the sand layers. The smaller sand layers can also be identified on the V_p/V_s contrast generated from the inverted result, but they are not as distinct as on the log contrast. In general, the S-wave velocity and the V_p/V_s contrast show the best potential to identify sand layers, and there is a good agreement between inverted sections and the well logs. The velocity and density contrasts have been compared in value with corresponding log contrasts for the major reflector at 0.6 s. The P-wave velocity contrast varies between 1% and 2% along this reflector on the inverted section, and the log shows a value around 1%. The S-wave velocity contrast varies between 2% and 5% on the inverted section, and the log contrast shows 1%. The density contrast varies between 3% and 5%, while the log contrast shows a value of 8%. Finally, the V_p/V_s contrast varies between 2% and 4% along the reflector at 0.5 on the inverted section, while the log contrast has a value of 1%. The noise level in resulting velocity and density contrasts has been estimated by looking at the amplitude variations over a 40ms time window around the major reflection at 0.6 s. The noise level has the same magnitude for Vp contrast, Vs contrast and density contrast.

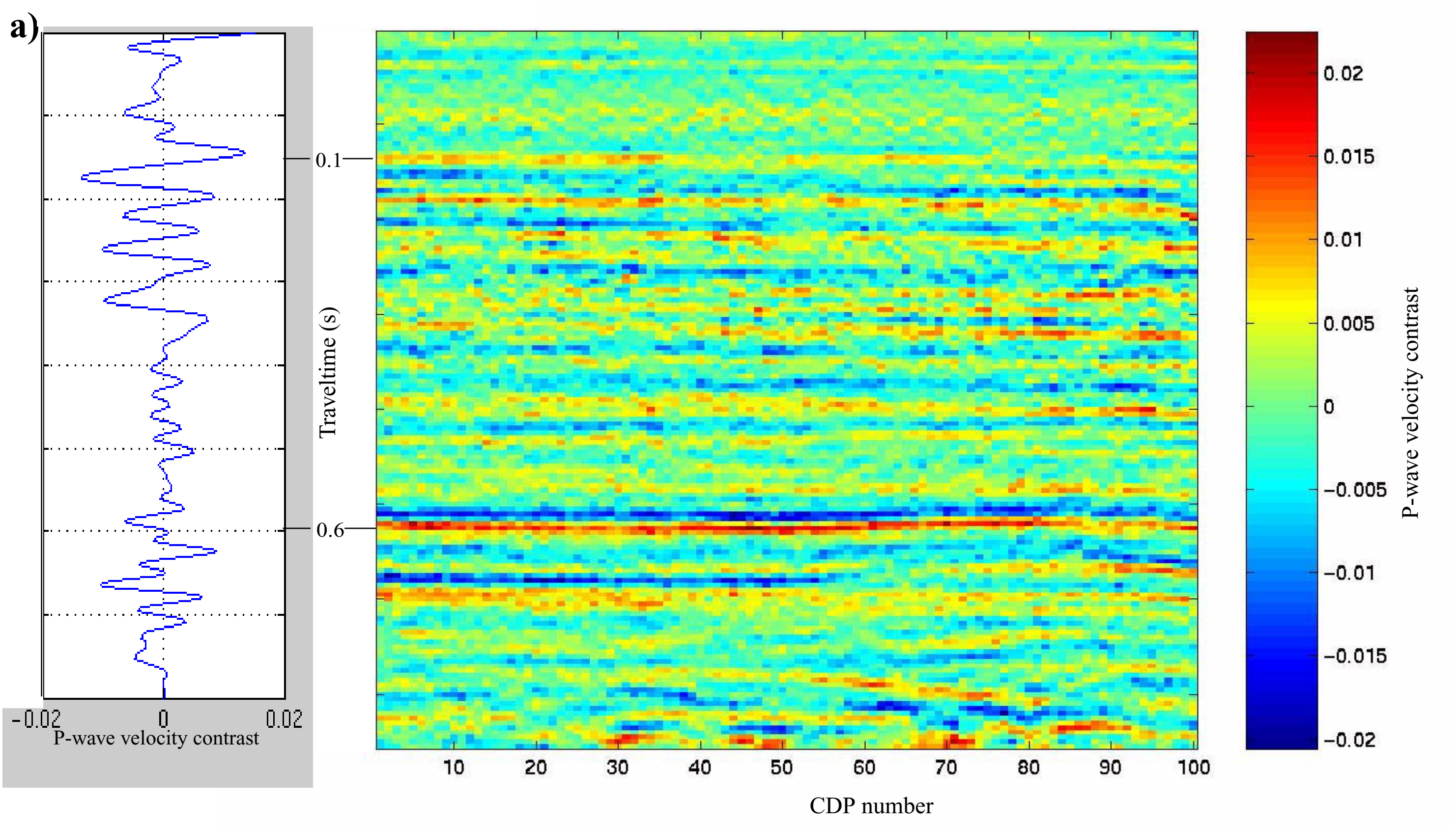

FIGURE 14a. Inverted sections; P-wave velocity contrast from log (left), and from joint inversion (right). The well logs are stretched to fit the interval on the seismic sections.

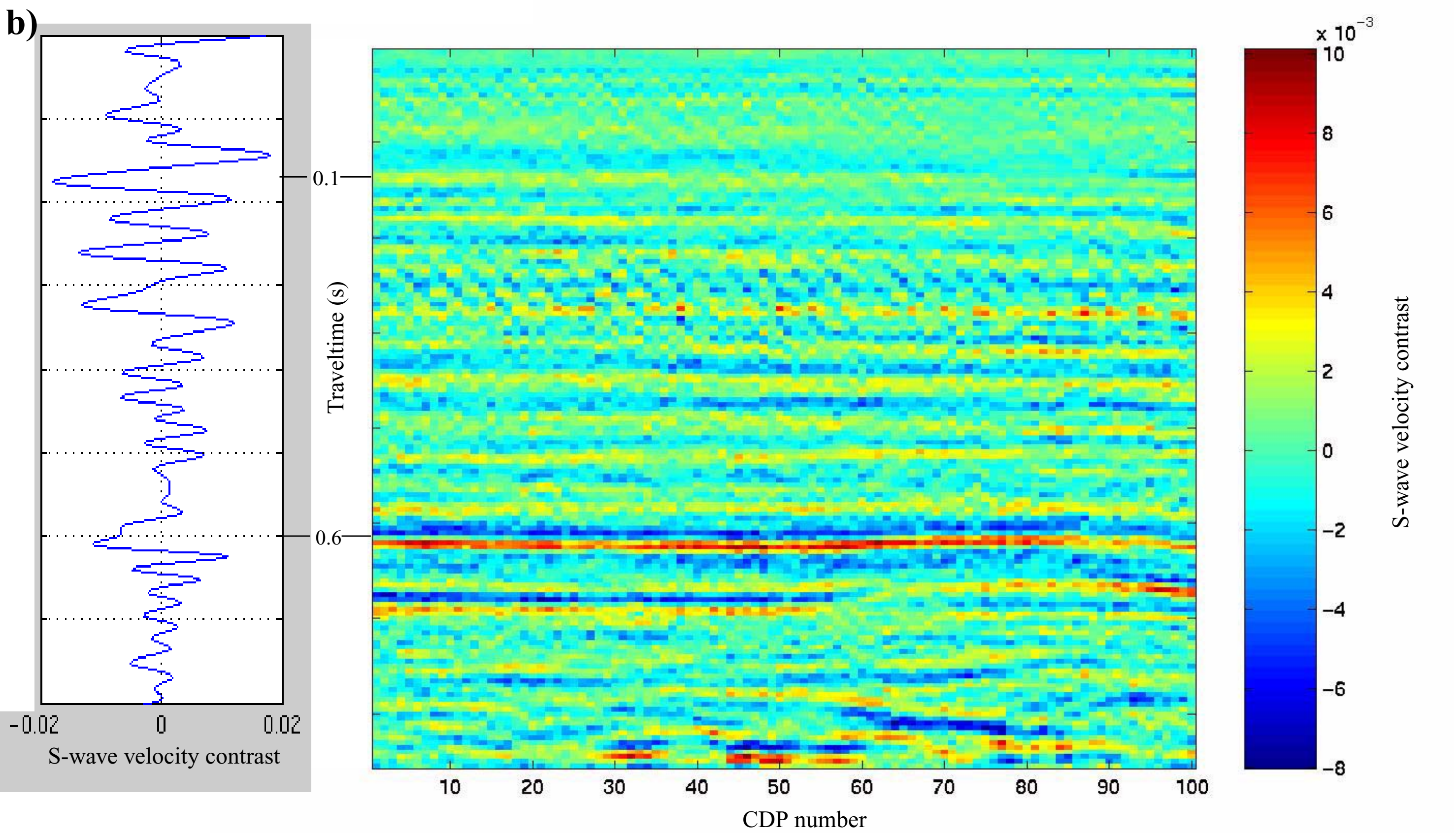

FIGURE 14b. Inverted sections; S-wave velocity contrast from log (left), and from joint inversion (right). The well logs are stretched to fit the interval on the seismic sections.

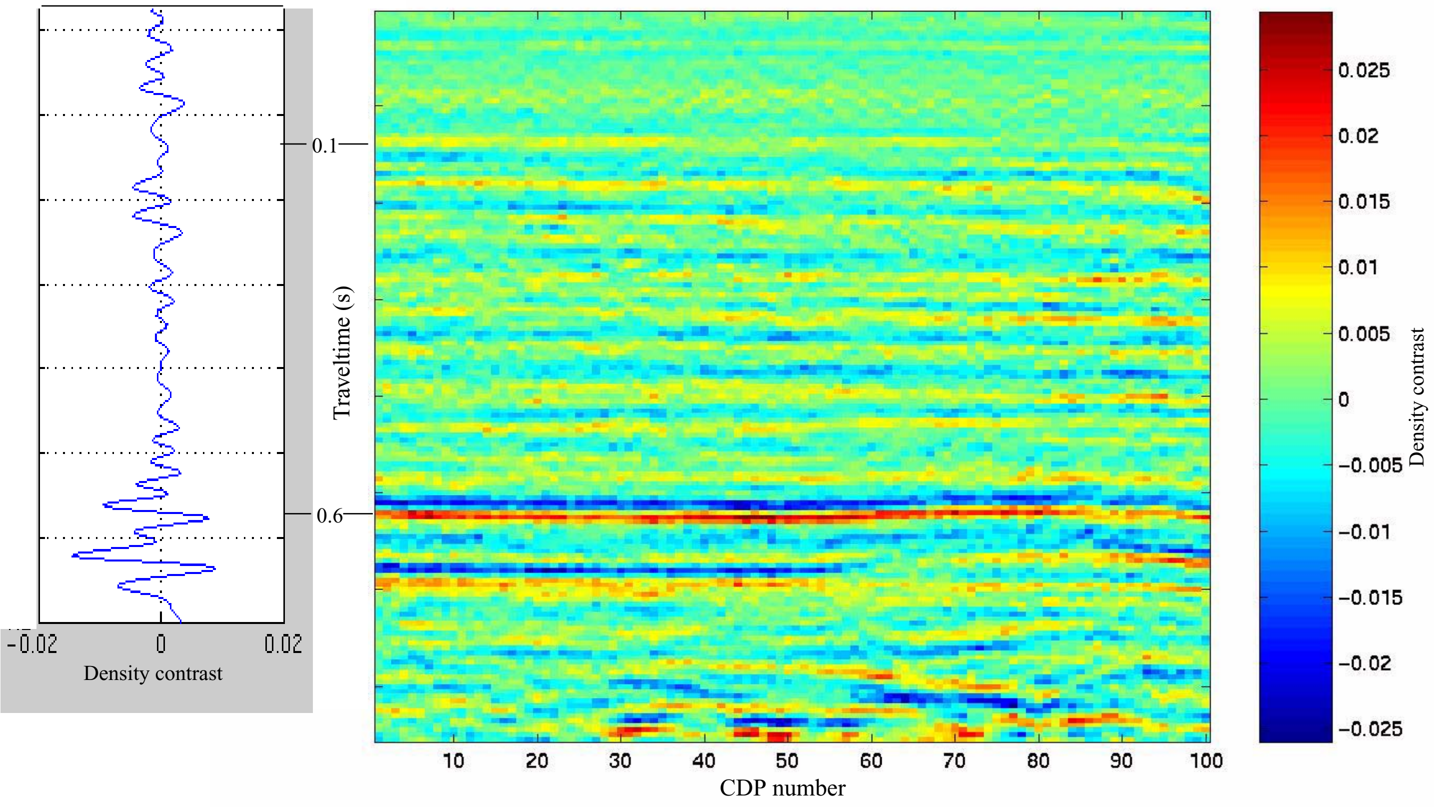

FIGURE 15a. Inverted sections; Density contrast from log (left), and from joint inversion (right). The well logs are stretched to fit the interval on the seismic sections.

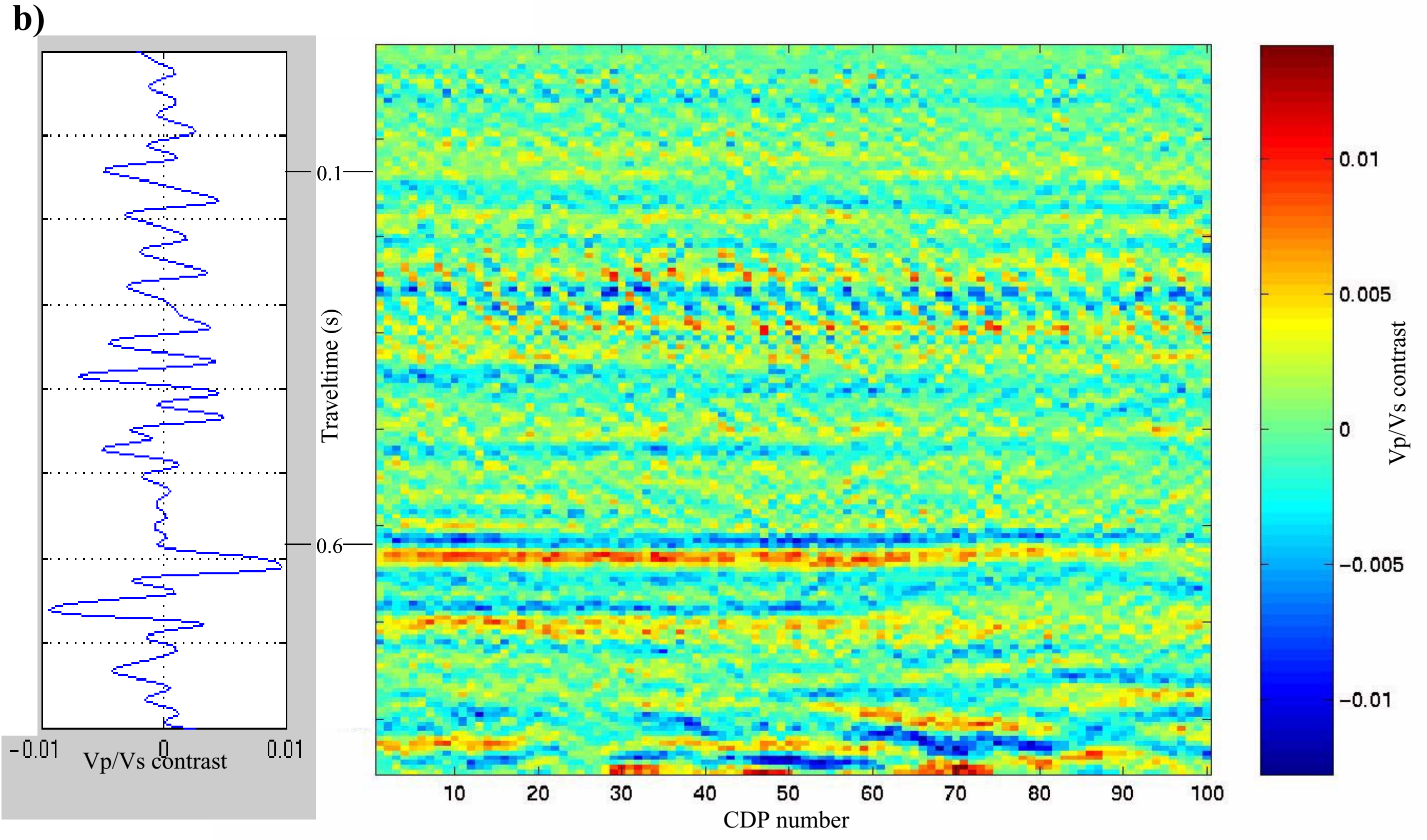

FIGURE 15b. Inverted sections; Vp/Vs-contrast from log (left), and from joint inversion (right). The well logs are stretched to fit the interval on the seismic sections.

Discussion

Results of synthetic tests show that joint inversion produces stable results when exposed to noise. The methodology is not sensitive to small variations in the V_p/V_s ratio. The joint inversion produces better results than both PP inversion and PS inversion for synthetic seismic data with noise. In addition, joint inversion also gives information of P-wave velocities that are unobtainable from PS seismic data alone.

The main challenge of the methodology is to convert PP and PS seismic amplitudes into true reflection coefficients. This step requires information from well logs. Other factors affecting the AVO response of the seismic data are absorption and the lack of true amplitude processing. Seismic waves travelling through the earth experience absorption. The inversion methodology does not take into account the effect of absorption on the AVO response. Inverse Q-filtering should be included in the seismic processing to remove the effect of absorption. True amplitude pre-stack time (or depth) migration is also a key step, but in most cases true amplitudes can not be guaranteed. In our field example, the geology consists of horizontal layers, and therefor amplitude errors are not as severe as for more complex geometries.

For horizontal layers and hyperbolic move-out (as in the shallow formation in the field data example) incidence angles can be estimated from the offset distribution using stacking velocities. However, for deeper layers in dipping formations, this procedure will introduce errors in the angle distributions. Uncertainty in incidence angles contributes most to the total uncertainty in density and velocity contrasts (Veire and Landrø, 2004), as is also observed for the synthetic tests presented here. This indicates that a better method for determining the incidence angles should be used for more complex reservoir geometries. A more precise angle distribution could be found by ray tracing methods.

The inversion does not include anisotropy in the earth model directly. However, the method requires seismic data to be properly NMO corrected as well as unambiguous

P and S event registration to produce meaningful results. In the presence of anisotropy, kinematic anisotropy should be taken into account when performing the NMO corrections on common conversion point (CCP) gathers.

If dipping layers are present, the assumption that the radial component of geophone data represents PS-event is not necessarily valid anymore. Furthermore, PP-sections might be polluted by shear energy. In the shallow example presented here, the layers are horizontal, and the assumptions made about PP- and PS seismic data should be valid.

Ma (2001) described an inversion method from P- and S-wave reflectivity data (P-velocity and S-velocity contrasts) to acoustic and shear impedances, pointing out a few problems with P- and S- contrasts; the results are boundary rather than layer effects, and the wavelet effects are still in the P- and S-contrasts. These problems are also relevant for the present method. One solution could be to implement an additional inversion scheme like the one presented by Ma (2001), going to layer velocities and layer density.

Conclusions

A joint inversion method for PP- and PS seismic data has been presented and tested on both synthetic seismic data and field multi-component seismic data. The new methodology requires no knowledge of wavelets from the two data sets, and this is seen as an advantage.

P-wave velocity contrasts, S-wave velocity contrasts, and density contrasts are computed for a simple synthetic 1D model. We find that the presented inversion technique is more stable than inversion of PP seismic data or PS seismic data alone. For synthetic data without noise, separate inversion methods produced results of the same quality as joint inversion. However, when 1% noise is added to the seismic data, the quality of the results from joint inversion is better than results from separate inversions. If PS seismic data contains more noise than PP seismic data, synthetic tests show that the quality of the results increases if PP data are weighted more than PS data in the inversion.

The joint inversion is not sensitive to errors in the background V_p/V_s model. Stable results were produced both with systematic errors and random noise in the V_p/V_s model. The inversion results are most affected by errors in incidence angles. Random noise in incidence angles produces results with some high frequency noise. However, the inversion results are sensitive to systematic errors above 4% in incidence angles.

Inversion of field data shows that sand layers identified from well logs can be identified on inverted sections. In this case study, the S-wave velocity contrast and the V_p/V_s contrast show the best correlation between well logs and seismic inversion, and have the best potential as lithology indicators. Estimated velocity and density contrasts have the same noise level when calculated in a 40 ms window around the major reflector at 0.6s.

Acknowledgements

We acknowledge the VISTA/Statoil research programme for financial support. Special thanks to Mark Thompson, Iren Måløy, Inger Kloster Osmundsen and Roy Sørbel for valuable help. Thanks to the associate editor and to reviewers for valuable comments.

Appendix A - Least squares system

The coefficients in the least square system of equations (Eqn. 4) is given below.

$$
\begin{aligned}
a_{11} &= \sum_{j=1}^{m} \frac{1}{2\cos^4\theta_{pj}} \qquad a_{12} = \sum_{j=1}^{m} -4\gamma^2(\tan\theta_{pj})^2 = a_{21} \\
a_{13} &= \sum_{j=1}^{m} \frac{1-4\gamma^2\sin^2\theta_{pj}}{2\cos^2\theta_{pj}} = a_{31} \\
a_{22} &= \sum_{i=1}^{n} \frac{8\sin^2\theta_{pi}}{\cos^2\theta_{si}} \cdot (\gamma^2\sin^2\theta_{pi} - \gamma\cos\theta_{pi}\cos\theta_{si})^2 + \sum_{j=1}^{m} 32\gamma^4\sin^4\theta_{pj} \\
a_{23} &= \sum_{i=1}^{n} \frac{-\sin^2\theta_{pi}}{2\cos^2\theta_{si}}(1-2\gamma^2\sin^2\theta_{pi} + 2\gamma\cos\theta_{pi}\cos\theta_{si})(4\gamma^2\sin^2\theta_{pi} - 4\gamma\cos\theta_{pi}\cos\theta_{si}) \\
&\quad - \sum_{j=1}^{m} (1-4\gamma^2\sin^2\theta_{pj})(4\gamma^2\sin^2\theta_{pj}) = a_{32} \\
a_{33} &= \sum_{i=1}^{n} \frac{\sin^2\theta_{pi}}{2\cos^2\theta_{si}}(1-2\gamma^2\sin^2\theta_{pi} + 2\gamma\cos\theta_{pi}\cos\theta_{si})^2 \\
&\quad + \sum_{j=1}^{m} \frac{1}{2}(1-4\gamma^2\sin^2\theta_{pj})^2 \\
b_1 &= \sum_{j=1}^{m} \frac{R^*{}_{PP}(\theta_p)}{\cos^2\theta_{pj}} \\
b_2 &= \sum_{i=1}^{n} R^*{}_{PS}(\theta_p, \theta_s)\frac{\sin\theta_{pi}}{\cos\theta_{si}}(4\gamma^2\sin^2\theta_{pi} - 4\gamma\cos\theta_{pi}\cos\theta_{si}) \\
&\quad - \sum_{j=1}^{m} 8R^*{}_{PP}(\theta_p)\gamma^2\sin^2\theta_{pj} \\
b_3 &= \sum_{i=1}^{n} -R^*{}_{PS}(\theta_p, \theta_s)\frac{\sin\theta_{pi}}{\cos\theta_{si}}(1-2\gamma^2\sin^2\theta_{pi} + 2\gamma\cos\theta_{pi}\cos\theta_{si}) \\
&\quad + \sum_{j=1}^{m} R^*{}_{PP}(\theta_p)(1-4\gamma^2\sin^2\theta_{pj})
\end{aligned}
\tag{A-1}
$$

Exploring the uncertainty in joint inversion of PP- and PS seismic data

Helene Hafslund Veire* and Martin Landrø*.
****Department of Petroleum Engineering and Applied Geophysics, Norwegian University of Science and Technology, N-7491 Trondheim, Norway.***

Presented at the 65th EAGE Conference and Exhibition in Stavanger, 2003. Submitted to Geophysical Prospecting.

Abstract

Relationships between rock physical parameters and seismic properties are often empirical and highly non-unique. To utilize rock physical information obtained from seismic data in reservoir modelling, it is essential to estimate associated uncertainties. Here, we have studied uncertainties in P-wave velocity contrasts, S-wave velocity contrasts, and density contrasts resulting from a joint inversion of PP- and PS-seismic data by assuming independent variables. The uncertainty is calculated both for an inversion method using Gardner's relationship between density and P-wave velocity as one of the basic assumptions, for a system using an empirical porosity-velocity relationship, and for a system using no relationship between velocity and density. We have investigated how total uncertainty varies as a function of uncertainty in measured PP- and PS-reflection coefficients, V_s/V_p model, and P-wave and S-wave incidence angles for joint inversion of PP and PS seismic data and for inversion

of PP seismic data alone. The calculations are presented for a simple two-layer synthetic model and multi-component field seismic data from the North Sea.

We find that the total uncertainty in P-wave velocity, S-wave velocity and density contrasts is lower for joint inversion of PP- and PS seismic data compared to the uncertainty in inversion of PP seismic data alone. In addition, the uncertainty is reduced by using empirical relationships between density and P-wave velocity to simplify the equation system. The S-wave velocity contrast has the largest total uncertainty, about twice the size of the uncertainty in the P-wave velocity. The density contrast has the same uncertainty as the P-wave velocity contrast.

Introduction

Elastic parameters derived from seismic data are valuable input in reservoir characterization since they can be related to lithology and fluid content of the reservoir through empirical velocity - porosity or velocity - pressure relationships. The empirical relations between physical properties of rocks and fluids and seismic data are highly non-unique, thus there are large uncertainties in reservoir models built from seismic data. To be able to utilize the information from seismic inversion in reservoir modelling and simulation, we need to quantify the uncertainty in the estimations. This can be done through a deterministic analysis of uncertainty by assuming independent variables in the calculations (Landrø, 2002), or by doing a more rigorous study in a stochastic framework, introducing both correlation between variables and spatial correlation (e.g. Mosegaard and Tarantola (1995), Bosch (1999), Malinverno and Leaney (2000), Eidsvik et al. (2002), Veire et al. (2004)).

Several authors, e.g. Tjåland and Ursin (1992), and de Nicolao et al. (1993), have studied the information content of the reflection coefficient matrix. It is difficult to get reliable estimates for more than two of three parameters when only PP seismic data is studied (Tjåland and Ursin, 1992). The problem of instability is less pronounced for linearized inversion of PS-data (see Jin, 1999 and Jin et al. 2000), since the linearized PS-reflection coefficient depends only on the S-wave velocity ratio and the density ratio. Simultaneous inversion techniques combining PP seismic data with SS seismic data was introduced by Lörtzer and Berkhout (1993). They showed that combining PP seismic data with SS seismic data using statistical inversion techniques improved the inversion results. Margrave et al. (2001) presented a joint inversion for PP- and PS seismic data using a weighted stacking technique, estimating acoustic and elastic impedance contrasts. Veire and Landrø (2001 and 2004) presented a least-squares joint inversion estimating P-wave velocity (V_p), S-wave velocity (V_s), and density (ρ) contrasts. Garotta et al. (2002) performed joint inversion of PP- and PS seismic data through extraction of V_p/V_s-sections, by combining time correlation of PP- and PS seismic data with AVO information.

In this study, we investigate uncertainties in P-wave velocity, S-wave velocity, and density contrasts resulting from the joint inversion techniques of PP- and PS-seismic data described by Veire and Landrø (2001, 2004) by assuming independent variables. For sandstone reservoirs, Gardner's relationship (Gardner et al, 1974) between P-wave velocity and density can be introduced to reduce the non-uniqueness of the equation system and thus stabilize the inversion. For chalk reservoirs, porosity-velocity relations are more precise than Gardner's relationship. For these reservoirs, an empirical relationship between porosity and P-wave velocity can be used together with the basic relationship between density and porosity. In order to evaluate the effect of simplifying the inversion by introducing empirical relationships between the different variables, the uncertainty is calculated both for a system using Gardner's relationship between density and velocity, for a system using an empirical porosity-velocity relationship, and for a system using no relationship between velocity and density.

The inversion method presented here require as input a trend model of the V_s/V_p model, information about P- and S-wave incidence angles, and PP- and PS-seismic amplitudes calibrated to reflection coefficients. Both the V_s/V_p model and the information about P-and S-wave incidence angles can be obtained from stacking velocities, but there can be large uncertainties related to this process. The V_s/V_p model uncertainties are related to mispicking of stacking velocities, estimation of interval velocities from stacking velocities using Dix' formula, and to the fact that we use a coarse trend model instead of detailed interval velocities. Uncertainties in incidence angles are also related to stacking velocities and the conversion to interval velocities, and the fact that we use Snell's law to estimate the angles. These calculations are only valid for horizontal isotropic layers. When anisotropy and dipping layers are present, wavefronts are not always perpendicular to raypaths. Uncertainties can be reduced by using a ray tracing procedure to determine angle distributions, but uncertainties caused by errors in the velocity model will still be present. In addition to noise already in the data, calibrating PP- and PS seismic amplitudes to reflection coefficients might introduce serious systematic errors. For the simplified system using Gardner's equation and the porosity-velocity relationship, we also have uncertainties related to the empirical relationships. These are included in the analysis, through uncertainties in the parameters in the empirical relationships. The uncertainties in the empirical parameters can be estimated by looking at confidence intervals of the empirical relationships.

In this paper we have investigated how the total uncertainty of the inverted velocity and density contrasts varies as a function of uncertainty in measured PP- and PS-reflection coefficients, the V_s/V_p model, and P-wave and S-wave incidence angles. No uncertainty from other sources, e.g. overburden effects, source directivity, or topography, have been included in the analysis.

First, the inversion methodology will be presented for the three inversion systems. Next, the derivation of the uncertainty is shown. Finally, uncertainty calculations are demonstrated for a simple two-layer synthetic model and field multi-component seismic data from the North Sea.

Methodology

Aki and Richard's (1980) approximations of the Zoeppritz's equations for PP and PS reflection coefficients for a two-layer model are given by:

$$R_{PP}(\theta_p) = \frac{1}{2}(1-4\gamma^2\sin^2\theta_p)\frac{\Delta\rho}{\rho} + \frac{1}{2\cos^2\theta_p}\frac{\Delta V_p}{V_p} - 4\gamma^2\sin^2\theta_p\frac{\Delta V_s}{V_s} \quad , (1)$$

$$\begin{aligned} R_{PS}(\theta_p, \theta_s) = {} & 2\frac{\sin\theta_p}{\cos\theta_s}[\gamma^2\sin^2\theta_p - \gamma\cos\theta_s\cos\theta_p]\frac{\Delta V_s}{V_s} \\ & -\frac{\sin\theta_p}{2\cos\theta_s}[1-2\gamma^2\sin^2\theta_p + 2\gamma\cos\theta_p\cos\theta_s]\frac{\Delta\rho}{\rho} \end{aligned} \quad . (2)$$

Here, $\Delta V_p = V_{p2} - V_{p1}$, $V_p = (V_{p1} + V_{p2})/2$, and $\gamma = V_s/V_p$. V_{p1} and V_{p2} are velocities above and below the interface respectively. θ_p is P-wave incidence angle, and θ_s is S-wave incidence angle.

By combining PP- and PS reflection coefficients and doing a least square estimation, we solve the equation system for relative changes in P-wave velocity $\Delta V_p/V_p$, S-wave velocity $\Delta V_s/V_s$, and density $\Delta\rho/\rho$. The least square system is defined as (Veire and Landrø, 2001, 2004)

$$LS = \sum_{i=1}^{n}[R^*_{PS}(\theta_{p,i}, \theta_{s,i}) - R_{PS}(\theta_{p,i}, \theta_{s,i})]^2 + \sum_{j=1}^{m}[R^*_{PP}(\theta_{p,j}) - R_{PP}(\theta_{p,j})]^2 \quad (3)$$

Here, R_{Px} is linearized PP and PS reflection coefficients defined above, where x is either P or S. R^*_{Px} indicates measured seismic data (PP and PS) where the amplitudes are calibrated to represent reflection coefficients. The summation is done over all incidence angles for PP reflection coefficients ($j = 1\ldots m$) and PS reflection coefficients ($i = 1\ldots n$). It is also possible to include a weighting of the PP and PS seismic data, see Veire and Landrø (2004) for further details. To find the least square solution, we differentiate the equation system with respect to $\Delta\rho/\rho$, $\Delta V_p/V_p$, and $\Delta V_s/V_s$, and find the minimum values. This yields a system of equations:

$$\mathbf{A}\cdot\left[\frac{\Delta V_p}{V_p}\ \frac{\Delta V_s}{V_s}\ \frac{\Delta\rho}{\rho}\right]^T = c, \qquad (4)$$

where $\mathbf{A}$ is a 3x3 matrix, and c is a 3x1 vector. $\mathbf{A}$ is symmetrical, and depends only on the angle of incidence and a trend model of the P-wave velocity and the S-wave velocity**,** while the vector c also depends on the information about the PP- and PS reflection coefficients as a function of angle in the seismic data. Using the original Aki and Richard's reflection coefficients, $\mathbf{A}$ and c for the system are given in Appendix A.

The resulting equation system can be solved using Singular Value Decomposition to stabilize the inversion. However, it is also possible to include empirical relationship between e.g. P-wave velocity and density to reduce the equation system. Both Smith and Gidlow (1987) and Margrave et al. (2001) used Gardner's relationship (Gardner et al, 1974) between P-wave velocity and density to simplify the inversion. Lörtzer and Berkhout (1993) also prefered to use empirical relationships instead of mathematical stabilization, since this is more geologically meaningful. In this study, we have used Gardner's relationship between P-wave velocity and density and a relationship between P-wave velocity and porosity to reduce the equation system and stabilize the inversion. Gardner's relationship (Gardner et al, 1974) can be given as

$$\rho = a_1 V_p^{\ b_1} \quad , \qquad (5)$$

where a_1=1.741, and b_1=0.25 for P-wave velocity in km/s and density in g/cm^3. Differentiating this expression gives the relative change in density as a function of the relative change in P-wave velocity as $\Delta\rho/\rho = b_1(\Delta V_p/V_p)$. Inserting this expression in Aki and Richard's (1980) expressions for P- and S-wave reflection coefficients gives

$$R_{PP}(\theta_p) = \frac{1}{2}\left(b_1 - 4b_1\gamma^2\sin^2\theta_p + \frac{1}{(\cos\theta_p)^2}\right)\frac{\Delta V_p}{V_p} - 4\gamma^2\sin^2\theta_p\frac{\Delta V_s}{V_s} \quad .(6)$$

$$\begin{aligned} R_{PS}(\theta_p, \theta_s) &= 2\frac{\sin\theta_p}{\cos\theta_s}[\gamma^2\sin^2\theta_s - \gamma\cos\theta_s\cos\theta_p]\frac{\Delta V_s}{V_s} \\ &-\frac{b_1\sin\theta_p}{2\cos\theta_s}[1 - 2\gamma^2\sin^2\theta_s + 2\gamma\cos\theta_p\cos\theta_s]\frac{\Delta V_p}{V_p} \end{aligned} \quad .(7)$$

Using the least squares formulation presented above (Eqn. 3), the new 2x2 matrix **A** and vector **c** is given in .

Gardner’s relationship is normally used for sandstone reservoirs, especially in the Gulf of Mexico. For chalk reservoirs, empirical relationships between P-wave velocity and porosity used together with the basic relationship between density and porosity can be used to find a more suitable relationship between P-wave velocity and density:

$$\begin{aligned} V_p &= a_2 + b_2\phi \qquad \rho = \rho_F\phi + \rho_S(1-\phi) \\ \rho &= \rho_F\left(\frac{V_p - a_2}{b_2}\right) + \rho_S\left(1 - \left(\frac{V_p - a_2}{b_2}\right)\right) \end{aligned} \quad . \quad (8)$$

Here, ρ_F is the density of the reservoir fluid, ρ_S is the density of the matrix, ρ is the bulk density, and ϕ is the porosity. The factors a_2 and b_2 are empirical constants that need to be determined for each field. Differentiating this expression gives the relative change in density as a function of the relative change in P-wave velocity

$$(\Delta\rho/\rho) = \frac{V_p(\rho_F - \rho_S)}{b_2\rho}\cdot(\Delta V_p/V_p). \quad (9)$$

Inserting this expression in Aki and Richard’s (1980) expressions for the P- and S-wave reflection coefficients gives

$$R_{PP}(\theta_p) = \frac{1}{2}\left((1-4\gamma^2\sin^2\theta_p)\frac{V_p(\rho_F-\rho_S)}{b_2\rho}+\frac{1}{(\cos\theta_p)^2}\right)\frac{\Delta V_p}{V_p}-4\gamma^2\sin^2\theta_p\frac{\Delta V_s}{V_s}. \tag{10}$$

$$\begin{aligned} R_{PS}(\theta_p, \theta_s) = {} & 2\frac{\sin\theta_p}{\cos\theta_s}[\gamma^2\sin^2\theta_s-\gamma\cos\theta_s\cos\theta_p]\frac{\Delta V_s}{V_s} \\ & -\frac{\sin\theta_p}{2\cos\theta_s}[1-2\gamma^2\sin^2\theta_s+2\gamma\cos\theta_p\cos\theta_s]\left(\frac{V_p(\rho_F-\rho_S)}{b_2\rho}\right)\frac{\Delta V_p}{V_p} \end{aligned} \tag{11}$$

Using the least squares formulation presented above (Eqn. 3), the new 2x2 matrix **A** and the vector **c** is given in .

To explore the uncertainty in the results of these different joint inversion algorithms, we assume that there is no correlation between the different parameters. For a function $S(x, y, \ldots)$ the uncertainty in uncorrelated parameters is given by

$$\delta S = \sqrt{\left(\frac{\partial S}{\partial x}\cdot\delta x\right)^2+\left(\frac{\partial S}{\partial y}\cdot\delta y\right)^2+\ldots} \quad . \tag{12}$$

Here, δS is total uncertainty in S, $\partial S/\partial x$ is partial derivative of the function S with respect to the parameter x, δx is uncertainty in the parameter x, etc. We investigate uncertainties for the basic system (Eqn. 3), the system with Gardner's relation, and the system using the empirical relationship between velocity and porosity. Uncertainties are calculated by differentiating the solutions of the least squares equation system. Uncertainties are calculated as a function of uncertainties of measured PP reflection coefficients, measured PS reflection coefficients, the V_s/V_p model (γ), P- and S- incidence angles, the Gardner-parameter b_1, and the parameter b_2 from the porosity-velocity relationship. The exact solutions are given in Appendices A and B, together with the derivatives of the expressions.

Results

Synthetic example

The uncertainties in relative change in P-wave velocity, S-wave velocity and density have been estimated for a two-layer synthetic model and multicomponent field seismic data from the North Sea. The synthetic model is described in Table 1. The PP- and PS reflection coefficients were estimated using Zoeppritz's equations; the AVA-response (Amplitude versus angle) for this model is shown in Figure 1. To investigate how the different parameters affect the uncertainty of the inversion results, the uncertainty caused by the parameters have been added successively to the total uncertainty.

Vp (m/s)	Vs (m/s)	Density (kg/m^3)
2000	900	2100
2200	1000	2200

Table 1: Two layer synthetic model

As an example, we present expressions for uncertainties in V_p, V_s and density contrasts as a function of uncertainty in measured PP and PS reflection coefficients only, for the basic equation system, the equation system with Gardner's relationship, and the equation system with an empirical porosity-velocity relationship. The derivatives of the matrices A and c with respect to the measured PP- and PS reflection coefficients for all three cases are given in . The expressions for the other derivatives are more complicated and will not be presented here.

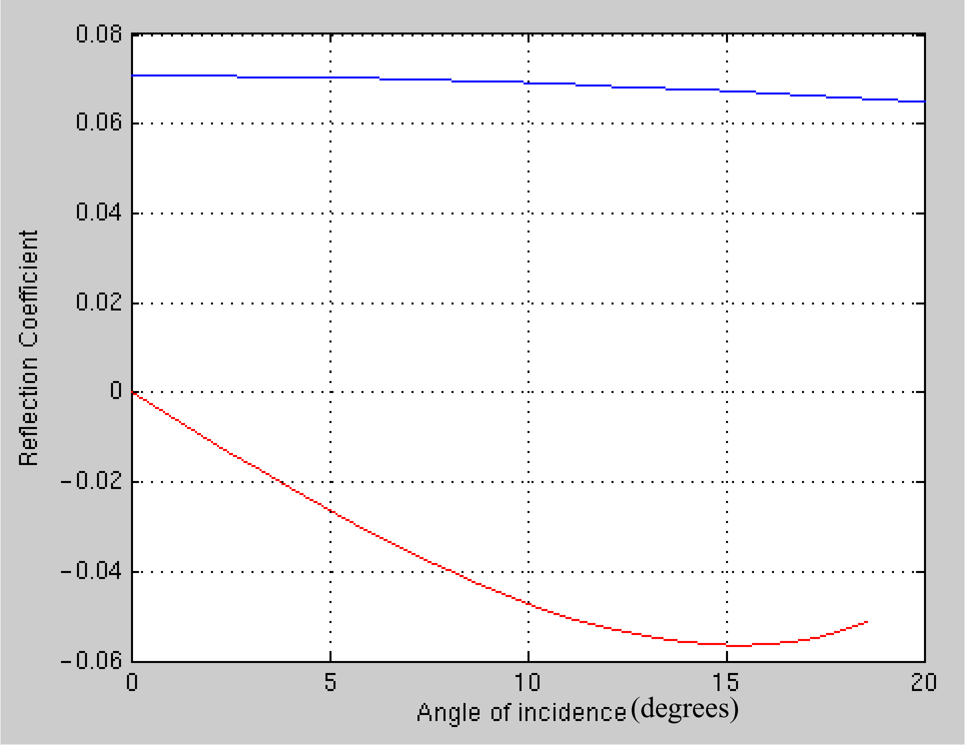

FIGURE 1. Plot of AVA response for synthetic model with PS reflection coefficient in red and PP reflection coefficient in blue.

For the model presented above, the matrices A and c (Eqn. 4 and Appendix A) for basic reflection coefficients are given by

$$A = \begin{bmatrix} 14.44 & -2.75 & 10.82 \\ -2.75 & 3.35 & 1.43 \\ 10.82 & 1.43 & 12.46 \end{bmatrix} \qquad c = \begin{bmatrix} 1.59 \\ 0.15 \\ 1.76 \end{bmatrix} , \tag{13}$$

Here, the first column of the matrix A is related to P-wave velocity contrast in the least squares equation system, the second column is related to S-wave velocity contrast, and the third column is related to density contrast. For the equation system with Gardner's relationship we get

$$A = \begin{bmatrix} 10.04 & -1.21 \\ -1.21 & 1.68 \end{bmatrix} \qquad c = \begin{bmatrix} 1.00 \\ 0.08 \end{bmatrix} . \tag{14}$$

The first column of A is related to P-wave velocity contrast in the least squares equation system, and the second column is related to S-wave velocity contrast. For the equation system with the empirical porosity-velocity relationship the system is given by

$$A = \begin{bmatrix} 21.23 & -0.76 \\ -0.76 & 1.68 \end{bmatrix} \qquad c = \begin{bmatrix} 1.56 \\ 0.08 \end{bmatrix} . \tag{15}$$

Again, the first column of A is related to P-wave velocity contrast in the least squares equation system, and the second column is related to S-wave velocity contrast. This gives for the derivatives of the basic system with respect to measured PP and PS reflection coefficients

$$\begin{array}{lll} \frac{\partial}{\partial Rpp}\left(\frac{\Delta Vp}{Vp}\right) = -0.53 & \frac{\partial}{\partial Rpp}\left(\frac{\Delta Vs}{Vs}\right) = 2.67 & \frac{\partial}{\partial Rpp}\left(\frac{\Delta \rho}{\rho}\right) = 2.29 \\ \frac{\partial}{\partial Rps}\left(\frac{\Delta Vp}{Vp}\right) = -10.60 & \frac{\partial}{\partial Rps}\left(\frac{\Delta Vs}{Vs}\right) = 15.79 & \frac{\partial}{\partial Rps}\left(\frac{\Delta \rho}{\rho}\right) = 10.13 \end{array} ,(16)$$

for the system with Gardner’s relationship;

$$\begin{array}{lll} \frac{\partial}{\partial Rpp}\left(\frac{\Delta Vp}{Vp}\right) = 2.73 & \frac{\partial}{\partial Rpp}\left(\frac{\Delta Vs}{Vs}\right) = 0.71 & \frac{\partial}{\partial Rpp}\left(\frac{\Delta \rho}{\rho}\right) = 0.63 \\ \frac{\partial}{\partial Rps}\left(\frac{\Delta Vp}{Vp}\right) = -0.51 & \frac{\partial}{\partial Rps}\left(\frac{\Delta Vs}{Vs}\right) = -3.15 & \frac{\partial}{\partial Rps}\left(\frac{\Delta \rho}{\rho}\right) = -0.12 \end{array} \tag{17}$$

and for the system with the empirical porosity-velocity relation;

$$\begin{array}{lll} \frac{\partial}{\partial Rpp}\left(\frac{\Delta Vp}{Vp}\right) = 1.51 & \frac{\partial}{\partial Rpp}\left(\frac{\Delta Vs}{Vs}\right) = -0.58 & \frac{\partial}{\partial Rpp}\left(\frac{\Delta \rho}{\rho}\right) = 1.31 \\ \frac{\partial}{\partial Rps}\left(\frac{\Delta Vp}{Vp}\right) = -0.33 & \frac{\partial}{\partial Rps}\left(\frac{\Delta Vs}{Vs}\right) = -2.93 & \frac{\partial}{\partial Rps}\left(\frac{\Delta \rho}{\rho}\right) = -0.29 \end{array} \tag{18}$$

The total uncertainty in the P-wave contrast ($\delta(\Delta V_p/V_p)$), the S-wave contrast ($\delta(\Delta V_s/V_s)$), and the density contrast ($\delta(\Delta\rho/\rho)$) as a function of the measured PP and PS reflection coefficients only are given as (assuming independent variables)

$$\begin{aligned}
\delta\left(\frac{\Delta V_p}{V_p}\right) &= \sqrt{\left(\frac{\partial}{\partial Rpp}\left(\frac{\Delta V_p}{V_p}\right)\cdot \delta Rpp\right)^2 + \left(\frac{\partial}{\partial Rps}\left(\frac{\Delta V_p}{V_p}\right)\cdot \delta Rps\right)^2}\\
\delta\left(\frac{\Delta V_s}{V_s}\right) &= \sqrt{\left(\frac{\partial}{\partial Rpp}\left(\frac{\Delta V_s}{V_s}\right)\cdot \delta Rpp\right)^2 + \left(\frac{\partial}{\partial Rps}\left(\frac{\Delta V_s}{V_s}\right)\cdot \delta Rps\right)^2}\\
\delta\left(\frac{\Delta \rho}{\rho}\right) &= \sqrt{\left(\frac{\partial}{\partial Rpp}\left(\frac{\Delta \rho}{\rho}\right)\cdot \delta Rpp\right)^2 + \left(\frac{\partial}{\partial Rps}\left(\frac{\Delta \rho}{\rho}\right)\cdot \delta Rps\right)^2}
\end{aligned} \quad , \quad (19)$$

Here, δRpp is the uncertainty in the measured PP reflection coefficient, and δRps is the uncertainty in the measured PS reflection coefficient. The results for different uncertainties in the PP and PS reflection coefficient are shown in Tables 2 to 4. In Figures 2 to 4 the uncertainty in the relative change in P-wave velocity, S-wave velocity and density as a function of the uncertainty in the measured PP- and PS reflection coefficients are shown for the joint inversion, joint inversion with Gardner's relationship, and for joint inversion with the empirical porosity-velocity relationship. The uncertainty in PP-inversion as a function of the measured PP reflection coefficient and the P-wave angle of incidence is also shown in these figures. We observe that the total uncertainty is largest for the S-wave velocity for all three cases. This is in accordance with what we observe by calculating $\partial(\Delta V_p/V_p)/(\partial Rpp)$, $\partial(\Delta V_s/V_s)/(\partial Rpp)$, and $\partial(\Delta\rho/\rho)/(\partial Rpp)$ from Eqn. 1; $\partial(\Delta V_p/V_p)/(\partial Rpp)$ and $\partial(\Delta\rho/\rho)/(\partial Rpp)$ are of the same size, while $\partial(\Delta V_s/V_s)/(\partial Rpp)$ is by far the largest.

	d(Vp-contrast)	d(Vs-contrast)	d(ρ-contrast)
dRpp=0, dRps=0.005	0.0530	0.0790	0.0506
dRpp=0.005, dRps=0	0.0027	0.0134	0.0114
dRpp=0.005, dRps=0.005	0.0531	0.0801	0.0519

Table 2: Uncertainties in the relative density and velocity contrasts, basic system

	d(Vp-contrast)	d(Vs-contrast)	d(ρ-contrast)
dRpp=0, dRps=0.005	0.0025	0.0157	0.0006
dRpp=0.005, dRps=0	0.0137	0.0036	0.0031
dRpp=0.005, dRps=0.005	0.0139	0.0161	0.0314

Table 3: Uncertainties in the relative density and velocity contrasts, with Gardner’s relationship

	d(Vp-contrast)	d(Vs-contrast)	d(ρ-contrast)
dRpp=0, dRps=0.005	0.0017	0.0147	0.0014
dRpp=0.005, dRps=0	0.0076	0.0029	0.0065
dRpp=0.005, dRps=0.005	0.0077	0.0149	0.0067

Table 4: Uncertainties in the relative density and velocity contrasts, with an empirical porosity-velocity relationship

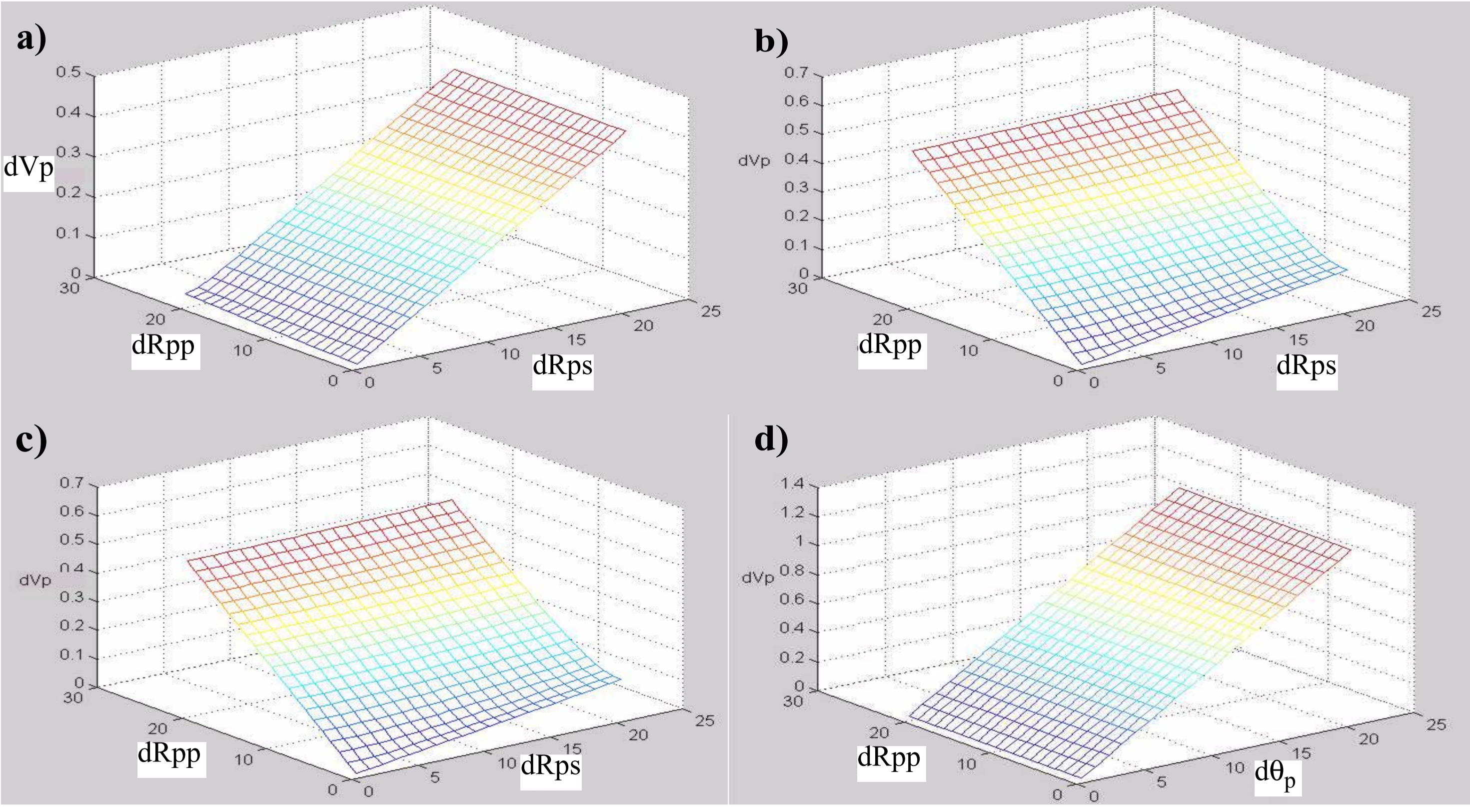

FIGURE 2. Uncertainty in estimated P-wave velocity contrast as a function of uncertainty in the measured PP - and PS-reflection coefficient for a) the basic equation system, b) the system with Gardner's relationship, c) the system with empirical porosity-velocity relationship. d) Uncertainty in P-wave velocity contrast as a function of measured PP reflection coefficient and P-wave angle of incidence for inversion of PP seismic data.

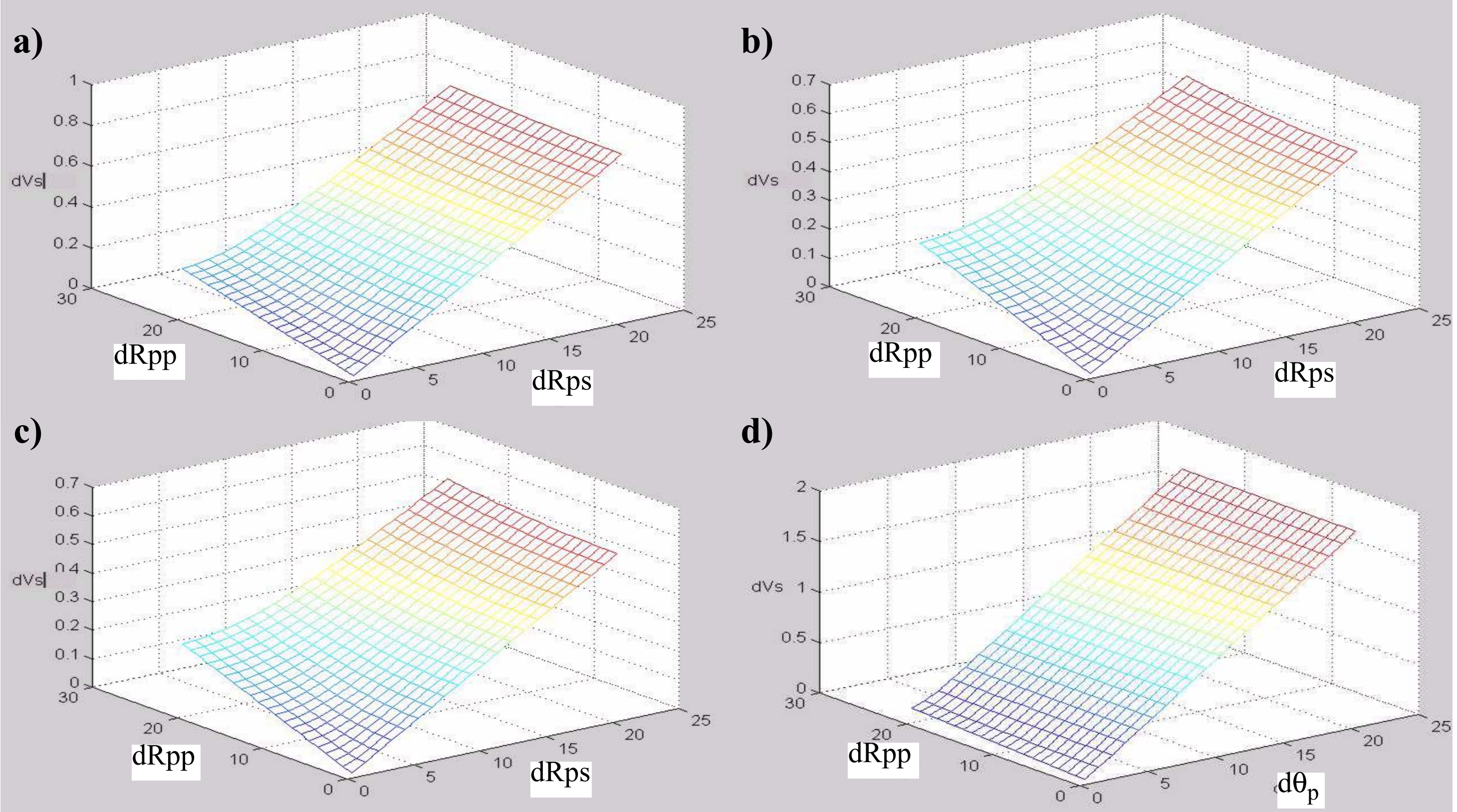

FIGURE 3. Uncertainty in estimated relative change in S-wave velocity as a function of uncertainty in the measured PP- and PS-reflection coefficient for a) the basic equation system, b) the system with Gardner's relationship, and c) the system with empirical porosity-velocity relationship. d) Uncertainty in S-wave velocity contrast as a function of measured PP reflection coefficient and P-wave angle of incidence for inversion of PP seismic data.

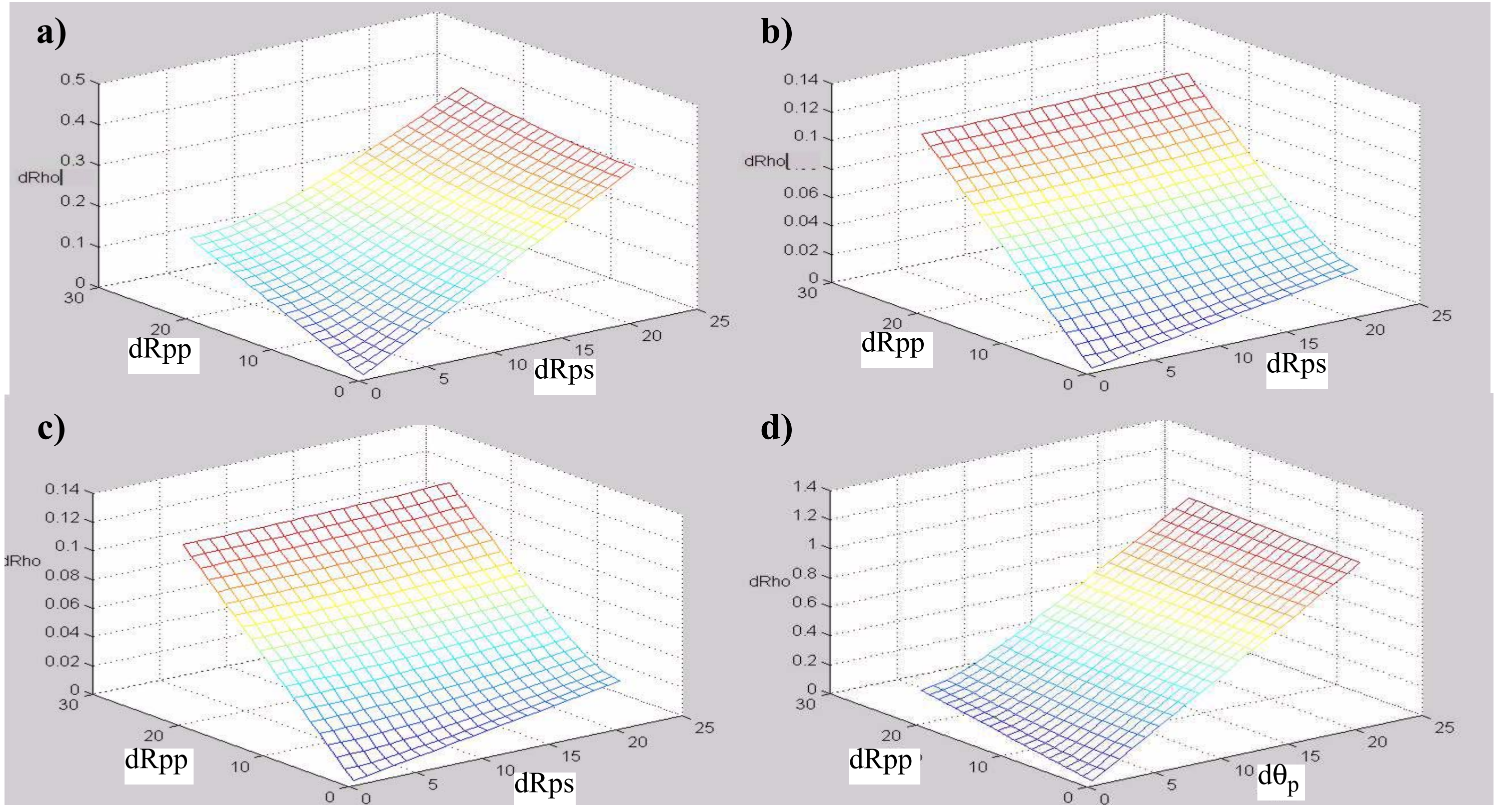

FIGURE 4. Uncertainty in estimated relative change in density as a function of uncertainty in the measured PP- and PS-reflection coefficient for a) the basic equation system, b) the system with Gardner's relationship, and c) the system with empirical porosity-velocity relationship. d) Uncertainty in density contrast as a function of measured PP reflection coefficient and P-wave angle of incidence for inversion of PP seismic data.

The uncertainty in joint inversion is lower than uncertainty in inversion of PP-seismic alone, as would be expected, since joint inversion show better results than PP-inversion on synthetic data (Veire and Landrø, 2001 and 2004). The uncertainty is reduced in the simplified systems compared to the original system for both P-wave velocity, S-wave velocity, and density. The uncertainty in measured PS reflectivity dominates the total uncertainty for both velocities and density for the original system. For S-wave velocity we observe the same trends for the system with Gardner's relationship and the empirical porosity-velocity relationship. For P-wave velocity and density, uncertainty in measured PP reflection coefficient dominates the total uncertainty in the equation system with Gardner's relationship and the empirical porosity-velocity relationship. From the equation systems given in Appendices A and B, we observe that there are no changes in the coefficients related to S-wave velocity, thus the uncertainty for S-wave velocity is expected to have the same shape for the three systems, as shown in Figure 3. The terms from coefficients related to density have been included in the coefficients related to P-wave velocity, and the uncertainty related to the P-wave velocity is expected to change for the simplified systems. The density contrast is a linear function of P-wave velocity contrast, and thus uncertainty for density and P-wave velocity show the same trends.

Next, uncertainty in the V_s/V_p model, P and S-wave incidence angles were added successively to the uncertainties presented above. For the simplified equation systems using Gardner's relation and the empirical porosity-velocity relationship, uncertainty in the parameters b_1 and b_2 (Eqn. (5) and (8)) are also included. The results are shown in Figures 5-7. For all figures the blue curve is uncertainty as a function of uncertainty in the measured PP reflection coefficients, with no uncertainty in any of the other parameters. Then an uncertainty of 10% in the measured PS reflectivity ($\delta Rps = 0.005$) was added (red curve), thus the total uncertainty is a sum of the uncertainty in the measured PP and PS reflectivity. Next, an uncertainty of 15% in the V_s/V_p model ($\delta(V_s/V_p) = 0.07$) was included in the uncertainty calculations (green curve), then 10% uncertainty first in P-wave incidence angle ($\delta\theta_p = 0.05$) (yellow curve) and then 15% in S-wave incidence angle ($\delta\theta_s = 0.05$)(cyan curve) was added, and finally 10% uncertainty in the b_1 and b_2 parameters (magenta curve) was included.

Figure 5 shows a set of curves of uncertainty in P-wave velocity contrast for a) the original system, b) the simplified system with Gardner's relation, and c) the simplified system with the empirical porosity-velocity relationship, adding uncertainty in different parameters successively for each of the curves. Uncertainty in P-wave velocity due to uncertainty in measured PS reflection coefficient is larger than uncertainty due to uncertainty in PP reflection coefficient for the original system, whilst for the two simplified systems, uncertainty from measured PP reflection coefficient dominates. For joint inversion, the largest effect is caused by uncertainty in P-wave incidence angles and V_s/V_p model. Uncertainty in S-wave incidence angle is negligible compared to impact from other parameters. For the two simplified systems, uncertainties in measured PP reflection coefficient and V_s/V_p model have the largest impact. Uncertainty in P- and S-wave incidence angles, and in the parameters in Gardner's relationship and the empirical porosity-velocity relationship are negligible compared to uncertainty in measured PP reflection coefficient. The total uncertainty, i.e. the uncertainty in P-wave velocity contrasts when uncertainties in all parameters are included, is largest for the original system.

The uncertainty in S-wave velocity contrast as a function of the different parameters is shown in Figure 6. For the basic joint inversion, uncertainty in P-wave incidence angles and the V_s/V_p model again dominates the total uncertainty. For the simplified systems, uncertainty in the V_s/V_p model dominates the total uncertainty. The uncertainty in S-wave incidence angles and Gardner parameter b is negligible compared to uncertainty in other parameters. The total uncertainty for S-wave velocity is larger than the total uncertainty for P-wave velocity both for the original and the simplified systems.

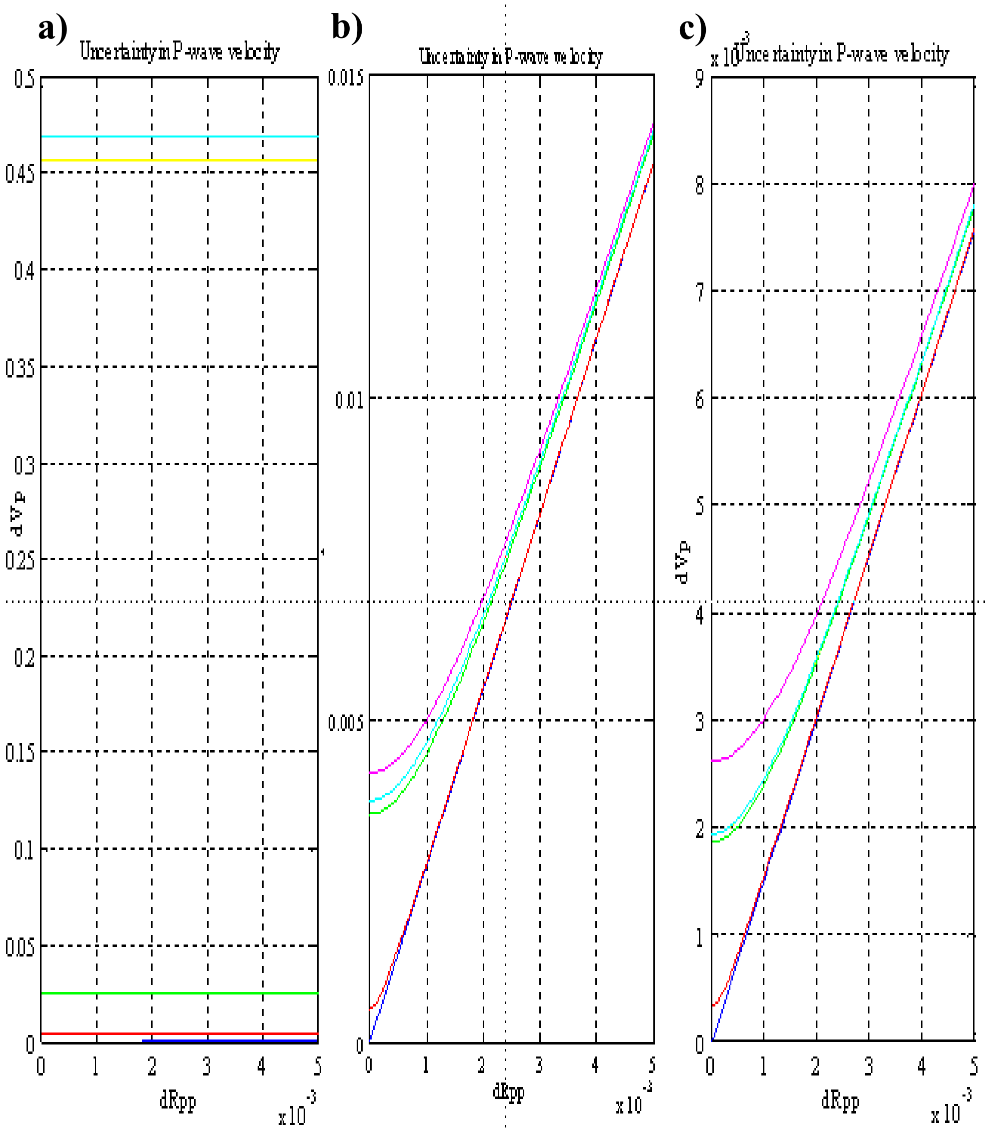

FIGURE 5. Uncertainty in estimated relative change in P-wave velocity as a function of uncertainty in the measured PP reflection coefficient for different uncertainties in all parameters for a) the basic equation system, b) using Gardner's relationship, and c) using an empirical porosity-velocity relationship. The blue line represents the base case with uncertainty in only the PP reflection coefficient. Uncertainty in the rest of the parameters has been added successively; PS reflection coefficient (red line), the previous plus the V_s/V_p model (green line). Finally, the uncertainty in the PP angle of incidence (yellow line), and the PS angle of incidence (cyan line), and in the parameters in Gardner's relationship and the empirical porosity-velocity relationship (mangenta line) were added to the total uncertainty.

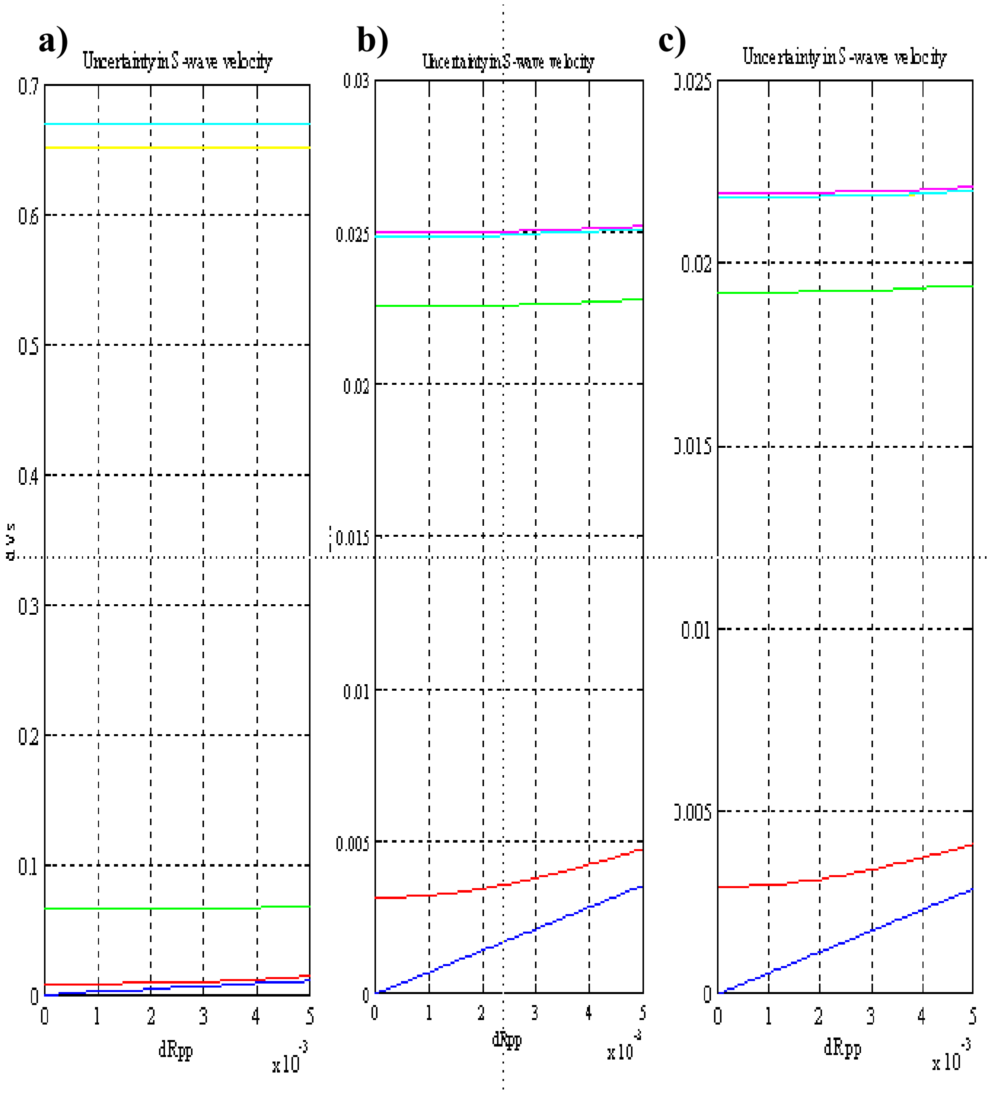

FIGURE 6. Uncertainty in estimated relative change in S-wave velocity as a function of uncertainty in the measured PP reflection coefficients for different uncertainties in all parameters using a) the basic equation system, b) Gardner's relationship, and c) an empirical porosity-velocity relationship. The blue line represents the base case with uncertainty in only the PP reflection coefficient. Uncertainty in the rest of the parameters has been added successively; PS reflection coefficient (red line), the previous plus the V_s/V_p model (green line). Finally, the uncertainty in the PP angle of incidence (yellow line), and the PS angle of incidence (cyan line), and in the parameters in Gardner's relationship and the empirical porosity-velocity relationship (mangenta line) were added to the total uncertainty.

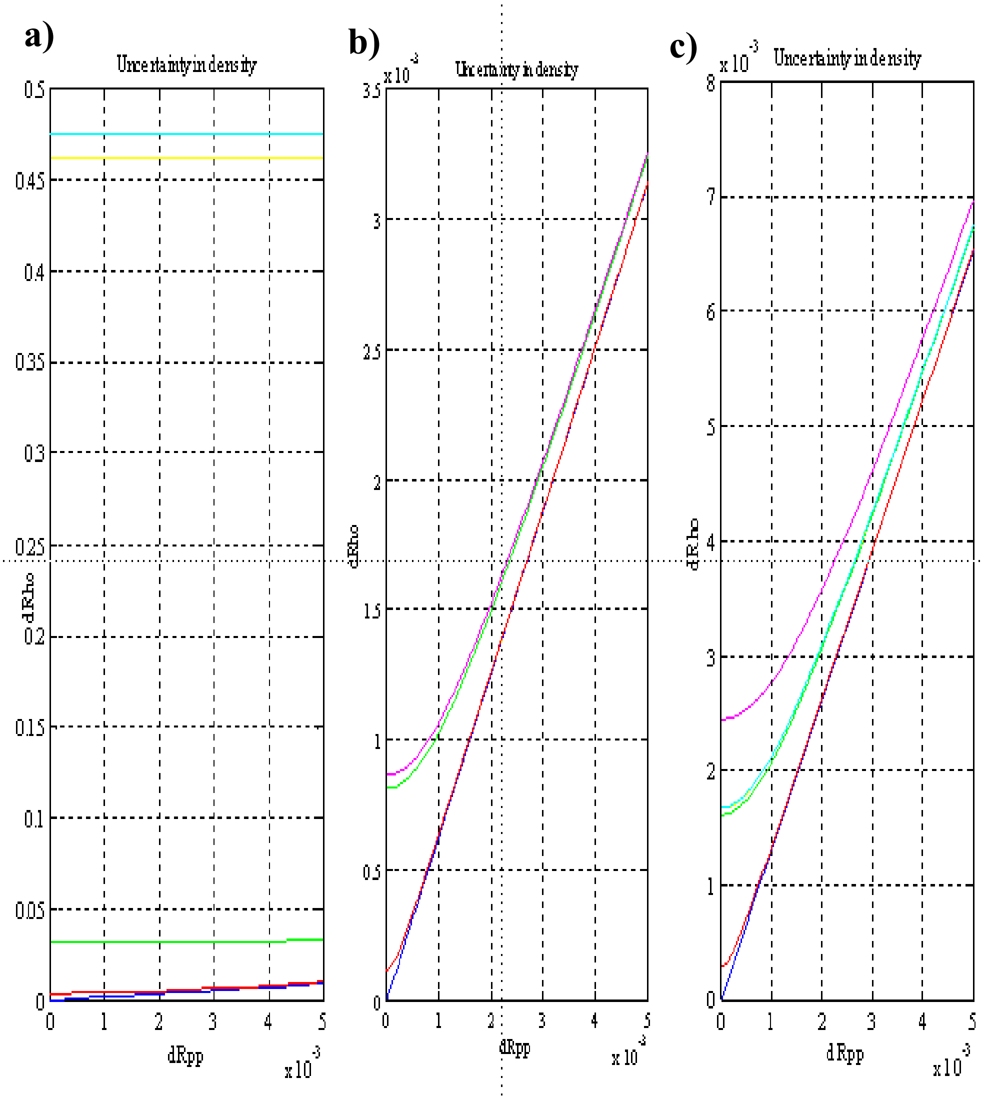

FIGURE 7. Uncertainty in estimated relative change in density as a function of uncertainty in the measured PP reflection coefficient for different uncertainties in all parameters using a) the basic equation system, b) Gardner's relationship, and c) an empirical porosity-velocity relationship. The blue line represents the base case with uncertainty in only the PP reflection coefficient. Uncertainty in the rest of the parameters has been added successively; PS reflection coefficient (red line), the previous plus the V_s/V_p model (green line). Finally, the uncertainty in the PP angle of incidence (yellow line), and the PS angle of incidence (cyan line), and in the parameters in Gardner's relationship and the empirical porosity-velocity relationship (mangenta line) were added to the total uncertainty.

Finally, uncertainty in density contrast as a function of different parameters is shown in Figure 7 for all three equation systems. For the original system we observe the same trends for density contrast as for P- and S-wave velocity contrast, whilst for the two simplified systems, uncertainty in density contrast follows the same trends as uncertainty in P-wave velocity contrast, since there is a linear relationship between P-wave velocity contrast and density contrast for these systems. For the simplified system with a porosity-velocity relationship, uncertainty in empirical parameter has a non-negligible impact. Total uncertainty for the density contrast is of the same size as total uncertainty in P-wave velocity for the original system, and uncertainty in the two simplified systems is smaller that for the original system.

Field data example

The uncertainty in the inversion methodology has also been investigated on a multicomponent data set from the North Sea, see Figure 8 for a cross section of migrated P/Z- and PS seismic data. The simultaneous inversion of these data are presented in Veire and Landrø (2004), and we refer to this article for more details on processing and inversion. Figure 9 shows prestack move out corrected gathers of the P/Z- and PS seismic data.

The V_s/V_p model needed as trend model in the inversion, and to scale the PS data from PS travel time to P/Z travel time was estimated by combining information from well logs and stacking velocities for P/Z- and PS data using Dix' formula. The V_s/V_p model varies between 0.56 and 0.6, and assuming a 10% error in these estimates, we set the uncertainty in the V_s/V_p model to $\delta(V_s/V_p) = 0.06$ in our calculations. The offset distribution was transformed to angle distribution using (Bale et al., 2001)

$$\theta = \arcsin\left(\frac{xV_{int}}{tV_{NMO}^2}\right) . \tag{20}$$

from Snell's law and assuming hyperbolic moveout. Here, θ is the angle of incidence, x is the offset, t is the traveltime, V_{int} is the interval velocity, and V_{NMO} is the NMO-velocity (assumed to be equal to the RMS-velocity). P-wave incidence angles varies between 1.7 and 17 degrees, and S-wave incidence angles range from 1 to 10 degrees for this test. Assuming 10% uncertainty in both P- and S-wave incidence angles, we use an error of 0.03 radians (1,7 degrees) for the P-wave incidence angles and 0.02 radians (1 degree) for the S-wave incidence angles in the calculations.

Finally, seismic amplitudes were calibrated to represent reflection coefficients. From a set of given V_p, V_s and densities, reflection coefficients for one major reflection were calculated using Eqn. 1 and 2. Seismic amplitudes were scaled to the level of reflection coefficients using one calibration factor for all offsets. The V_p and V_s trend models were estimated from stacking velocities as described above, and densities were estimated from Gardner's relation (Mavko et al. 1998). Only one calibration factor was used for all offsets, assuming that the AVO response of seismic data have been preserved during processing. Reflection coefficients for P/Z seismic data has a maximum absolute value of 0.013 and PS seismic reflection coefficient has a maximum absolute value of 0.0016 for this example, giving uncertainties 0.001 and 0.0002 respectively when assuming an error of 10%.

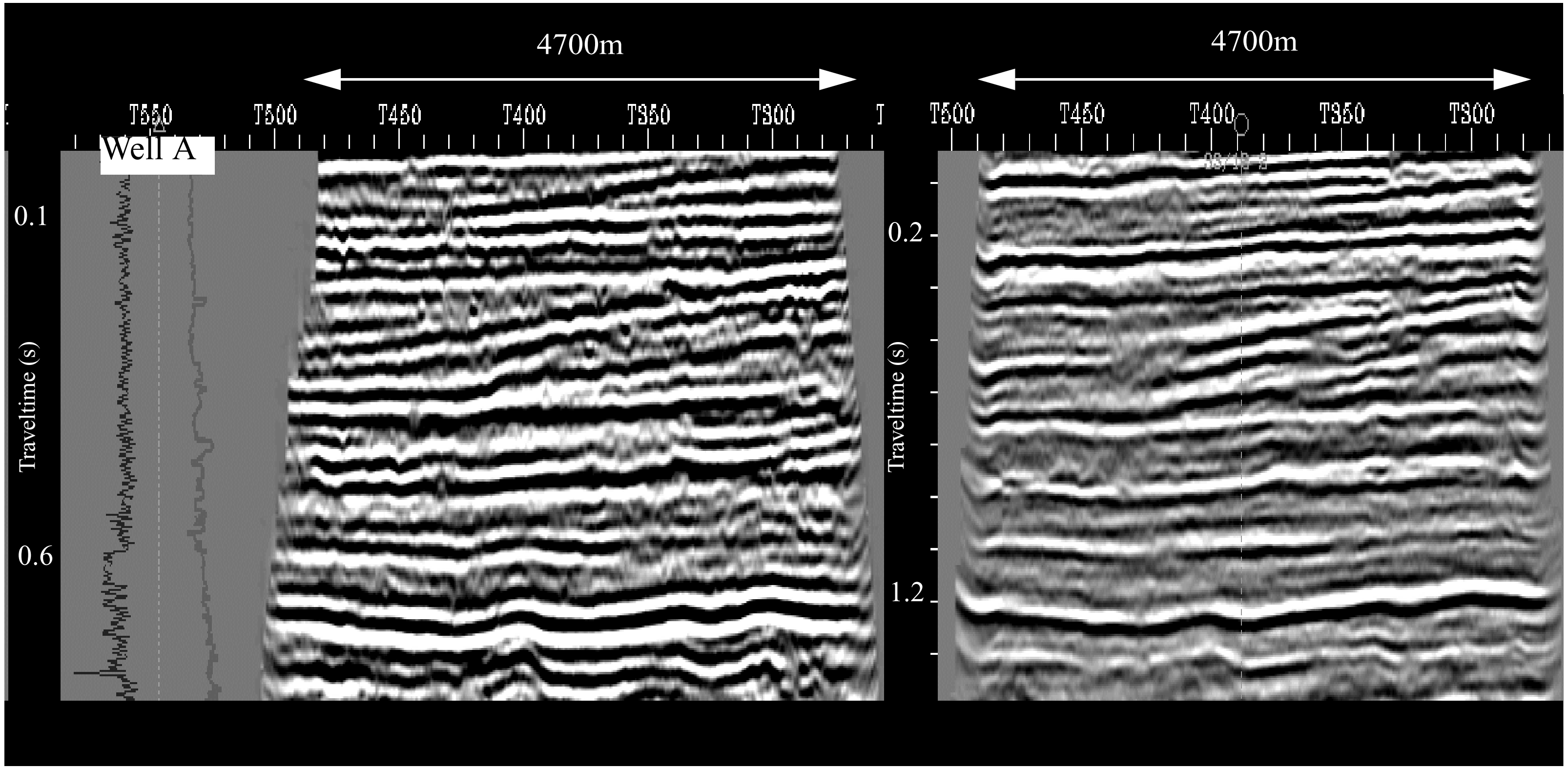

FIGURE 8. (a) P/Z-section with gamma-log (left) and density log (right), and (b) PS-section in the overburden formation. Note different time scales.

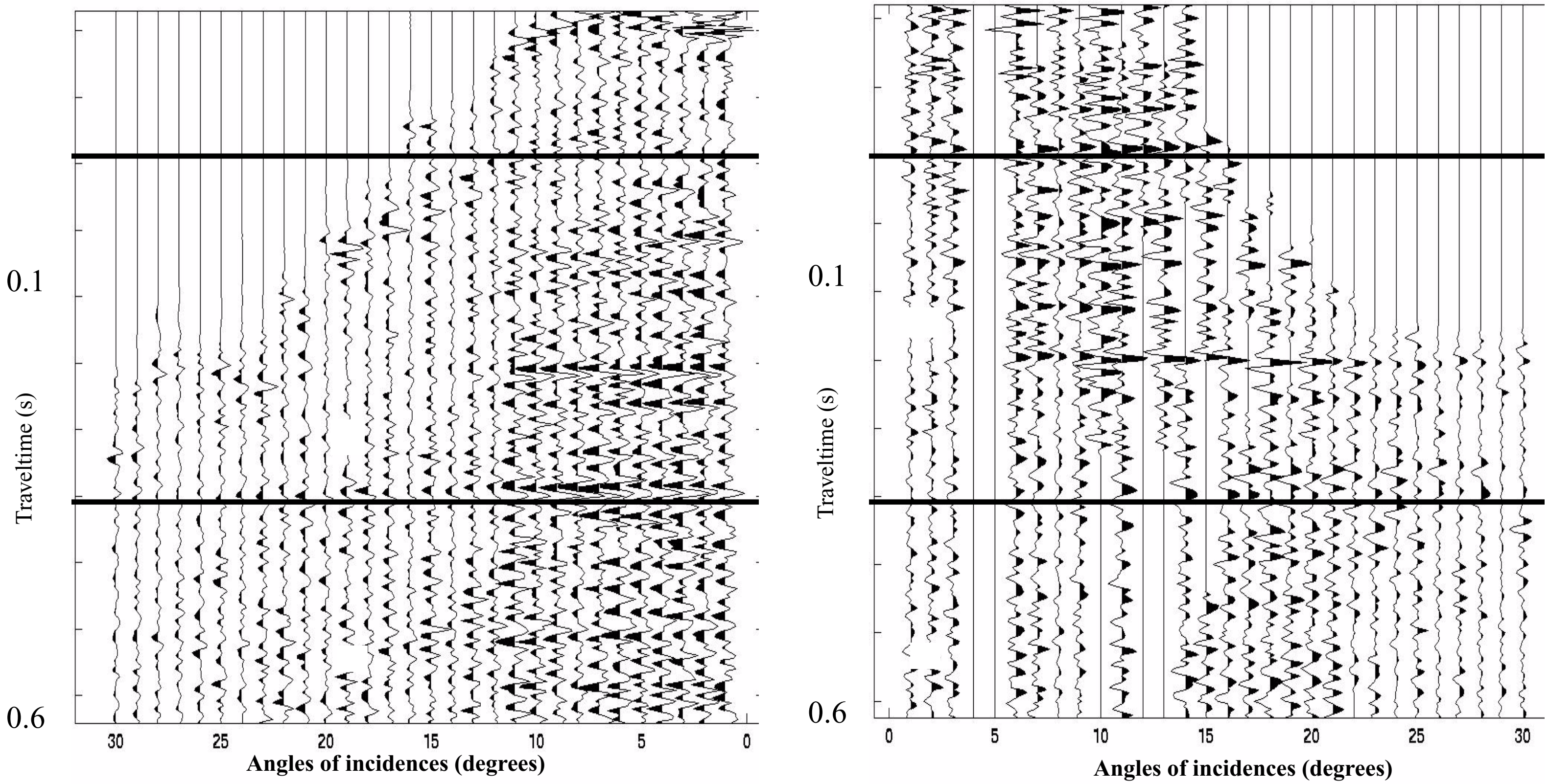

FIGURE 9. P/Z (left) and PS (right) prestack gathers after scaling (PS time to PP time). The inversion has been performed in the time window 300 - 500 ms (indicated by the horizontal lines).

The inversion was performed in a time window containing sand layers in a formation above the reservoir zone (Figure 8) using the basic equation system and the simplified system with Gardner's equation. Results for relative change in P-wave velocity and S-wave velocity are shown for both systems in Figures 10 and 11, with corresponding uncertainties. The V_p-contrast varies between -0.02 and 0.02, and the V_s-contrast varies between -0.01 and 0.001 for the basic system. For the simplified system, both V_p-contrast and V_s-contrast varies between -0.02 and 0.02. This is in the same range as contrasts calculated from V_p and V_s well logs (Veire and Landrø, 2004). The total uncertainty (including uncertainty in measured reflection coefficients, gamma ratio, and incidence angles) using the basic equation system for P-wave velocity contrast has a mean value of 0.0002, which means 10% uncertainty in the estimated velocity contrasts. For S-wave velocity contrast the mean value of total uncertainty is 0.001, again meaning 10% uncertainty in the estimated velocity contrasts. For the simplified system using Gardner's relationship, the total uncertainty in P-wave velocity contrast has a mean value of 0.0026, meaning 13% uncertainty in the estimated velocity contrasts. The uncertainty in S-wave velocity for the simplified system has a mean value of 0.0027, which means 13% uncertainty in the estimated velocity contrasts. Total uncertainty for the S-wave contrast is larger than the uncertainty in the P-wave velocity contrast for joint inversion, but not for all areas in the simplified inversion. The uncertainties are larger using the simplified system with Gardner's relationship than for the basic joint inversion. The results for density has not been shown here, but they follow the trends of the P-wave velocity. For this field data example, we observe that the largest contributors to the total uncertainty are uncertainties in the P-wave reflection coefficient, the converted wave reflection coefficient, and uncertainty in the P-wave incidence angles. These factors contribute approximately 100 times as much as uncertainty in the S-wave incidence angles and 10 times as much as uncertainty in the V_s/V_p model.

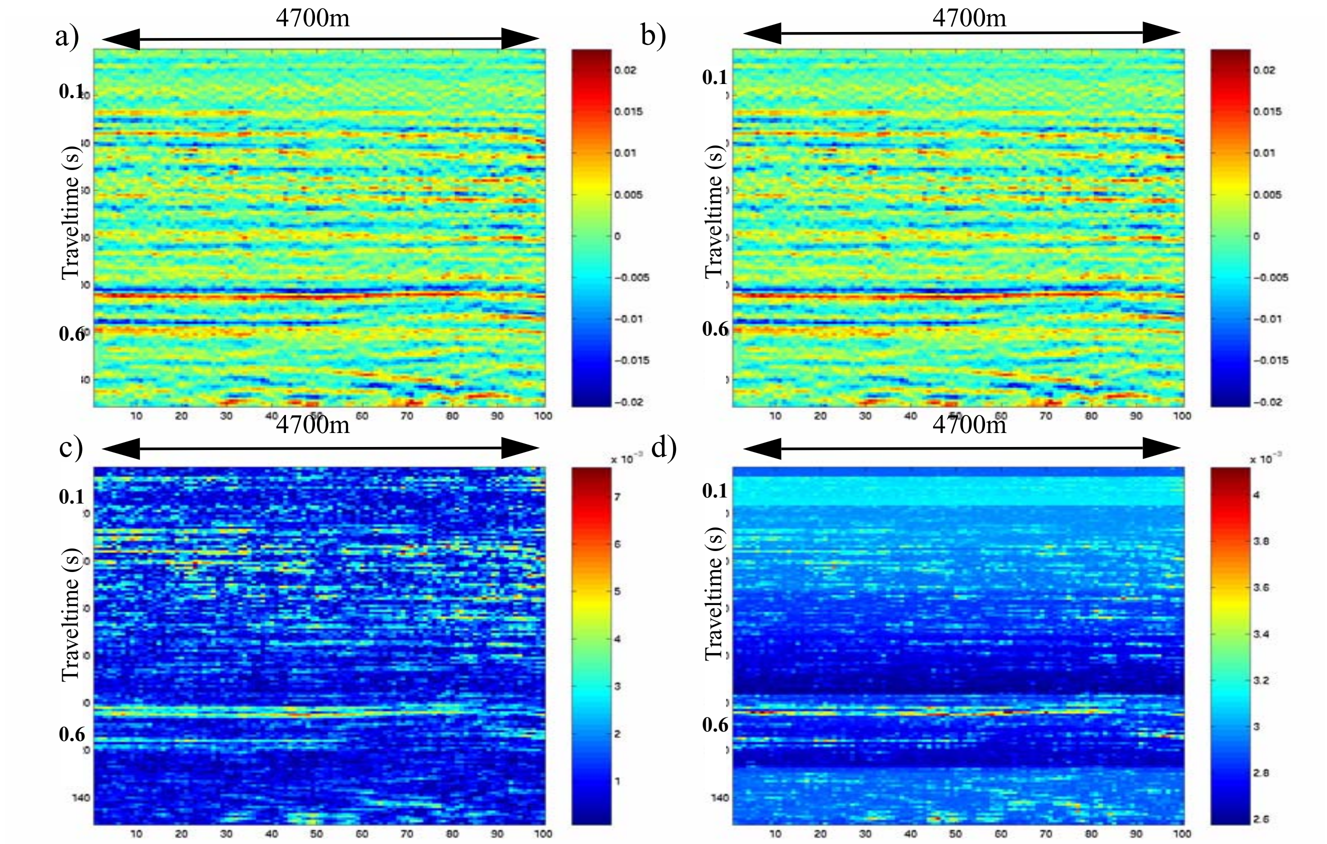

FIGURE 10. Vp-contrast from joint inversion; a) inversion using basic system, b) inversion using simplified system with Gardner's relationship, c) total uncertainty in Vp-contrast from basic inversion, and d) total uncertainty in Vp-contrast from inversion using Gardner's relationship.

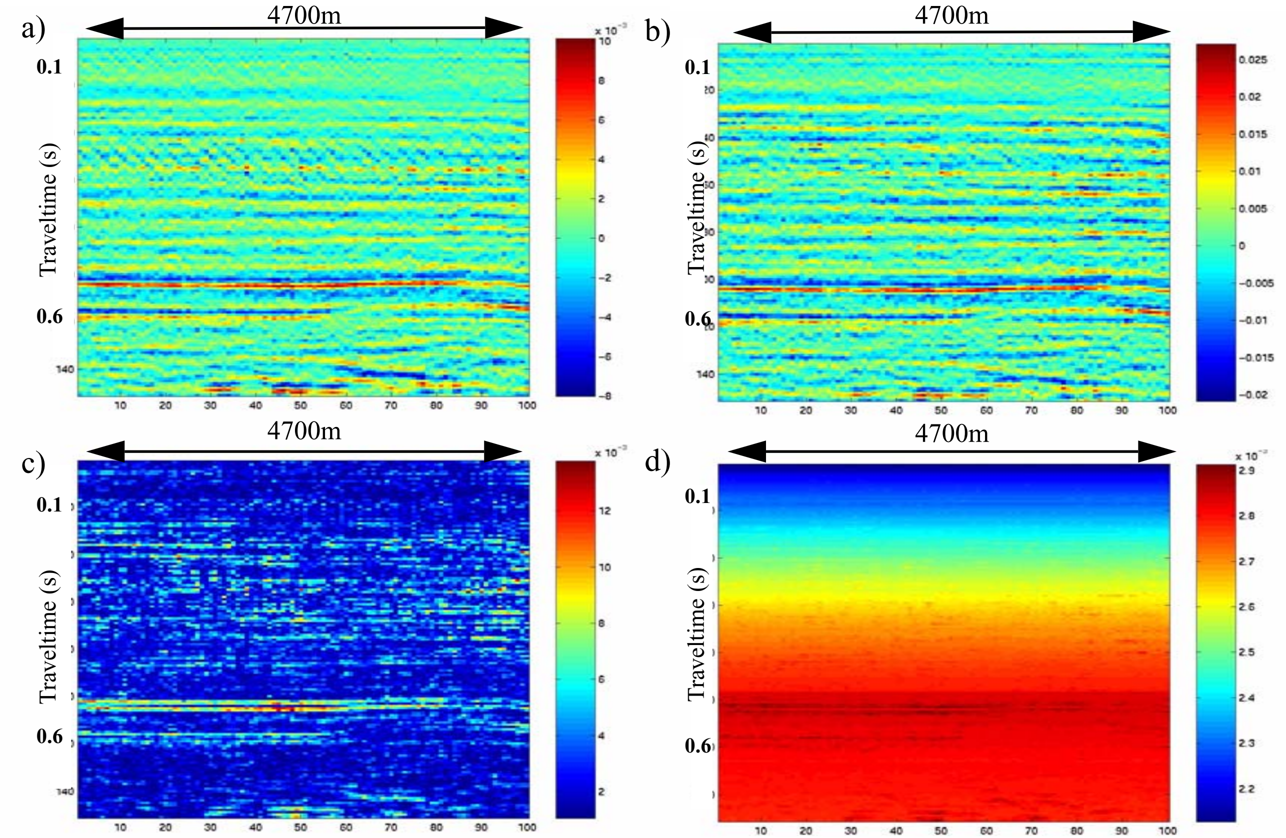

FIGURE 11. Vs-contrast from joint inversion; a) inversion using basic system, b) inversion using simplified system with Gardner's relationship, c) total uncertainty in Vs-contrast from basic inversion, and d) total uncertainty in Vs-contrast from inversion using Gardner's relationship.

Discussion

In most studies on non-linear inversion, a sensitivity analysis of the Jacobi matrix is included. The uncertainty analysis done in this study can be compared to such sensitivity analysis, but in addition we look at the total uncertainty in the system by adding the uncertainty in the different parameters together, assuming independent variables.

In this study we have investigating the effect of uncertainty in parameters like V_s/V_p model, incidences angles, and parameters in the empirical relationships. We have included uncertainty in the measured PP- and PS-seismic data in a general sense without studying causes of uncertainties in measured seismic data. Systematic errors caused by source directivity will affect the data different from general seismic noise. Factors like anisotropy and absorption might introduce additional systematic errors. Anisotropy can be introduced in the equation system using Thomson’s linearized anisotropic version of the Zoeppritz’s equation (Thomson, 1993), but this will give a larger system with more unknowns, probably leading to increased total uncertainty.

In addition, we have assumed independent parameters to simplify the calculations. Most of the parameters in this inversion process are dependent on each other, for instance the same stacking velocities have been used to estimate both the V_s/V_p model and incidence angles. The most complete way to include the cross correlation between the different parameters is probably to do a stochastic inversion in a Bayesian framework, where the correlation between the different parameters is specified in the prior model. An excellent example is presented by Buland and Omre (2003). They performed Bayesian stochastic inversion of PP AVO data, but this procedure might be extended to joint inversion of PP- and PS AVO data.

Including Gardner’s relationship or the porosity - velocity relationship as a constraint in the least squares system, instead of reducing the equation system before inserting it in the least squares system is a more mathematically correct way of treating constraints to the inversion. However, the equation system resulting from these constraints will be more complex than the simplified system presented here.

Results of synthetic tests show that joint inversion is not sensitive to noise and to variation in the V_s/V_p model, however these factors contribute most to total uncertainty for joint inversion. Joint inversion produces better results than PP inversion for all parameters, and measured against PS inversion we see better results for density change, and comparable results for S-wave velocity. In addition, joint inversion also gives information of P-velocities that are unobtainable from PS seismic data only.

Results from the test on field multicomponent data show similar trends as synthetic tests, but differences between total uncertainty for P-wave velocity contrast and S-wave velocity contrast are smaller. In addition, the different inversion methods have comparable uncertainties.

Conclusions

The uncertainty in simultaneous inversion of PP- and PS-seismic data has been investigated through deterministic sensitivity analysis. Both the full systems based on Aki and Richard's linearizations of Zoeppritz's equations, and simplified systems using empirical relationships to relate P-wave velocity and density have been analyzed. We find that empirical relationships reduce the uncertainty in the inversion for all parameters. Furthermore, total uncertainty in joint inversion of PP- and PS seismic data is smaller than total uncertainty in inversion of PP seismic data alone. The largest total uncertainty is seen for the S-wave velocity contrast. For inversion using a porosity-velocity relationship, we find that S-wave uncertainty is twice the uncertainty in P-wave velocity and density. For inversion using Gardner' relationship and for the case without any empirical relations, uncertainty in S-wave velocity is approximately 30% larger than uncertainty in P-wave velocity contrast and density contrast.

From synthetic examples we find that uncertainty in P-wave incidence angles represent the largest contribution to the total uncertainty for velocities and density contrasts. The uncertainty in velocity and density coming from uncertainty in P-wave angle of incidence is more than 10 times larger than the uncertainty coming from uncertainty for instance in the V_s/V_p model. Uncertainty in S-wave incidence angle and in PP and PS reflection coefficients are negligible compared to the uncertainty in P-wave angle of incidence. However, for S-wave velocity contrasts, the largest uncertainty arises from uncertainty in the V_s/V_p model. For P-wave velocity and density contrasts, contribution from uncertainty in the V_s/V_p model is largest when uncertainty in PP and PS reflection coefficients is small. When uncertainty in reflection coefficients increase, they dominate the total uncertainty for P-wave velocity and density contrasts.

Total uncertainties for inversion of field multicomponent data show similar trends as synthetic tests but differences between uncertainties in velocity contrasts and between different methods are smaller than for synthetic tests. In addition, we observe that uncertainty in the reflection coefficients and the P-wave incidence angle contribute the most to the total uncertainty for this field data test. The contribution from uncertainties in S-wave incidence angles are 1/100 of the uncertainty coupled to uncertainties in the reflection coefficients, and the contribution from the V_s/V_p model are 1/10 of the uncertainty coming from uncertainties in the reflection coefficients.

Acknowledgements

We acknowledge the VISTA/Statoil research programme for financial support. Special thanks to Mark Thompson, Iren Måløy, Inger Kloster Osmundsen and Roy Sørbel for valuable help.

Appendix A - Least squares system

The coefficients in the original least square equation system (Eqn. 4) is given below

$$a_{11} = \sum_{j=1}^{m} \frac{1}{2(\cos\theta_{pj})^4} \qquad a_{12} = \sum_{j=1}^{m} -4\gamma^2(\tan\theta_{pj})^2 = a_{21}$$

$$a_{13} = \sum_{j=1}^{m} \frac{1-4\gamma^2\sin^2\theta_{pj}}{2(\cos\theta_{pj})^2} = a_{31}$$

$$a_{22} = \sum_{i=1}^{n} \frac{8\sin^2\theta_{pi}}{\cos^2\theta_{si}} \cdot (\gamma^2\sin^2\theta_{pi} - \gamma\cos\theta_{pi}\cos\theta_{si})^2 + \sum_{j=1}^{m} 32\gamma^4\sin^4\theta_{pj}$$

$$a_{23} = \sum_{i=1}^{n} \left(\frac{-2\sin^2\theta_{pi}}{\cos^2\theta_{si}} (1-2\gamma^2\sin^2\theta_{pi} + 2\gamma\cos\theta_{pi}\cos\theta_{si}) \right.$$

$$\left. \cdot (\gamma^2\sin^2\theta_{pi} - \gamma\cos\theta_{pi}\cos\theta_{si}) \right)$$

$$- \sum_{j=1}^{m} (1-4\gamma^2\sin^2\theta_{pj})(4\gamma^2\sin^2\theta_{pj}) = a_{32}$$

$$.a_{33} = \sum_{i=1}^{n} \frac{\sin^2\theta_{pi}}{2\cos^2\theta_{si}} (1-2\gamma^2\sin^2\theta_{pi} + 2\gamma\cos\theta_{pi}\cos\theta_{si})^2 \tag{A-1}$$

$$+ \sum_{j=1}^{m} \frac{1}{2}(1-4\gamma^2\sin^2\theta_{pj})^2$$

$$c_1 = \sum_{j=1}^{m} \frac{R^*_{PP}(\theta_p)}{(\cos\theta_{pj})^2}$$

$$c_2 = \sum_{i=1}^{n} R^*_{PS}(\theta_p, \theta_s) \frac{\sin\theta_{pi}}{\cos\theta_{si}} (4\gamma^2\sin^2\theta_{pi} - 4\gamma\cos\theta_{pi}\cos\theta_{si})$$

$$- \sum_{j=1}^{m} 8R^*_{PP}(\theta_p)\gamma^2\sin^2\theta_{pj}$$

$$c_3 = \sum_{i=1}^{n} -R^*_{PS}(\theta_p, \theta_s) \frac{\sin\theta_{pi}}{\cos\theta_{si}} (1-2\gamma^2\sin^2\theta_{pi} + 2\gamma\cos\theta_{pi}\cos\theta_{si})$$

$$+ \sum_{j=1}^{m} R^*_{PP}(\theta_p)(1 - 4\gamma^2\sin^2\theta_{pj})$$

The exact solution to the equation system given in Eqn. 4 is given by:

$$
\begin{aligned}
\frac{\Delta Vp}{Vp} &= \frac{-a_{12}a_{33}c_2 + a_{12}a_{23}c_3 + a_{13}a_{23}c_2 - a_{13}a_{22}c_3 + a_{33}a_{22}c_1 - a_{23}^2c_1}{a_{11}a_{33}a_{22} - a_{11}a_{23}^2 - a_{13}^2a_{22} + 2a_{23}a_{13}a_{12} - a_{33}a_{12}^2} \\
\frac{\Delta Vs}{Vs} &= \frac{-a_{11}a_{33}c_2 + a_{11}a_{23}c_3 + a_{13}^2c_2 - a_{13}a_{12}c_3 + a_{33}a_{12}c_1 - a_{23}a_{13}c_1}{a_{11}a_{33}a_{22} - a_{11}a_{23}^2 - a_{13}^2a_{22} + 2a_{23}a_{13}a_{12} - a_{33}a_{12}^2} \\
\frac{\Delta \rho}{\rho} &= \frac{-a_{11}a_{23}c_2 + a_{11}a_{22}c_3 + a_{23}a_{12}c_1 + a_{13}a_{12}c_2 - a_{12}^2c_3 - a_{13}a_{22}\cdot c_1}{a_{11}a_{33}a_{22} - a_{11}a_{23}^2 - a_{13}^2a_{22} + 2a_{23}a_{13}a_{12} - a_{33}a_{12}^2}
\end{aligned}
\qquad \text{(A-1)}
$$

The differentiation of these expressions are given by

$$
\begin{aligned}
\frac{\partial}{\partial m_i}\left(\frac{\Delta Vp}{Vp}\right) = \frac{1}{C}\Bigg[&[a_{33}a_{22} - a_{23}^2]\cdot\frac{\partial c_1}{\partial m_i} + (a_{13}a_{23} - a_{12}a_{33})\cdot\frac{\partial c_2}{\partial m_i} \\
&+ a_{12}(a_{23} - a_{13}a_{22})\cdot\frac{\partial c_3}{\partial m_i} + (a_{23}c_3 - a_{33}c_2)\cdot\frac{\partial a_{12}}{\partial m_i} \\
&+ (a_{23}c_2 - a_{22}c_3)\cdot\frac{\partial a_{13}}{\partial m_i} + (a_{33}c_1 - a_{13}c_3)\cdot\frac{\partial a_{22}}{\partial m_i} \\
&+ (a_{12}c_3 + a_{13}c_2 - 2a_{23}c_1)\cdot\frac{\partial a_{23}}{\partial m_i} + (a_{22}c_1 - a_{12}c_2)\cdot\frac{\partial a_{33}}{\partial m_i}\Bigg] - \left(\frac{B}{C^2}\frac{\partial C}{\partial m_i}\right)
\end{aligned}
\qquad \text{(A-2)}
$$

$$
\begin{aligned}
\frac{\partial}{\partial m_i}\left(\frac{\Delta Vs}{Vs}\right) = \frac{1}{C}\Bigg[&[a_{33}a_{12} - a_{23}a_{13}]\cdot\frac{\partial c_1}{\partial m_i} + (a_{13}^2 - a_{11}a_{33})\cdot\frac{\partial c_2}{\partial m_i} \\
&+ (a_{11}a_{23} - a_{13}a_{12})\cdot\frac{\partial c_3}{\partial m_i} + (a_{22}c_3 - a_{33}c_2)\cdot\frac{\partial a_{11}}{\partial m_i} \\
&+ (a_{33}c_1 - a_{13}c_3)\cdot\frac{\partial a_{12}}{\partial m_i} + (2a_{13}c_2 - a_{23}c_1 - a_{12}c_3)\cdot\frac{\partial a_{13}}{\partial m_i} \\
&+ (a_{11}c_3 - a_{13}c_1)\cdot\frac{\partial a_{23}}{\partial m_i} + (a_{12}c_1 - a_{11}c_2)\cdot\frac{\partial a_{33}}{\partial m_i}\Bigg] - \left(\frac{D}{C^2}\cdot\frac{\partial C}{\partial m_i}\right)
\end{aligned}
\qquad \text{(A-3)}
$$

$$
\begin{aligned}
\frac{\partial}{\partial m_i}\left(\frac{\Delta\rho}{\rho}\right) = \frac{1}{C}\Bigg[& [a_{23}a_{12} - a_{13}a_{22}]\cdot\frac{\partial c_1}{\partial m_i} + (a_{13}a_{12} - a_{11}a_{23})\cdot\frac{\partial c_2}{\partial m_i} \\
& + (a_{11}a_{22} - a_{12}^2)\cdot\frac{\partial c_3}{\partial m_i} + (a_{22}c_3 - a_{23}c_2)\cdot\frac{\partial a_{11}}{\partial m_i} \\
& + (a_{23}c_1 + a_{13}c_2 - 2a_{12}c_3)\cdot\frac{\partial a_{12}}{\partial m_i} + (a_{12}c_2 - a_{22}c_1)\cdot\frac{\partial a_{13}}{\partial m_i} \\
& + (a_{11}c_3 - a_{13}c_1)\cdot\frac{\partial a_{22}}{\partial m_i} + (a_{12}c_1 - a_{11}c_2)\cdot\frac{\partial a_{23}}{\partial m_i}\Bigg] - \left(\frac{E}{C^2}\cdot\frac{\partial C}{\partial m_i}\right)
\end{aligned}
\qquad \text{(A-4)}
$$

$$
\begin{aligned}
\frac{\partial C}{\partial m_i} = \Bigg[& (a_{22}a_{33} - a_{23}^2)\cdot\frac{\partial a_{11}}{\partial m_i} + (2a_{23}a_{13} - 2a_{12}a_{33})\cdot\frac{\partial a_{12}}{\partial m_i} \\
& + (2a_{23}a_{12} - 2a_{13}a_{22})\cdot\frac{\partial a_{13}}{\partial m_i} + (a_{11}a_{33} - a_{13}^2)\cdot\frac{\partial a_{22}}{\partial m_i} \\
& + (2a_{12}a_{13} - 2a_{23}a_{11})\cdot\frac{\partial a_{23}}{\partial m_i} + (a_{11}a_{22} - a_{12}^2)\cdot\frac{\partial a_{33}}{\partial m_i}
\end{aligned}
\qquad \text{(A-5)}
$$

where B is the nominator of $\Delta Vp/Vp$, D is the nominator of $\Delta Vs/Vs$, E is the nominator of $\Delta\rho/\rho$, and C is the denominator of $\Delta Vp/Vp$, $\Delta Vs/Vs$, and $\Delta\rho/\rho$.

Appendix B - Simplified least squares equation system

The coefficients in the least square equation system with Gardner’s relationship is given as:

$$
\begin{aligned}
a_{11} &= \sum_{j=1}^{m} \frac{1}{4}\left((1-4\gamma^2\sin^2\theta_{pj})A + \frac{1}{\cos^2\theta_{pj}}\right)^2 \\
&\quad + \sum_{i=1}^{n} \left(\frac{A\sin\theta_{pi}}{2\cos\theta_{si}}(1-2\gamma^2\sin^2\theta_{pi} + 2\gamma\cos\theta_{pi}\cos\theta_{si})\right)^2 \\
a_{12} &= \sum_{j=1}^{m} -2\gamma^2(\sin\theta_{pj})^2 \cdot \left((1-4\gamma^2\sin^2\theta_{pj})A + \frac{1}{\cos^2\theta_{pj}}\right) \\
&\quad - \sum_{i=1}^{n} \left\{ \frac{A(\sin^2\theta_{pi})}{\cos^2\theta_{si}} \cdot (1-2\gamma^2\sin^2\theta_{pi} + 2\gamma\cos\theta_{pi}\cos\theta_{si}) \right. \\
&\qquad \left. \cdot (\gamma^2\sin^2\theta_{pi} - \gamma\cos\theta_{pi}\cos\theta_{si}) \right\} = a_{21}
\end{aligned}
\tag{B-1}
$$

$$
\begin{aligned}
a_{22} &= \sum_{j=1}^{m} 16\gamma^4(\sin\theta_{pj})^4 + \sum_{i=1}^{n} \frac{4\sin^2\theta_{pi}}{(\cos\theta_{si})^2}(\gamma^2\sin^2\theta_{pi} - \gamma\cos\theta_{pi}\cos\theta_{si})^2 \\
c_1 &= \sum_{j=1}^{m} \frac{1}{2}R^*{}_{PP}(\theta_p)\left((1-4\gamma^2\sin^2\theta_{pj})A + \frac{1}{\cos^2\theta_{pj}}\right) \\
&\quad - \sum_{i=1}^{n} \frac{R^*{}_{PS}(\theta_p, \theta_s)A\sin\theta_{pi}}{2\cos\theta_{si}}(1-2\gamma^2\sin^2\theta_{pi} + 2\gamma\cos\theta_{pi}\cos\theta_{si}) \\
c_2 &= -\sum_{j=1}^{m} R^*{}_{PP}(\theta_p)4\gamma^2\sin^2\theta_{pj} \\
&\quad + \sum_{i=1}^{n} \frac{R^*{}_{PS}(\theta_p, \theta_s)2\sin\theta_{pi}}{\cos\theta_{si}}(\gamma^2\sin^2\theta_{pi} - \gamma\cos\theta_{pi}\cos\theta_{si})
\end{aligned}
$$

Here, $A = b_1$ for the system using Gardner’ relationship, and $A = \frac{V_p(\rho_F - \rho_S)}{b_2\rho}$ for the system with the empirical porosity-velocity relationship.

The exact solution to the equation system is given as

$$\begin{aligned} \frac{\Delta Vp}{Vp} &= \frac{a_{22}c_1 - a_{12}c_2}{a_{11}a_{22} - (a_{12})^2} \\ \frac{\Delta Vs}{Vs} &= \frac{a_{11}c_2 - a_{12}c_1}{a_{11}a_{22} - (a_{12})^2} \end{aligned} \tag{B-2}$$

Differentiating this solution gives

$$\begin{aligned} \frac{\partial}{\partial m_i}\left(\frac{\Delta Vp}{Vp}\right) &= \frac{c_1 \cdot \frac{\partial a_{22}}{\partial m_i} - c_2 \cdot \frac{\partial a_{12}}{\partial m_i} + a_{22} \cdot \frac{\partial c_1}{\partial m_i} - a_{12} \cdot \frac{\partial c_2}{\partial m_i}}{a_{11}a_{22} - (a_{12})^2} \\ &\quad - \frac{(a_{22}c_1 - a_{12}c_2) \cdot \left(a_{22} \cdot \frac{\partial a_{11}}{\partial m_i} + a_{11} \cdot \frac{\partial a_{22}}{\partial m_i} - 2a_{12} \cdot \frac{\partial a_{12}}{\partial m_i}\right)}{(a_{11}a_{22} - (a_{12})^2)^2} \\ \frac{\partial}{\partial m_i}\left(\frac{\Delta Vs}{Vs}\right) &= \frac{c_2 \cdot \frac{\partial a_{11}}{\partial m_i} - c_1 \cdot \frac{\partial a_{12}}{\partial m_i} + a_{11} \cdot \frac{\partial c_2}{\partial m_i} - a_{12} \cdot \frac{\partial c_1}{\partial m_i}}{a_{11}a_{22} - (a_{12})^2} \\ &\quad - \frac{(a_{11}c_2 - a_{12}c_1) \cdot \left(a_{22} \cdot \frac{\partial a_{11}}{\partial m_i} + a_{11} \cdot \frac{\partial a_{22}}{\partial m_i} - 2a_{12} \cdot \frac{\partial a_{12}}{\partial m_i}\right)}{(a_{11}a_{22} - (a_{12})^2)^2} \\ \frac{\partial}{\partial m_i}\left(\frac{\Delta \rho}{\rho}\right) &= \frac{\partial A}{\partial m_i} \cdot \frac{\Delta Vp}{Vp} + A \cdot \frac{\partial}{\partial m_i}\left(\frac{\Delta Vp}{Vp}\right) \end{aligned} \tag{B-3}$$

Appendix C - Differentiation of least squares matrices

The derivatives of the matrices $\mathbf{A}$ and c from the basic least squares system with respect to the measured PP- and PS reflection coefficients are given by

$$\frac{\partial a_{11}}{\partial R_{PP}} = 0, \frac{\partial a_{12}}{\partial R_{PP}} = 0, \frac{\partial a_{13}}{\partial R_{PP}} = 0, \frac{\partial a_{22}}{\partial R_{PP}} = 0, \frac{\partial a_{23}}{\partial R_{PP}} = 0, \frac{\partial a_{33}}{\partial R_{PP}} = 0$$

$$\frac{\partial c_1}{\partial R_{PP}} = \sum_{j=1}^{m} \frac{1}{(\cos\theta_{pj})^2}, \quad \frac{\partial c_2}{\partial R_{PP}} = \sum_{j=1}^{m} -8\gamma^2(\sin\theta_{pj})^2 \tag{C-1}$$

$$\frac{\partial c_3}{\partial R_{PP}} = \sum_{j=1}^{m} (1 - 4\gamma^2(\sin\theta_{pj})^2)$$

and

$$\frac{\partial a_{11}}{\partial R_{PS}} = 0, \frac{\partial a_{12}}{\partial R_{PS}} = 0, \frac{\partial a_{13}}{\partial R_{PS}} = 0, \frac{\partial a_{22}}{\partial R_{PS}} = 0, \frac{\partial a_{23}}{\partial R_{PS}} = 0, \frac{\partial a_{33}}{\partial R_{PS}} = 0$$

$$\frac{\partial c_1}{\partial R_{PS}} = 0, \quad \frac{\partial c_2}{\partial R_{PS}} = \sum_{i=1}^{n} \frac{\sin\theta_{pi}}{\cos\theta_{si}}(4\gamma^2(\sin\theta_{pi})^2 - 4\gamma\cos\theta_{pi}\cos\theta_{si}) \tag{C-2}$$

$$\frac{\partial c_3}{\partial R_{PS}} = \sum_{i=1}^{n} -\frac{\sin\theta_{pi}}{\cos\theta_{si}}(1 - 2\gamma^2(\sin\theta_{pi})^2 + 2\gamma\cos\theta_{pi}\cos\theta_{si})$$

Differentiating the matrices **A** and **c** from the least squares system with Gardner's equation and the empirical porosity-velocity relationship with respect to the measured PP and PS reflection coefficients give

$$\frac{\partial a_{11}}{\partial R_{PP}} = 0, \frac{\partial a_{12}}{\partial R_{PP}} = 0, \frac{\partial a_{22}}{\partial R_{PP}} = 0$$

$$\frac{\partial c_1}{\partial R_{PP}} = \sum_{j=1}^{m} \frac{1}{2}\left((1 - 4\gamma^2\sin^2\theta_{pj})A + \frac{1}{\cos^2\theta_{pj}}\right), \quad \frac{\partial c_2}{\partial R_{PP}} = \sum_{j=1}^{m} -4\gamma^2(\sin\theta_{pj})^2 \tag{C-3}$$

and

$$\frac{\partial a_{11}}{\partial R_{PS}} = 0, \frac{\partial a_{12}}{\partial R_{PS}} = 0, \frac{\partial a_{22}}{\partial R_{PS}} = 0$$

$$\frac{\partial c_1}{\partial R_{PS}} = -\sum_{i=1}^{n} \frac{A \sin\theta_{pi}}{2\cos\theta_{si}}(1 - 2\gamma^2 \sin^2\theta_{pi} + 2\gamma \cos\theta_{pi} \cos\theta_{si}). \tag{C-4}$$

$$\frac{\partial c_2}{\partial R_{PS}} = \sum_{i=1}^{n} \frac{2\sin\theta_{pi}}{\cos\theta_{si}}(\gamma^2 (\sin\theta_{pi})^2 - \gamma \cos\theta_{pi} \cos\theta_{si})$$

Simultaneous anisotropic inversion of PP- and PS seismic data

Helene Hafslund Veire* and Martin Landrø*.
****Department of Petroleum Engineering and Applied Geophysics, Norwegian University of Science and Technology, N-7491 Trondheim, Norway.***

Introduction

Estimation of reservoir parameters from seismic data is an important step in the reservoir characterization process. However, there are large uncertainties associated with seismic reservoir characterization, since the relationships between seismic data and reservoir parameters are highly non-unique. Increased confidence in estimated parameters might have a potentially large impact in reservoir model building.

Traditionally, only compressional seismic data (PP seismic) was acquired and analyzed. Tjåland and Ursin (1992), and de Nicolao et al. (1993), have studied the information content of the reflection coefficient matrix. They find that it is difficult to get reliable estimates for more than two out of three parameters (P-wave velocity, S-wave velocity, and density) with only one set of seismic data (e.g. only PP-data) due to instability in the equation systems. Because of this, inversion to acoustic impedance (AI) and elastic impedance (EI) (Connolly, 1999) from PP seismic data have often been used. However, the ability to estimate velocities and densities separately would be even more valuable in e.g. gas filled reservoirs. A small amount of gas will have large impact on P-wave velocity, making it difficult to estimate gas saturation from impedances only.

Recently, converted seismic waves (PS seismic data) have also been acquired and used in seismic reservoir characterization, mainly for enhanced imaging e.g. in gas clouds, but also to estimate reservoir parameters. Duffaut et al. (2000) introduced the concept of shear wave elastic impedance (SEI) calculated from PS seismic data, to be used together with acoustic impedance and elastic impedance in the reservoir characterization process. The problem of instability in inversion is less pronounced for linearized inversion of PS-data (Jin et al. 2000), since only PS reflection coefficients depend on S-wave velocity contrast and density contrast. In addition, several authors have shown (Margrave et al., 2001, Veire and Landrø, 2001, Garotta et al., 2002, and Carcuz and Ikelle, 2003) that by combining two sets of independent measurements (PP seismic data and PS seismic data) improved results compared to inversion of PP data alone can be produced.

Veire and Landrø (2001) presented simultaneous least squares inversion of PP and PS seismic data using Aki and Richard's (1980) approximations of Zoeppritz's equation for reflection coefficients. This inversion method is valid for isotropic media only, and correct velocity contrasts can not be produced for anisotropic media. Anisotropy is defined as variations of physical properties with the direction in which it is measured (Sheriff, 1999, Sheriff and Geldart, 1999). There are several causes of anisotropy, among others 1) crystalline anisotropy, caused by anisotropy in the crystal structure, 2) lithological or granular anisotropy caused by e.g. elongated grains aligned within the rocks, 3) anisotropy induced by non-horizontal fracturing, and 4) long-wavelength/thin layer anisotropy where the seismic wavelength is larger than the thickness of isotropic layers, causing isotropic layers to appear anisotropic of nature. In this report, possible causes of anisotropy will not be discussed. We will focus on the methodology to include anisotropy in seismic inversion.

Okoye et al. (1996) used least square inversion of seismic traveltimes of PP first-arrival traveltimes only to determine the elastic anisotropy parameter δ^*. This anisotropy parameter controls P-wave spatial resolution and vertical P-wave velocity of a transversely isotropic material. Ikelle (1996) presented a 3D anisotropic linearized inversion algorithm that is a combination of 3D prestack imaging and AVAZ inversion. Plessix and Bork (2000) studied amplitude versus angle (AVA) responses in vertical transversely isotropic (VTI) media. They found that by combining PS seismic data with PP seismic data in seismic inversion, S-wave impedance and the anisotropy parameter δ is coupled, but the instability of the system is reduced.

In this paper, a joint least squares inversion methodology (Veire and Landrø, 2001) has been extended to anisotropic media using Thompson's (1993) anisotropic expression for PP reflection coefficients and Sollid and Ursin's (2003) expression for PS reflection coefficients. Output of the inversion is relative change in P-wave velocity, relative change in S-wave velocity, and relative change in density, and changes in the anisotropy parameters epsilon and delta across an interface. The methodology has been tested on synthetic data including anisotropy. Results show that anisotropic inversion produces better results compared to isotropic inversion of seismic data with anisotropy, but there are still instabilities in the system. The inversion have been tested on multicomponent seismic data with common mid-point (CMP) sorting, and on data that have been sorted to common conversion points (CCP sorting). In CMP sorting we make the assumption that the mid-point between source and receiver is coinciding with the reflection point, but this is only valid for PP seismic data acquired over a horizontally layered earth model. In CCP sorting, the location of reflection points is estimated using information about P- and S-wave velocities and traveltimes. The conversion point, where incoming P-waves is converted to outgoing S-waves is normally assumed to be the same as the reflection point. Conversion of P-waves to S-waves can occur at all interfaces, but due to the loss of energy in each conversion, only the first converted mode is normally strong enough to be recorded. Omitting CCP-sorting for multicomponent seismic data might cause a disturbed AVO-response, since data from several reflection points are merged together in the same AVO-gather.

Methodology

Thomson’s (1993) approximation of Zoeppritz’s equations for PP reflection coefficients and Sollid and Ursin’s (1993) approximation for PS reflection coefficients for anisotropic media is given by:

$$
\begin{aligned}
R_{PP} &= \frac{1}{2}\left(\frac{\Delta\rho}{\rho}+\frac{\Delta V_p}{V_p}\right)+\frac{1}{2}\left(\frac{\Delta V_p}{V_p}-4\gamma^2\left(\frac{\Delta\rho}{\rho}+2\frac{\Delta V_s}{V_s}\right)+\Delta\delta\right)\sin^2\theta_p \\
&\quad +\frac{1}{2}\left(\frac{\Delta V_p}{V_p}-\Delta\delta+\Delta\varepsilon\right)\sin^2\theta_p(\tan\theta_p)^2
\end{aligned}
\qquad (1)
$$

and

$$
\begin{aligned}
R_{PS} &= 2\frac{\sin\theta_p}{\cos\theta_s}[\gamma^2\sin^2\theta_p-\gamma\cos\theta_s\cos\theta_p]\frac{\Delta V_s}{V_s} \\
&\quad -\frac{\sin\theta_p}{2\cos\theta_s}[1-2\gamma^2\sin^2\theta_p+2\gamma\cos\theta_p\cos\theta_s]\frac{\Delta\rho}{\rho} \\
&\quad +\frac{\sin^2\theta_p}{\sin\theta_p\cos\theta_s+\sin\theta_s\cos\theta_p}\left[\frac{1}{2}\Delta\delta+\sin^2\theta_p(\Delta\varepsilon-\Delta\delta)\right]
\end{aligned}
\quad , \qquad (2)
$$

where $\Delta V_p = V_{p02}-V_{p01}$, $V_p = (V_{p01}+V_{p02})/2$, and $\gamma = V_s/V_p$. Here, V_{p0x} are normal incidence velocities for P-waves, V_{s0x} are normal incidence velocities for S-waves, and ρ_{0x} is density. The parameters $\Delta\delta$ and $\Delta\varepsilon$ are change in anisotropy parameters ε and δ over an interface, θ_p is P-wave incidence angle, and θ_s is the S-wave incidence angle. The anisotropy parameter ε describes P-wave anisotropy related to horizontal and vertical P-wave velocity, and δ is P-S anisotropy parameter (Thomsen,1993).

By combining PP- and PS reflection coefficients and doing a least square estimation, we solve the equation system for relative changes in P-wave velocity $(\Delta V_p)/V_p$, relative changes in S-wave velocity $(\Delta V_s)/V_s$, relative changes in density $(\Delta\rho)/\rho$, and changes the anisotropy parameters $\Delta\delta$ and $\Delta\varepsilon$. The least square system is defined as

$$LS = \sum_{i=1}^{N} [R^*_{PS}(\theta_p, \theta_s) - (R_{PS}(\theta_p, \theta_s))]^2 + \sum_{j=1}^{M} [R^*_{PP}(\theta_p) - R_{PP}(\theta_p)]^2 \quad . \quad (3)$$

Here, R^*_{PP} and R^*_{PS} indicates measured seismic data, where amplitudes are calibrated to represent reflection coefficients. R_{PP} and R_{PS} represents the linearized reflection coefficients given in Eqn. 1 and 2, where x is either P or S. The summation is done over all incidence angles for PP ($j = 1\ldots m$) and PS reflection coefficients ($i = 1\ldots n$). To find the least square solution, we differentiate the equation system with respect to $\Delta\rho/\rho$, $\Delta V_p/V_p$, $\Delta V_s/V_s$, $\Delta\delta$, and $\Delta\varepsilon$, and solve for the minimum values. This yields a system of equations:

$$\mathbf{A} \cdot \left[\frac{\Delta V_p}{V_p}\ \frac{\Delta V_s}{V_s}\ \frac{\Delta\rho}{\rho}\ \Delta\varepsilon\ \Delta\delta\right]^T = \mathbf{b} \qquad (4)$$

where $\mathbf{A}$ is a 5x5 matrix, and $\mathbf{b}$ is a 5x1 matrix. $\mathbf{A}$ is symmetrical, and depends only on incidence angles and the ratio γ, whilst the vector $\mathbf{b}$ also depends on information about PP- and PS reflection coefficients as a function of angle in the seismic data. $\mathbf{A}$ and $\mathbf{b}$ are given in . It is also possible to introduce a weight parameter in Eqn. 3 if one of the datasets is assumed to be more reliable than the others, as is done in the isotropic inversion (Veire and Landrø, 2003). However, for simplicity this is not done here.

The system of equations is solved by Singular Value Decomposition to ensure stability of the solution. Singular value decomposition is well-suited for solving linear equations with instabilities. The matrix $\mathbf{A}$ is factored into $\mathbf{A} = \mathbf{Q}\Sigma\mathbf{Q}^T$, where $\mathbf{Q}$ is an orthogonal matrix that consists of the eigenvectors of A^TA, and Σ is a diagonal matrix with the singular values. The singular values are defined as the square roots of the non-zero eigenvalues of A^TA. The SVD can be stabilized by adding a small positive number to the diagonal of the original matrix A (called SVD damping). Singular values for the resulting least square system of equations are better balanced than singular values for inversion of PP- or PS-data alone. For the first reflector of the synthetic example given in Figure 1, singular values for joint inversion and separate inversion of PP and PS are given in Table 1. We observe that the anisotropic system is more unstable than the isotropic system (larger difference between the smallest and largest eigenvalue), and the inversion results vary when eigenvalues are perturbed.

	S.V.1	S.V. 2	S.V. 3	S.V. 4	S.V. 5
Anisotropic inversion with CCP sorting	21.32	4.66	0.124	0.005	0.0009
Isotropic inversion with CCP sorting	43.10	9.41	0.004		
Anisotropic inversion without CCP sorting	25.50	11.41	0.16	0.12	0.0001
Isotropic inversion without CCP sorting	43.26	9.79	0.005		

Table 1: Singular values for the first reflectors.

Results

Synthetic anisotropic seismic PP and PS seismic data were generated using the Norsar2D seismic modelling package. A simple model with 4 interfaces (5 layers) were made. Figure 1 shows a plot of the P-wave velocity model, and Table 2 lists all model parameters. Anisotropy was included in the three middle layers.

Travetime	V_p (m/s)	V_s (m/s)	ρ (kg/m^3)	Epsilon	Delta
100 ms	1900	1000	2300	0	0
300 ms	1800	947	2100	0.1	0.05
500 ms	2000	1053	2200	0.2	0.15
620 ms	2100	1150	2400	0.05	0.01
bottom	2300	1211	2550	0	0

Table 2: Model with anisotropy, parameters are given for the layer above.

Synthetic models were ray traced and convolved with a Ricker wavelet with center frequency 30 Hz (Figure 2). No geometrical spreading was included in the seismogram modelling. Figure 3 shows common-offset gathers for synthetic PP- and PS seismic data.

The horizontal distance of the conversion point from the source can be estimated by (Fromm et al., 1985)

$$x_{CCP} = \frac{x}{1 + \frac{V_s}{V_p}} \tag{5}$$

Here, x_{CCP} is location of the CCP, x is distance between source and receiver, and V_s/V_p is the ratio between S-wave velocity and P-wave velocity. The seismic data were NMO corrected and CCP sorted using non-hyperbolic traveltime grids and grids indicating the location of the CCPs (CCP grids). The CCP grids were produced in ray tracing and used to remove some of the kinematic anisotropic effects. PS seismic data were event correlated with PP seismic data (Figure 4), and finally the seismic data were calibrated to reflection coefficients and run through the inversion procedure. To test the sensitivity of the inversion to noise in the seismic data, one test was run with random noise added to the seismic data after event correlation.

Information about incidence and reflection angles, prestack traveltimes and common conversion points were produced during ray tracing. Figure 5 shows the distribution of P-wave incidence angles for the first interface (right), and the distribution of P-wave common conversion points (CCP) for the same interface (left). For an isotropic model with horizontal layers, the CCPs would be coincident with the common midpoints (CMP), and the CCP grid would show parallel patterns. For the anisotropic model the CCPs do not coincide with the CMPs and we get a skewed pattern. The incidence angles increase with increasing offset, though with a non-parallel trend that increases for increasing offset.

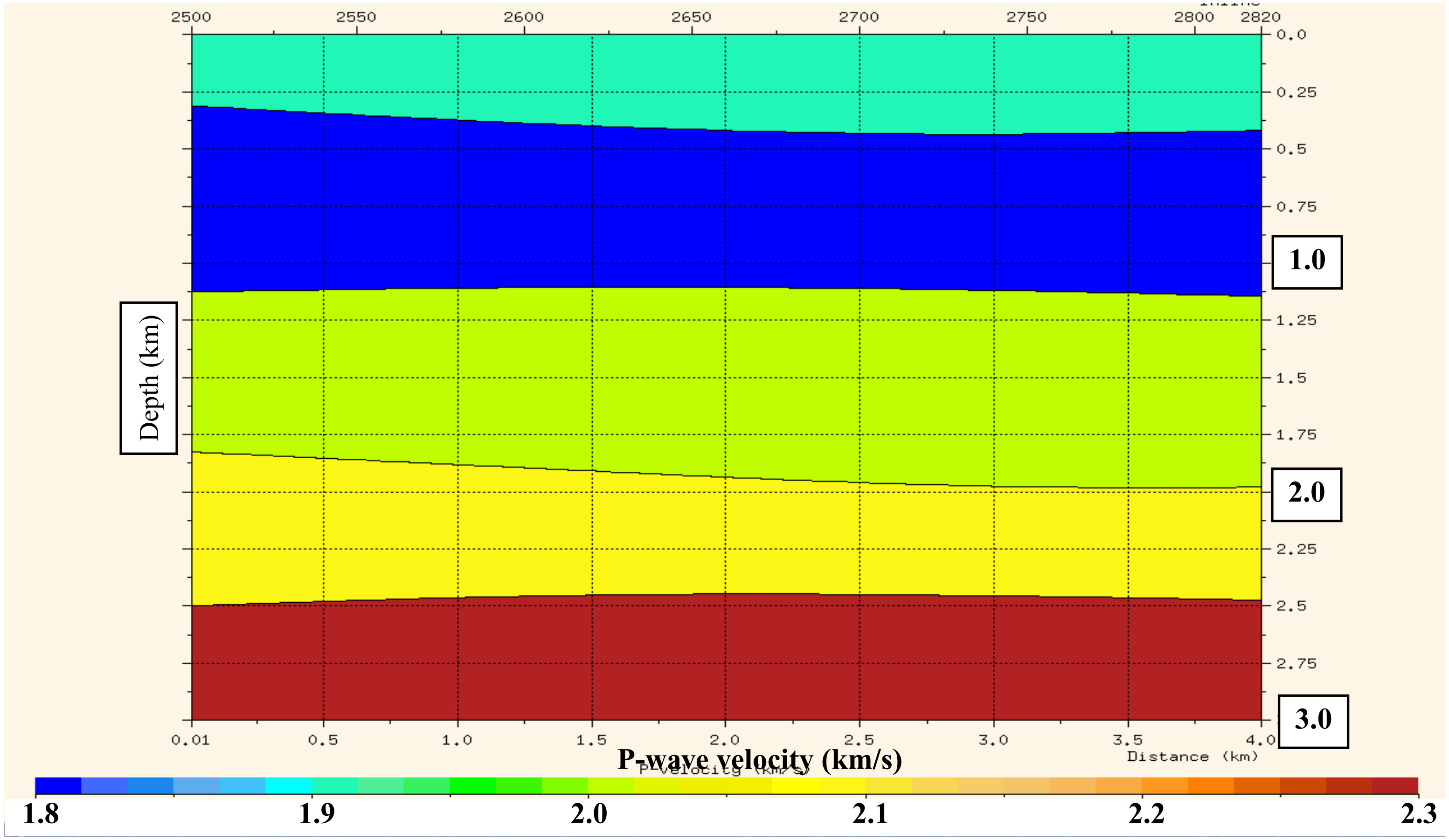

FIGURE 1. Synthetic model, P-wave velocities.

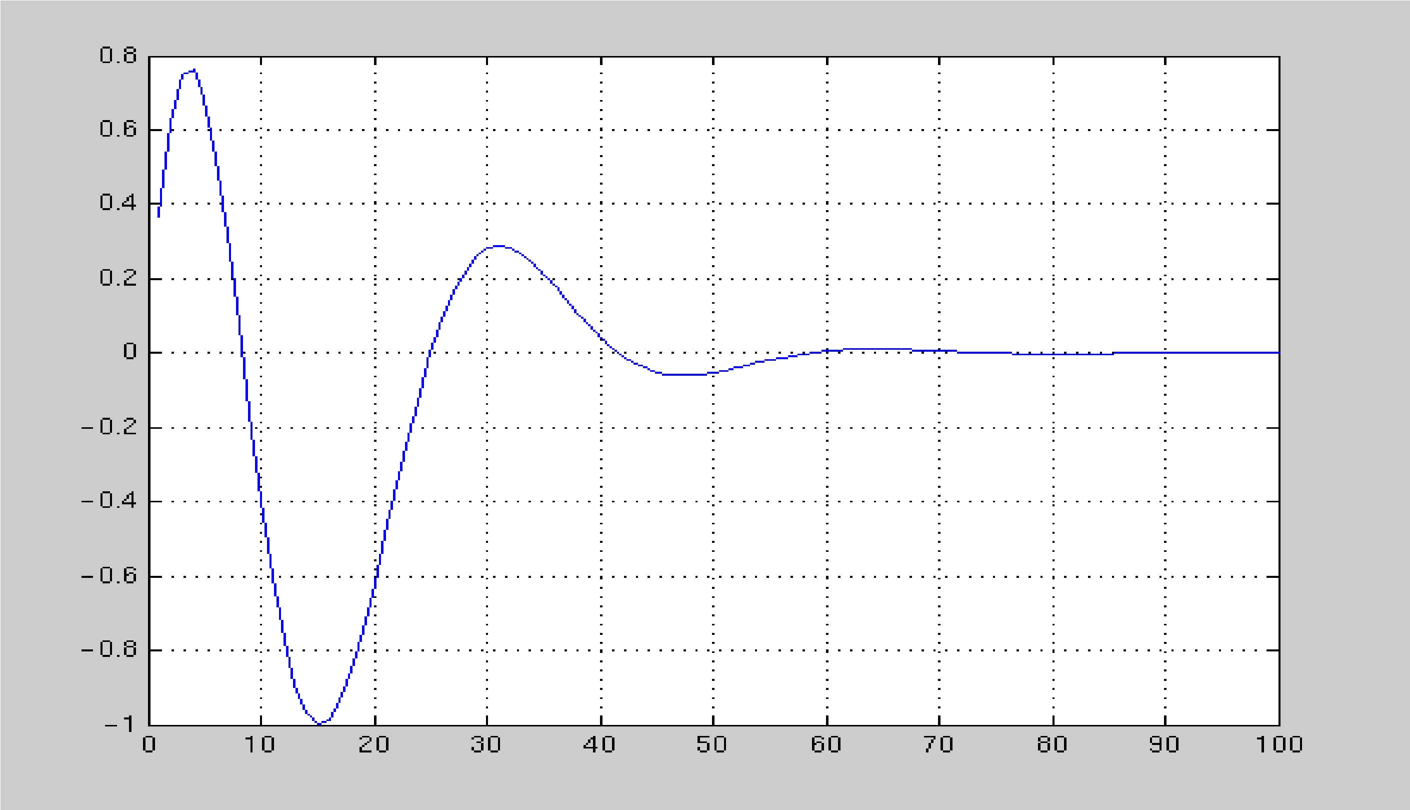

FIGURE 2. Synthetic wavelet used for modelling.

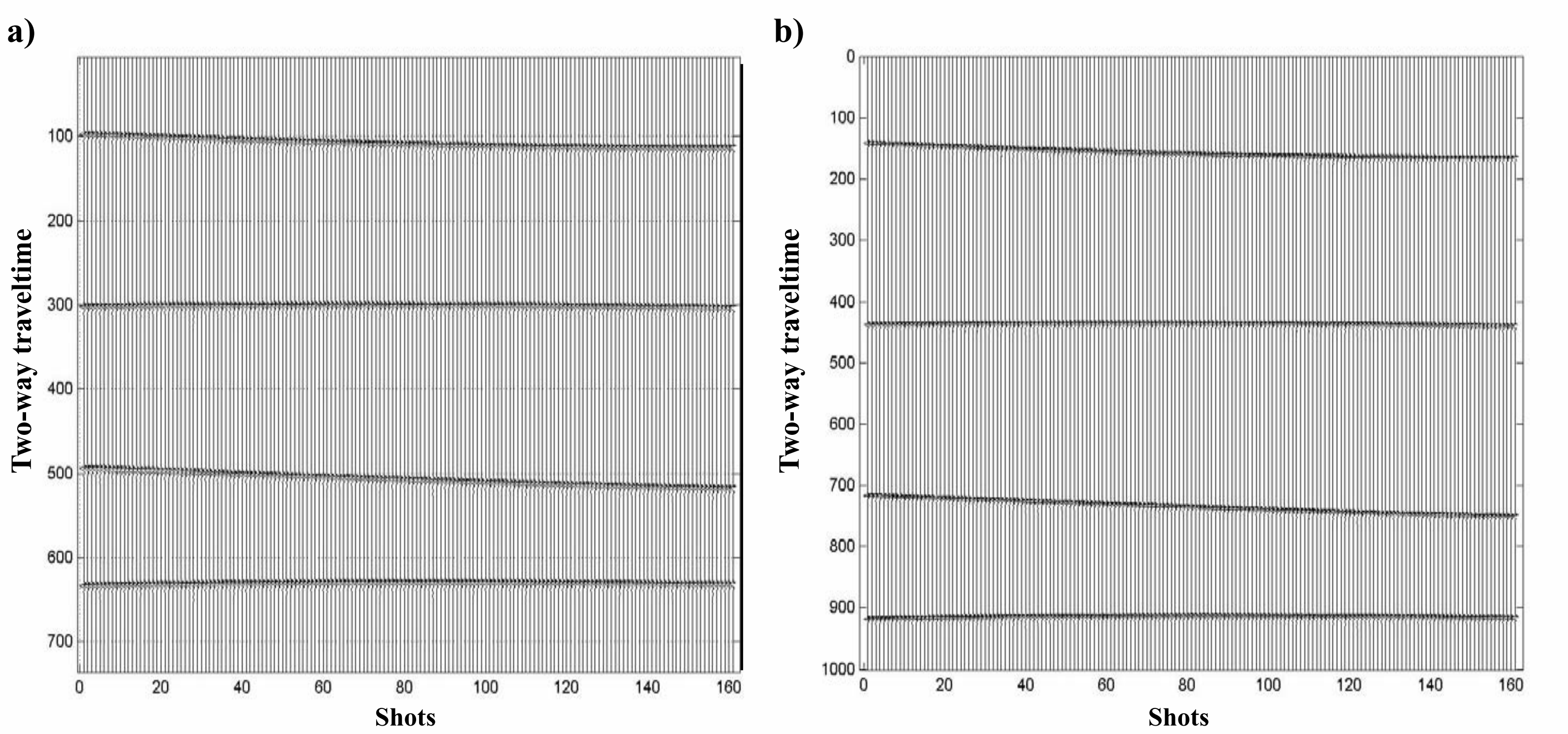

FIGURE 3. Common offset gathers of anisotropic model; a) PP seismic data, and b) PS seismic data. Note the different time axis.

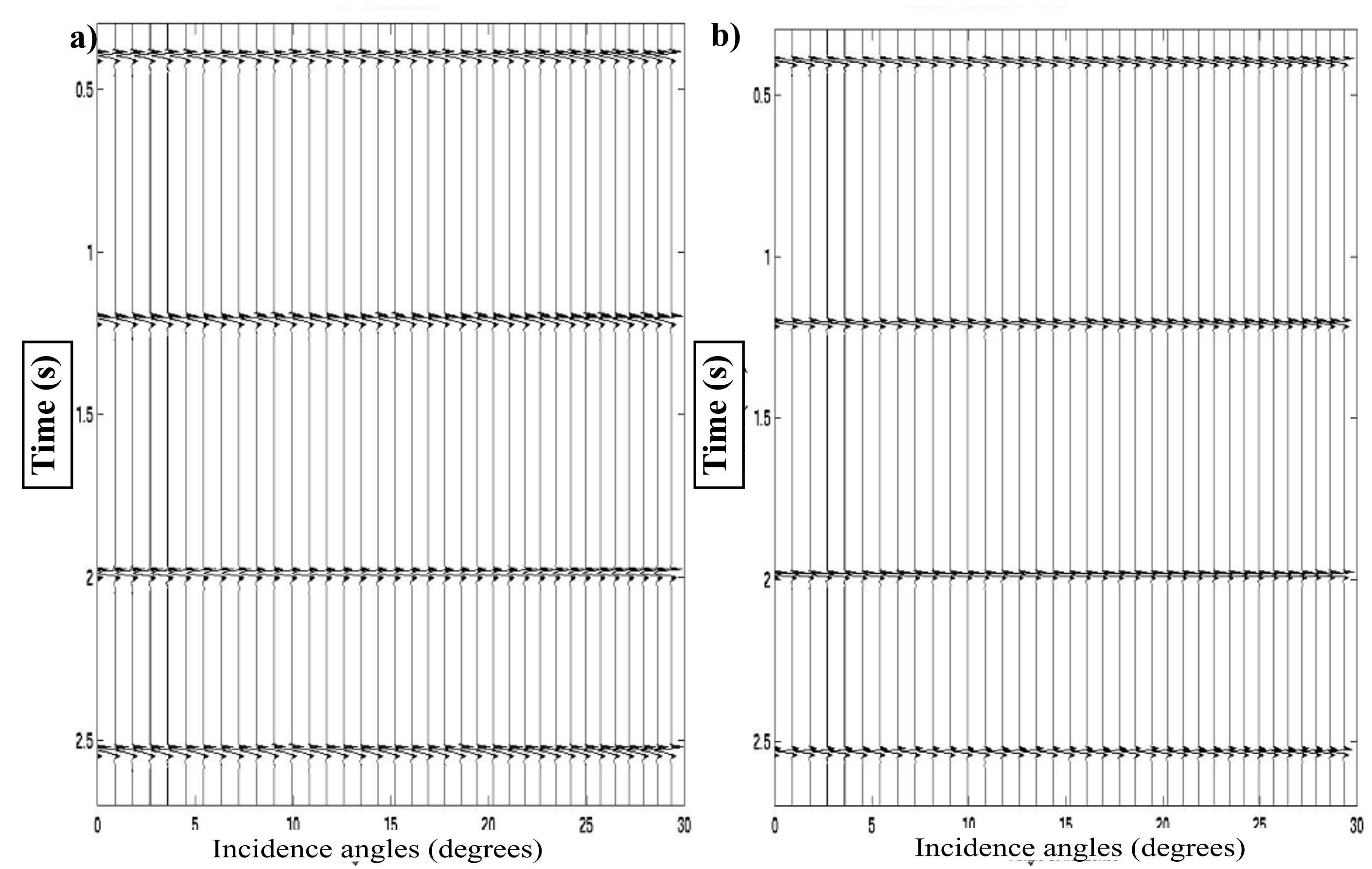

FIGURE 4. Offset gathers of anisotropic model; a) PP seismic data, and b) PS seismic data calibrated to PP traveltime.

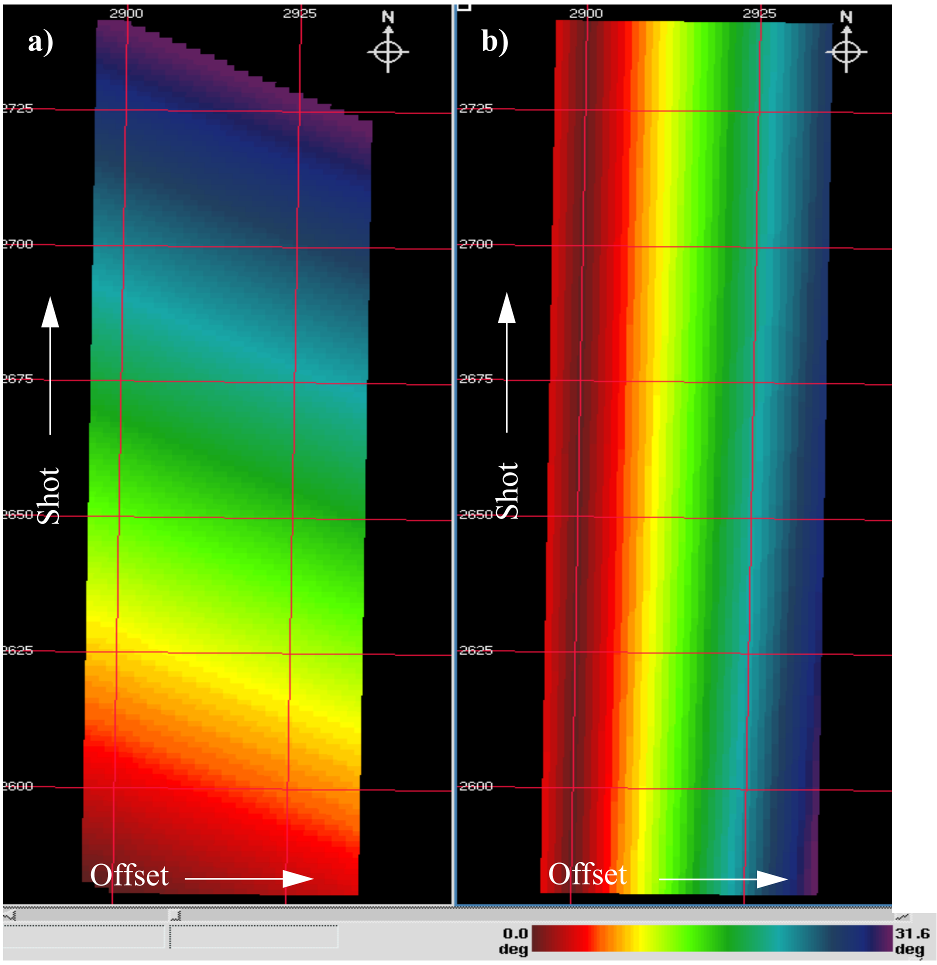

FIGURE 5. Plots showing a) CCP distribution of the synthetic P-wave seismic data, and b) distribution of P-wave incidence angles for the first interface.

Results for one trace of the first reflector are shown in Figures 6 - 11 together with results from isotropic inversion of the same data set. In general, anisotropic inversion produces better results than isotropic inversion. In addition, anisotropic inversion is robust to random noise for all tests. Results of the anisotropic inversion are in good agreement with exact contrasts both for P-wave velocity contrast, S-wave velocity contrast, and density contrast. Results with CCP sorting are slightly better than results without CCP sorting. Isotropic inversion produces good results for P-wave velocity contrast and density contrast. The S-wave velocity contrast has wrong sign and it is 4 times too large in absolute value for isotropic inversion. There is almost no difference in results with and without CCP sorting for isotropic inversion.

In addition to velocities- and density contrasts, anisotropic inversion also produces estimates of changes in the anisotropy parameters epsilon and delta. Estimated changes in both epsilon parameter and delta parameter have the wrong sign in all inversion tests. Absolute values of the delta parameter are of the correct order of magnitude. The estimates of the epsilon parameter are too small.

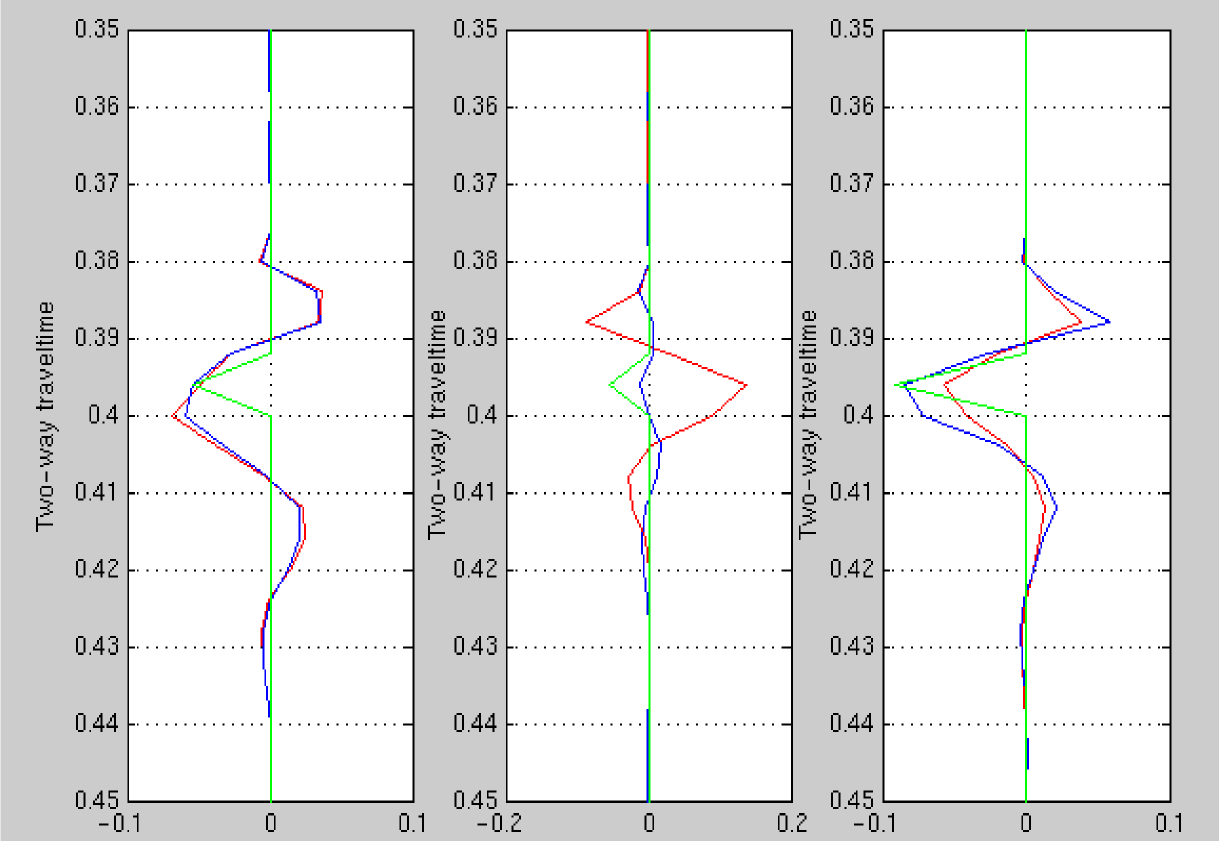

FIGURE 6. Relative change in P-wave velocity (left), S-wave velocity (middle), and density (right) for the first reflector in the model. The green curve is the exact relative change, the red curve is the result of isotropic inversion, and the blue curve is the result of anisotropic inversion without CCP sorting.

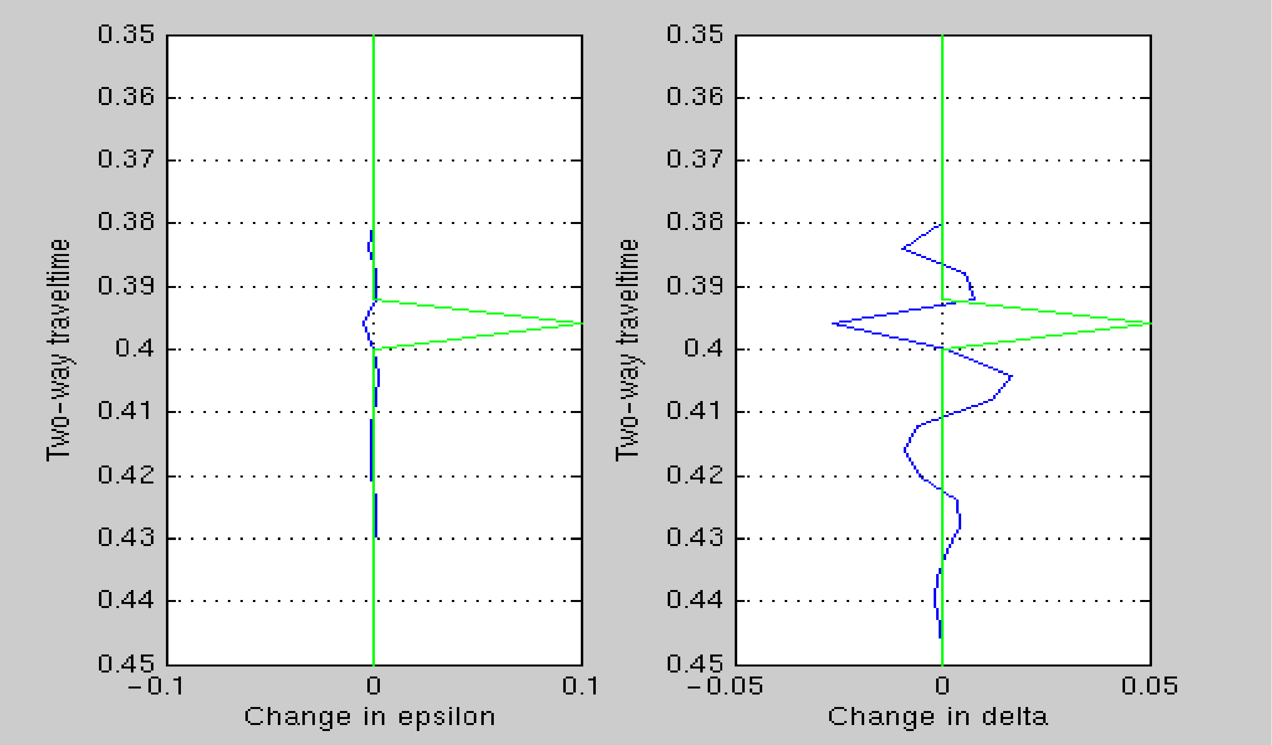

FIGURE 7. Change in the anisotropic parameters ε and δ for the first reflector in the model. The green curve is the exact relative change, and the red curve is the result of anisotropic inversion without CCP sorting.

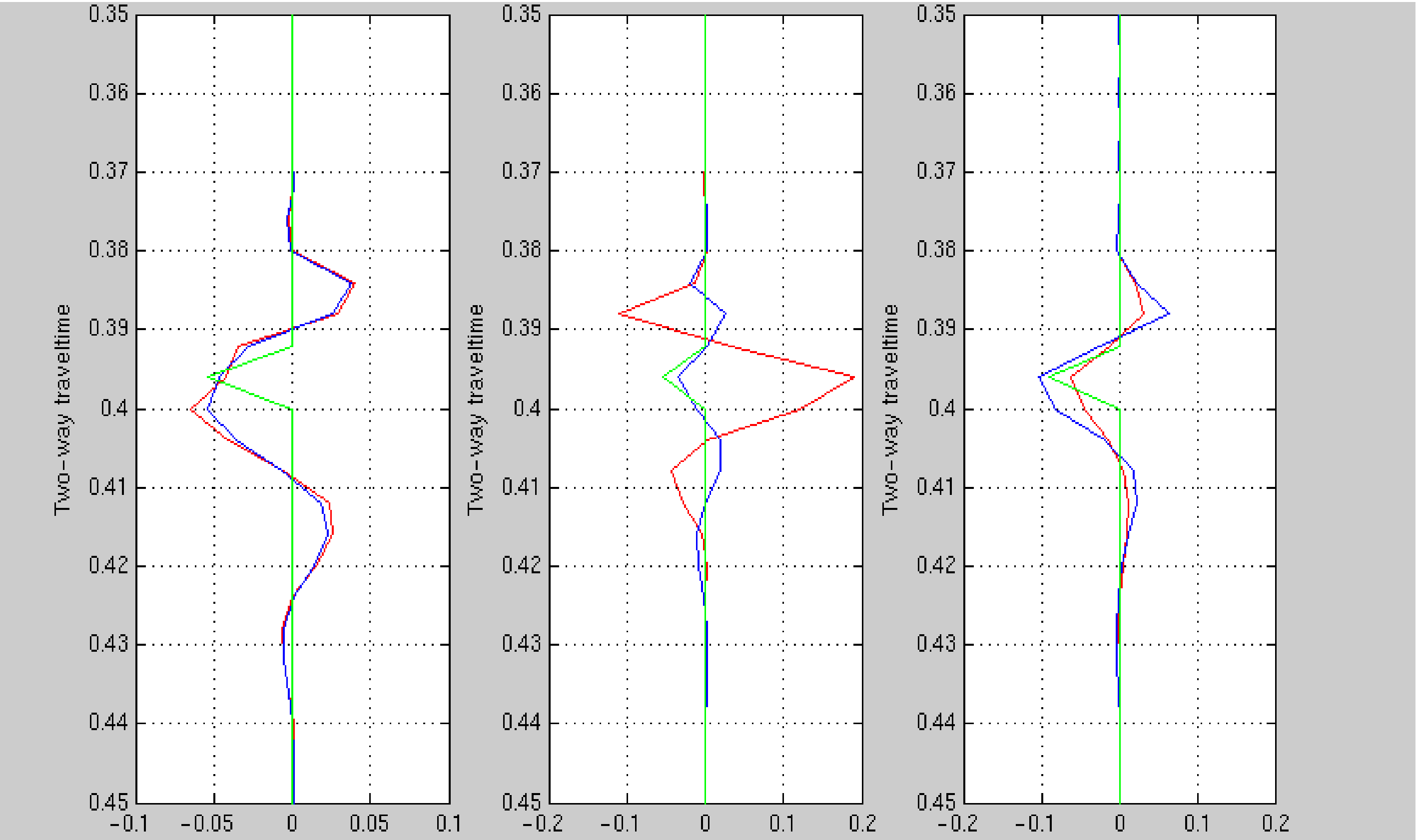

FIGURE 8. Relative change in P-wave velocity (left), S-wave velocity (middle), and density (right) for the first reflector in the model. The green curve is the exact relative change, the red curve is the result of isotropic inversion, and the blue curve is the result of anisotropic inversion with CCP sorting.

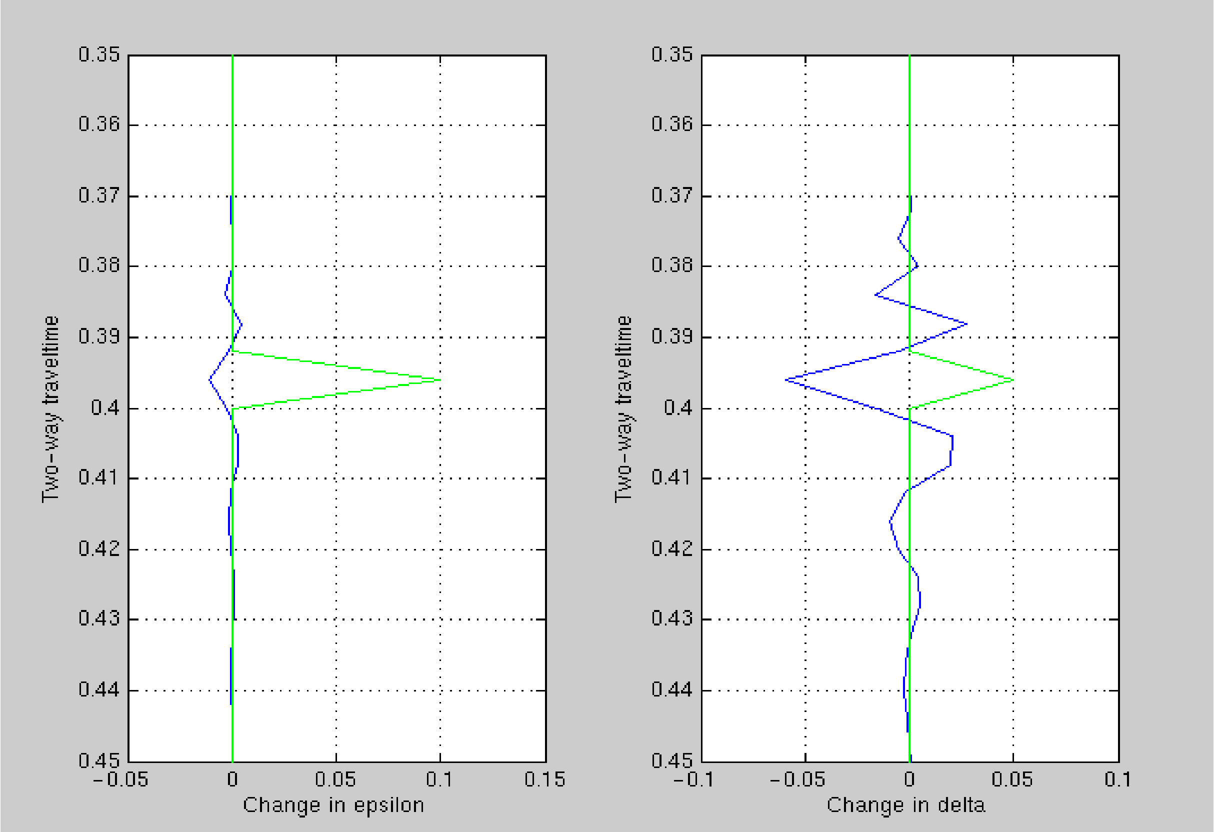

FIGURE 9. Change in the anisotropic parameters ε and δ for the first reflector in the model. The green curve is the exact relative change, and the blue curve is the result of anisotropic inversion with CCP sorting.

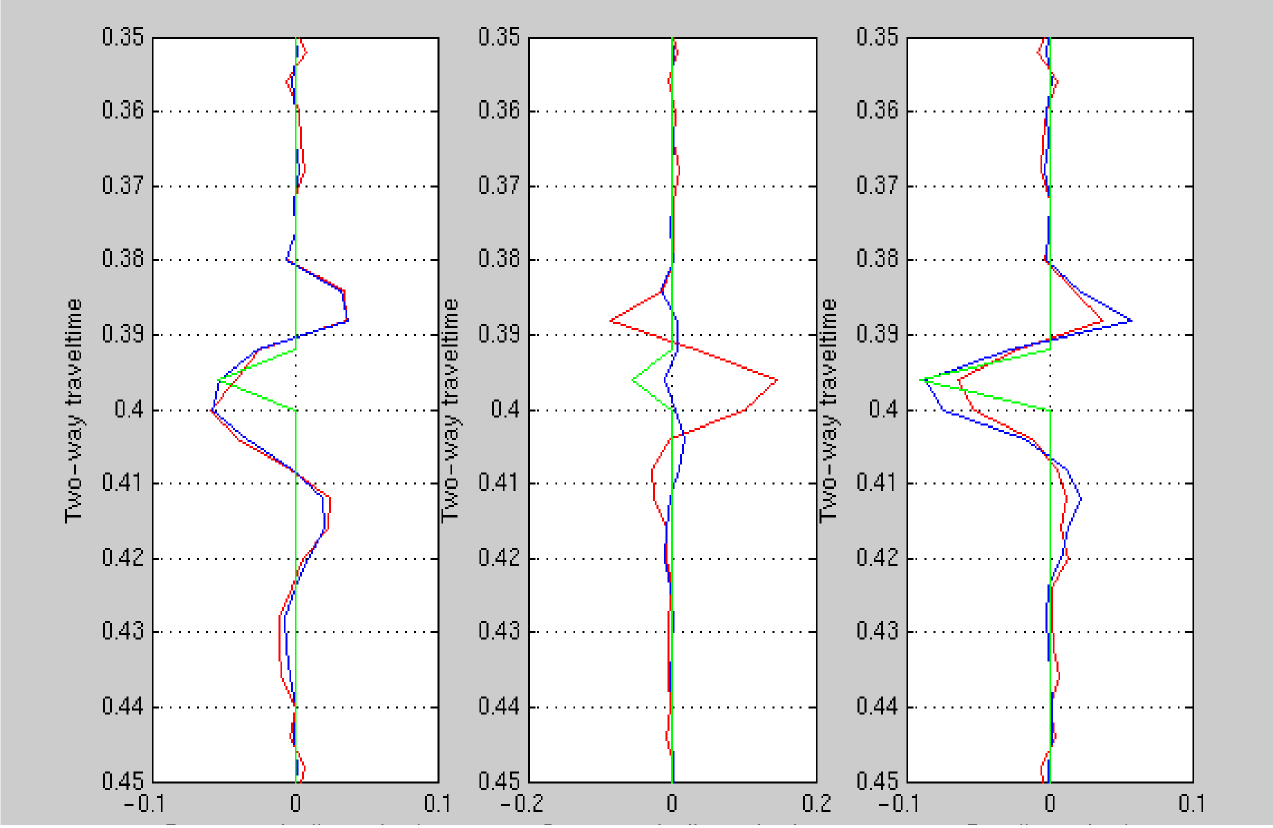

FIGURE 10. Relative change in P-wave velocity (left), S-wave velocity (middle), and density (right) for the first reflector in the model. The green curve is the exact relative change, the red curve is the result of isotropic inversion of synthetic seismic data with noise, and the blue curve is the result of anisotropic inversion of synthetic seismic data with noise.

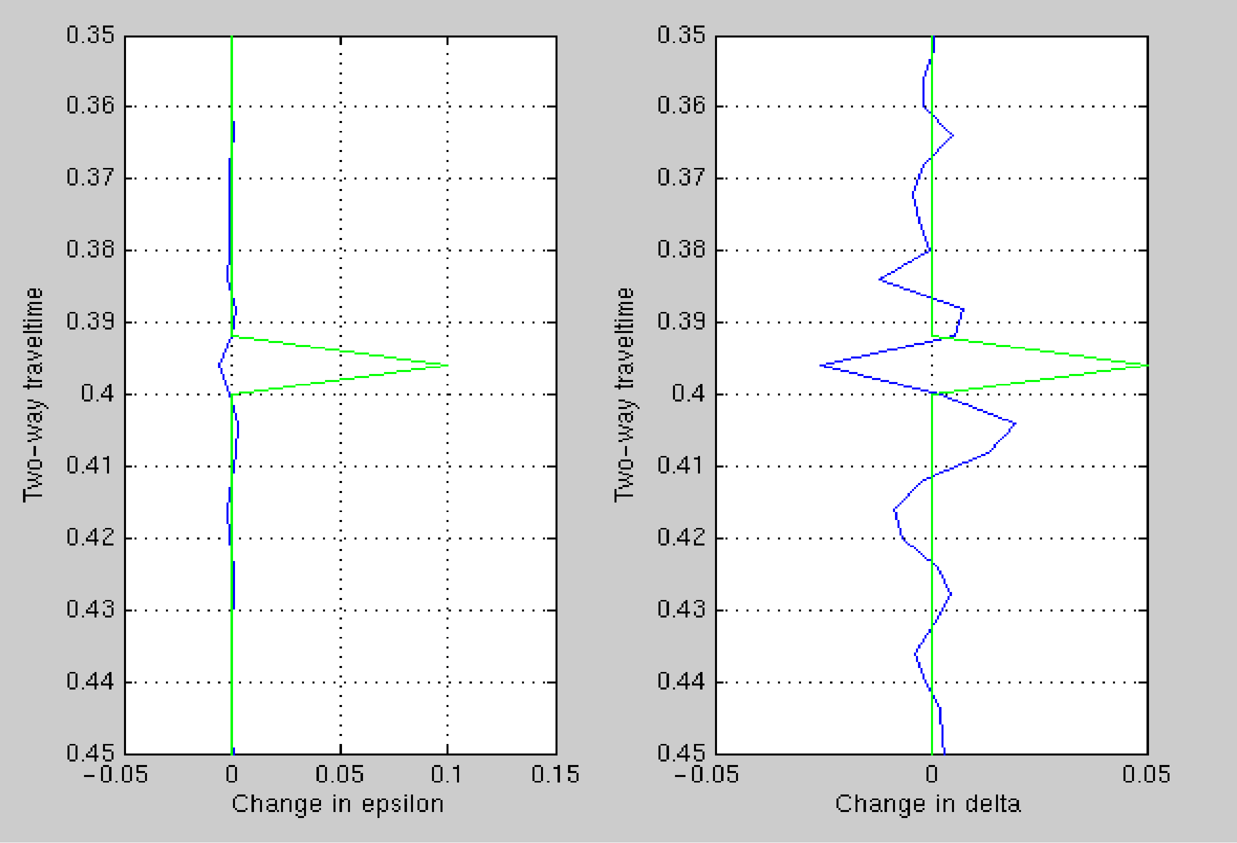

FIGURE 11. Change in the anisotropic parameters ε and δ for the first reflector in the model. The green curve is the exact relative change, and the red curve is the result of anisotropic inversion of synthetic seismic data with noise.

Discussion

By performing CCP sorting and NMO correction using non-hyperbolic move-out grids, we take into account kinematic effects of anisotropy. Effects on amplitudes are, however, not taken into account. This will reduce the quality of isotropic inversion of data with seismic anisotropy. The simultaneous least squares anisotropic inversion methodology presented here produces better results than simultaneous isotropic inversion. However, the system of equations is more unstable than the corresponding system for isotropic inversion. This is probably caused by the increased number of parameters.

As for the isotropic inversion method, this method requires unambiguous calibration of PS seismic data to PP traveltimes. If this is not done properly, non-corresponding events in the two data sets will be viewed together in the least squares system of equations. To obtain the Vp/Vs model required to scale PS seismic data to PP travel times, stacking velocities for PP- and PS data can be transformed to interval velocities using Dix' formula. Resulting velocities need to be quality controlled with interval velocities from well logs. To obtain a more accurate Vp/Vs model, corresponding reflection events in the P/Z- and PS seismic data can be interpreted and calibrated to well log data (e.g. Grechka et al., 2002).

Omitting the CCP-sorting for multicomponent seismic data might cause a disturbed AVO-response, since data from several reflection points are merged together in the same AVO-gather. In the synthetic example presented here, results of anisotropic inversion are only marginally better on data with CCP-sorting. Results of isotropic inversion do not change the same way. However, this model consists of almost horizontal layers with no lateral velocity variations. From Eqn. 5 we see that the CCP distribution varies with the ratio between S-wave and P-wave velocity. Lateral variations in the velocity fields will thus influence the CCP sorting, and the effect of CCP-sorting on real data will probably be more pronounced than on horizontal layered model.

Conclusions

In this paper, a joint least squares inversion methodology has been extended to anisotropic media. Output of the inversion is relative changes in P-wave velocity, relative changes in S-wave velocity, and relative changes in density. In addition, changes in the anisotropy parameters, ε and δ, across an interface are estimated. Synthetic results show that anisotropic inversion produces better results compared to isotropic inversion of seismic data with anisotropy. However, there are still instabilities in the inversion. Results of anisotropic inversion are of good for P-wave velocity contrast, S-wave velocity contrast and density contrast. Estimated changes in the anisotropy parameters ε and δ are wrong. Performing inversion on CCP-sorted seismic data improved the estimated S-wave velocity contrast compared to inversion on seismic data without CCP sorting for this synthetic example.

Appendix A - Least squares system with anisotropy

The coefficients in the least square equation system (Eqn. 4) is given below.

$$
\begin{aligned}
a_{11} &= \sum_{j=1}^{M}\left(\frac{1}{2}+\frac{1}{2}\sin^2\theta_{pj}+\frac{1}{2}\sin^2\theta_{pj}\tan^2\theta_{pj}\right)^2 \\
a_{12} &= \sum_{j=1}^{M}\left(\frac{1}{2}+\frac{1}{2}\sin^2\theta_{pj}+\frac{1}{2}\sin^2\theta_{pj}\tan^2\theta_{pj}\right)(-4\gamma^2\sin^2\theta_{pj}) = a_{21} \\
a_{13} &= \sum_{j=1}^{M}\left(\frac{1}{2}+\frac{1}{2}\sin^2\theta_{pj}+\frac{1}{2}\sin^2\theta_{pj}\tan^2\theta_{pj}\right)\left(\frac{1}{2}-2\gamma^2\sin^2\theta_{pj}\right) = a_{31} \\
a_{14} &= \sum_{j=1}^{M}\left(\frac{1}{2}+\frac{1}{2}\sin^2\theta_{pj}+\frac{1}{2}\sin^2\theta_{pj}\tan^2\theta_{pj}\right)\left(\frac{1}{2}\sin^2\theta_{pj}\tan^2\theta_{pj}\right) = a_{41} \\
a_{15} &= \sum_{j=1}^{M}\left(\frac{1}{2}+\frac{1}{2}\sin^2\theta_{pj}+\frac{1}{2}\sin^2\theta_{pj}\tan^2\theta_{pj}\right)\left(\frac{1}{2}\sin^2\theta_{pj}-\frac{1}{2}\sin^2\theta_{pj}\tan^2\theta_{pj}\right) = a_{51} \\
a_{22} &= \sum_{i=1}^{N}\left(\frac{2\sin\theta_{pi}}{\cos\theta_{si}}(\gamma^2\sin^2\theta_{pi}-\gamma\cos\theta_{pi}\cos\theta_{si})\right)^2+\sum_{j=1}^{M}(-4\gamma^2\sin^2\theta_{pj})^2
\end{aligned}
\tag{A-1}
$$

$$a_{23} = \sum_{i=1}^{N}\left(-\frac{2\sin^2\theta_{pi}}{\cos^2\theta_{si}}\right)(\gamma^2\sin^2\theta_{pi}-\gamma\cos\theta_{pi}\cos\theta_{si})(1-2\gamma^2(\sin\theta_{pi})^2+2\gamma\cos\theta_{pi}\cos\theta_{si}) + \sum_{j=1}^{M}(-4\gamma^2\sin^2\theta_{pj})\left(\frac{1}{2}-2\gamma^2\sin^2\theta_{pj}\right) = a_{32}$$

$$a_{24} = \sum_{i=1}^{N}\frac{2\sin\theta_{pi}}{\cos\theta_{si}}(\gamma^2\sin^2\theta_{pi}-\gamma\cos\theta_{pi}\cos\theta_{si})\left(\frac{\sin^4\theta_{pi}}{\sin\theta_{pi}\cos\theta_{si}+\sin\theta_{si}\cos\theta_{pi}}\right) + \sum_{j=1}^{M}(-4\gamma^2\sin^2\theta_{pj})\left(\frac{1}{2}\sin^2\theta_{pj}\tan^2\theta_{pj}\right) = a_{42}$$

$$a_{25} = \sum_{i=1}^{N}\frac{2\sin\theta_{pi}}{\cos\theta_{si}}(\gamma^2\sin^2\theta_{pi}-\gamma\cos\theta_{pi}\cos\theta_{si})\left(\frac{\sin^2\theta_{pi}\left(\frac{1}{2}-\sin^2\theta_{pi}\right)}{\sin\theta_{pi}\cos\theta_{si}+\sin\theta_{si}\cos\theta_{pi}}\right) + \sum_{j=1}^{M}(-4\gamma^2\sin^2\theta_{pj})\left(\frac{1}{2}\sin^2\theta_{pj}-\frac{1}{2}\sin^2\theta_{pj}\tan^2\theta_{pj}\right) = a_{52}$$

$$a_{33} = \sum_{i=1}^{N}\frac{\sin^2\theta_{pi}}{4\cos^2\theta_{si}}(1-2\gamma^2\sin^2\theta_{pi}+2\gamma\cos\theta_{pi}\cos\theta_{si})^2 + \sum_{j=1}^{M}\left(\frac{1}{2}-2\gamma^2\sin^2\theta_{pj}\right)^2$$

$$a_{34} = \sum_{i=1}^{N}-\frac{\sin\theta_{pi}}{2\cos\theta_{si}}(1-2\gamma^2\sin^2\theta_{pi}+2\gamma\cos\theta_{pi}\cos\theta_{si})\left(\frac{\sin^4\theta_{pi}}{\sin\theta_{pi}\cos\theta_{si}+\sin\theta_{si}\cos\theta_{pi}}\right) + \sum_{j=1}^{M}\left(\frac{1}{2}-2\gamma^2\sin^2\theta_{pj}\right)\left(\frac{1}{2}\sin^2\theta_{pj}\tan^2\theta_{pj}\right) = a_{43}$$

$$a_{35} = \sum_{i=1}^{N}-\frac{\sin\theta_{pi}}{2\cos\theta_{si}}(1-2\gamma^2\sin^2\theta_{pi}+2\gamma\cos\theta_{pi}\cos\theta_{si})\left(\frac{\left(\frac{1}{2}-\sin^2\theta_{pi}\right)\sin^2\theta_{pi}}{\sin\theta_{pi}\cos\theta_{si}+\sin\theta_{si}\cos\theta_{pi}}\right)$$

$$+\sum_{j=1}^{M}\left(\frac{1}{2}-2\gamma^2\sin^2\theta_{pj}\right)\left(\frac{1}{2}\sin^2\theta_{pj}-\frac{1}{2}\sin^2\theta_{pj}\tan^2\theta_{pj}\right) = a_{53}$$

$$\begin{aligned}
a_{44} &= \sum_{i=1}^{N}\left(\frac{\sin^4\theta_{pi}}{\sin\theta_{pi}\cos\theta_{si}+\sin\theta_{si}\cos\theta_{pi}}\right)^2+\sum_{j=1}^{M}\left(\frac{1}{2}\sin^2\theta_{pj}\tan^2\theta_{pj}\right)^2\\
a_{45} &= \sum_{i=1}^{N}\frac{\left(\frac{1}{2}-\sin^2\theta_{pi}\right)\sin^6\theta_{pi}}{(\sin\theta_{pi}\cos\theta_{si}+\sin\theta_{si}\cos\theta_{pi})^2}+\sum_{j=1}^{M}\left(\frac{1}{2}\sin^2\theta_{pj}\tan^2\theta_{pj}\right)\left(\frac{1}{2}\sin^2\theta_{pj}-\frac{1}{2}\sin^2\theta_{pj}\tan^2\theta_{pj}\right)=a_{54}\\
a_{55} &= \sum_{i=1}^{N}\left(\frac{\left(\frac{1}{2}-\sin^2\theta_{pi}\right)\sin^2\theta_{pi}}{\sin\theta_{pi}\cos\theta_{si}+\sin\theta_{si}\cos\theta_{pi}}\right)^2+\sum_{j=1}^{M}\left(\frac{1}{2}\sin^2\theta_{pj}-\frac{1}{2}\sin^2\theta_{pj}\tan^2\theta_{pj}\right)^2\\
b_1 &= \sum_{j=1}^{M}R^*{}_{pp}(\theta_{pj})\left(\frac{1}{2}+\frac{1}{2}\sin^2\theta_{pj}+\frac{1}{2}\sin^2\theta_{pj}\tan^2\theta_{pj}\right)\\
b_2 &= \sum_{i=1}^{N}R^*{}_{ps}(\theta_{pj})\frac{2\sin\theta_{pi}}{\cos\theta_{si}}(\gamma^2\sin^2\theta_{pi}-\gamma\cos\theta_{pi}\cos\theta_{si})+\sum_{j=1}^{M}R^*{}_{pp}(\theta_{pj})(-4\gamma^2\sin^2\theta_{pj})\\
b_3 &= \sum_{i=1}^{N}R^*{}_{ps}(\theta_j)\frac{\sin\theta_{pi}}{2\cos\theta_{si}}(1-2\gamma^2\sin^2\theta_{pi}+2\gamma\cos\theta_{pi}\cos\theta_{si})+\sum_{j=1}^{M}R^*{}_{pp}(\theta_{pj})\left(\frac{1}{2}-2\gamma^2\sin^2\theta_{pj}\right)
\end{aligned}\tag{A-2}$$

$$
\begin{aligned}
b_4 &= \sum_{i=1}^{N} R^*{}_{ps}(\theta_j)\left(\frac{\sin^4\theta_{pi}}{\sin\theta_{pi}\cos\theta_{si}+\sin\theta_{si}\cos\theta_{pi}}\right)+\sum_{j=1}^{M} R^*{}_{pp}(\theta_{pj})\left(\frac{1}{2}\sin^2\theta_{pj}\tan^2\theta_{pj}\right)\\
b_5 &= \sum_{i=1}^{N} R^*{}_{ps}(\theta_j)\left(\frac{\left(\frac{1}{2}-\sin^2\theta_{pi}\right)\sin^2\theta_{pi}}{\sin\theta_{pi}\cos\theta_{si}+\sin\theta_{si}\cos\theta_{pi}}\right)+\sum_{j=1}^{M} R^*{}_{pp}(\theta_{pj})\left(\frac{1}{2}\sin^2\theta_{pj}-\frac{1}{2}\sin^2\theta_{pj}\tan^2\theta_{pj}\right)
\end{aligned}
\tag{A-3}
$$

Discrimination between pressure and fluid saturation changes from marine multicomponent time lapse seismic data

Martin Landrø*, Helene Hafslund Veire*, Kenneth Duffaut§ and Nazih Najjar¤
****Department of Petroleum Engineering and Applied Geophysics, Norwegian University of Science and Technology, N-7491 Trondheim, Norway, §Statoil Research Centre, Postuttak 7005 Trondheim, Norway, ¤Saudi Aramco, P.O. Box 1290 Dharan 31311, Saudi Arabia.***
Presented at the 71st Ann. Mtg., Soc. Expl. Geophys., San Antonio 2001. Published in Geophysics, 68, 1592-1599.

Abstract

Explicit expressions for computation of saturation and pressure related changes from marine multicomponent time lapse seismic data are presented. Necessary input is PP and PS stacked data for the baseline seismic survey and the repeat survey. Compared to earlier methods based on PP data only, this method is expected to be more robust since two independent measurements are used in the computation. Due to a lack of real marine multicomponent time lapse seismic data sets, the methodology is tested on synthetic data sets, illustrating strengths and weaknesses of the proposed technique. Testing 10 scenarios for various changes in pore pressure and fluid saturation we find that it is more robust for most cases to use the proposed 4D PP/PS technique instead of a 4D PP AVO technique. The fit between estimated and "real" changes in water saturation and pore pressure were good for most cases. In average we find that the deviation in estimated saturation changes is 8% and 0.3 MPa for the estimated

pore pressure changes. For PP AVO we find that the corresponding average errors are 9% and 1.0 MPa. In the present method, only 4D PP and PS amplitude changes are used in the calculations. It is straightforward to include use of 4D travel time shifts in the algorithm, and if reliable time shifts can be measured, this will most likely further stabilize the presented method.

Introduction

Prediction of overpressured zones from seismic data have been tested and reported by several researchers, such as, Reynolds (1970) and Bilgeri and Ademeno (1982). The basic tool in such studies has been velocity analysis. By detecting areas where the estimated velocities deviate from the expected compaction trend (velocity increase versus depth), potential overpressure regions are identified by anomalous velocity decreases. For reservoir monitoring purposes, however, this approach is not appropriate for two reasons: First, for normal reservoir depths (2000 m and deeper) conventional velocity analysis is not sufficiently accurate to determine pore pressure changes of 5-6 MPa (or lower, see Kvam and Landrø, 2001). Second, when pore pressure changes and fluid saturation changes are both present, it is impossible to discriminate between the two from P-wave velocity analysis only. In most time lapse seismic studies, seismic differences between a base line and a monitor survey are analyzed and interpreted as either a pressure effect or a fluid effect. In the Magnus 4D study (Watts et al., 1996), the main seismic changes were attributed to pore pressure changes, while in the Gullfaks (Landrø et al., 1999) and the Draugen (Gabriels et al., 1999) 4D seismic studies, most of the seismic changes were interpreted as fluid related.

For some fields or segments within a field, both fluid and pressure changes have approximately the same degree of impact on the seismic data. In such cases the use of time lapse AVO analysis offers an opportunity to discriminate between the two effects (Tura and Lumley, 1998; Tura and Lumley, 1999; Landrø, 2001a). The major weakness of time-lapse AVO is the lack of seismic repeatability, which influences the quality of the results. As discussed by Cambois (2000), there are many effects that limit precise use of P-wave AVO data, such as wavelet variations with offset, residual multiple energy, residual NMO etc. For time-lapse AVO, many of these effects are reduced simply due to the fact that we commit the same error twice and then subtract one from the other. However, for wavelet variations from base to monitor survey (as opposed to wavelet variations with offset), specific matching filters should be used. Still, there are major uncertainties associated with time lapse AVO (Landrø, 2001). This paper shows that the combined use of PP and PS time lapse seismic data will reduce the overall uncertainty when estimating pressure and saturation changes. Therefore, the main objective of the present paper is to develop and test a methodology for discriminating fluid pressure and saturation changes directly from time lapse PP and PS seismic stacks.

The technique of acquiring marine multicomponent data was demonstrated by Berg et al., 1994, to image through gas clouds. Since then, multicomponent data has been used for various purposes, as for instance shale-sand discrimination (MacLeod et al., 1999). Landrø et al. (1999b) proposed to use shear wave elastic impedance as a well calibration tool, and this concept was later tested on a multicomponent data set from the Statfjord Field (Duffaut et al., 2000).

There are other production related changes which have impact on time lapse seismic data, such as gas injection, temperature changes, etc. In this paper, however, the focus will be on the discrimination between pore pressure and fluid saturation changes. In the following, a method to estimate fluid and pressure related changes directly from repeated PP and PS partially stacked data will be presented.

Saturation and pressure versus seismic parameters

Distinguishing between fluid saturation and pore pressure changes from seismic data requires knowledge about how seismic parameters are influenced by such changes. In the Gullfaks 4D project (Landrø et al., 1999a) a rock physics model calibrated with well log measurements was used to predict the seismic effect of substituting oil with water. The basic equation in the rock physics modeling is the Gassmann equation (Gassmann, 1951). Repeated logging in wells typically shows a change in water saturation from values around 10% (preproduction) to values around 70-80% (postproduction). The relationship between saturation changes and P-wave velocity after calibrating the Gassmann model to some of the wells at the Gullfaks Field is shown in Figure 1. A slightly non-linear relationship is observed. The relationship between seismic parameters and saturation changes can thus be approximated by linear functions to first order at the Gullfaks Field.

A common way to obtain a relationship between seismic parameters and pressure changes is to perform ultrasonic measurements on several cores taken from various formations. A typical curve for P-wave velocity versus effective pressure changes is displayed in Figure 2. This curve represents the average of 29 dry core measurements from the Gullfaks Field. A similar trend is found for the S-wave velocity versus effective pressure, based on the same 29 plug measurements. The Gullfaks reservoir rock is of early and middle Jurassic age, representing shallow marine to fluvial deposits. The reservoir depth is approximately 2000 m. The initial pore pressure is 32 MPa, and the vertical overburden/external stress is approximately 38 MPa. Typical porosities are around 30 percent. All measurements were made on dry core samples. Comparison of dry and brine saturated acoustic core measurements shows that the compressional velocities are higher in brine-saturated rock. The saturation effect is more pronounced at lower effective vertical stresses (Winkler, 1985). The effective vertical stress is equal to the vertical stress minus the pore pressure. This means that a pore pressure increase will lead to a decreased effective vertical stress. In comparison with the velocity versus saturation curve shown in Figure 1, the curve in Figure 2 is highly non-linear. As will be shown later, this non-linear behavior requires a second order approximation of the relationship between seismic parameters and pressure changes. A summary of the rock physics feasibility study for Gullfaks is shown in Figure 3. To test the proposed algorithm for a variety of pressure-saturation changes, an industrial rock physics modeling tool (Petrotools) was used (after calibration to the measurements).

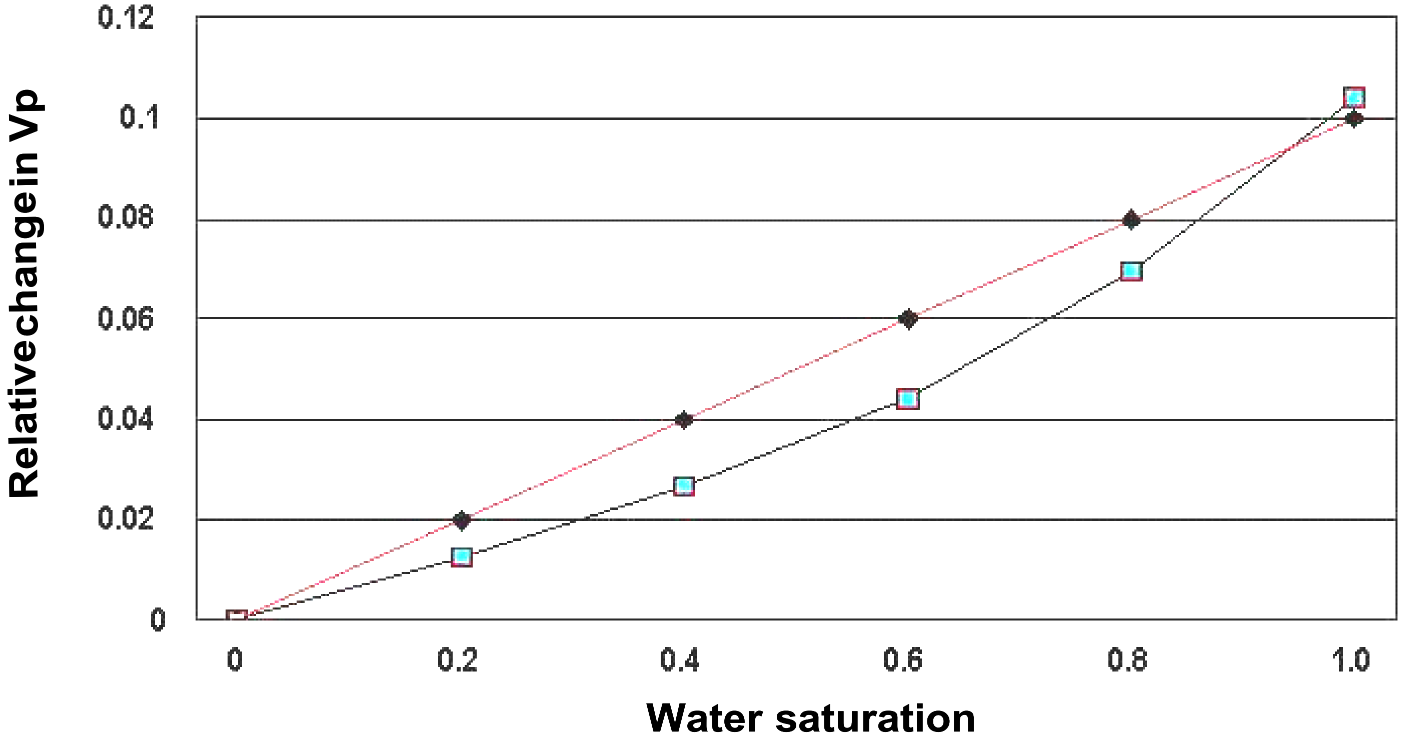

FIGURE 1. Typical modeled (Gassmann) relationship between relative change in P-wave velocity and change in water saturation (line with squares). Also shown is the straight line approximation used in the data example (line with diamonds).

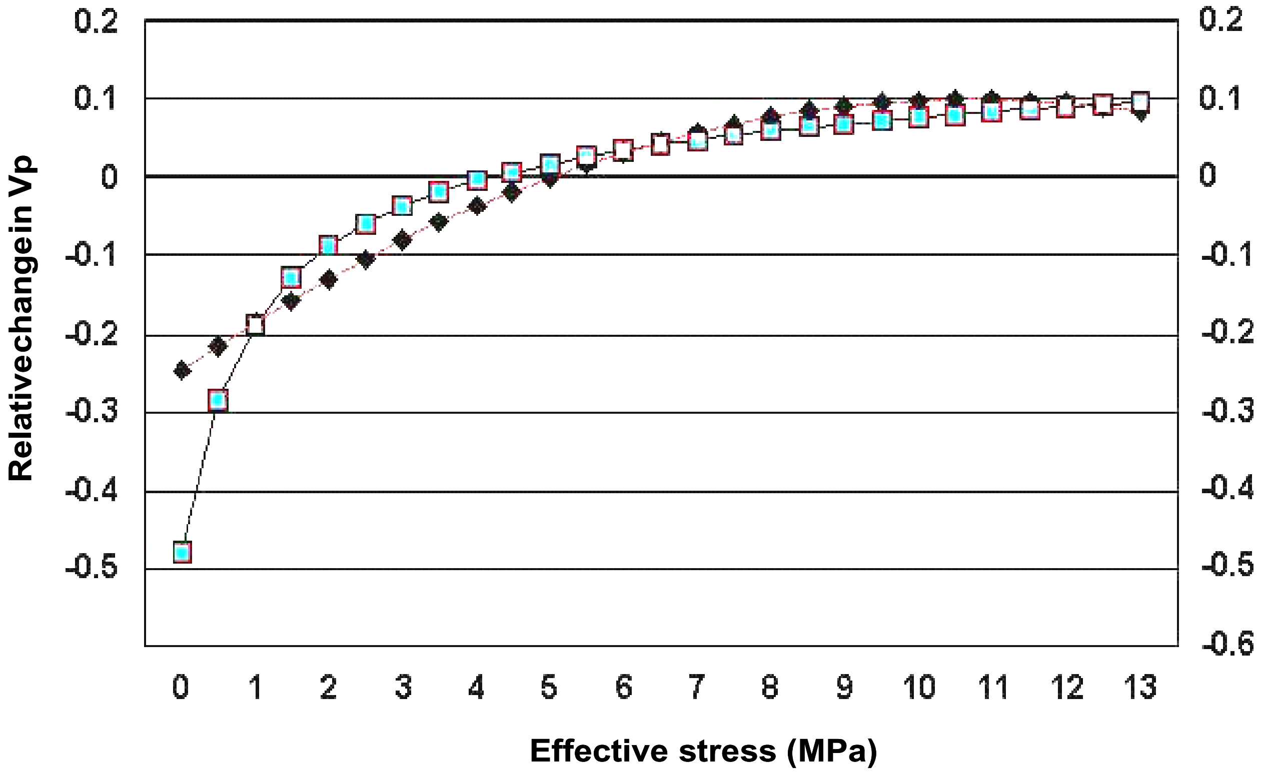

FIGURE 2. Relative P-wave velocity change versus change in net effective pressure (line with squares). Initial net pressure at Gullfaks is assumed to be around 5-6 MPa, and expected changes in net pressure might range from -5 MPa (for a pore pressure increase) to + 5MPa (for a pore pressure decrease). The diamond line shows the second order approximation used in the data example.

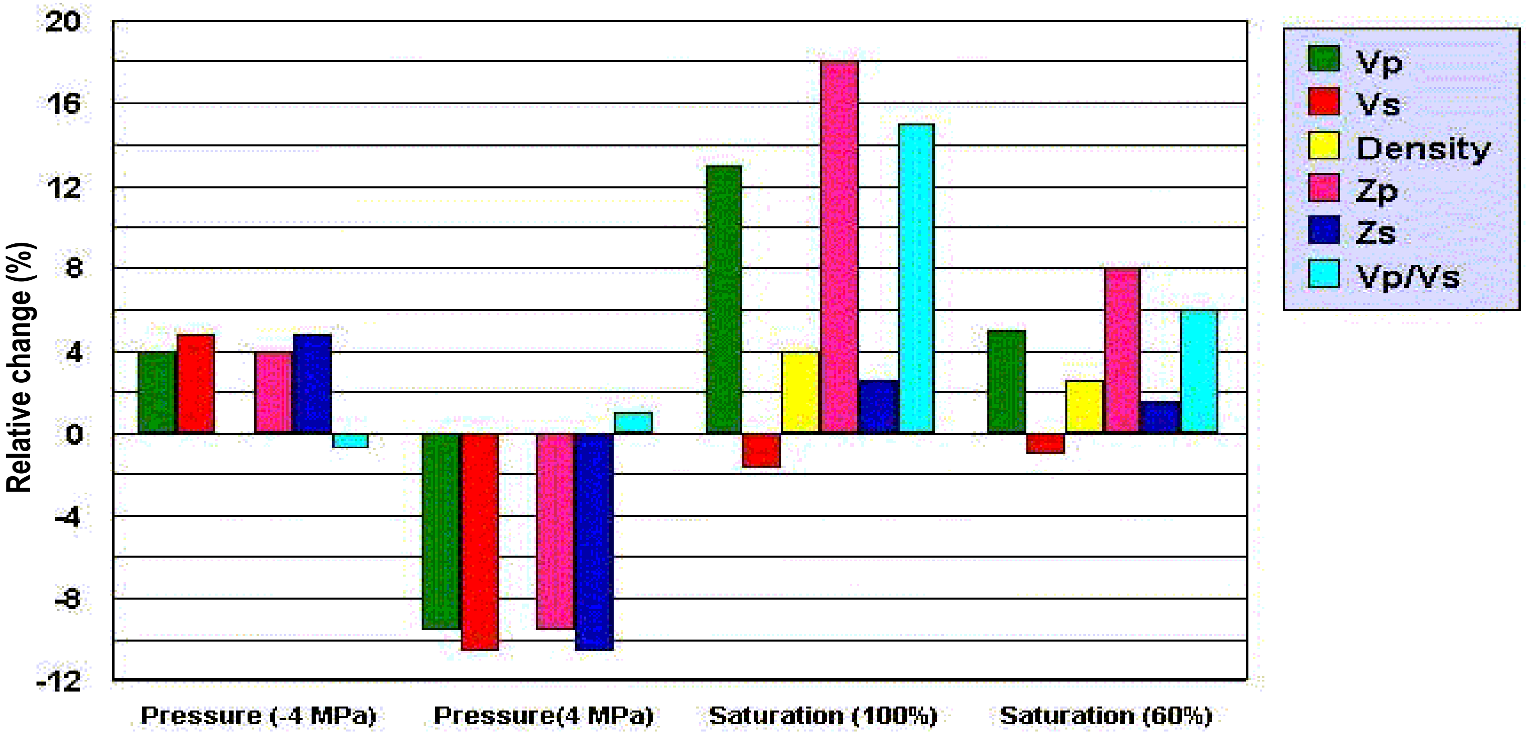

FIGURE 3. Expected relative changes (%) in various seismic parameters (Vp, Vs, density, P-acoustic impedance, S-acoustic impedance and Vp/Vs-ratio, from left to right for each histogram) due to changes in pore pressure and water saturation. 60% change in water saturation means from 20 to 80%. Zp and Zs denote P- and S-wave impedances, respectively. Average porosity is 30%, initial pore pressure is 32 MPa and the reservoir depth is approximately 2000 m. (Figure reprinted with permission from Petroleum Geoscience).

The validity of curves such as those shown in Figure 1 and Figure 2 should be discussed. Is it valid to compare velocities measured at high frequencies with seismic velocities? Is it valid to compare pressure measurements made on a dry core sample that has gone through reloading and loading several times with actual stress conditions in the reservoir rock? Despite all these concerns, numerical models obtained from the rock physics study were used as a link between reservoir production changes and seismic changes.

Methodology

The methodology is basically an extension of the method presented by Landrø (2001a). Consider a two-layer model: a cap rock layer (layer 1, shale) above a reservoir layer (layer 2, sand). For simplicity the situation when only fluid saturation changes occur in layer 2 will first be studied, next only pressure changes in layer 2 will be examined. The P-wave velocity in layer 1 (α_1) is assumed to remain constant between the baseline and the repeated survey, as well as for the S-wave velocity (β_1) and the density (ρ_1). In layer 2 (which is assumed to be the porous reservoir layer) the pre-production parameters are denoted α_2, β_2 etc. The same parameters after fluid substitution in layer 2 are denoted α_2', β_2' etc. The lithological parameter contrast in P-wave velocity is $\Delta\alpha = \alpha_2 - \alpha_1$, while the parameter contrast due to fluid changes in layer 2 can be expressed as $\Delta\alpha^F = \alpha_2' - \alpha_2$, or more precisely

$$\Delta\alpha^F = \alpha_2[S_W(t_2)] - \alpha_2[S_W(t_1)], \tag{1}$$

where S_W denotes water saturation, t_1 and t_2 denote the timing for the baseline and monitor seismic surveys, respectively, and subscript 2 of α_2 etc. refers to layer 2. The reflection coefficient prior to production is (Aki and Richards, 1980):

$$R(\theta) = \frac{1}{2}\left(\frac{\Delta\alpha}{\alpha} + \frac{\Delta\alpha}{\alpha}\right) - \frac{2\beta^2}{\beta^2}\left(\frac{\Delta\rho}{\rho} + \frac{2\Delta\beta}{\beta}\right)\sin^2\theta + \frac{\Delta\alpha}{2\alpha}\tan^2\theta, \tag{2}$$

where $\alpha = (\alpha_1 + \alpha_2)/2$ etc. After fluid substitution in layer 2 the post-production reflection coefficient is found to be

$$R_1^{PP}(\theta) = \frac{1}{2}\left(\frac{\Delta\rho'}{\rho'} + \frac{\Delta\alpha'}{\alpha'}\right) - \frac{2\beta'^2}{\alpha'^2}\left(\frac{\Delta\rho'}{\rho'} + \frac{2\Delta\beta'}{\beta'}\right)\sin^2\theta + \frac{\Delta\alpha'}{2\alpha'}\tan^2\theta, \qquad (3)$$

where

$$\begin{aligned} \Delta\alpha' &= \alpha_2' - \alpha_1 = \alpha_2 + \Delta\alpha^F - \alpha_1 = \Delta\alpha + \Delta\alpha^F \\ \alpha' &= (\alpha_1 + \alpha_2 + \Delta\alpha^F)/2 = \alpha(1 + \Delta\alpha^F/2\alpha) \end{aligned} . \qquad (4)$$

Assuming that $\frac{\Delta\alpha}{\alpha} \ll 1$ and $\frac{\Delta\alpha^F}{\alpha} \ll 1$ and neglecting higher order terms or combinations of them in either $\frac{\Delta\alpha}{\alpha}$ or $\frac{\Delta\alpha^F}{\alpha}$ we obtain

$$\begin{aligned} R_1^{PP}(\theta) = {} & \frac{1}{2}\left(\frac{\Delta\rho}{\rho} + \frac{\Delta\alpha}{\alpha}\right) - \frac{2\beta^2}{\alpha^2}\left(\frac{\Delta\rho}{\rho} + \frac{2\Delta\beta}{\beta}\right)\sin^2\theta + \frac{\Delta\alpha}{2\alpha}\tan^2\theta \\ & + \frac{1}{2}\left(\frac{\Delta\rho^F}{\rho} + \frac{\Delta\alpha^F}{\alpha}\right) - \frac{2\beta^2}{\alpha^2}\left(\frac{\Delta\rho^F}{\rho} + \frac{2\Delta\beta^F}{\beta}\right)\sin^2\theta + \frac{\Delta\alpha^F}{2\alpha}\tan^2\theta \end{aligned} . \qquad (5)$$

In the above derivation the following approximation for the velocity ratio term has been used:

$$\frac{\beta'}{\alpha'} = \frac{\beta\left(1 + \frac{\Delta\beta^F}{2\beta}\right)}{\alpha\left(1 + \frac{\Delta\alpha^F}{2\alpha}\right)} \approx \frac{\beta}{\alpha}. \qquad (6)$$

The delta-terms in this velocity ratio ($\frac{\Delta\beta^F}{2\beta}, \frac{\Delta\alpha^F}{2\alpha}$) are to be multiplied with other delta-terms inside the brackets of Eqn. 5, ($\frac{\Delta\rho}{\rho} + \frac{2\Delta\beta}{\beta}$), but since they will give second order terms they can be neglected. A detailed derivation including second order terms can be found in Landrø (2001a). Furthermore, for fluid substitution one can assume that the shear modulus remains constant, meaning that the $\sin^2\theta$-term in Eqn. 5 does not change under fluid substitution. This can be seen in the following way: keeping the shear modulus constant means that $\beta^2\rho$ is constant, leading to the result that $\frac{\Delta\rho^F}{\rho} + \frac{2\Delta\beta^F}{\beta} = 0$ for fluid substitution. For fluid substitution Eqn. 5 therefore reads

$$R_1^{PP}(\theta) \approx R_0(\theta) + \frac{1}{2}\left(\frac{\Delta\rho^F}{\rho} + \frac{\Delta\alpha^F}{\alpha}\right) + \frac{\Delta\alpha^F}{2\alpha}\tan^2\theta, \qquad (7)$$

which again means that the change in reflectivity (to the lowest order) due to fluid saturation change in layer 2 is

$$\Delta R^{PP;F}(\theta) \approx \frac{1}{2}\left(\frac{\Delta\rho^F}{\rho} + \frac{\Delta\alpha^F}{\alpha}\right) + \frac{\Delta\alpha^F}{2\alpha}\tan^2\theta. \tag{8}$$

A numerical example testing the differences between using this approximate expression for reflectivity changes and using the “exact” equations, shows a deviation in reflectivity of 4% at zero incidence angle and 1% at an angle of 30 degrees (Landrø, 2001).

For pressure changes it is reasonable to assume that the density remains practically unchanged. Assume that the bulk density can be written as

$$\rho = \phi\rho_f + (1-\phi)\rho_s, \tag{9}$$

where ϕ is the porosity and ρ_f and ρ_s are the fluid and matrix densities, respectively. For a sandstone reservoir, the changes in porosity due to pressure changes are generally small, and hence the changes in density due to pressure changes are also negligible. This is confirmed by the core measurement results shown in Figure 3. A corresponding equation for the reflectivity change due to a change in the pore pressure (P) can therefore be approximated (again to the lowest order) by

$$\Delta R^{PP;P}(\theta) \approx \frac{1}{2}\frac{\Delta\alpha^P}{\alpha} - \frac{4\beta^2}{\alpha^2}\frac{\Delta\beta^P}{\beta}\sin^2\theta + \frac{\Delta\alpha^P}{2\alpha}\tan^2\theta. \tag{10}$$

The previous analysis considered PP data only, we can extend the same analysis to PS data. A reasonable approximation (assuming weak contrasts and small angles) for the PS-reflection coefficient can be obtained from Aki and Richards (1980):

$$\begin{aligned} R_0^{PS}(\theta) &= -\frac{1}{2}\left((1+2K)\frac{\Delta\rho}{\rho} + 4K\frac{\Delta\beta}{\beta}\right)\sin\theta \\ &+ K\left(\left(K+\frac{1}{2}\right)\left(\frac{\Delta\rho}{\rho} + 2\frac{\Delta\beta}{\beta}\right) - \frac{K}{4}\frac{\Delta\rho}{\rho}\right)\sin^3\theta \end{aligned} \tag{11}$$

where $K = \frac{\beta}{\alpha}$ denotes the Vs to Vp ratio. In order to obtain full consistency between Eqn. (10) and (11) we should choose $\tan^2\theta \approx \sin^2\theta$ (corresponding to the small angle approximation made in Eqn. 11) in Eqn. 10. However, for the current examples, we have chosen to keep Eqn. 10 as it is. Calculating the same changes in the PS reflection coefficient as for the PP reflection coefficient yields:

$$\begin{aligned}\Delta R^{PS;F}(\theta) &= -\frac{1}{2}\frac{\Delta\rho^F}{\rho}\sin\theta - \frac{K^2}{4}\frac{\Delta\rho^F}{\rho}\sin^3\theta \\ \Delta R^{PS;P}(\theta) &= -2K\frac{\Delta\beta^P}{\beta}\sin\theta + 2K\left(K+\frac{1}{2}\right)\frac{\Delta\beta^P}{\beta}\sin^3\theta\end{aligned} \quad . \qquad (12)$$

A reasonable assumption for the relative variation of the seismic parameters with respect to fluid saturation and effective pressure changes can be written (using first order expansion with respect to saturation changes and second order with respect to pressure changes):

$$\begin{aligned}\frac{\Delta\alpha_2}{\alpha_2} &\approx k_\alpha\Delta S + l_\alpha\Delta P + m_\alpha\Delta P^2 \\ \frac{\Delta\beta_2}{\beta_2} &\approx k_\beta\Delta S + l_\beta\Delta P + m_\beta\Delta P^2 \ , \\ \frac{\Delta\rho_2}{\rho_2} &\approx k_\rho\Delta S\end{aligned} \qquad (13)$$

where ΔS and ΔP denote the changes in oil saturation and effective pressure, respectively. $k_\alpha, k_\beta, k_\rho, l_\alpha, l_\beta, m_\alpha, m_\beta$ are empirical parameters estimated from, for instance, the saturation change curve in Figure 1 and the pressure change curve in Figure 2. It should be noted that the assumptions given in Eqn. 13 are reasonable approximations for the Gullfaks Field. For other fields with different reservoir properties, more advanced approximations might be necessary (e.g. Meadows, 2001). These parameters will generally be spatially variant. In practice however, it is impossible to measure these parameters at all positions in space. Therefore, a realistic approach would be to estimate one parameter set for each formation, or to assume that one average parameter set is representative for the whole field. As an example, the relative P-wave velocity increase (based on the average curve as shown in Figure 2) due to a pore pressure decrease of 4 MPa was estimated to be 4% with a standard deviation of 1.5% (corresponding to an uncertainty of 40%). The standard deviation was computed on the basis of all 29 core samples used in the Gullfaks study. The total change in reflectivity due to the combined effect of fluid and pressure changes can thus be written

$$\begin{aligned}\Delta R^{PP} &\approx \frac{1}{2}(k_\rho \Delta S + k_\alpha \Delta S + l_\alpha \Delta P + m_\alpha \Delta P^2) + \frac{1}{2}(k_\alpha \Delta S + l_\alpha \Delta P + m_\alpha \Delta P^2)\tan^2\theta \\ &\quad -4K^2(l_\beta \Delta P + m_\beta \Delta P^2)\sin^2\theta \\ \Delta R^{PS} &\approx -\frac{1}{2}k_\rho \Delta S \cdot \sin\theta - \frac{K^2}{4}k_\rho \Delta S \cdot \sin^3\theta - 2K(l_\beta \Delta P + m_\beta \Delta P^2)\sin\theta \\ &\quad + 2K\left(K + \frac{1}{2}\right)(l_\beta \Delta P + m_\beta \Delta P^2)\sin^3\theta\end{aligned} \tag{14}$$

For differencing time lapse seismic data the most robust method is to work on stacked sections (Andorsen and Landrø, 2000), hence, Eqn. 14 need to be integrated over a given angle span, see Appendix A. After integration, we have

$$\begin{aligned}\Delta R^{PP} &\approx \frac{1}{2}(k_\rho \Delta S + k_\alpha \Delta S + l_\alpha \Delta P + m_\alpha \Delta P^2)i_0 + \frac{1}{2}(k_\alpha \Delta S + l_\alpha \Delta P + m_\alpha \Delta P^2)i_3 \\ &\quad -4K^3(l_\beta \Delta P + m_\beta \Delta P^2)i_2 \\ \Delta R^{PS} &\approx -\frac{1}{2}k_\rho \Delta S \cdot i_1 - \frac{K^2}{4}k_\rho \Delta S \cdot i_4 - 2K(l_\beta \Delta P + m_\beta \Delta P^2)i_1 \\ &\quad + 2\left(K\left(K + \frac{1}{2}\right)(l_\beta \Delta P + m_\beta \Delta P^2)i_4\right)\end{aligned} \tag{15}$$

where i_0 - i_4 are given in Appendix A. Rearranging these terms gives

$$\begin{aligned}\Delta R^{PP} &\approx a_1 \Delta S + a_2 \Delta P + a_3 \Delta P^2 \\ \Delta R^{PS} &\approx b_1 \Delta S + b_2 \Delta P + b_3 \Delta P^2,\end{aligned} \tag{16}$$

where the coefficients are given by

$$\begin{aligned}
a_1 &= \frac{1}{2}k_\rho i_0 + \frac{1}{2}k_\alpha i_0 + \frac{1}{2}k_\alpha i_3\\
a_2 &= \frac{1}{2}l_\alpha i_0 + \frac{1}{2}l_\alpha i_3 - 4K^2 l_\beta i_2\\
a_3 &= \frac{1}{2}m_\alpha i_0 + \frac{1}{2}m_\alpha i_3 - 4K^2 m_\beta i_2\\
b_1 &= -\frac{1}{2}k_\rho i_1 - \frac{K^2}{4}k_\rho i_4\\
b_2 &= -2Kl_\beta i_1 + 2K\left(K + \frac{1}{2}\right)l_\beta i_4\\
b_3 &= -2Km_\beta i_1 + 2K\left(K + \frac{1}{2}\right)m_\beta i_4
\end{aligned} \quad . \qquad (17)$$

Solving Eqn. 16 for ΔP and ΔS gives

$$\begin{aligned}
\Delta P &= \frac{\frac{b_2}{b_1}a_1 - a_2 \pm \sqrt{\left(a_2 - \frac{b_2}{b_1}a_1\right)^2 - 4\left(a_3 - \frac{b_3}{b_1}a_1\right)\left(\frac{a_1}{b_1}\Delta R^{PS} - \Delta R^{PP}\right)}}{2\left(a_3 - \frac{b_3}{b_1}a_1\right)}\\
\Delta S &= \frac{\Delta R^{PP} - \frac{a_3}{b_3}\Delta R^{PS} - \left(a_2 - \frac{b_2}{b_3}a_3\right)\Delta P}{a_1 - \frac{b_1}{b_3}a_3}
\end{aligned} \quad . \qquad (18)$$

Assuming that ΔR^{PP} and ΔR^{PS} can be estimated from stacked marine multicomponent time lapse seismic data (well calibration prior to the differencing is essential), Eqn. 15 can be solved for saturation and pressure changes.

Synthetic data example

Simple synthetic models with two layers were generated to test the validity of the methodology for the combination of PP and PS time-lapse data. In the synthetic models, the rock physical properties of the cap rock layer and the layer below the reservoir zone have been kept constant, and only the parameters of the reservoir rock have been changed. The reservoir rock is assumed to be buried at 2000m depth, and the initial properties are taken from a well in the Gullfaks field in the North Sea. The basic rock and fluid properties are given in Table 1. The relationship between the seismic parameters and pressure have been found through statistical analysis of ultrasonic measurements from dry cores of various formations (Figure 2). The seismic parameters for different scenarios for saturated reservoir rock have then been calculated using Gassmann's equation.

Water Salinity	3.5%
Density of oil	880 kg/m^3
GOR (Gas Oil Ratio)	90
Density of gas	0.76 kg/m^3
Temperature	72^o C
Initial effective pressure	6 MPa

Table 1: Initial rock and fluid parameters

Reflection coefficients have been calculated using Zoeppritz' equations for angles from 0 to 45 degrees, for the different reservoir models. The reflection coefficients have been convolved with a wavelet extracted from PP seismic data from the Gullfaks Field, calibrated to the reflection coefficients and stacked (for angles 0 - 45 degrees for PP-data, and either 0 - 45 degrees or 15 - 45 degrees for PS-data) for the different models. Figure 5 shows the PP and PS prestack synthetic seismograms for a scenario with water saturation 10% and effective pressure 6MPa, and Figure 6 shows the same synthetic seismograms with noise added. Figure 7 shows stacked traces (0 - 45 degrees) for PP and PS seismic data for the preproduction scenario described above, and a post production scenario with water saturation 50% and effective pressure 8 MPa. The time-lapse differences between the stacked data for PP and PS seismic are also shown.

The parameters describing the relationship between changes in seismic properties and saturation and pressure changes were estimated through statistical analysis of all the models with initial effective pressure 6MPa, and a positive water saturation change (Figure 5).

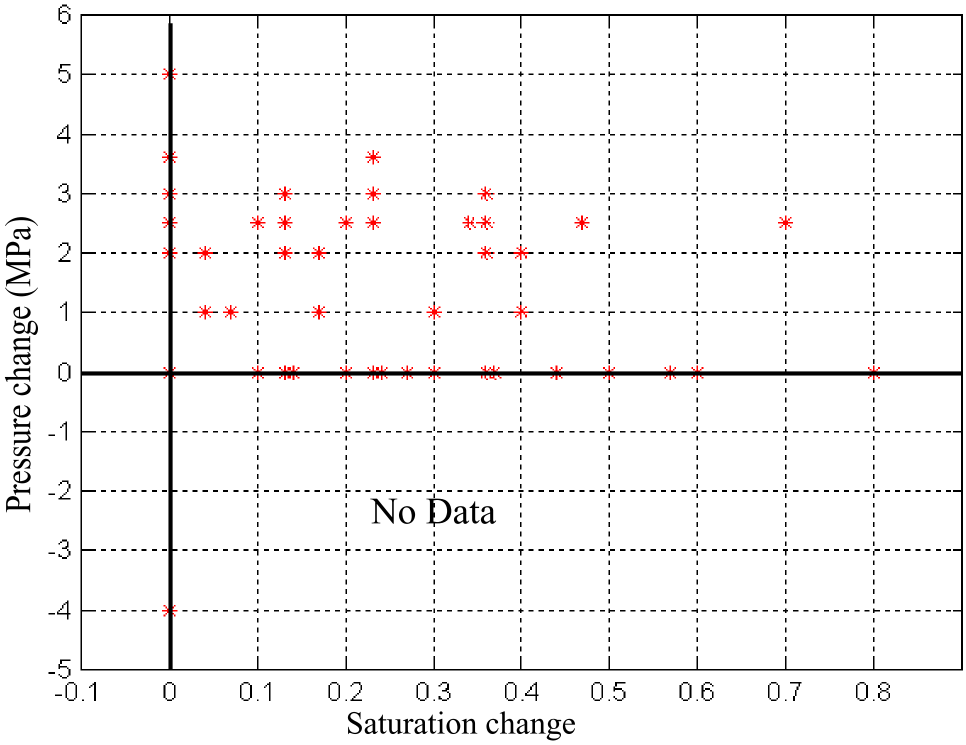

FIGURE 4. Change in saturation versus change in pressure for all models (initial effective pressure 6 MPa).

The estimated relationships are given by

$$\frac{\Delta\alpha_2}{\alpha_2} \approx 0.12\Delta S + 0.0121\Delta P - 0.005\Delta P^2$$
$$\frac{\Delta\beta_2}{\beta_2} \approx -0.015\Delta S + 0.0196\Delta P - 0.0021\Delta P^2 . \qquad (19)$$
$$\frac{\Delta\rho_2}{\rho_2} \approx 0.0293\Delta S$$

Using Eqn. 19, and assuming $\frac{V_p}{V_s} = \frac{\alpha}{\beta} = 2$ (for the models tested, the $\frac{V_p}{V_s}$-ratio varies between 1.92 and 2.15), Eqn. 16 give the following relationship between the change in reflectivity and the change in saturation and pressure:

$$\begin{aligned}\Delta R^{PP} &\approx 0.0715\Delta S - 0.0387\Delta P + 0.0043\Delta P^2 \\ \Delta R^{PS} &\approx -0.0066\Delta S - 0.0078\Delta P + 0.000835\Delta P^2\end{aligned}, \qquad (20)$$

Pairs of two models representing pre- and post-production stages have been analyzed to estimated the pressure and saturation changes from the seismic data. Differences between pre- and post production scenarios were computed for both PP- and PS-data, and the estimated changes in effective pressure and saturation were calculated using Eqn. 20.

For the example given in Figures 5, 6, and 7 (line 2 in Table 2), the initial effective pressure was 6 MPa, and the initial water saturation was 10%. The PP and PS date for this example were stacked from 0-45 degrees. After production, the effective pressure was 8 MPa and the water saturation was 50%, giving $\Delta S = 0.4$ and $\Delta P = 2 MPa$. By using Eqn. 20, the pressure change was estimated to be 1.68 MPa, and the saturation difference was estimated to be 0.34. This gives an error of 16% for the pressure change estimate, and 15% for the saturation change estimate.

Figure 6 shows a plot of the same initial model with random noise added to the gathers. The signal to noise ratio is 0.9 for the PP-data and 0.75 for the PS-data. With this noise level, the pressure change was estimated to be 1.75 MPa, and the saturation change estimated to be 0.33. This gives an error of 12.5% for the pressure change estimate and 17.5% for the saturation change estimate. Table 2 shows the results for 10 different production scenarios. Table 4 shows the estimated change in saturation and effective pressure for the same production scenarios used in Table 2, but using only time-lapse PP AVO data, as in Landrø (2001). The production changes estimated from multi-component data are overall better than the estimations using PP AVO data alone, however, the estimated change in effective pressure has improved the most. In average we find that the deviation in estimated saturation changes for the PP-PS-method described in ths paper is 8% and 0.3 MPa for the estimated pore pressure changes. For the PP AVO method we find that the corresponding average errors are 9% (saturation change) and 1.0 MPa (pressure change). In a second noise test, the signal to noise ratio level was reduced to 0.4, and the results are listed in the last column of Table 2. The average errors for the PP-PS-method were then 12% for saturation changes and 1.3 MPa for pressure changes.

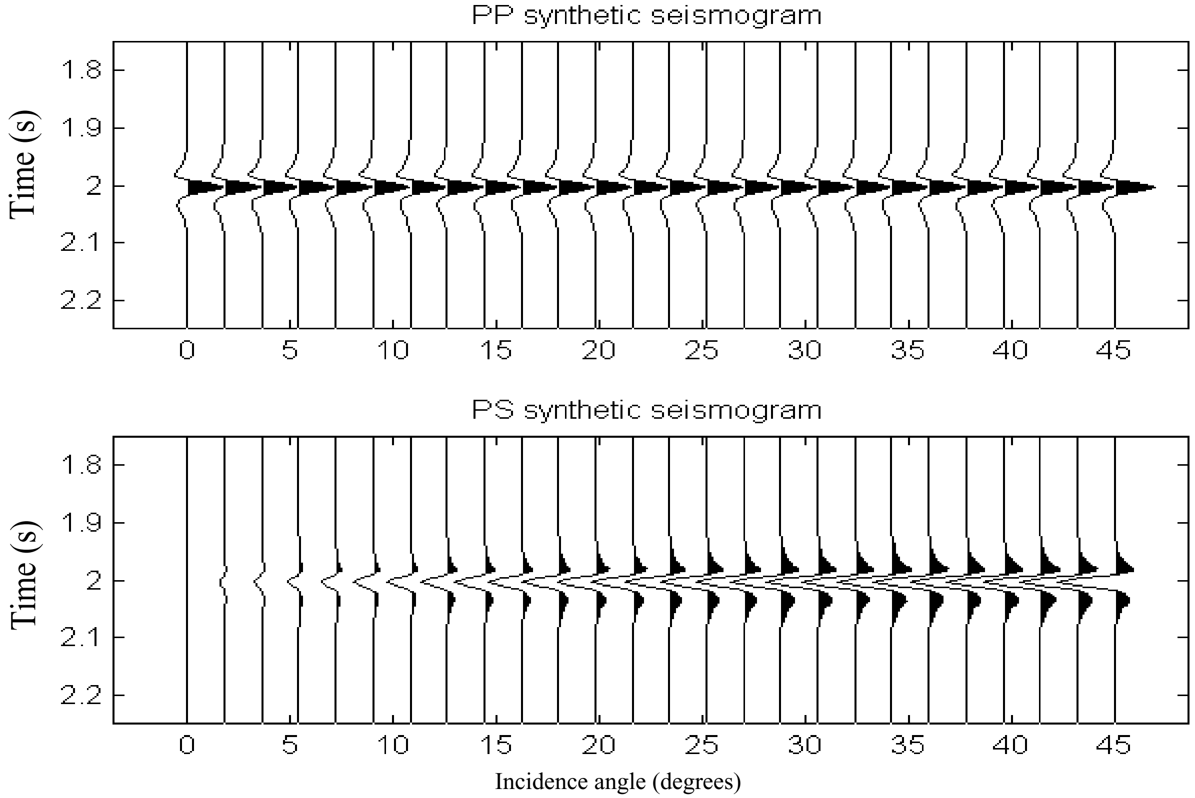

FIGURE 5. Baseline synthetic seismograms (angle gather) for PP (top) and PS reflections (bottom) for a model with initial pressure 6 MPa, and 10% initial water saturation.

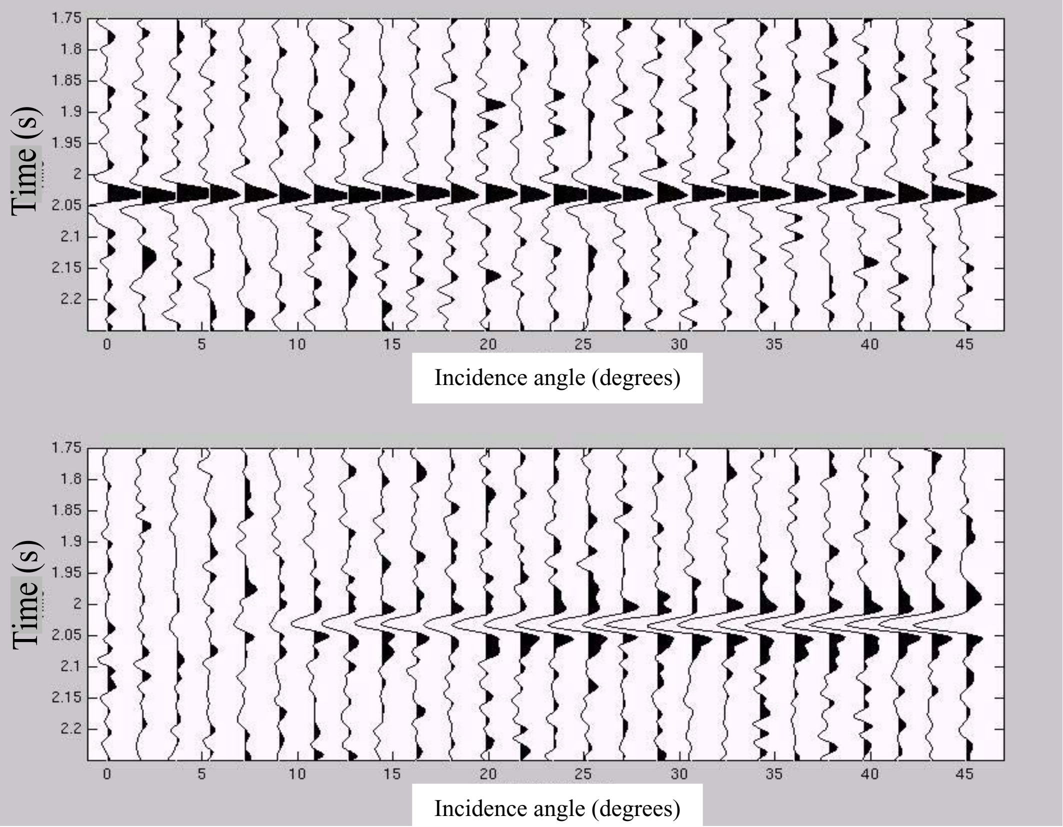

FIGURE 6. Baseline synthetic seismograms for PP and PS reflections (angle gather) with noise for a model with initial pressure 6 MPa, and 10% initial water saturation.

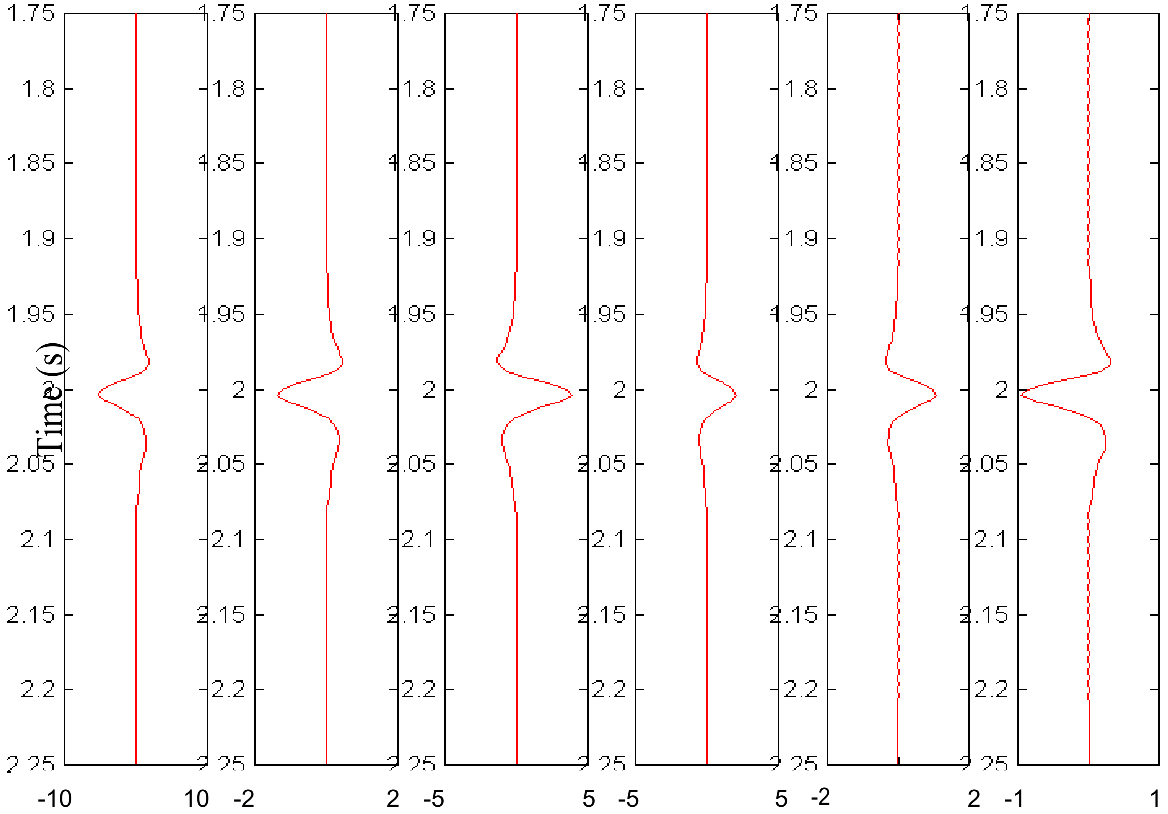

FIGURE 7. Stacked traces for PP and PS reflections for initial model, time-lapse model and the difference (time-lapse model - initial model).

Sw1 / Sw2	Real Sw Change	Est. Sw change	With noise SNR=1	With noise SNR=0.4	P1 / P2 (MPa)	Real P Change (MPa)	Est. P change (MPa)	With noise SNR=1	With noise SNR=0.4
0.1 / 0.33	0.23	0.16	0.16	0.23	6 / 6	0	0.1	0.06	-2.9
0.1 / 0.5	0.4	0.34	0.33	0.12	6 / 8	2	1.68	1.75	2.5
0.1 / 0.6	0.5	0.41	0.39	0.47	6 / 6	0	0.24	0.30	-1.46
0.1 / 0.9	0.8	0.84	0.83	0.94	6 / 6	0	0.10	0.13	-2.3
0.1 / 0.4	0.3	0.24	0.23	0.01	6 / 7	1	0.88	1.06	2.8
0.33/ 0.4	0.07	0.08	0.07	0.1	6 / 7	1	0.77	0.81	2.1
0.33 / 0.5	0.17	0.19	0.17	0.4	6 / 8	2	1.55	1.52	-0.5
0.1 / 0.1	0	-0.30	-0.30	-0.3	6 / 2	-4	-3.0	-3.0	-4.3
0.1 / 0.7	0.6	0.52	0.50	0.3	6 / 6	0	0.16	0.18	-0.06
0.46 / 0.5	0.04	0.08	0.08	0.1	6 / 8	2	1.53	1.50	2.1

Table 2: Estimation of saturation and effective pressure changes from 4D 4C seismic data. Sw1 and Sw2 are the saturation before and after production, and P1 and P2 are the effective pressure before and after production.

Sw1 / Sw2	Real Sw change	Est. Sw change	A	B	C	P1 / P2 (MPa)	Real P change (MPa)	Est. P change (MPa)	A	B	C
0.1 / 0.33	0.23	0.16	0.15	0.16	0.16	6 / 6	0	0.1	0.13	0.09	0.05
0.1 / 0.5	0.4	0.34	0.33	0.24	0.30	6 / 8	2	1.68	2.35	2.14	1.92
0.1 / 0.6	0.5	0.41	0.32	0.31	0.46	6 / 6	0	0.24	-0.06	0.45	-0.05
0.1 / 0.9	0.8	0.84	0.93	0.79	0.86	6 / 6	0	0.10	0.09	0.47	-0.02
0.1 / 0.4	0.3	0.24	0.17	0.3	0.24	6 / 7	1	0.88	0.64	0.66	1.0
0.33/ 0.4	0.07	0.08	0.01	0.06	0.15	6 / 7	1	0.77	1.59	0.81	0.58
0.33 / 0.5	0.17	0.19	0.22	0.08	0.30	6 / 8	2	1.55	0.65	2.25	0.47
0.1 / 0.1	0	-0.30	-0.24	-0.29	-0.26	6 / 2	-4	-3.0	-2.68	-3.15	-3.54
0.1 / 0.7	0.6	0.52	0.62	0.55	0.59	6 / 6	0	0.16	-0.21	-0.11	0.06
0.46 / 0.5	0.04	0.08	0.15	0.07	0.09	6 / 8	2	1.53	1.6	0.54	2.2

Table 3: Estimation of saturation and effective pressure changes from 4D 4C seismic data with noise and reflection coefficient perturbations. A: 10% increase in Vp, Vs and density for post poduction and preproduction model, B: 10% decrease in Vp, Vs and density for preproduction model, no change in postproduction model, C: 10% increase in Vp, Vs, density for preproduction model, and 5% increase in Vp, Vs, and density in post production model. Sw1 and Sw2 are the saturation before and after production, and P1 and P2 are the effective pressure before and after production.

Sw1 / Sw2	Real Saturation Change	Estimated saturation change with noise	P1 / P2 (MPa)	Real Pressure Change (MPa)	Estimated Pressure change with noise (MPa)
0.1 / 0.33	0.23	0.20	6 / 6	0	-0.29
0.1 / 0.5	0.4	0.46	6 / 8	2	0.49
0.1 / 0.6	0.5	0.5	6 / 6	0	-0.71
0.1 / 0.9	0.8	0.98	6 / 6	0	-1.4
0.1 / 0.4	0.3	0.31	6 / 7	1	0.29
0.33/ 0.4	0.07	0.13	6 / 7	1	0.28
0.33 / 0.5	0.17	0.27	6 / 8	2	0.59
0.1 / 0.1	0	-0.30	6 / 2	-4	-2.2
0.1 / 0.7	0.6	0.61	6 / 6	0	-0.13
0.46 / 0.5	0.04	0.16	6 / 8	2	0.67

Table 4: Estimation of saturation and effective pressure changes from 4D PP AVO seismic data. Sw1 and Sw2 are the saturation before and after production, and P1 and P2 are the effective pressure before and after production.

In addition to a noise sensitivity test, the reflection coefficient used to calibrate the seismic amplitudes were perturbated by perturbing the velocity and density model. Table 3 shows the results for three different perturbations; 10% increase of velocities and densities for both the preproduction and the post production model, 10% decrease of the velocities and density of the preproduction model only, and finally 10% increase in the velocoties and densities of the preproduction model, and 5% increase of the velocities and density of the post production model. The estimated changes in saturation are stable to the reflection coefficient perturbations, but the pressure estimates have lower quality.

Finally, a test was done with different stacking angles for the PP- and PS data to investigate if the removal of the weak amplitudes around zero-offset on the PS-data would improve the results. The PP-data were stacked from 0 - 45 degrees as before, whilst the PS data were stacked from 15 degrees to 45 degrees in angle of incidence. This test was performed to study the impact of offset range on the PS data with a low signal to noise ratio (PS-amplitudes are zero at zero offset and generally weak in amplitude for small incidence angles; therefore, the lowest signal to noise ratios will occur for low offsets). For data with noise, the results were not as good as for the case where the same stacking angles were used for both PP- and PS- data, although the differences were small.

Conclusions

Approximate formulas for computation of saturation- and pressure-related changes from time lapse PP and PS stacked seismic data have been derived and successfully tested on synthetic data. The formulas are explicit expressions related to PP and PS stacks and are therefore well suited for direct implementation in a processing package or a seismic interpretation system. Necessary input to obtain the equations is a rock physics model that relates changes in the seismic parameters to changes in pressure and saturation.

The method was tested for 10 production scenarios, representing various degrees of saturation and pressure changes. It discriminates reasonably well between fluid saturation changes and pore pressure changes for most cases. A regression technique was used to build empirical rock physics relations between the seismic parameters and the fluid and pressure saturation parameters. For one scenario that was outside the database used for the regression analysis, a large deviation in the estimated water saturation was found, for all other scenarios, the deviations between the estimated and real changes were small.

In the present method, only time lapse amplitude changes in PP and PS are used. Use of time lapse travel time changes in PP and PS is probably the most promising way of reducing the uncertainties in the final saturation and pressure estimates. So far, very few real data examples (repeated marine, multicomponent data) are available, which means that the proposed algorithm has not been tested on real data.

Acknowledgements

Ketil Brekke Johansen is acknowledged for performing the rock physics modelling used as a basis for the present work. The financial support through the EC ATLASS project, ENK6-CT-2000-00108 is acknowledged, as well as the ATLASS project partners: NTNU, TU Delft, CGG, Eni-Agip, Norsk Hydro, Shell and Statoil. Helene Hafslund Veire acknowledges the support from the VISTA Ph.D. programme. Finally, the reviewers and associate editor are acknowledged for constructive reviews.

Appendix A- Integration over angle span

For differencing time lapse seismic data the most robust method is to work on stacked sections (Andorsen and Landrø, 2000), hence, Eqn. 14 need to be integrated over a given angle span. Let

$$
\begin{aligned}
i_0 &= \frac{1}{\theta_2 - \theta_1} \cdot \int_{\theta_1}^{\theta_2} d\theta = 1 \\
i_1 &= \frac{1}{\theta_2 - \theta_1} \cdot \int_{\theta_1}^{\theta_2} \sin\theta d\theta = \frac{1}{\theta_2 - \theta_1}(\cos\theta_1 - \cos\theta_2) \\
i_2 &= \frac{1}{\theta_2 - \theta_1} \cdot \int_{\theta_1}^{\theta_2} \sin^2\theta d\theta = \frac{1}{\theta_2 - \theta_1}\left(\frac{1}{2}(\theta_2 - \theta_1) - \frac{1}{4}(\sin 2\theta_2 - \sin 2\theta_1)\right) \qquad \text{(A-1)} \\
i_3 &= \frac{1}{\theta_2 - \theta_1} \cdot \int_{\theta_1}^{\theta_2} \tan^2\theta d\theta = \frac{1}{\theta_2 - \theta_1}(\tan\theta_2 - \tan\theta_1 - (\theta_2 - \theta_1)) \\
i_4 &= \frac{1}{\theta_2 - \theta_1} \cdot \int_{\theta_1}^{\theta_2} \sin^3\theta d\theta = \frac{1}{\theta_2 - \theta_1}\left(-(\cos\theta_2 - \cos\theta_1) + \frac{1}{3}(\cos^2\theta_2 - \cos^2\theta_1)\right)
\end{aligned}
$$

Stochastic inversion of pressure and saturation changes from time-lapse AVO data

Helene Hafslund Veire*, Hilde Grude Borgos, and Martin Landrø*.
****Department of Petroleum Engineering and Applied Geophysics, Norwegian University of Science and Technology, N-7491 Trondheim, Norway.***
[1] Schlumberger Stavanger Research, Risabergvn. 3, N-4056 Tananger, Norway

Presented at the 73rd Ann. Mtg., Soc. Expl. Geophys., 2003. Submitted to Geophysics.

Abstract

Effects of pressure and fluid saturation can have the same degree of impact on seismic data, thus they are often inseparable by analysis of a single stacked seismic data set. In such cases, the use of time lapse AVO analysis offers an opportunity to discriminate the two effects. To be able to utilize information about pressure and saturation related changes in reservoir modelling and simulation, we need to quantify the uncertainty in the estimations. One way of analyzing uncertainties is by formulating the problem in a Bayesian framework. Here, the solution of the problem will be represented by a probability density function, providing estimations of uncertainties as well as direct estimations of the properties. In this paper, a stochastic model for estimation of pressure and saturation changes from time-lapse seismic AVO data has been investigated within a Bayesian framework. Well-known rock physical relationships have been used to set up a prior stochastic model. PP reflection coefficient differences have been used to establish a likelihood model for linking reservoir

variables and time-lapse seismic data. The methodology incorporates correlation between different variables of the model, as well as spatial dependencies for each of the variables. In addition, information about possible bottlenecks causing large uncertainties in the estimations can be identified through sensitivity analysis of the system. The method has been tested on 1D synthetic data and on field time-lapse seismic AVO data from the Gullfaks Field in the North Sea.

Introduction

The traditional way of predicting overpressured zones from seismic data has been through velocity analysis, by detecting areas where velocities estimated from seismic data deviate from a normal trend (Martinez et al., 1991). Fluid effects are often analyzed by investigating AVO effects on PP seismic data, e.g. Ostrander (1984), Smith and Gidlow (1987), Castagna et al. (1994 and 1998). However, saturation and pressure changes can have approximately the same degree of impact on stacked seismic data. This makes it impossible to separate pressure and fluid saturation effects from a single set of stacked PP seismic data. In such cases, use of time lapse AVO analysis offers an opportunity to discriminate the two effects (Tura and Lumley, 1998 and 1999; Landrø, 2001). Another approach is to do simultaneous analysis of stacked time lapse multicomponent (PP- and PS) seismic data (Landrø et al., 2003, Stovas et al., 2003).

It is important to quantify uncertainty in the estimations to be able to utilize information about pressure and saturation related changes in reservoir modelling and simulation. Landrø (2002) presented a deterministic analysis of uncertainty in the estimation of pressure and saturation changes from time-lapse AVO-data and travel time differences, assuming independent variables. Incorporation of dependencies between different variables can be done by formulating the problem in a Bayesian framework. Theoretical rock physical relationships will be used to set up a prior model of depedencies between different variables (e.g. Mosegaard and Tarantola, 1995). In addition, general field information obtained from regional geologic trends and field analogs can also be introduced in the prior model. Reservoir variables are then linked to measured time lapse seismic data by a likelihood model. The posterior probability can be found by applying Bayes rule, thus combining general knowledge from the prior model and reservoir specific observations through the likelihood model. The solution of the problem will thereby be represented by a probability density function (pdf), providing information about uncertainty in the estimations, as well as estimates of the parameters themselves. In addition, it will be possible to identify conflicts between prior model and measured seismic data, and to evaluate the advantage of introducing new data. The stochastic framework is well suited to combine data from different sources (e.g. well logs, seismic data, field analogs) while keeping track of the uncertainties in the data. Finally, a stochastic representation makes it possible to include spatial dependencies in the estimation of the variables. Other examples of how different types of geophysical and well log data have been integrated in a stochastic framework to estimate various properties of the subsurface can be found in e.g. Bosch (1999), Malinverno and Leaney (2000), Eidsvik et al. (2002), and Mazzotti and Zamboni (2003).

In the following, a stochastic model for estimating fluid and pressure related changes directly from repeated pressure wave offset data through a Bayesian framework is presented. The methodology have been tested on synthetic seismic data and field seismic data from the Gullfaks Field in the North Sea.

Methodology

Reservoir model

Through well known rock physical relationships, links between changes in seismic variables $\Delta t, \Delta r0, \Delta g$ and reservoir parameters ΔS_w and ΔP are set up. Here, Δt represents directly measurable time-lapse change in seismic two-way travel time over the reservoir interval. The variables $\Delta r0, \Delta g$ are time-lapse changes in AVO intercept and gradients, computed by linear regression of partial stacks. Finally, ΔS_w and ΔP are changes in saturation and pressure due to production.

Changes in the reservoir model ΔR_x is represented by the following stochastic variables:

$$\Delta R_x = \left\{ \Delta S_{w,x}, \Delta P_x, \frac{\Delta\alpha_x}{\alpha_x}, \frac{\Delta\beta_x}{\beta_x}, \frac{\Delta\rho_x}{\rho_x} \right\} , \tag{1}$$

where $x = (x_1, x_2, x_3)$ implies the location of the point in the 3D grid, $\Delta S_{w,x}$ denotes change in saturation due to production, ΔP_x is change in pressure due to production, $\Delta\alpha_x/\alpha_x$ is relative time lapse change in P-wave velocity, $\Delta\beta_x/\beta_x$ is relative time lapse change in S-wave velocity, and $\Delta\rho_x/\rho_x$ is relative time lapse change in density. The properties of the 5-dimensional random variable ΔR_x are specified through the probability density function (pdf) $f(\Delta R_x)$. The goal of the methodology presented here is to calculate the conditional pdf $f(\Delta R_x|\Delta r_{0,x}, \Delta g_x)$, represented by expectation values and covariance matrices for $\Delta R_x = \{\Delta S_{w,x}, \Delta P_x, \Delta\alpha_x/\alpha_x, \Delta\beta_x/\beta_x, \Delta\rho_x/\rho_x\}$ conditioned on time lapse changes in intercept and gradients computed from time lapse seismic AVO data. Expectation values then serve as optimal estimates of the time lapse changes and the covariances represent the associated uncertainties.

All reservoir variables and available data are related through forward models. Dependencies between different reservoir variables are shown in the stochastic graph in Figure 1. Here, a thick arrow indicates a deterministic relation, while a thin arrow indicates a stochastic relationship. Well log data are assumed to be direct measurements of reservoir variables with negligible errors compared to errors from seismic data, thus there is a deterministic relationship between well log data and reservoir variables. It is possible to introduce stochastic relationships between well log measurements and reservoir variables by assuming non-negligible errors on well log measurements, but this is not done here. The prior model assumptions are based on available reservoir knowledge and general rock physical relationships. Arrows between reservoir variables inside the box define the prior distribution. In this case, the available reservoir knowledge comes from well log information and time lapse change in travel time, but regional geological information might also be used. Links between reservoir variables and seismic amplitude data are given in the likelihood model, defined by arrows out of the box.

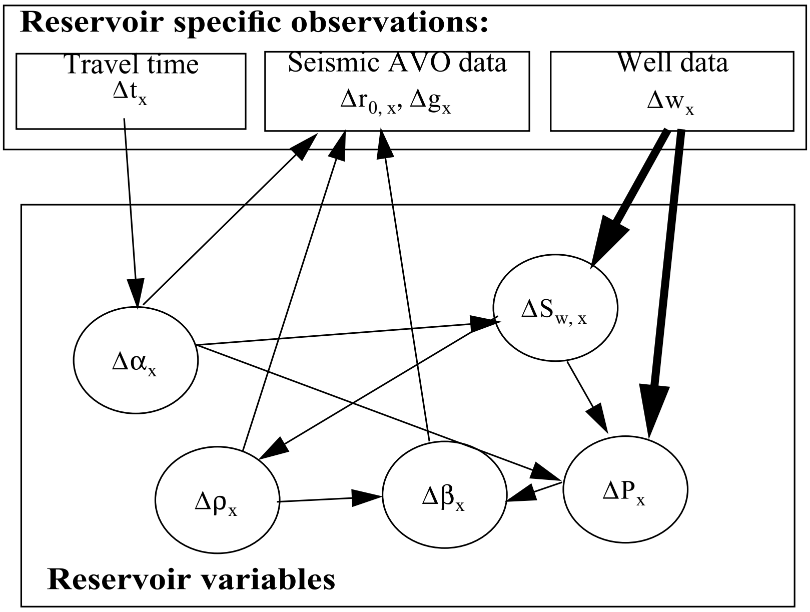

FIGURE 1. Stochastic network: A thick arrow indicates a deterministic relation, while a thin arrow indicates a stochastic relationship. The arrows between reservoir variables represent rock physical relationships, defining the prior distribution, and the arrow out of the box defines the likelihood model.

Prior model

The prior model connecting production related changes in reservoir parameters with changes in seismic two-way travel time is defined by combining well-known rock physical relationships, e.g. Gassmann's equation and the Hertz-Mindlin equations. If production related time lapse changes in rock and fluid properties are small, basic rock physical relationships can be differentiated to obtain approximate linear relationships between relative changes in the parameters. These relationships provide expectation values for the prior distributions, and we assume that the major trends are captured this way. Uncertainties and errors in the rock physical relationships and in the trend model of reservoir properties are accounted for by adding Gaussian errors to all expectation values. The combination of linear relationships and Gaussian errors implies that the prior distributions are all Gaussian distributions. It is also possible to introduce other types of error distributions, but this can make the posterior distribution analytically intractable. In such cases, we would have to use Markov chain Monte Carlo sampling (Hastings, 1970) to be able to estimate posterior mean values and variances, and the calculations will be more computer intensive.

The relationship between relative change in P-wave velocity ($\Delta\alpha_x/\alpha_x$) and relative change in travel time due to production is based on differentiating the basic relationship ($t = 2Z/\alpha$) between zero offset interval travel time (t), thickness of layer (Z), and P-wave velocity (α). This gives

$$\left[\frac{\Delta\alpha_x}{\alpha_x}\right] = -\frac{\Delta t_x}{t_x} + U_{\Delta\alpha}, \tag{2}$$

where $U_{\Delta\alpha}$ is assumed to be a Gaussian distributed error, with mean value 0. Hence, the variance σ_α^2 of $U_{\Delta\alpha}$ defines the uncertainty in Eqn. 2, and it should be estimated by analyzing well logs and core data. The variable t_x is two-way travel time over the reservoir interval, and Δt_x is time lapse change in travel time due to production. Here, Δt_x is treated as an exact observation, but the error of the measurement is included in the Gaussian error together with the error of the model. The relative change in P-wave velocity contrast will thus follow a Gaussian distribution with expectation value given by $-\Delta t_x/t_x$ and variance given by σ_α^2. A prior model may be assigned to

Δt_x, treating the travel time change as a stochastic variable as well.

Relative change in density ($\Delta\rho_x/\rho_x$) as a function of change in saturation ($\Delta S_{w,x}$) can be described by

$$\left[\frac{\Delta\rho_x}{\rho_x}\middle|\Delta S_{w,x}\right] = \frac{\phi_x(\rho_w - \rho_{HC})}{\rho_x}\Delta S_{w,x} + U_{\Delta\rho}, \tag{3}$$

where ρ_x is density trend model, ϕ_x is porosity of the reservoir, ρ_w is density of the reservoir water, and ρ_{HC} is density of the hydrocarbon in the reservoir. The trend model of density and porosity is allowed to vary over the reservoir, both horizontally and vertically. The error of the relationship, $U_{\Delta\rho}$, is assumed to be Gaussian distributed with mean value 0 and variance σ_ρ^2. This expression is derived from the basic relationship between density, porosity and saturation (Mavko et al, 1998)

$$\rho_x = (1-\phi)\cdot\rho_M + \phi_x\cdot[S_w(\rho_w + (1-S_w)\rho_{HC})], \tag{4}$$

where ρ_M is density of the rock matrix. The porosity of the reservoir can change due to production (e.g. compaction on Ekofisk changes the porosity, Guilbot and Smith, 2002), but we make the assumption of constant porosity during the time lapse period for these calculations.

Relative changes in P-wave velocity can be caused by e.g. changes in saturation and pressure, changes in temperature of the reservoir, compaction of the reservoir, and chemical reactions of the reservoir rocks due to production. Here, we make the assumption of no compaction of the reservoir rocks, and that velocity changes caused by temperature changes and chemical changes are negligible. This means that relative change in P-wave velocity can be separated into saturation-related changes ($\Delta\alpha_x^F/\alpha_x$) and pressure related changes ($\Delta\alpha_x^P/\alpha_x$), giving

$$\frac{\Delta\alpha_x}{\alpha_x} = \frac{\Delta\alpha_x^F}{\alpha_x} + \frac{\Delta\alpha_x^P}{\alpha_x}. \tag{5}$$

By differentiating Gassmann’s equation (Gassmann, 1951) with respect to velocity, density and fluid modulus, we get an expression for change in P-wave velocity as a function of change in density and fluid modulus

$$\frac{\Delta\alpha_x{}^F}{\alpha_x} = -\frac{1}{2}\frac{\Delta\rho_x}{\rho_x} + \frac{\phi(K_m - K_{fr})^2}{2\rho_x\alpha_x{}^2K_f\left(1 - \phi_x + \frac{\phi_x K_m}{K_f} - \frac{K_{fr}}{K_m}\right)^2} \cdot \frac{\Delta K_f}{K_f}. \tag{6}$$

Here, K_m is bulk modulus of the matrix, and K_f is bulk modulus of the fluid. Changes in fluid modulus are found by differentiating

$$\frac{1}{K_f} = \frac{S_{w,x}}{K_w} + \frac{1 - S_{w,x}}{K_{HC}}, \tag{7}$$

where $S_{w,x}$ is water saturation, K_w is fluid modulus of water, and K_{HC} is fluid modulus of the hydrocarbon in the reservoir. This is the Reuss lower bound (often called isostress average) for an isotropic, linear, and elastic case (Mavko et al., 1998). For a combination of liquids with zero shear modulus the Reuss average gives the effective modulus of the mixture. The relative change in fluid modulus is then given by

$$\frac{\Delta K_f}{K_f} = \frac{\Delta S_{w,x}}{S_{w,x}}\left[\frac{K_w - K_{HC}}{K_{HC} - K_w + \frac{K_w}{S_{w,x}}}\right]. \tag{8}$$

We observe that if $S_{w,x}$ is close to zero, this equation breaks down. No analysis has been done to find the lower limit of $S_{w,x}$ for this equation to be valid. However, we assume that even before production starts, the reservoir does not have $S_{w,x} = 0$. Changes in P-wave velocity as a function of change in pressure (ΔP_x) (assuming no change in density as a function of change in pressure) can be derived from a modified version of the Hertz-Mindlin model for normal compression of identical spheres (Vidal et al., 2002). Vidal et al. (2002) found that both P-wave velocity and S-wave velocity are related to pressure as a power of approximately 1/10 instead of 1/6 as given by the original Hertz-Mindlin model. In the Hertz-Mindlin model the effective bulk modulus for dry rock is given by

$$K_{eff} = \left[\frac{C^2(1 - \phi_x)^2 G^2 P_x}{18\pi^2(1 - \nu)^2}\right]^{\frac{1}{3}}, \tag{9}$$

and the effective shear modulus is given by

$$G_{eff} = \frac{(5-4\nu)}{5(2-\nu)} \cdot \left[\frac{3C^2(1-\phi_x)^2 G^2 P_x}{2\pi^2(1-\nu)^2}\right]^{\frac{1}{3}}, \tag{10}$$

where G is shear modulus of the grain material, P_x is hydrostatic confining pressure, ϕ_x is porosity, ν is the Poisson's ratio for the grain material, and C is the average number of contacts per sphere. Introducing these expression in the basic expression for P-wave velocity ($\alpha^2 = \left(K + \frac{4}{3}G\right)/\rho_x$), gives $\alpha_x = \mathrm{const} \cdot P_x^{1/6}$. We will instead use $\alpha_x = \mathrm{const} \cdot P_x^{1/10}$ as suggested by Vidal et al. (2002), even though this changes the dimension of the constant in front of the pressure term. By differentiation we get

$$\frac{\Delta\alpha_x^{P}}{\alpha_x} = \frac{\Delta P_x}{10 P_x}. \tag{11}$$

The accuracy of this model can be discussed, and the velocity-pressure relationship should be validated on core data from the reservoir to be analyzed. By combining Eqn. 5, Eqn. 6, Eqn. 8, and Eqn. 11, and solving for the change in pressure, we get the prior model for the distribution of change in pressure, conditioned by relative change in P-wave velocity and change in saturation:

$$\begin{aligned} \left[\Delta P_x \middle| \frac{\Delta\alpha_x}{\alpha_x}, \Delta S_{w,x}\right] &= \frac{1}{C_3}\frac{\Delta\alpha_x}{\alpha_x} - C_4 \Delta S_{w,x} + U_{\Delta P} \\ C_1 &= \frac{\phi_x (K_w - K_{HC})(K_m - K_{fr})^2}{2\rho_x \alpha_x^2 S_{w,x} K_f \left(K_{HC} - K_w + \frac{K_w}{S_{w,x}}\right)\left(1 - \phi_x + \frac{\phi_x K_m}{K_f} - \frac{K_{fr}}{K_m}\right)^2} \\ C_2 &= -\left(\frac{\phi_x(\rho_w - \rho_{HC})}{2\rho_x}\right) \qquad C_3 = \frac{1}{10 P_x} \qquad C_4 = \frac{C_1 + C_2}{C_3} \end{aligned} \tag{12}$$

The uncertainty of these relationships is accounted for through the Gaussian distributed error $U_{\Delta P}$ with mean value 0 and variance given by σ_P^2.

Changes in S-wave velocity due to production depend on changes in saturation through changes in density, and on changes in pressure through changes in the shear modulus given by the modified Hertz-Mindlin model (Vidal et al., 2002). The relationship between pressure and S-wave velocity is found by inserting Eqn. 10 in the basic expression for S-wave velocity ($\beta_x{}^2 = G/\rho_x$), giving $\beta_x = \mathrm{const} \cdot P_x{}^{1/10}$. By differentiating these we get

$$\begin{aligned} \frac{\Delta\beta_x{}^F}{\beta_x} &= -\frac{\Delta\rho_x}{2\rho_x} \\ \frac{\Delta\beta_x{}^P}{\beta_x} &= \frac{\Delta P_x}{10P_x} \\ \left[\frac{\Delta B_x}{B_x}\middle|\Delta\rho_x, \Delta P_x\right] &= \frac{\Delta\beta_x{}^F}{\beta_x} + \frac{\Delta\beta_x{}^P}{\beta_x} + U_{\Delta\beta} = -\frac{\Delta\rho_x}{2\rho_x} + \frac{\Delta P_x}{10P_x} + U_{\Delta\beta} \end{aligned} \tag{13}$$

Here, P_x is a trend model for effective pressure, and $U_{\Delta\beta}$ is the Gaussian distributed error of the relationship, with mean value 0 and variance σ_β^2.

In addition, a prior distribution for change in saturation given relative change in P-wave velocity is needed. As a first assumption, relative change in P-wave velocity is related to change in saturation through a simple linear relationship, adding onto this a large variance, making the prior distribution wide:

$$\left[\Delta S_{w,x}\middle|\frac{\Delta\alpha_x}{\alpha_x}\right] = \frac{1}{2(C_1 + C_2)}\frac{\Delta\alpha_x}{\alpha_x} + U_{S_w}. \tag{14}$$

Again, U_{S_w} is the Gaussian distributed error of the relationship, with mean value 0 and variance $\sigma_{s_w}{}^2$. This relationship is found by assuming zero change in effective pressure in Eqn. 12.

The pdf of the reservoir variables is then on the form

$$\begin{aligned} f(R_x) &= f\left(\Delta S_{w,x}, \Delta P_x, \frac{\Delta\alpha_x}{\alpha_x}, \frac{\Delta\beta_x}{\beta_x}, \frac{\Delta\rho_x}{\rho_x}\right) = \\ & f\left(\frac{\Delta\alpha_x}{\alpha_x}\right) \cdot f\left(\Delta S_{w,x}\middle|\frac{\Delta\alpha_x}{\alpha_x}\right) \cdot f\left(\frac{\Delta\rho_x}{\rho_x}\middle|\Delta S_{w,x}\right) \cdot f\left(\Delta P_x\middle|\frac{\Delta\alpha_x}{\alpha_x}, \Delta S_{w,x}\right) \cdot f\left(\frac{\Delta\beta_x}{\beta_x}\middle|\Delta P_x, \frac{\Delta\rho_x}{\rho_x}\right) \end{aligned} \tag{15}$$

Here, $f(\Delta\alpha_x/\alpha_x)$ is the prior pdf of relative change in P-wave velocity (Eqn. 2), $f(\Delta S_{w,x}|\Delta\alpha_x/\alpha_x)$ is the prior pdf of change in saturation given relative change in P-wave velocity (Eqn. 14), $f(\Delta\rho_x/\rho_x|\Delta S_{w,x})$ is the prior pdf of relative change in density given change in saturation (Eqn. 3), $f(\Delta\beta_x/\beta_x|\Delta P_x, \Delta\rho_x/\rho_x)$ is the prior pdf of relative change in S-wave velocity given change in pressure and relative change in density (Eqn. 13), and $f(\Delta P_x|\Delta\alpha_x/\alpha_x, \Delta S_{w,x})$ is the prior pdf of change in pressure given relative change in P-wave velocity and change in saturation (Eqn. 12).

Likelihood model, seismic

The likelihood model for seismic data describes how measured changes in seismic amplitudes are related to relative change in the seismic parameters P-wave velocity, S-wave velocity and density. We use the formulation from Landrø (2001), where time lapse changes in AVO intercept and gradient are related to time-lapse change in P-wave velocity, S-wave velocity and density. This gives a likelihood model of the form

$$\left[\Delta r_{0,x}\Delta g_x \middle| \frac{\Delta\alpha}{\alpha_x}, \frac{\Delta\beta_x}{\beta_x}, \frac{\Delta\rho_x}{\rho_x}\right] = \mu_x + U_D \tag{16}$$

where the error term U_D is assumed to be Gaussian distributed with mean value zero and covariance matrix given by

$$\Sigma_D = \begin{bmatrix} \sigma_{D11} & \sigma_{D12} \\ \sigma_{D12} & \sigma_{D22} \end{bmatrix}. \tag{17}$$

The σ_{Dii}-elements in the covariance matrix represents uncertainty in the time lapse change in AVO intercept and gradient. The σ_{Dij}-elements represents the covariance between time lapse change in intercept and time lapse change in gradient. The error term includes both error in seismic measurements, error due to linearization of Zoeppritz' equations, and errors in the trend model of elastic parameters for reservoir and cap rock. The covariance matrix of seismic variables is found by a simple statistical analysis of the synthetic AVO seismic data. The vector μ_x is given by

$$\mu_x = \begin{bmatrix} \mu_{\Delta r_{0,x}} \\ \mu_{\Delta g_x} \end{bmatrix} = \begin{bmatrix} \frac{1}{2}\left(\frac{\Delta\rho_x}{\rho_x} + \frac{\Delta\alpha_x}{\alpha_x}\right) \\ \frac{\Delta\alpha_x}{2\alpha_x} - 4 \cdot \frac{\beta_x^2}{\alpha_x^2} \cdot \frac{\Delta\beta_x}{\beta_x} \end{bmatrix}. \tag{18}$$

Posterior model

The posterior pdf can be found using Bayes rule:

$$f(\Delta R_x|\Delta r_{0,x}, \Delta g_x) = C \cdot f(\Delta r_{0,x}, \Delta g_x|\Delta R_x) \cdot f(\Delta R_x), \tag{19}$$

where C is the normalizing constant $f(\Delta r_{0,x}, \Delta g_x)^{-1}$, $f(\Delta r_{0,x}, \Delta g_x|\Delta R_x)$ is the likelihood function, and $f(\Delta R_x)$ is the prior pdf. By inserting the expressions from the prior pdf into Eqn. 19, we get the following expression for the posterior pdf:

$$\begin{aligned} f(\Delta R_x|\Delta t_x, \Delta r_{0,x}, \Delta g_x) &= \text{const} \cdot f(\Delta r_{0,x}, \Delta g_x|\Delta R_x) \cdot f(\Delta\alpha_x) \cdot f(\Delta S_{w,x}|\Delta\alpha_x) \\ &\quad \cdot f(\Delta\rho_x|\Delta S_{w,x}) \cdot f(\Delta P_x|\Delta\alpha_x, \Delta S_{w,x}) \cdot f(\Delta\beta_x|\Delta P_x, \Delta\rho_x) \end{aligned} \tag{20}$$

Since all the factors of the prior and likelihood model are Gaussian distributions, and the expectations are linear relationships, the posterior distribution will be a five-dimensional Gaussian distribution on the form

$$f(\Delta R_x|\Delta t_x, \Delta r_{0,x}, \Delta g_x) = \text{const} \cdot \exp\left(-\frac{1}{2}(x - \mu_{R,x})' S^{-1}(x - \mu_{R,x})\right), \tag{21}$$

where $\mu_{R,x}$ is the five-dimensional posterior mean value vector, and S is the 5x5 posterior covariance matrix. This expression is analytically tractable. By rearranging the expressions in Eqn. 20 to the form of Eqn. 21, an expression for the inverse of the covariance matrix of the posterior model is found (Appendix A, Eqn. A-1). The mean value vector can be found numerically by solving the equation system resulting from trying to match Eqn. 20 to the form of Eqn. 21 (Appendix A, Eqn. A-2 - A-3). In Chapter 6, general expressions to calculate the posterior mean and covariance are presented.

Through the field data example presented below we try to show how the posterior uncertainty vary as the prior model and the likelihood model change. In general, it is important that the prior model does not constrain the posterior distribution too much. If the prior distribution is narrow, the measured seismic data have restricted influence on the posterior results. We observe that if the prior and likelihood variances are large, the variance of the posterior model will be smaller than the variance of the prior model. If the variance of the prior model is small and the prior model is in conflict with information obtained from measured time lapse changes, the posterior variance can be larger than the prior variance.

Spatial model

The prior, likelihood, and posterior models defined above are point based models with correlation between variables, while grid points have been treated as being statistically independent laterally. Next, we include dependencies laterally between grid points, to improve spatial continuity in the results. The spatial continuity is represented by defining the prior model to be a Markov random field (Winkler, 1995). The marginal prior pdfs $f(\Delta R_x)$ of the properties ΔR_x in grid points x are as defined in Eqn. 15, while the joint prior pdf of all grid points contains an additional term $\varphi(\Delta R_x, \Delta R_y)$ where x and y are neighbor grid points in the Markov field, denoted $x \sim y$:

$$f(\Delta\tilde{R}) = \exp\left(-\sum_{x \sim y} \varphi(\Delta R_x, \Delta R_y)\right)\prod_x f(\Delta R_x) \qquad (22)$$

The function $\varphi(\Delta R_x, \Delta R_y)$ controls the spatial continuity of the Markov field, defined to be non-zero only for neighbor grid points. The function value is close to zero if ΔR_x and ΔR_y have similar values, and increases as the difference between ΔR_x and ΔR_y increases, thus giving highest value of the pdf for spatially continuous values of reservoir properties. The similarity between ΔR_x and ΔR_y is measured by a distance function resembling the Mahalanobis distance coming from the Gaussian prior distribution. There are no cross correlation terms between the reservoir variables in the distance function, i.e. it is diagonal in the reservoir variables. The function $\varphi(\Delta R_x, \Delta R_y)$ is inherited by the posterior pdf, thus also the posterior pdf is a Markov field. Due to a non-tractable posterior pdf, Markov chain Monte Carlo (MCMC) sampling (Hastings, 1970) is applied to generate spatially dependent samples from this posterior pdf.

Examples

Synthetic model example

Three-layer synthetic models have been generated to validate the methodology before testing it on field seismic data from the Gullfaks Field in the North Sea. In the synthetic models, the rock physical properties of the cap rock layer and the layer below the reservoir zone have been kept constant, and only the parameters of the reservoir rock have been perturbed. The reservoir rock is assumed to be buried at 2000m depth, and the thickness is set to approximately 500m. The initial properties are taken from a well in the Gullfaks Field in the North Sea. The basic rock and fluid properties are given in Table 1. The relationship between seismic parameters and pressure was found through statistical analysis of ultrasonic measurements from dry cores of various formations. Seismic parameters for different scenarios for saturated reservoir rock have then been calculated using Gassmann's equation.

From the synthetic reservoir models, reflection coefficients were calculated using Zoeppritz' equations for angles from 0 to 20 degrees. These reflection coefficients were convolved with a 30Hz Ricker wavelet. Near trace stacks and far trace stacks were produced from the resulting synthetic AVA seismograms. Intercept and gradient sections were estimated by linear regression of the near and fare stacks. Table 2 shows seismic parameters of two synthetic models, a preproduction scenario with water saturation 10% and effective pressure 2MPa, and a post production scenario with water saturation 50% and effective pressure 8MPa. AVA synthetic seismograms for the two models are shown in Figure 2. We observe a change in AVA response for both the top and the base of the reservoir zone, and a time shift of the base reservoir interface. There is no time shift of the top reservoir interface, since the seismic properties of the cap rock is equal for all scenarios.

Porosity	0.30	Density of oil	880 kg/m^3
Fluid modulus, water	2.73 GPa	Density of water	1012 kg/m^3
Fluid modulus, oil	1.2 GPa	Bulk modulus, matrix	34.1 GPa
		Bulk modulus, frame	6.15 GPa

Table 1: Initial rock and fluid parameters

	Preproduction: Sw=10%, P=2MPa	**Postproduction: Sw=50%, P=8MPa**
	α=1900 m/s	α=1900 m/s
Overburden	β=995 m/s	β=995 m/s
	ρ=1950 kg/m^3	ρ=1950 kg/m^3
	α=2066 m/s	α=2384 m/s
Reservoir	β=1075 m/s	β=1193 m/s
	ρ=2131 kg/m^3	ρ=2156 kg/m^3
	α=2510 m/s	α=2510 m/s
Below reservoir	β=1164 m/s	β=1164 m/s
	ρ=2201 kg/m^3	ρ=2201 kg/m^3

Table 2: Seismic properties for 3-layer synthetic models

	$\Delta\alpha/\alpha$	$\Delta\rho/\rho$	$\Delta\beta/\beta$	**ΔSw/Sw**	**ΔP/P**
$\Delta\alpha/\alpha$	1.0000	-0.0473	0.3423	0.2832	0.3825
$\Delta\rho/\rho$		1.0000	-0.3461	0.0587	-0.0753
$\Delta\beta/\beta$			1.0000	-0.5860	0.8159
ΔSw/Sw				1.0000	-0.7374
ΔP/P					1.0000

Table 3: Correlation matrix (symmetric) for synthetic data

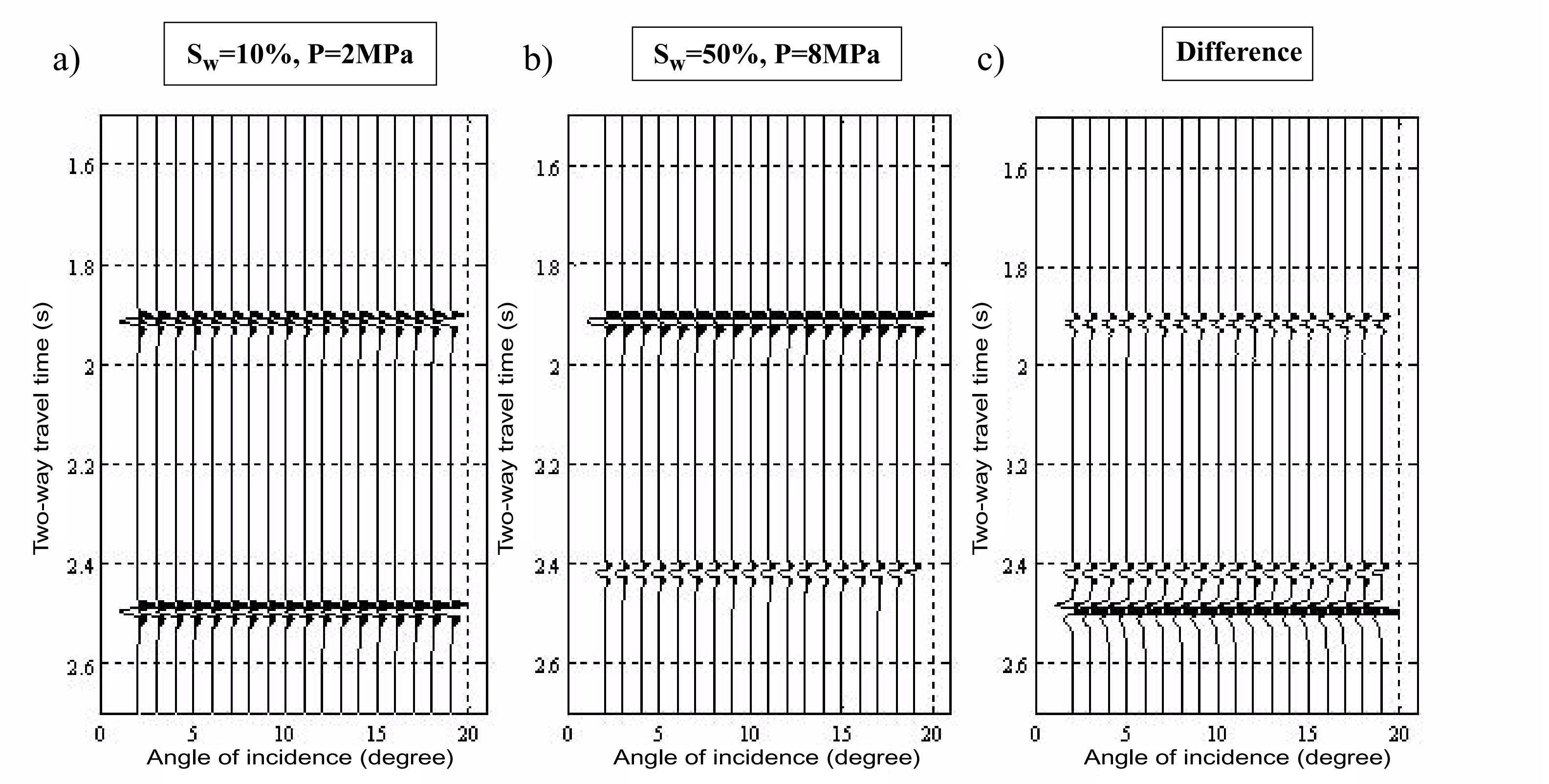

FIGURE 2. Synthetic seismograms of models with a) Water saturation 10% and effective pressure 2 MPa (preproduction), b) Water saturation 50% and effective pressure 8MPa (post-production), and c) Difference section (post production - preproduction).

Pairs of two models representing pre- and post-production stages were analyzed together to estimate pressure and saturation changes from the seismic data. From measured difference in zero offset travel time in the reservoir zone and from differences in AVO intercept and gradient along the top of the reservoir, the covariance matrix and vector of expectation values for the posterior Gaussian distribution of the change in reservoir variables ($\Delta R_x = (\Delta S_{w,x}, \Delta P_x, \Delta\alpha_x/\alpha_x, \Delta\beta_x/\beta_x, \Delta\rho_x/\rho_x)$) were estimated. This gives us an estimate of the most likely time lapse change in saturation and pressure based on time lapse travel time and AVO changes. Trend models and prior uncertainties for P-wave velocity, S-wave velocity, density, water saturation, and pressure were different for all cases. Table 3 shows the correlation matrix for the synthetic test in Figure 2. The correlation matrix is calculated directly from the covariance matrix for this production scenario. Note the large correlation between change in pressure and relative change in S-wave velocity. The measured change in AVO intercept and gradient and the change in zero offset travel time thickness for the reservoir zone were influencing the expectation value of the Gaussian distribution. Calculated expectation values from 6 different production scenarios are shown in Table 4.

Sw1/Sw2	P1/P2	Sw diff.	P diff.	Est. Sw diff. (St. dev.)	Est. P diff. (St.dev.)	Est. α contrast	Est. β contrast	Est. ρ contrast
0.1/0.9	2/6	0.8	4	0.85 (0.42)	3.37 (2.40)	0.17	0.07	0.02
0.1/0.5	2/8	0.4	6	0.65 (0.62)	3.91 (4.11)	0.13	0.06	0.01
0.1/0.6	2/6	0.5	4	0.56 (0.45)	2.64 (2.57)	0.13	0.06	0.01
0.5/0.9	8/6	0.4	-2	0.13 (0.59)	0.42 (5.19)	0.02	0.003	0.01
0.6/0.9	6/6	0.3	0	0.14 (0.45)	0.50 (2.62)	0.03	0.01	0.01
0.5/0.6	8/6	0.1	-2	-0.06 (0.48)	-0.48 (3.83)	-0.01	0.006	-0.0001

Table 4: Synthetic results, individual prior models

Sw1/Sw2	P1/P2	Sw diff.	P diff.	Est. Sw diff.	Est. P diff.
0.1/0.9	2/6	0.8	4	0.77	2.58
0.1/0.5	2/8	0.4	6	0.51	2.19
0.1/0.6	2/6	0.5	4	0.50	2.02
0.5/0.9	8/6	0.4	-2	0.27	0.39
0.6/0.9	6/6	0.3	0	0.27	0.56
0.5/0.6	8/6	0.1	-2	-0.01	-0.17

Table 5: Synthetic results, deterministic approach

Calculated expectation values for large changes in saturation and pressure are close to the real values. For models with a pressure decrease or no change in pressure combined with small saturation changes, calculated expectation values are of lower quality. Calculated standard deviations are large for all models. The posterior uncertainty is smaller than the prior uncertainty for saturation changes for most models, and larger than the prior uncertainty for pressure changes (average prior standard deviation for saturation change was 0.55, and 2 MPa for pressure changes). Here, the prior models were set close to the real preproduction models and the high posterior variances are not caused by imprecise prior models. Since the variance of the change in pressure increase from prior to posterior model, one possible solution is that the modified Hertz-Mindlin model is not an optimal choice for the relationship between pressure and velocity in this case. We have compared the results with saturation and pressure change estimates from a deterministic estimation method (Landrø, 2001) applied on the same synthetic data sets (Table 5). The deterministic method produces slightly better saturation change estimates than the stochastic estimates for all cases, while the stochastic pressure change estimates are better than the deterministic pressure change estimates.

Field data example

The Gullfaks Field is situated in the Tampen Spur area of the North Sea, in the eastern part of a major NNE-trending fault block. The reservoir sands are of early and middle Jurassic age, with shallow marine to fluvial deposits. The first seismic survey was shot in 1985, and the production started in 1986. The Gullfaks time-lapse study have been presented by e.g. Landrø et al. (1999b), and Sønneland et al. (1997), and the main objective of the study has been to identify potentially undrained reservoir compartments (Landrø et al., 1999b). Alsos et al. (2002) presented a quantitative 4D seismic study of the Gullfaks Field, where they classified the change in saturation as either large change, small change or no change, by combining seismic time lapse attributes with the height of the oil column. However, they did not separate the pressure and saturation changes.

In this study, we have analyzed the seismic data acquired in 1985 and 1996. The 1985 and 1996 data sets were acquired with different configurations, with some of the major differences being the number of sources and streamers. The 1985 survey was shot with one source and two streamers 53 m apart, while the 1996 survey was shot with 2 sources (50 m separation) and 6 streamers with 100 m separation. The streamer length for the 1985 data was 2400 m, with 384 channels. The 1996 survey had a streamer length of 3600 m and 288 channels. In addition, different source - and receiver equipment was used. The processing of the 1996 data was done in parallel with a reprocessing of the 1985 data to try to compensate for differences caused by the different acquisition configuration.

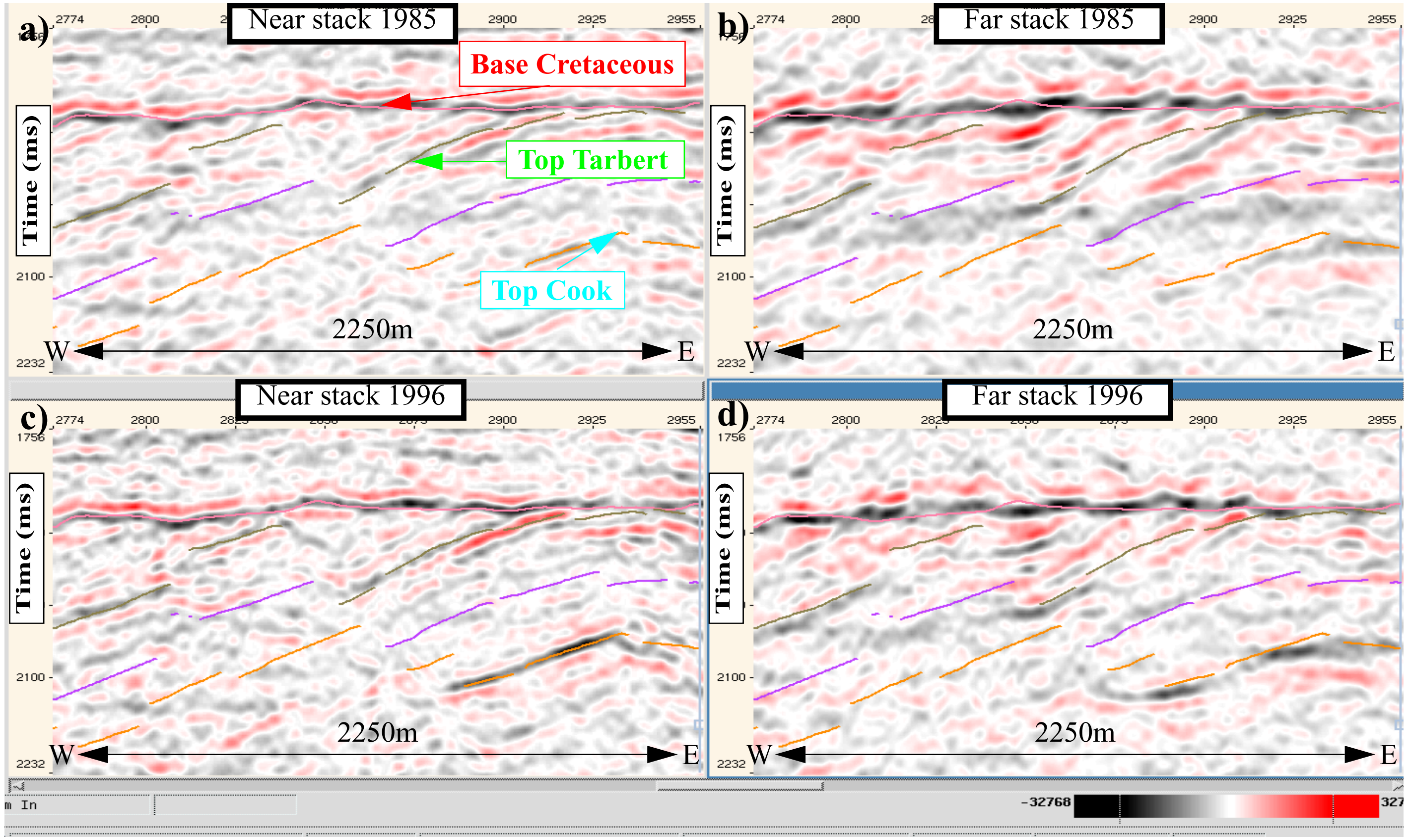

FIGURE 3. Seismic section through Gullfaks partial stacks for the 1985 - 1996 analysis: a) Near offset stack 1985, b) Far offset stack 1985, c) Near offset stack 1996, d) Far offset stack 1996.

Both processing sequences included band-pass filtering, spherical divergence correction, Tau-p-deconvolution, NMO correction, Radon demultiple, DMO correction, prestack time migration of each offset separately, and computation of partial stacks. The stacking and migration velocities were kept constant between the two surveys, to minimize introduction of processing related differences. Cross-equalization were performed to match the 1996 data to the 1985 data. This included global phase- and frequency matching, and a trace by trace amplitude scaling with a time window of 1000 ms. Figure 3 show seismic partial stacks from the same line for the 1985 - 1996 analysis. The strong amplitude at the top of the Cook Formation in the 1996 data compared to the 1985 data (Figure 3) was attributed to increasing pressure around an injector well close to the seismic line.

The stochastic inversion method requires as input a trend model, in addition to the difference in two way zero offset travel time reservoir thickness, and time-lapse change in AVO intercept and gradient. We have used the near- and far offset partial stacks for the 1985 and 1996 study to estimate the AVO parameters in the reservoir interval. The offset stacks have identical offset ranges for pairs of seismic vintages; the near stack consists of offsets from 750m - 1350m, and the far offset stack contains offsets from 1950m - 2450m approximately. The difference in two way travel time thickness was found on the full stack data set, by interpreting the base of the reservoir interval on both the 1985 and the 1996 data sets (assuming no change along the top of the reservoir) and taking the differences (Figure 5). Integrated reflection strength volume attributes were generated over the reservoir interval on the offset cubes for both the 1985 and the 1996 data. Figure 4 shows integrated reflection strength for the 1985 data in the Tarbert Formation. The attribute grids were calibrated to reflection coefficients by using a trend model built from well log data for P-wave velocity, S-wave velocity, and density. One calibration factor was used for all the offset cubes from the 1985 and 1996 data set. The AVO intercept and gradient were constructed by linear regression of the calibrated attributes for near- and far offsets. Finally difference grids were calculated for the AVO intercept and gradient (Figure 5), by subtracting the 1996 data from the 1985 data.

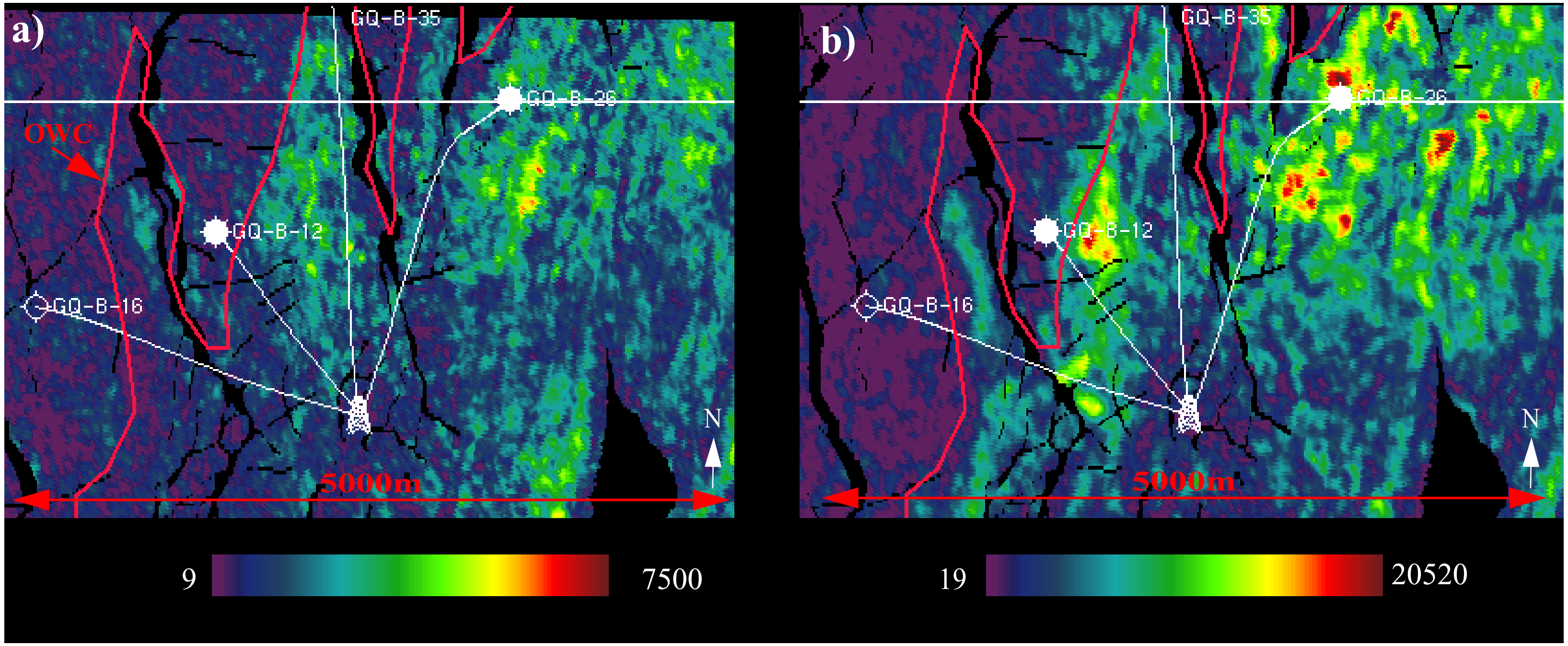

FIGURE 4. Integrated reflection strength in time window from Top Tarbert and 40 ms down on a) Near stack base survey (1985), and b) Far stack base survey. The white line indicates the seismic line shown in Figure 3.

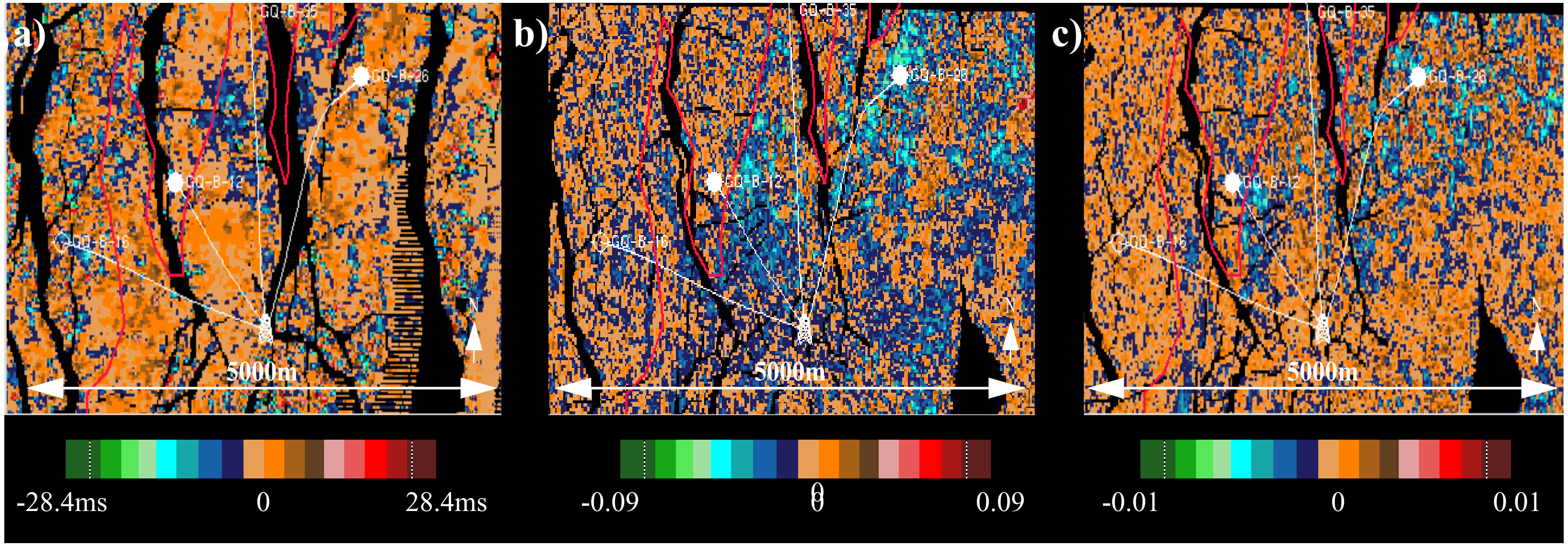

FIGURE 5. Difference attributes for the 1985 - 1996 analysis of the Tarbert formation: a) Time lapse change in reservoir travel time thickness, b) time lapse change in AVO intercept, and c) time lapse change in AVO gradient.

The covariance matrix of the posterior pdf was calculated from the prior and likelihood model, giving one posterior covariance matrix for the whole field. Different parameters for the prior models were tested to analyze how the uncertainty propagate from the prior model to the posterior model. First, the prior parameters estimated from synthetic Gullfaks data were used. This model has prior standard deviations for the saturation and pressure changes of 0.4 and 1 MPa respectively, and it is considered to be a strong prior model. The posterior standard deviations were calculated to be 0.21 and 2.2 MPa for saturation and pressure changes respectively. The fact that the posterior standard deviations are larger than the prior standard deviations for pressure changes indicates that the prior model is too strong (small standard deviations), and that the seismic data does not support this strong prior model. The correlation matrix (Table 6) was calculated from the posterior covariance matrix, and we observe a strong correlation between saturation and P-wave velocity. This strong correlation is caused by the strong prior model, enforcing the change in saturation to be proportional to the relative change in P-wave velocity (Eqn. 14). The correlation between relative change in P-wave velocity and pressure change is also large, and this is linked to the strong prior model. In addition, we observe a relatively large correlation between time-lapse S-wave velocity contrast and change in pressure, as seen in the synthetic example. Figure 6 shows the expectation values for changes in saturation and pressure for this prior model. Since the differences were calculated by subtracting the 1996 data from the 1985 data, a negative change in saturation means an increase in water saturation and in effective pressure. We observe that the estimated changes in saturation and pressure show trends from the input time lapse change in travel time thickness. Again, this is caused by the strong prior model, enforcing the posterior model to be similar to the prior model related to the travel time changes.

	Δα/α	Δρ/ρ	Δβ/β	ΔSw/Sw	ΔP/P
Δα/α	1.00	-0.14	0.52	0.81	0.75
Δρ/ρ		1.00	-0.28	0.10	-0.10
Δβ/β			1.00	-0.28	0.60
ΔSw/Sw				1.00	-0.32
ΔP/P					1.00

Table 6: Correlation matrix (symmetric) for Tarbert Form. (1985 - 1996) - strong prior

	Δα/α	Δρ/ρ	Δβ/β	ΔSw/Sw	ΔP/P
Δα/α	1.00	-0.11	0.45	0.07	0.40
Δρ/ρ		1.00	0.15	0.45	0.28
Δβ/β			1.00	0.02	0.93
ΔSw/Sw				1.00	0.07
ΔP/P					1.00

Table 7: Correlation matrix (symmetric) for Tarbert Form. (1985 - 1996) - weak prior

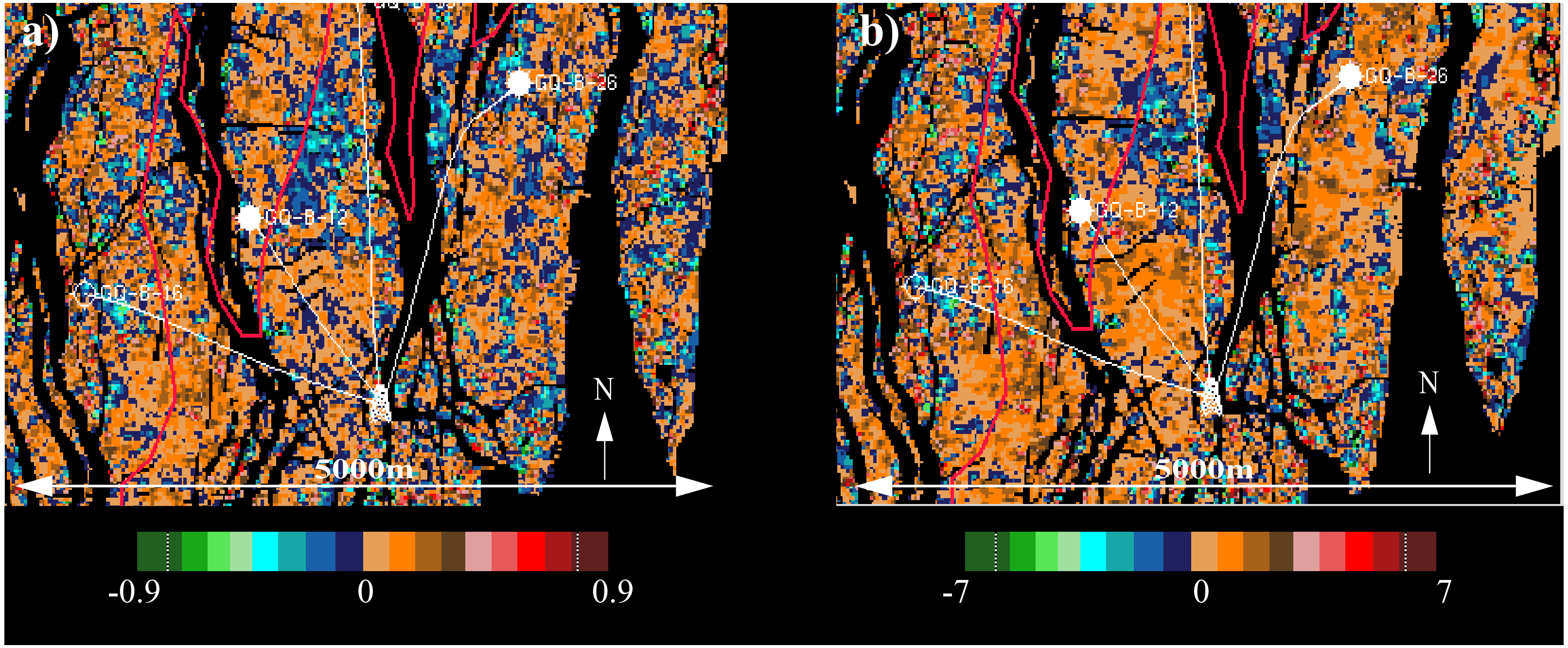

FIGURE 6. **Expectation grids for saturation and pressure changes 1985 - 1996: a) Saturation change and, b) pressure change, both with strong prior model from TWT. The red line is the original oil-water contact (OWC).**

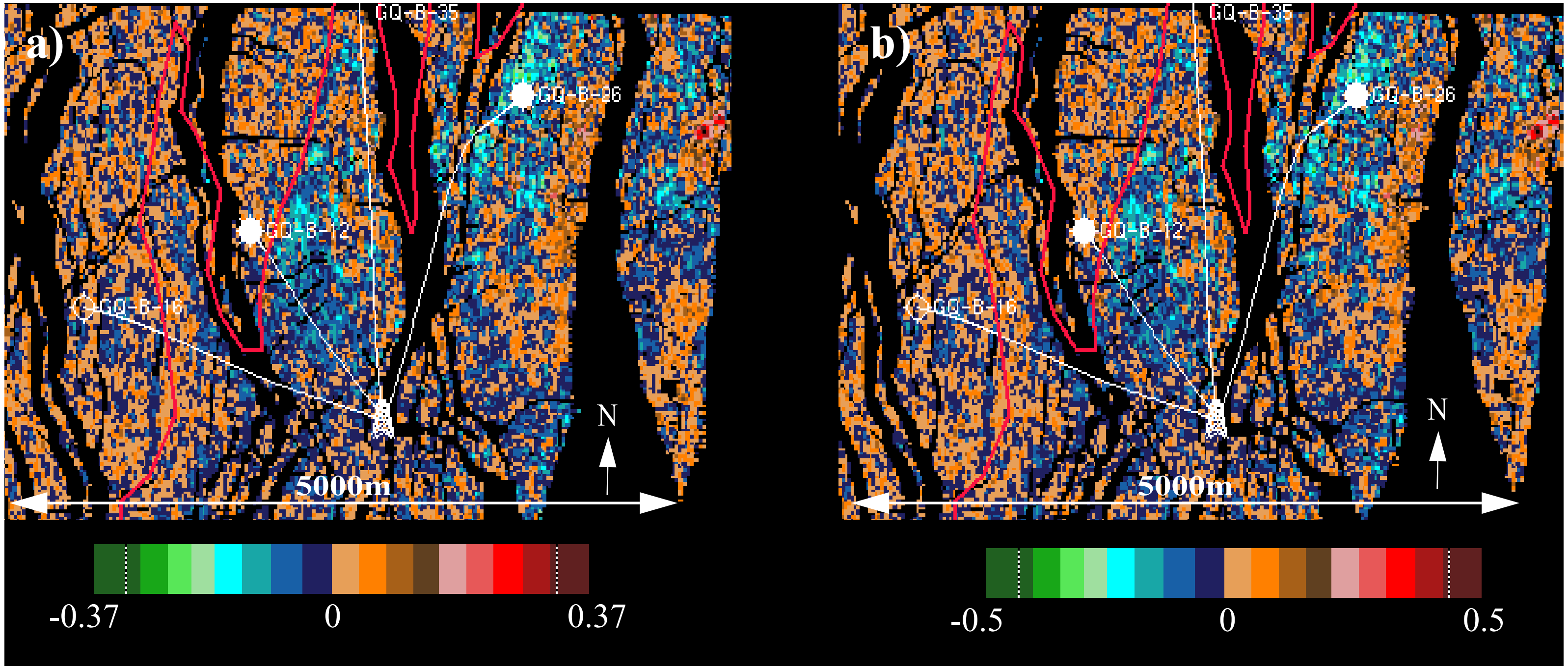

FIGURE 7. Expectation grids for saturation and pressure changes 1985 - 1996: a) Saturation change and, b) pressure change, both with zero change in TWT.

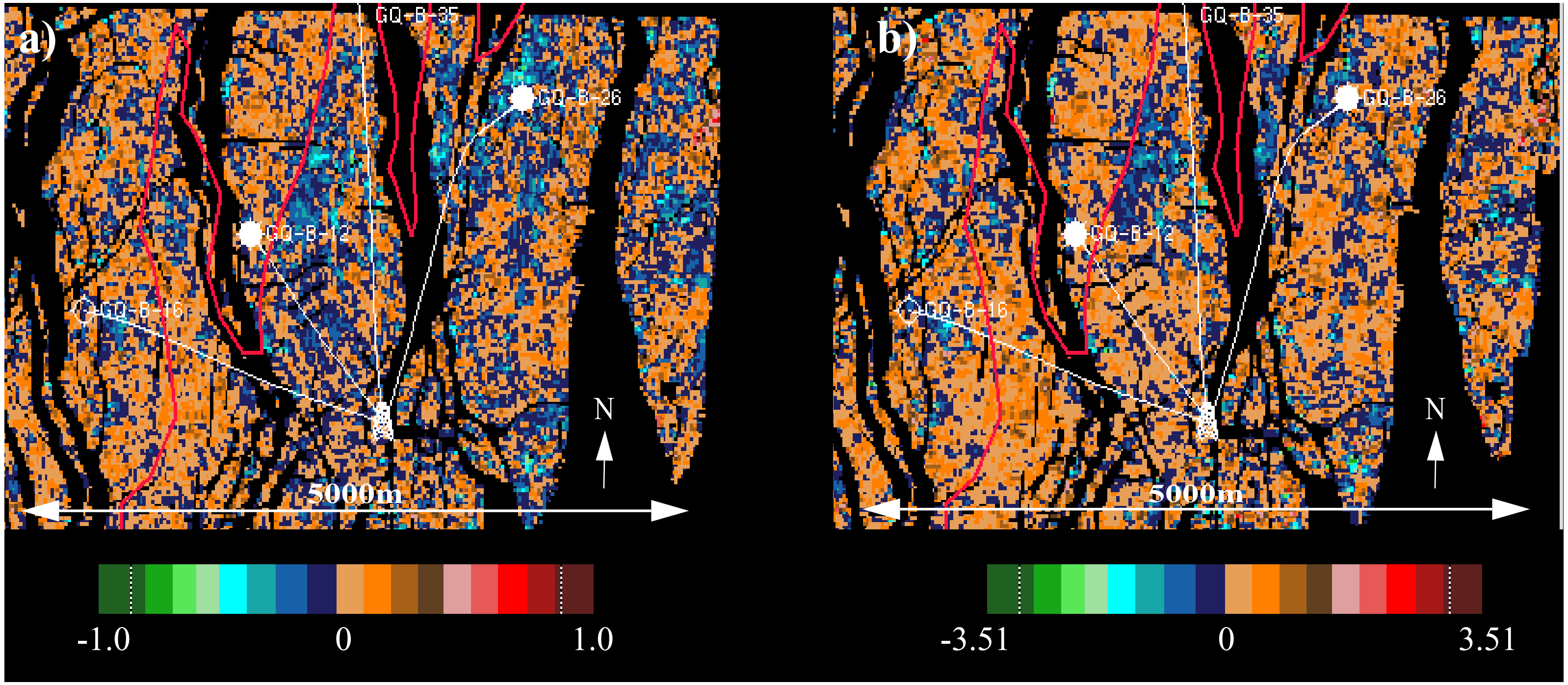

FIGURE 8. Expectation grids for saturation and pressure changes 1985 - 1996: a) Saturation change and, b) pressure change, both with weak prior model from TWT.

To demonstrate the influence of the likelihood model, we performed one test with the assumption that there were no time lapse changes in the travel time thickness over the reservoir zone. Figure 7 shows the expected change in saturation and pressure for this prior model. The other parameters in the prior model were equal to the parameters for the previous case. This makes the estimated change in saturation and pressure resemble the input time lapse seismic AVO attributes. The cause of this is that the assumption of zero time lapse change in travel time implies a prior model with no expected change in saturation (Eqn. 2 and Eqn. 14). However, the maps will not look identical since there is uncertainty added both to Eqn. 2 and Eqn. 14. The value range of the estimated change in pressure and saturation for this model is smaller than the value range for the prior model with a time lapse travel time change.

Since we assume that the error in the prior model of P-wave velocity change (from time lapse change in travel time thickness) is large, we want to include more information from the time lapse change in seismic AVO parameters. We made a test with a weaker prior model, i.e. we used the same trend model as above, but the errors in the prior model were assumed to be larger than before. The standard deviations for saturation and pressure changes in the prior model is set to 3 and 20 MPa respectively. This gives large posterior standard deviations of saturation and pressure changes; 2.6 and 10.1 MPa respectively. In this case, the seismic data give results that are within the range of the weaker prior model, and the standard deviations have decreased compared to the prior model. Both the prior and the posterior standard deviations for saturation change are larger than what is expected to be physically meaningful, but the resulting posterior expectation values are within the physical range of change in saturation. The prior standard deviation was chosen to be this large in order to demonstrate the effect of a weak prior model. The correlation matrix calculated from the covariance matrix of the posterior distribution for this case is shown in Table 7. Note the large correlation between change in S-wave velocity and change in pressure, as seen in the synthetic tests and the test with a strong prior model. In addition, we observe that the strong correlation between change in saturation and relative change in

P-wave velocity is absent here. This does not mean that P-wave velocity is not affected by changes in saturation, but rather that the prior model is not correct, and the seismic data does not support the prior model relationship between saturation and velocity. The correlation between change in pressure and change in P-wave velocity has also decreased, but not as much as the correlation between saturation change and changes in P-wave velocity. Again, we believe that the decrease in correlation is caused by the weak prior model, allowing the posterior estimates to vary more from the prior model. The expectation values for changes in saturation and pressure from this model is shown in Figure 8. Indeed, we observe that the estimated pressure and saturation changes now show features from both time lapse change in travel time and time lapse change in AVO parameters.

Finally, the prior model is defined as a Markov random field, and spatial dependencies between grid points are included. The results with spatial dependencies are shown in Figure 9, with simulated saturation (top) and pressure (bottom) obtained from MCMC sampling. The plots to the left show the expectation value of pressure and saturation without spatial dependencies in the prior model. The middle plots show the estimated expectation value with spatial dependencies, given by the average value of 1000 MCMC simulations. The rightmost plots show the pointwise variance in the estimated saturation and pressure changes with spatial dependencies, also estimated from the 1000 simulations. To secure convergence of the MCMC sampling algorithm, 1000 burn in runs were used before starting to sample from the Markov field model. The expectation values from the Markov random field are indeed smoother than the corresponding expectation values without spatial dependencies, and some of the spurious points are removed while still preserving the overall trends. The marginal standard deviations (point by point) of the posterior model including spatial dependencies varies between 0.53MPa and 1.46MPa with a mean standard deviation of 1.01MPa for pressure changes and 0.14 to 0.39 with a mean standard deviation of 0.31 for saturation changes, which is lower than the constant variances of the posterior distribution without spatial dependencies.

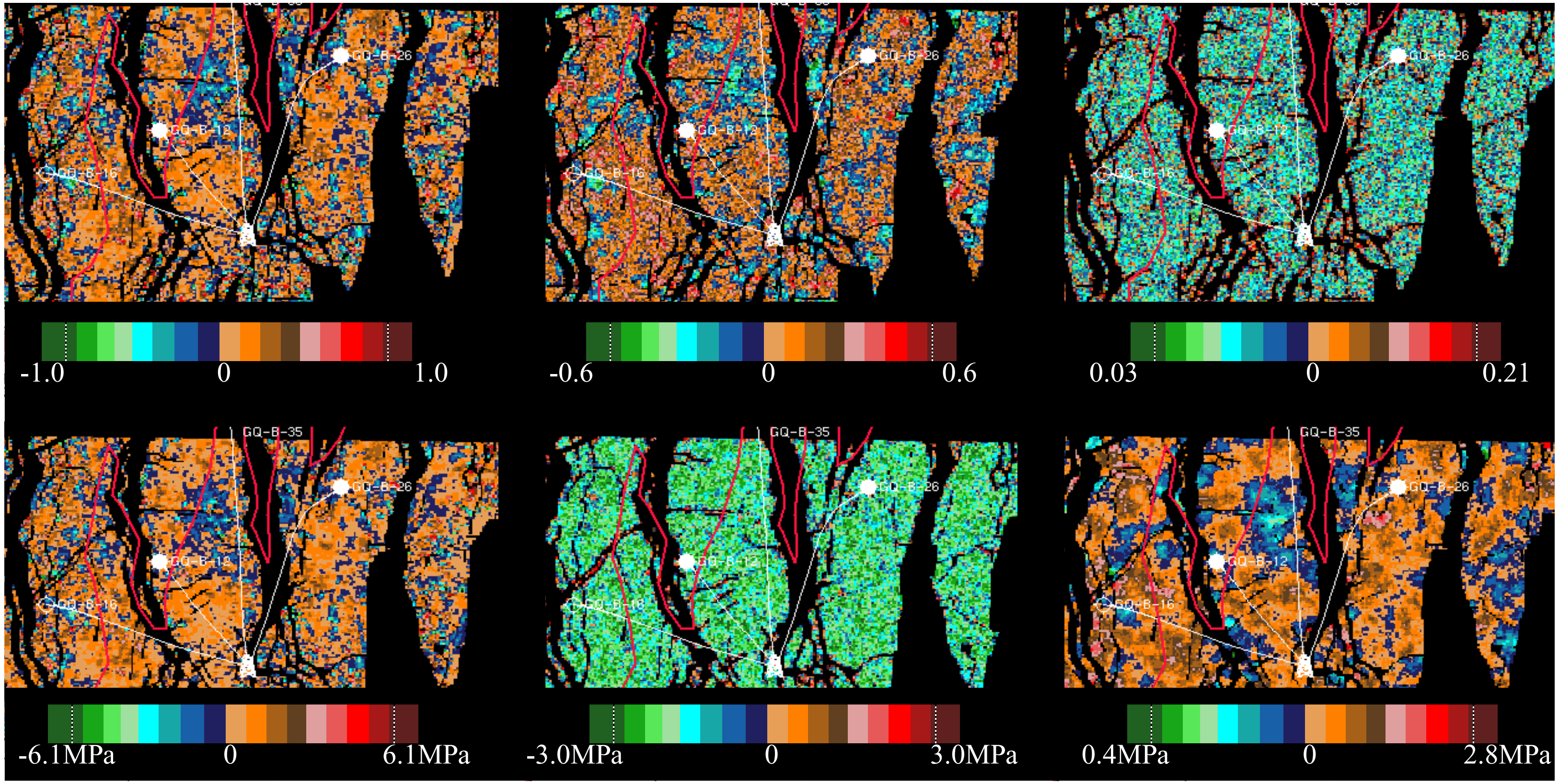

FIGURE 9. Simulated saturation and pressure changes 1985 - 1996 with spatial dependencies: a) Expectation value for saturation, b) saturation change with spatial dependencies, c) pointwise variance in saturation estimate, d) expectation value for

pressure change, e) pressure change with spatial dependencies, and f) pointwise variance in pressure estimate.

We have compared the results of the stochastic estimation with well information and with results of the deterministic estimation of pressure and saturation changes performed by Landrø (1999a) and Alsos et al., (2002). North east of the water injector well B-12 we observe an increase in water saturation (negative change) from 1985 to 1996 (Figure 8). This increase is also observed on the deterministic results of Landrø (1999a) and Alsos et al. (2002). The increase is interpreted as the northward movement of the water front from the B-12 injector, and it has been confirmed by the horizontal producer C-36 finding water in this area in early 1998 (Landrø, 1999a). Around the injector well B-26 we observe an increase in water saturation from 1985 to 1996 (Figure 8), and this is also observed in the deterministic results (Landrø, 1999b and Alsos et al., 2002). This anomaly is probably related to the injection of water in the B-26 well. In this area and the area northeast to well B-12 we observe an increase in effective pressure (corresponding to a pore pressure decrease) from 1985 to 1996. According to well pressure measurements, an average decrease in pore pressure of about 2 MPa is observed in these two segments, which is not too far from the estimated values around 1.5 MPa. However, there are very few case studies published where a pore pressure decrease can be detected from time lapse seismic data. Another feature of the estimated pressure changes (Figure 8b) that does not seem realistic is the spatial distribution. Although there is a fault (not shown on Figure 8b) north of well B-12 that could act as a pressure barrier, this fault does not coincide with the estimated pressure anomaly (The fault is approximately 500 m to the north of the anomaly). On the other hand, there is a possibility that injector well B-12 might give better pressure support to the South and South-East and thereby explain the dimming of the pressure anomaly to the South of the well. It is well known that B-12 has given good pressure support to the South, while the well control in the northern direction is lacking. East of well B-16 an increase in the water saturation from 1985 to 1996 can be observed. Since this is below the original oil-water contact (OWC) we believe it is caused by noise in the time lapse change in travel time thickness of the reservoir (changes in the same area are observed on the map of time lapse changes in travel time thickness, Figure 5).

Well observations in this area indicate typical saturation changes within the range of 30-50%, a number that also fits well with the results obtained by Alsos et al. (2002). Our saturation change estimates (Figure 7, 20-25% maximum) are somewhat lower than these observations. Measured pore pressure reductions in this reservoir segment are of the order of 2-3 MPa, far above our estimates of 0.2-0.3 MPa. This confirms the trend observed in the synthetic example, where estimates of changes in water saturation are more precise and have less uncertainty than pressure change estimates. To be able to reduce uncertainties and improve the estimates, the prior model should be spatially varying over the field. When spatial dependencies are included, the results are smoother and the mean standard deviation are significantly smaller than the standard deviations without spatial dependencies.

Discussion

The results from the synthetic tests and the tests on real Gullfaks data are promising. The methodology can produce quantitative estimates of time lapse changes in saturation and pressure, including information about the uncertainty in the estimations. However, there are limitations in the models that should be discussed.

The prior model is built from well known rock physical relationships, linking changes in saturation and pressure to changes in P-wave velocity, S-wave velocity and density. When specifying the prior model, one needs to be aware of the limitations in these relationships. Both the basic expression for the P-wave velocity, linking it with density, and the Hertz-Mindlin contact model for pressure and velocity make assumptions about isotropy, linearity, and elasticity. Laboratory measurements show deviations from the Hertz-Mindlin model (Vidal et al., 2002). We have used a modified Hertz-Mindlin, as proposed in Vidal et al. (2002), but even the modified Hertz-Mindlin is not optimal for all cases. In addition, we have made the assumption in the prior model that half the change in P-wave velocity can be attributed to change in saturation. For reservoirs were pressure changes dominate, this is obviously not optimal. However, the methodology can easily be updated to use other types of prior distributions for the saturation change.

The likelihood model uses a linearization of the expressions for the PP reflection coefficient valid up to 30 - 35 degrees only. For the linearized expressions to be valid, P-wave velocity contrasts, S-wave velocity contrasts, and density contrasts need to be small across the interfaces. In addition, no anisotropy is included in the prior and likelihood models. It is possible to include anisotropy of the reservoir in the likelihood model, but this will introduce even more variables that need to be linked to the reservoir parameters in the prior model, making the models more complicated.

A trend model of porosity, initial density and velocities of reservoir and cap rock is required to set up the prior and likelihood model. We have seen from the Gullfaks example that if the prior model is in conflict with the information obtained from seismic AVO data, the standard deviations of the predictions will be high. To be able to reduce uncertainties, the prior model should be as accurate as possible. This implies that the trend model should be spatially varying over the field, or that the analysis should be performed on a block by block basis, where the reservoir properties are more homogeneous.

The methodology can be used either over a vertical time window or on a point by point basis. If interval predictions are performed, the resulting estimates of reservoir property changes should be considered as average changes over the vertical interval. The estimates are only valid if the interval to be analyzed can be considered vertically homogeneous. It is also possible to do the estimations on a point by point basis vertically. In this case, the travel time changes can be computed by performing cross correlation checking between the time lapse seismic data sets.

Combining travel time changes with amplitude changes can be problematic. It is important to be consistent when choosing time window for amplitude attributes. If different windows are used for estimating change in travel time and change in seismic amplitudes, different production effects can be observed by the two measurement types. In addition, the travel time information has lower frequency than the amplitude information. However, this method is thought to be more robust than methods combining travel times and amplitudes directly. Here, we use the travel times to set up the prior model, which could be regarded as a trend model. This trend model is updated in the posterior model, using the seismic amplitudes from the likelihood model. Landrø and Stammeijer (2003) found that by using the same velocity model in the NMO correction of two time lapse seismic data sets, we introduce an angle dependency in the relationship between the relative time lapse travel time change ($\Delta t_x / t_x$), the time lapse velocity change ($\Delta\alpha_x / \alpha_x$) and the change in reservoir thickness ($\Delta z_x / z_x$)

$$\frac{\Delta t_x}{t_x} = \frac{\Delta z_x}{z_x} - (1 + \tan^2\theta)\frac{\Delta\alpha_x}{\alpha_x}. \tag{23}$$

Here, θ is the ray angle within the layer being considered. If we had interpreted the time lapse travel time change on the far offset data, the prior model for the change in velocity should be updated with the angle dependent factor (assuming here that $\Delta z_x / z_x$ is zero, i.e. no compaction). For a ray angle of 20 degrees, the correction in the estimated travel time change is about 13%. However, as we have picked the time lapse change in travel time on the stacked and migrated data, we assume that the error is small.

In the analysis presented here, the change in travel time was treated as an observation without error. Obviously this is a gross simplification. It is also possible to regard the travel time change as a stochastic variable with e.g. a mixed Gaussian distribution. For this situation, Monte Carlo simulations can be applied to estimate posterior mean and variance. In each simulation, the travel time change should first be randomly sampled from the mixed Gaussian distribution, then the prior model defined above should be used to estimate corresponding pressure and saturation changes conditioned on the travel time changes.

To be able to link the seismic data to density and velocities through the likelihood model, the seismic amplitudes need to be calibrated to reflection coefficients. This requires prior information about velocities and densities from e.g. well logs calibrated to the seismic data.

Difference maps of seismic amplitudes from the Tarbert Formation in the 1985 - 1996 analysis show several areas with large, continuous time-lapse changes. The difference maps for the reservoir time thickness show less pronounced changes. The base of the Tarbert Formation is difficult to map consistently, giving the difference maps a more noisy appearance. The prior model is built from the travel time information, and by using small variances in the prior model, the posterior model will be dominated by the trends in the travel time differences. With larger variances in the prior model, the posterior model is allowed to vary more from the prior model, and the amplitude information will influence the results to a larger degree. When using no change in reservoir time thickness as prior model, the expectation values are dominated by the trends from the seismic amplitude differences, but the estimated saturation and pressure changes tends to be on the low side, since the prior model indicates no change in saturation and pressure. Using a stochastic travel time model should reduce the influence of the travel time difference.

Conclusions

The methodology presented in this paper allows us to estimate pressure and saturation changes from time lapse AVO data, giving as additional information the uncertainty in the estimations. The method has been tested on time lapse synthetic seismic data and time lapse seismic AVO data from the Gullfaks Field in the North Sea. Both synthetic and real test show that there are large uncertainties in the estimation of pressure and saturation changes from time lapse PP AVO seismic data. For the synthetic cases, uncertainties in estimated change in pressure are larger than uncertainties in estimated change in saturation; for saturation changes the standard deviation is about

35% of the value range, and for pressure changes the standard deviation is about 75% of the value range. The stochastic method produces more accurate pressure change estimates than a deterministic method tested on the same synthetic data. The saturation estimates are of slightly lower quality for the stochastic method compared to the deterministic estimates. The results from the Gullfaks Field are qualitatively consistent with results from deterministic estimation of pressure and saturation changes from PP AVO data. Saturation change estimates are only slightly lower than observed saturation changes in wells. However, the pressure change estimates are too low compared to available well log information. The results depend on the quality of the prior trend model. This implies that the methodology should be run in smaller areas, where the prior model is valid for the whole area under investigation. In addition, when spatial dependencies are included, the marginal uncertainties are reduced.

In this field data study, time lapse change in P-wave velocity is the most important parameter for pressure-saturation discrimination, while time lapse change in density and S-wave velocity have a weaker coupling to the discrimination process. In addition, we observe that the correlation between P-wave velocity and S-wave velocity is non-negligible. In the synthetic examples, we observe a coupling between S-wave velocity changes and change in pressure.

Acknowledgements

Helene Hafslund Veire acknowledges the VISTA/Statoil research programme for financial support. We thank Statoil and their license partners, Norsk Hydro and Petoro, for permission to publish data from the Gullfaks Field. In addition, we thank Schlumberger for support, and Geir Våland Dahl for valuable discussions. Finally, we thank the assistant editor and two anonymous reviewers for valuable comments that improved the manuscript.

Appendix A - Covariance matrix

The inverse of the covariance matrix S for the five-dimensional gaussian posterior distribution is given by

$$
\begin{aligned}
S_{11} &= -2 \cdot \left[-\frac{\sigma_{D22}}{8|\Sigma_D|} + \frac{\sigma_{D21}}{4|\Sigma_D|} - \frac{\sigma_{D11}}{8|\Sigma_D|} - \frac{1}{2\sigma_\alpha^2} - \frac{1}{8\sigma_{sw}^2(C_1 + C_2)} + \frac{1}{2C_3^2\sigma_p^2} \right] \\
S_{21} &= S_{12} = -\left[-\frac{\sigma_{D22}}{4|\Sigma_D|} + \frac{\sigma_{D21}}{4|\Sigma_D|} \right] \\
S_{31} &= S_{13} = -2 \cdot \left[-\frac{\gamma^2\sigma_{D21}}{|\Sigma_D|} + \frac{\gamma^2\sigma_{D11}}{|\Sigma_D|} \right] \\
S_{41} &= S_{14} = 0 \\
S_{51} &= S_{15} = -\frac{1}{c_3\sigma_p^2} \\
S_{22} &= -2 \cdot \left[-\frac{\sigma_{D22}}{8|\Sigma_D|} - \frac{1}{8\sigma_\beta^2} - \frac{1}{2\sigma_p^2} \right] \\
S_{32} &= S_{23} = -\left[-\frac{2\gamma^2\sigma_{D21}}{|\Sigma_D|} - \frac{1}{2\sigma_\beta^2} \right] \\
S_{42} &= S_{24} = -\frac{\phi_x(\rho_w - \rho_{hc})}{\rho\sigma_\rho^2} \\
S_{52} &= S_{25} = -\frac{1}{20P_x\sigma_\beta^2} \\
S_{33} &= -2 \cdot \left[-\frac{8\gamma^4\sigma_{D11}}{|\Sigma_D|} - \frac{1}{2\sigma_\beta^2} \right] \\
S_{43} &= S_{34} = 0 \\
S_{53} &= S_{35} = -\frac{1}{10P_x\sigma_\beta^2} \\
S_{44} &= -2 \cdot \left[-\frac{1}{2\sigma_{sw}^2} - \frac{{\phi_x}^2(\rho_w - \rho_{hc})^2}{2\sigma_\rho^2{\rho_x}^2} + \frac{C_4^2}{2\sigma_p^2} \right] \\
S_{54} &= S_{45} = -\frac{C_4}{\sigma_p^2} \\
S_{55} &= -2 \cdot \left[-\frac{1}{200{P_x}^2\sigma_\beta^2} - \frac{1}{2\sigma_p^2} \right]
\end{aligned}
\tag{A-1}
$$

Here, $\gamma = \frac{\beta_x}{\alpha_x}$, $|\Sigma_D|$ is the determinant of the covariance matrix of the error in the likelihood model, and σ_{Dij} are the entries of the covariance matrix of the likelihood model.

The mean value vector of the posterior distribution can be found by solving the following equation system:

$$\mu_{R,x} = S \cdot \begin{bmatrix} A \\ B \\ C \\ 0 \\ 0 \end{bmatrix} \tag{A-2}$$

where

$$\begin{aligned} A &= \left[-\frac{\Delta r_{0,x}\sigma_{D22}}{2|\Sigma_D|} - \frac{\Delta g_x \sigma_{D21}}{2|\Sigma_D|} - \frac{\Delta r_{0,x}\sigma_{D21}}{2|\Sigma_D|} - \frac{\Delta g_x \sigma_{D11}}{2|\Sigma_D|} - \frac{\Delta t_x}{t_x \sigma_\alpha^2}\right] \\ B &= \left[\frac{\Delta r_{0,x}\sigma_{D22}}{2|\Sigma_D|} - \frac{\Delta g_x \sigma_{D21}}{2|\Sigma_D|}\right] \\ C &= \left[-\frac{4\gamma^2 \Delta r_{0,x}\sigma_{D21}}{|\Sigma_D|} - \frac{4\gamma^2 \Delta g_x \sigma_{D11}}{|\Sigma_D|}\right] \end{aligned} \tag{A-3}$$

Stochastic inversion of pressure and saturation changes from time-lapse multi component data

Helene Hafslund Veire[1], Hilde Grude Borgos[1], and Martin Landrø*,*
**Department of Petroleum Engineering and Applied Geophysics, Norwegian University of Science and Technology, N-7491 Trondheim, Norway.*
[1] Schlumberger Stavanger Research, Risabergvn. 3, N-4056 Tananger, Norway

Abstract

Knowledge about saturation and pressure distributions in a reservoir would be of great value both in the exploration and development phase of a reservoir. This kind of knowledge can help in evaluating the size of a field, in determining an optimal drainage pattern, and in deciding on optimal well designs to reduce risks for blowouts and damage on production equipment. In some cases, saturation and pressure effects have the same order of magnitude on seismic data. This makes it hard to distinguish between the two effects from a single set of stacked seismic data. By analyzing time lapse PP AVO or time lapse multicomponent seismic data it is possible to separate these effects. To be able to utilize information about saturation and pressure distributions in reservoir model building and simulation, information about uncertainty in the estimates is essential. It is possible to obtain information about uncertainties in the estimates through deterministic uncertainty analysis, assuming independent variables. However, the variables in these estimations are inherently dependent and should be treated as such. By formulating the problem in a Bayesian framework, both dependencies between the different variables and spatial dependencies can easily be included.

In this paper we present a method to estimate changes in saturation and pressure from time lapse multicomponent seismic data using a Bayesian estimation technique. Results of the estimations will be probability density functions (pdfs), giving immediate information about both parameter values and uncertainties. Results from tests on synthetic seismic data show that this method produces more precise estimates with lower uncertainty than a similar methodology based on only PP AVO time lapse seismic data. The largest improvement can be found for the pressure estimates, indicating that additional information about S-waves obtained from converted wave seismic data are essential for obtaining reliable information about the pressure distribution.

Introduction

Information about saturation and pressure distributions in the reservoir, and changes in these properties over time, would be of great value in the reservoir development process. In the exploration phase, information about saturation distributions could be used to evaluate the size of a field, and to determine optimal placement of wells. Distributions of effective pressure could be used to evaluate seal capacity of reservoirs, and to map possible hydrocarbon migration pathways, thereby increasing the general knowledge of the reservoir. In the production phase, knowledge about change in saturation over time will help in determining optimal drainage patterns. Information about effective pressure could be used to decide on optimal well design to reduce risks for blow-outs and damage on production equipment.

Traditionally, overpressured zones are mapped by detecting deviation in seismic propagation velocities from normal compaction trends. Dutta (2002) gives an excellent overview of the history and current state of the art in pressure estimation from seismic data. The traditional way of using seismic data as a hydrocarbon indicator has been through amplitude versus offset (AVO) analysis, e.g. Ostrander, (1984), Rutherford and Williams (1989), and Castagna and Smith (1998). Direct estimation of saturation distributions from seismic data has also been done previously, e.g. by calibrating seismic data to well log data through neural networks (e.g. Oldenziel et al., 2000) or through geostatistical estimation techniques e.g. similar to the porosity mapping presented by Doyen (1988). In some time-lapse seismic analysis, time lapse seismic differences can be attributed to being either dominantly pressure related (e.g. the Magnus Field, Watts et al., 1996), or dominantly saturation related (e.g. the Gullfaks Field, Landrø et al., 1999b, and the Draugen Field, Gabriels et al., 1999). In some cases, however, it is difficult to separate the effects of saturation and pressure from one set of stacked seismic data, since these effects can be of the same order of magnitude. In addition, Kvam and Landrø (2001) showed that it is difficult to estimate changes in effective pressure by analyzing stacking velocities from two time-lapse seismic data sets. However, by analyzing time-lapse changes in PP AVO seismic data, it is possible to estimate the production related effects on saturation and pressure simultaneously (e.g. Tura and Lumley, 1999, Landrø, 2001, and Veire et al., 2003, 2004).

Recently, converted seismic data (PS seismic data) have also been acquired and used in seismic reservoir characterization, mainly for enhanced imaging e.g. in gas clouds, but also to estimate reservoir parameters. Since shear waves do not propagate through fluids, combining shear-wave seismic data with compressional seismic data might increase our ability to separate fluid- and pressure effects from seismic data. Veire et al. (2003, 2004) found a strong correlation between relative change in S-wave velocities and change in effective pressure, indicating that combining pressure wave seismic data with converted wave seismic data might increase the quality of the results. In addition, several authors have shown (Margrave et al., 2001, Veire and Landrø, 2001, and Garotta et al., 2002) that combining PP seismic data and PS seismic data improve the estimates of acoustic properties, compared to inversion of PP data alone. Landrø et al. (2002) and Stovas et al. (2003) showed that simultaneous analysis of stacked time lapse multicomponent (PP- and PS) seismic data indeed improved the deterministic estimation of change in saturation and change in effective pressure.

In order to include saturation and pressure change estimates obtained from time lapse seismic data in reservoir modelling and simulation, information about uncertainty in the estimations is needed. One way to obtain uncertainty information is through deterministic uncertainty analysis, e.g. Landrø (2002). This type of analysis assumes the variables involved to be independent of each other, which is not the case here. To incorporate dependencies between different variables, stochastic estimation can be used. By formulating the problem in a Bayesian framework, the solution will be probability density functions (pdf), giving immediate information about both parameter values and associated uncertainties. An additional advantage of the stochastic representation is the possibility to include spatial dependencies in the estimations. Information from theoretical models can be represented through a prior probability distribution, and a likelihood model describes the degree of fit between measured seismic data and data predicted from theoretical models, e.g. Mosegaard and Tarantola (1995). Posterior probabilities can then be found by applying Bayes rule. Other examples of how different types of geophysical and well log data have been integrated in a stochastic framework to estimate various properties of the subsurface can be found in e.g. Malinverno and Leaney (2000), and Eidsvik et al. (2002).

In the following, a stochastic model to estimate fluid and pressure related changes directly from repeated multicomponent AVO data and travel time changes through a Bayesian framework is presented. The prior model is similar to the one presented in Veire et al. (2003, 2004), but a stochastic model for time lapse seismic travel time changes has also been included. The likelihood model is different since multicomponent time lapse seismic data is introduced, making the posterior model different as well. In addition, we present a more general model formulation of the posterior model. This will make it easier to quickly assess how changes in the prior model affects the posterior model. The methodology has been tested on synthetic seismic data, and the results show improved quality (lower uncertainty and better match with real values) compared to estimations done on time-lapse PP AVO seismic data alone.

Methodology

Reservoir model

Through well known rock physical relationships, links between measured seismic variables Δt_x, $\Delta r0pp_x$, Δgpp_x, $\Delta r0ps_x$, Δgps_x and reservoir parameters $\Delta S_{w,x}$ and ΔP_x are set up. Here, Δt represents directly measurable time-lapse change in seismic two-way travel time over the reservoir interval. The variables $\Delta PPR0, \Delta PPG$ are time-lapse changes in PP AVO intercept and gradient respectively, $\Delta PSR0, \Delta PSG$ are time-lapse changes in PS AVO intercept and gradient. The AVO intercepts and gradients are computed by linear regression of partial stacks. Finally, $\Delta S_{w,x}$ and ΔP_x are changes in saturation and pressure due to production.

The reservoir model ΔR_x is represented by the following stochastic variables:

$$\Delta R_x = \left\{ \Delta S_{w,x}, \Delta P_x, \frac{\Delta\alpha_x}{\alpha_x}, \frac{\Delta\beta_x}{\beta_x}, \frac{\Delta\rho_x}{\rho_x} \right\} , \qquad (1)$$

where $x = (x_1, x_2, x_3)$ implies the location and depth of the point in cartesian coordinates, $\Delta S_{w,x}$ denotes change in saturation due to production, ΔP_x is change in pressure due to production, $\Delta\alpha_x/\alpha_x$ is relative time lapse change in P-wave velocity, $\Delta\beta_x/\beta_x$ is relative time lapse change in S-wave velocity, and $\Delta\rho_x/\rho_x$ is relative time lapse change in density. Properties of the 5-dimensional random variable ΔR_x are specified through the probability density function $f(\Delta R_x|\Delta t_x)$. The goal of this method is to produce estimates of the properties of the conditional pdf $f(\Delta R_x|\Delta t_x, \Delta r0pp_x, \Delta gpp_x, \Delta r0ps_x, \Delta gps_x)$, i.e. expectance values and covariance matrices for $\Delta R_x = \{\Delta S_{w,x}, \Delta P_x, \Delta\alpha_x/\alpha_x, \Delta\beta_x/\beta_x, \Delta\rho_x/\rho_x\}$ conditioned on time lapse changes in AVO intercepts and gradients computed from multicomponent seismic data.

All reservoir variables and available data are related through forward models. The prior model assumptions are based on available reservoir knowledge and general rock physical relationships. In this case, available reservoir knowledge comes from well log information and time lapse change in travel time, but regional geological information might also be used. Links between reservoir variables and seismic amplitude data are given in the likelihood model.

Prior model

The prior model connecting production related changes in reservoir properties with changes in seismic two-way travel time is defined by combining well-known rock physical relationships, e.g. Gassmann and Hertz-Mindlin. If production related time lapse changes in rock and fluid properties are small, the basic rock physical relationships can be differentiated to obtain relationships between relative changes in the parameters. These relationships give expectation values for the prior distributions. Uncertainties and errors in the rock physical relationships and in the trend model of reservoir properties are accounted for by adding Gaussian errors to all expectation values. This implies that the prior distributions are all Gaussian distributions. It is also possible to introduce other types of error distributions, but this can make the posterior distribution analytically intractable. In such cases we would have to use Markov chain Monte Carlo sampling to be able to estimate posterior mean values and variances, and the calculations will be more computer intensive. A brief summary of the prior model is given here, a more detailed description can be found in Veire et al. (2003, 2004).

The prior pdf of relative change in P-wave velocity conditioned on relative change in travel time due to production, $f(\Delta\alpha_x/\alpha_x|\Delta t_x)$, is based on differentiating the basic relationship between zero offset interval travel time, thickness of layer, and P-wave velocity. This relationship is given by $t_x = 2Z_x/\alpha_x$, where t_x is zero offset interval travel time, Z_x is thickness of the layer, and α_x is P-wave velocity. The time lapse change in zero offset interval travel time can be treated either as an exact observation or as a stochastic variable. When considered an exact observation, the relationship between P-wave velocity change and travel time change can be expressed as

$$\left[\frac{\Delta\alpha_x}{\alpha_x}\right] = -\frac{\Delta t_x}{t_x} + U_{\Delta\alpha}, \tag{2}$$

where $U_{\Delta\alpha}$ is assumed to be a Gaussian distributed error. Since Eqn. 2 is assumed to be a reasonable estimate of small relative changes in P-wave velocity, the mean value of the error is set to 0. The variance σ_α^2 defines the uncertainty in Eqn. 2, and it should be estimated by analyzing well logs and core data. The variable Δt_x is the change in travel time due to production. To account for uncertainty in interpreting time lapse changes in travel time on seismic data, a stochastic model for zero offset two way travel time of the base reservoir interface can be introduced. When interpreting seismic interfaces, two types of errors may occur: 1) interpreting the wrong seismic event, and 2) smaller mispositioning of the interpretation on the correct seismic event. We assume that the seismic signal consists of one main peak and two side lobes. This is modelled by a multimodal Gaussian distribution function with three modes. The expectation values indicate the positions of the main peak and the side lobes, and the variances represent positioning uncertainty in each of the three events:

$$f(t_j) = \sum_{i=1}^{3} w_{ji} \cdot g(t_j|\mu_{ji}, \sigma_{ji}^2) \qquad , \sum_{i=1}^{3} w_{ji} = 1 . \tag{3}$$

Here, $f(t_j)$ is the pdf of the two-way travel time of the base reservoir, where j can be 1 or 2, indicating pre- and post production times, w_{ji} is a weight factor, and $g(t_j|\mu_{ji}, \sigma_{ji}^2)$ is a Gaussian probability distribution for mode i with expectation value μ_{ji} and variance σ_{ji}^2. The main peak is normally given the largest weight, assuming that this is the most likely position of the base reservoir interface. The main peak also has the smallest variance, indicating that uncertainty in picking the main peak is smaller than uncertainty in picking the side lobes. The travel time difference is obtained by subtracting the sampled value for pre- and post production traveltimes, assuming no production related change in the overburden. In the synthetic example presented below, we have tested both a stochastic and an exact model for travel time changes.

Relative change in density ($\Delta\rho_x/\rho_x$) as a function of change in saturation ($\Delta S_{w,x}$), $f(\Delta\rho_x/\rho_x|\Delta S_{w,x})$, can be found by differentiating the basic relationship between density, porosity and saturation (Mavko et al., 1998)

$$\rho_x = (1-\phi_x)\cdot\rho_M + \phi_x\cdot[S_{w,x}(\rho_w + (1-S_{w,x})\rho_{HC})]\,. \tag{4}$$

where ρ_x is density trend model, ρ_M is density of the rock matrix, ϕ_x is porosity of the reservoir, ρ_w is density of the reservoir water, and ρ_{HC} is density of the hydrocarbon in the reservoir. The porosity is allowed to vary over the reservoir, both horizontally and vertically, and we make the assumption that the porosity does not change due to production.

Relative changes in P-wave velocity can be caused by e.g. changes in saturation and pressure, changes in temperature of the reservoir, compaction of the reservoir, and chemical reactions of the reservoir rocks due to production. Here, we make the assumption of no compaction of the reservoir rocks, and that velocity changes caused by temperature changes and chemical changes are negligible. This means that relative change in P-wave velocity can be separated into a saturation-related change ($\Delta\alpha_x^F/\alpha_x$) and a pressure related change ($\Delta\alpha_x^P/\alpha_x$). The saturation related change can be found by combining a differentiation of Gassmann's equation (Gassmann, 1951), and a differentiation of the Reuss lower bound for fluid modulus, K_f, (Mavko et al., 1998):

$$\frac{1}{K_f} = \frac{S_{w,x}}{K_w} + \frac{1-S_{w,x}}{K_{HC}}, \tag{5}$$

where $S_{w,x}$ is water saturation, K_w is fluid modulus of water, and K_{HC} is fluid modulus of the hydrocarbon in the reservoir. Change in P-wave velocity as a function of change in pressure (ΔP_x) (assuming no change in density as a function of change in pressure) can be derived from a modified version of the Hertz-Mindlin model (Vidal et al., 2002) for normal compression of identical spheres. By combining these equations we can solve for change in pressure. This will give us a prior model for the distribution of change in pressure, given relative change in P-wave velocity and change in saturation, $f(\Delta P_x|\Delta\alpha_x/\alpha_x, \Delta S_{w,x})$.

Changes in S-wave velocity due to production depend on changes in saturation through changes in density ($\beta_x^2 = \mu/\rho_x$), and on changes in pressure through the shear modulus given by the modified Hertz-Mindlin model (Vidal et al., 2002). This gives us a prior pdf of relative change in S-wave velocity conditioned on change in pressure and relative change in density $f(\Delta\beta_x/\beta_x|\Delta P_x, \Delta\rho_x/\rho_x)$. In addition, a prior distribution for change in saturation given relative change in P-wave velocity, $f(\Delta S_{w,x}|\Delta\alpha_x/\alpha_x)$, is needed. As a first assumption, relative change in P-wave velocity is related to change in saturation through a simple linear relationship, adding onto this a large variance, making the prior distribution very wide. The prior pdf of the reservoir variables can then be expressed as:

$$\begin{aligned} f(\Delta R_x|\Delta t_x) &= f\left(\Delta S_{w,x}, \Delta P_x, \frac{\Delta\alpha_x}{\alpha_x}, \frac{\Delta\beta_x}{\beta_x}, \frac{\Delta\rho_x}{\rho_x}\middle|\Delta t_x\right) = f\left(\frac{\Delta\alpha_x}{\alpha_x}\middle|\Delta t_x\right) \\ &\cdot f\left(\Delta S_{w,x}|\frac{\Delta\alpha_x}{\alpha_x}\right)\cdot f\left(\frac{\Delta\rho_x}{\rho_x}\middle|\Delta S_{w,x}\right)\cdot f\left(\Delta P_x|\frac{\Delta\alpha_x}{\alpha_x}, \Delta S_{w,x}\right)\cdot\left(\frac{\Delta\beta_x}{\beta_x}\middle|\Delta P_x, \frac{\Delta\rho_x}{\rho_x}\right) \end{aligned} . \quad (6)$$

Likelihood model

The likelihood model for time lapse seismic data describes how measured changes in seismic amplitudes for multicomponent seismic data are related to relative changes in seismic parameters (P-wave velocity, S-wave velocity and density). Reflection coefficients for PP seismic data (Aki and Richards, 1980) is given by

$$R_0^{PP}(\theta) = \frac{1}{2}\left(\frac{\Delta^B\rho_x}{\rho_x} + \frac{\Delta^B\alpha_x}{\alpha_x}\right) - 2\gamma^2\left(\frac{\Delta^B\rho_x}{\rho_x} + \frac{2\Delta^B\beta_x}{\beta_x}\right)\sin^2\theta + \frac{\Delta^B\alpha_x}{2\alpha_x}\tan^2\theta, \quad (7)$$

where $\gamma = (\beta_x/\alpha_x)$ denotes the ratio between S-wave velocity and P-wave velocity, $\alpha_x = (\alpha_{x,1} + \alpha_{x,2})/2$, and $\Delta^B\alpha_x = \alpha_{x,2} - \alpha_{x,1}$ etc. Here, $\alpha_{x,1}$ and $\alpha_{x,2}$ means the P-wave velocity on each side of a reflection boundary, and Δ^B indicates that it is a boundary difference. A reasonable approximation (assuming weak contrasts and small angles) for the PS-reflection coefficient can be obtained from Aki and Richards (1980):

$$\begin{aligned} R_0^{PS}(\theta) &= -\frac{1}{2}\left((1+2\gamma)\frac{\Delta^B\rho_x}{\rho_x} + 4\gamma\frac{\Delta^B\beta_x}{\beta_x}\right)\sin\theta + \\ &+ \gamma\left(\left(\gamma+\frac{1}{2}\right)\left(\frac{\Delta^B\rho_x}{\rho_x} + 2\frac{\Delta^B\beta_x}{\beta_x}\right) - \frac{\gamma}{4}\frac{\Delta^B\rho_x}{\rho_x}\right)\sin^3\theta \end{aligned} , \qquad (8)$$

By assuming $\tan\theta = \sin\theta$ (valid for small angles), and using the formulation from Landrø et al. (2003) for time lapse changes in the reflection coefficients as a function of time-lapse changes in velocity and density contrasts, we obtain

$$\begin{aligned} \Delta R^{PP}(\theta) &\approx \frac{1}{2}\left(\frac{\Delta\rho_x}{\rho_x} + \frac{\Delta\alpha_x}{\alpha_x}\right) + \left(\frac{\Delta\alpha_x}{2\alpha_x} - 4\gamma^2\frac{\Delta\beta_x}{\beta_x}\right)(\sin\theta)^2 \\ \Delta R^{PS}(\theta) &= \left(-\frac{1}{2}\frac{\Delta\rho_x}{\rho_x} - 2\gamma\frac{\Delta\beta_x}{\beta_x}\right)\sin\theta + \left(2\gamma\left(\gamma+\frac{1}{2}\right)\frac{\Delta\beta_x}{\beta_x} - \frac{\gamma^2}{4}\frac{\Delta\rho_x}{\rho_x}\right)(\sin\theta)^3 \end{aligned} . \qquad (9)$$

Here, ΔR^{PP}, ΔR^{PS}, $\Delta\alpha$, etc. means time-lapse changes in reflectivity, velocities and densities. These relationships can be parameterized as intercepts and gradients

$$\begin{aligned} \Delta PPR0 &= \frac{1}{2}\left(\frac{\Delta\rho_x}{\rho_x} + \frac{\Delta\alpha_x}{\alpha_x}\right), \quad & \Delta PPG &= \frac{\Delta\alpha_x}{2\alpha_x} - 4\gamma^2\frac{\Delta\beta_x}{\beta_x} \\ \Delta PSR0 &= -\frac{1}{2}\frac{\Delta\rho_x}{\rho_x} - 2\gamma\frac{\Delta\beta_x}{\beta_x}, \quad & \Delta PSG &= 2\gamma\left(\gamma+\frac{1}{2}\right)\frac{\Delta\beta_x}{\beta_x} - \frac{\gamma^2}{4}\frac{\Delta\rho_x}{\rho_x} \end{aligned} \qquad (10)$$

Notice that the PS intercept is the $\sin\theta$-term in the expression for the PS reflection coefficient. This gives a likelihood model on the form

$$\left[\Delta D_x \middle| \frac{\Delta\alpha_x}{\alpha_x}, \frac{\Delta\beta_x}{\beta_x}, \frac{\Delta\rho_x}{\rho_x}\right] = \mu_{D,x} + U_D, \qquad (11)$$

where $\Delta D_x = [\Delta r0pp_x, \Delta gpp_x, \Delta r0ps_x, \Delta gps_x]$, and the error term $U_D = U_{\Delta r0pp_x, \Delta gpp_x, \Delta r0ps_x, \Delta gps_x}$ is assumed to be Gaussian distributed with expectation value zero and covariance matrix given by

$$\Sigma_{\Delta r0pp_x, \Delta gpp_x, \Delta r0ps_x, \Delta gps_x} = \begin{bmatrix} \sigma_{11} & \sigma_{12} & \sigma_{13} & \sigma_{13} \\ \sigma_{12} & \sigma_{22} & \sigma_{23} & \sigma_{24} \\ \sigma_{13} & \sigma_{23} & \sigma_{33} & \sigma_{34} \\ \sigma_{14} & \sigma_{24} & \sigma_{34} & \sigma_{44} \end{bmatrix} = \Sigma_D . \qquad (12)$$

The expectation vector $\mu_{D,\,x}$ is given by

$$\mu_{D,\,x} = \begin{bmatrix} \mu_{\Delta r0pp_x} \\ \mu_{\Delta gpp_x} \\ \mu_{\Delta r0ps_x} \\ \mu_{\Delta gps_x} \end{bmatrix} = \begin{bmatrix} \frac{1}{2}\left(\frac{\Delta\rho_x}{\rho_x} + \frac{\Delta\alpha_x}{\alpha_x}\right) \\ \frac{\Delta\alpha_x}{2\alpha_x} - 4 \cdot \gamma^2 \cdot \frac{\Delta\beta_x}{\beta_x} \\ -\frac{1}{2}\frac{\Delta\rho_x}{\rho_x} - \gamma\frac{\Delta\beta_x}{\beta_x} \\ 2\gamma\left(\gamma + \frac{1}{2}\right)\frac{\Delta\beta_x}{\beta_x} - \frac{\gamma^2}{4}\frac{\Delta\rho_x}{\rho_x} \end{bmatrix}. \tag{13}$$

The error term includes both the error in seismic measurements, error due to linearization of the Zoeppritz's equations, and errors in the trend model of elastic parameters for reservoir and cap rock. The covariance matrix of the seismic variables is found by simple statistical analysis of multicomponent AVO seismic data.

Posterior model

The posterior model can be found using Bayes rule

$$f(\Delta R_x|\Delta t_x, \Delta D_x) = C \cdot f(\Delta D_x|\Delta R_x) \cdot f(\Delta R_x|\Delta t_x), \tag{14}$$

where C is the normalizing constant, $f(\Delta D_x|\Delta R_x)$ is the likelihood model, and $f(\Delta R_x|\Delta t_x)$ is the prior model. By inserting expressions for the prior model, we obtain the following expression for the posterior model:

$$\begin{aligned} f(\Delta R_x|\Delta t_x, \Delta D_x) &= \mathrm{const} \cdot f(\Delta D_x|\Delta R_x) \cdot f(\Delta\alpha_x|\Delta t_x) \cdot f(\Delta S_{w,\,x}|\Delta\alpha_x) \\ &\cdot f(\Delta S_{w,\,x}|\Delta\alpha_x) \cdot f(\Delta\rho_x|\Delta S_{w,\,x}) \cdot f(\Delta P_x|\Delta\alpha_x, \Delta S_{w,\,x}) \cdot f(\Delta\beta_x|\Delta P_x, \Delta\rho_x) \end{aligned}. \tag{15}$$

Because all factors of the prior and likelihood model are Gaussian distributions, and since expectations are linear relationships, the posterior distribution will be a Gaussian distribution, and thus analytically tractable. For a Gaussian distribution in a Bayesian setting, an optimal unbiased estimator is the posterior conditional expectation. Uncertainty in the variable ΔR_x is represented by the posterior conditional covariance matrix. All terms in the inverse of the covariance matrix of the posterior model is given in explicit from in Appendix A.

A general description of the posterior distribution is obtained by expressing the expectation vector and covariance matrix as products of vectors and matrices derived from the prior and likelihood functions. By considering this general formulation, it is easier to assess how changes in the prior model and the likelihood model will affect the posterior model. The reservoir variables ΔR_x can be separated into $Z_x = (\Delta Sw_x, \Delta P_x)$ and $Y_x = (\Delta\alpha_x/\alpha_x, \Delta\beta_x/\beta_x, \Delta\rho_x/\rho_x)$. Only Y_x is involved in the likelihood model, which is denoted $D_x|Y_x \sim N(A_D Y_x, \Sigma_D)$. Here, $N(A_D Y_x, \Sigma_D)$ is a Gaussian distribution with expectation vector $A_D Y_x$ and covariance matrix Σ_D, D_x is time lapse change in seismic data (PP and PS intercepts and gradients), Σ_D is given in Eqn. 12, and (from Eqn. 10 and 13)

$$A_D = \begin{bmatrix} \frac{1}{2} & 0 & \frac{1}{2} \\ \frac{1}{2} & -4\cdot\gamma^2 & 0 \\ 0 & -\gamma & -\frac{1}{2} \\ 0 & 2\gamma\left(\gamma+\frac{1}{2}\right) & -\frac{\gamma^2}{4} \end{bmatrix} . \qquad (16)$$

For a likelihood model using only PP AVO seismic data (Veire et al., 2003, 2004), the covariance matrix will be a 2 by 2 matrix, and the matrix A_s is given by

$$A_D = \begin{bmatrix} \frac{1}{2} & 0 & \frac{1}{2} \\ \frac{1}{2} & -4\cdot\gamma^2 & 0 \end{bmatrix} . \qquad (17)$$

The final expression for the conditional expectation vectors and covariance matrices of the posterior five dimensional Gaussian distribution will then be on the form

$$E[\Delta R|D] = \begin{bmatrix} E[Z|D] \\ E[Y|D] \end{bmatrix} \text{ and } Cov[\Delta R|D] = \begin{bmatrix} Cov[Z|D] & Cov[Z,Y|D] \\ Cov[Z,Y|D]^T & Cov[Y|D] \end{bmatrix} . (18)$$

Here, all expressions involved are obtained using general calculations with Gaussian distributions. The detailed expressions are given in Appendix B.

Examples

Three-layer synthetic models have been generated to validate the methodology. In the synthetic models, rock physical properties of the cap rock layer and the layer below the reservoir zone have been kept constant, and only parameters of the reservoir rock have been perturbed. Initial properties of the reservoir rock are taken from a well in the Gullfaks Field in the North Sea. Basic rock and fluid properties are given in Table 1.

Fluid modulus, oil	1.2 GPa	Density of oil	880 kg/m^3
Fluid modulus, water	2.73 GPa	Density of water	1012 kg/m^3
Porosity	0.3	Bulk modulus, matrix	34.1 GPa
		Bulk modulus, frame	6.15 GPa

Table 1: Initial rock and fluid parameters

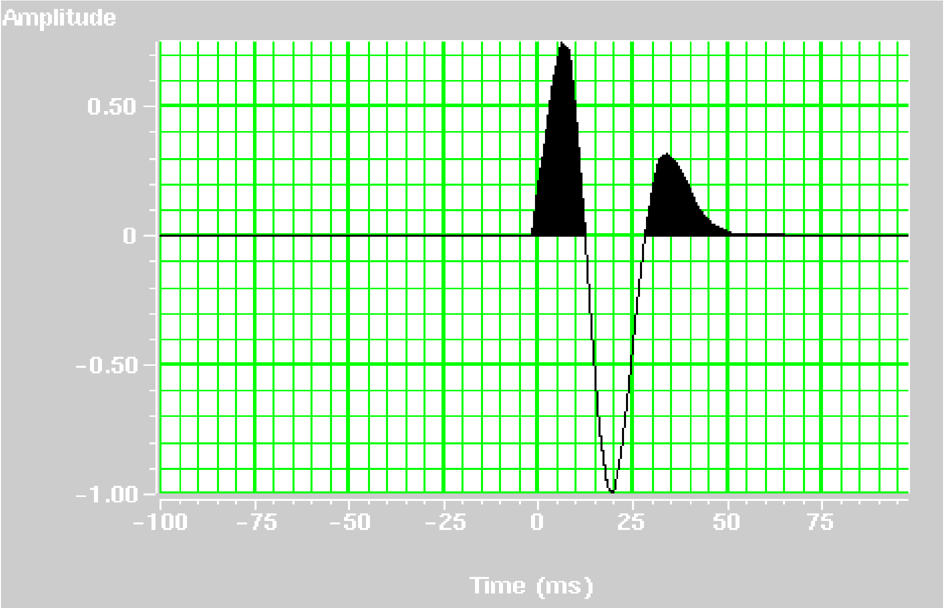

FIGURE 1. Ricker 30Hz, minimum phase wavelet used in synthetic modelling.

The relationship between seismic parameters and pressure was found through statistical analysis of ultrasonic measurements from dry cores of various formations from the Gullfaks Field. Seismic parameters for different scenarios for saturated reservoir rock were then calculated using Gassmann's equation. From synthetic reservoir models, pressure wave (PP) and converted wave (PS) synthetic seismic data were generated using Hampson Russell AVO modelling software. The full elastic wave equation was used to generate primary reflection coefficients. Reflection coefficients were convolved with a Ricker 30 Hz minimum phase wavelet (Figure 1) to produce synthetic seismograms. Effects of Q-factors were automatically compensated for, and the seismic data were moveout corrected using a non-hyperbolic moveout correction for converted synthetic seismic. From resulting synthetic AVO seismograms PP and PS intercept and gradient sections were generated. Table 2 shows seismic parameters from two synthetic models, a preproduction scenario with water saturation 10% and effective pressure 2MPa, and a post production scenario with water saturation 90% and effective pressure 6MPa. Synthetic AVO seismograms for the two models are shown in Figures 2a and 3a.

	Preprod.: Sw=10%, P=2MPa	**Postprod.: Sw=50%, P=8MPa**
Overburden	α=1900 m/s β=995 m/s ρ=1950 kg/m^3	α=1900 m/s β=995 m/s ρ=1950 kg/m^3
Reservoir	α=2066 m/s β=1075 m/s ρ=2131 kg/m^3	α=2288 m/s β=1155 m/s ρ=2181 kg/m^3
Below reservoir	α=2510 m/s β=1164 m/s ρ=2201 kg/m^3	α=2510 m/s β=1164 m/s ρ=2201 kg/m^3

Table 2: Seismic properties for 3-layer synthetic models

	$\Delta\alpha/\alpha$	$\Delta\rho/\rho$	$\Delta\beta/\beta$	$\Delta Sw/Sw$	$\Delta P/P$
$\Delta\alpha/\alpha$	1.00	-0.86	0.78	0.66	0.28
$\Delta\rho/\rho$		1.00	-0.78	-0.57	-0.21
$\Delta\beta/\beta$			1.00	0.48	0.32
$\Delta Sw/Sw$				1.00	-0.0
$\Delta P/P$					1.00

Table 3: Correlation matrix (symmetric) for synthetic example

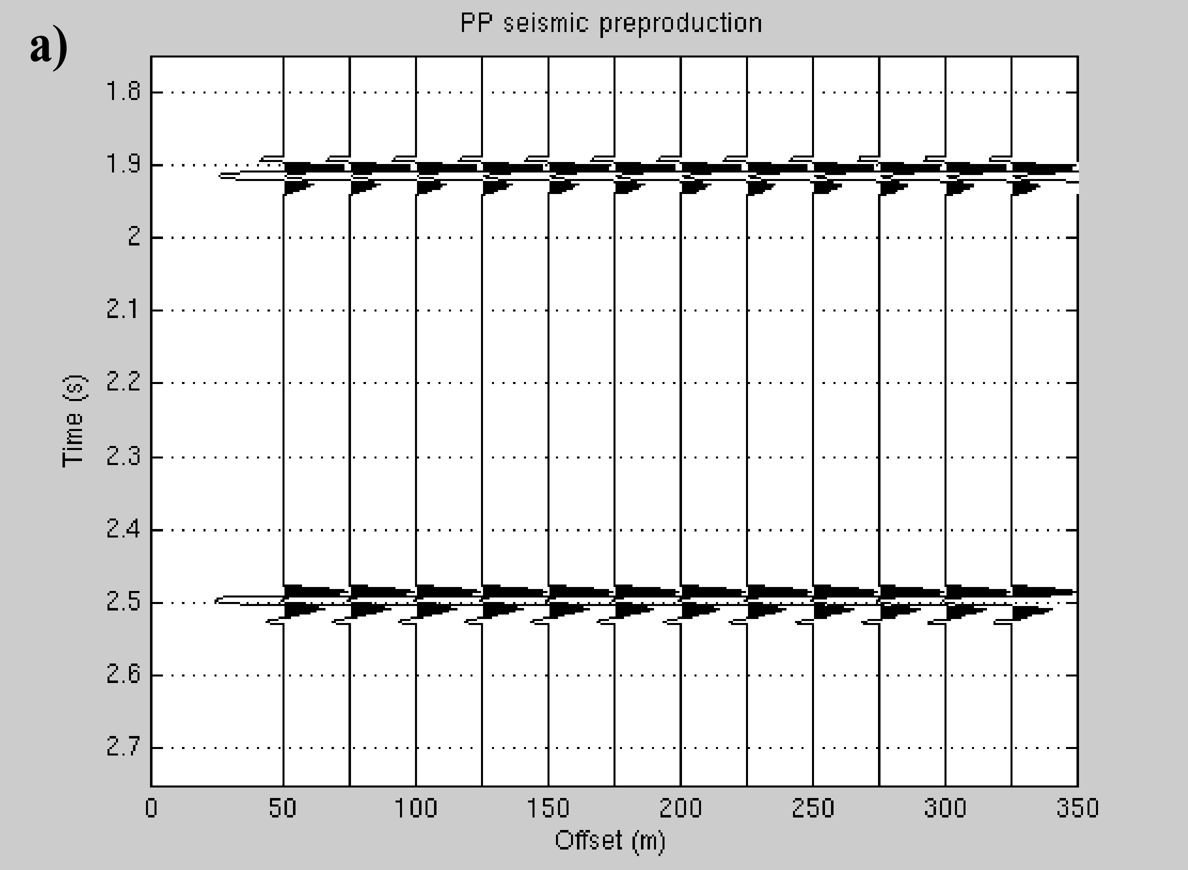

FIGURE 2a. Synthetic PP seismic: a) preproduction with water saturation 10% and initial pressure 2 MPa.

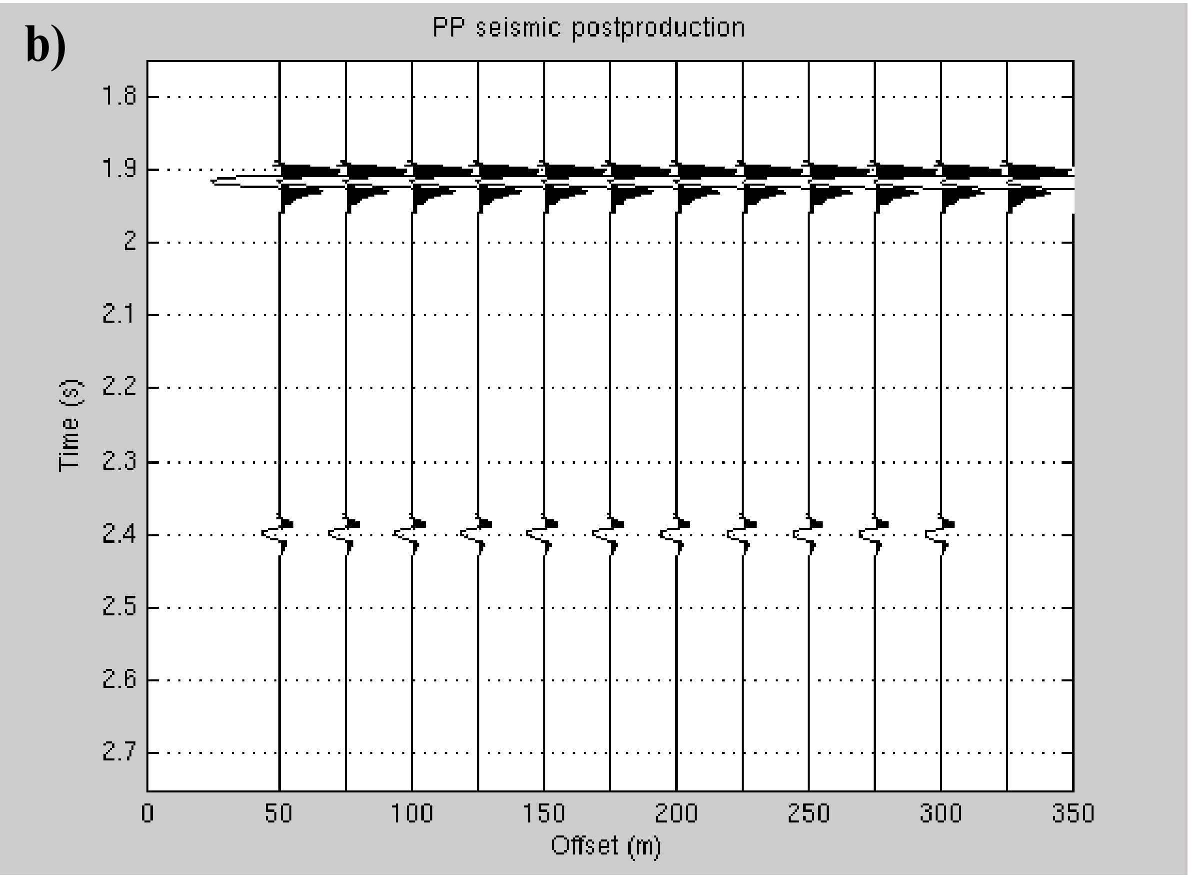

FIGURE 2b. Synthetic PP seismic: b) post production with water saturation 90% and pressure 6MPa.

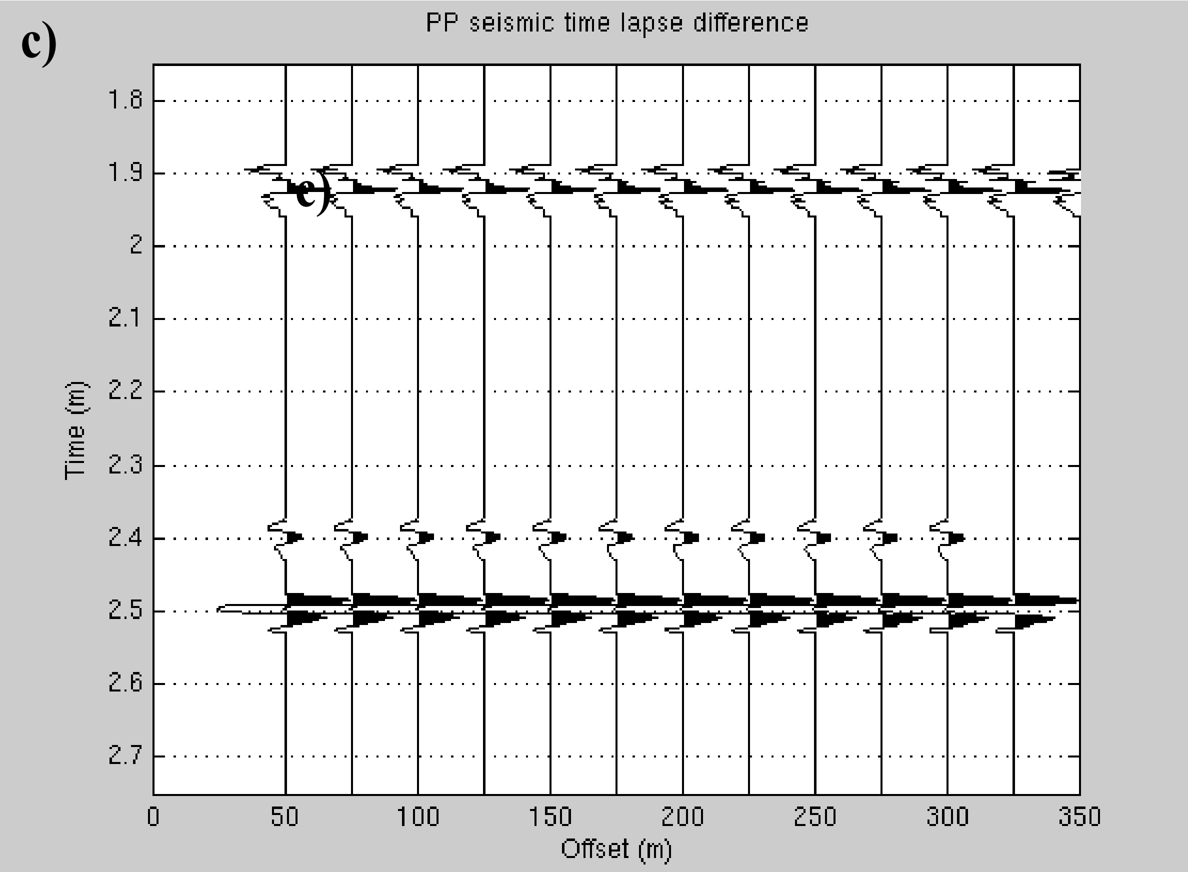

FIGURE 2c. Synthetic PP seismic: c) time-lapse difference.

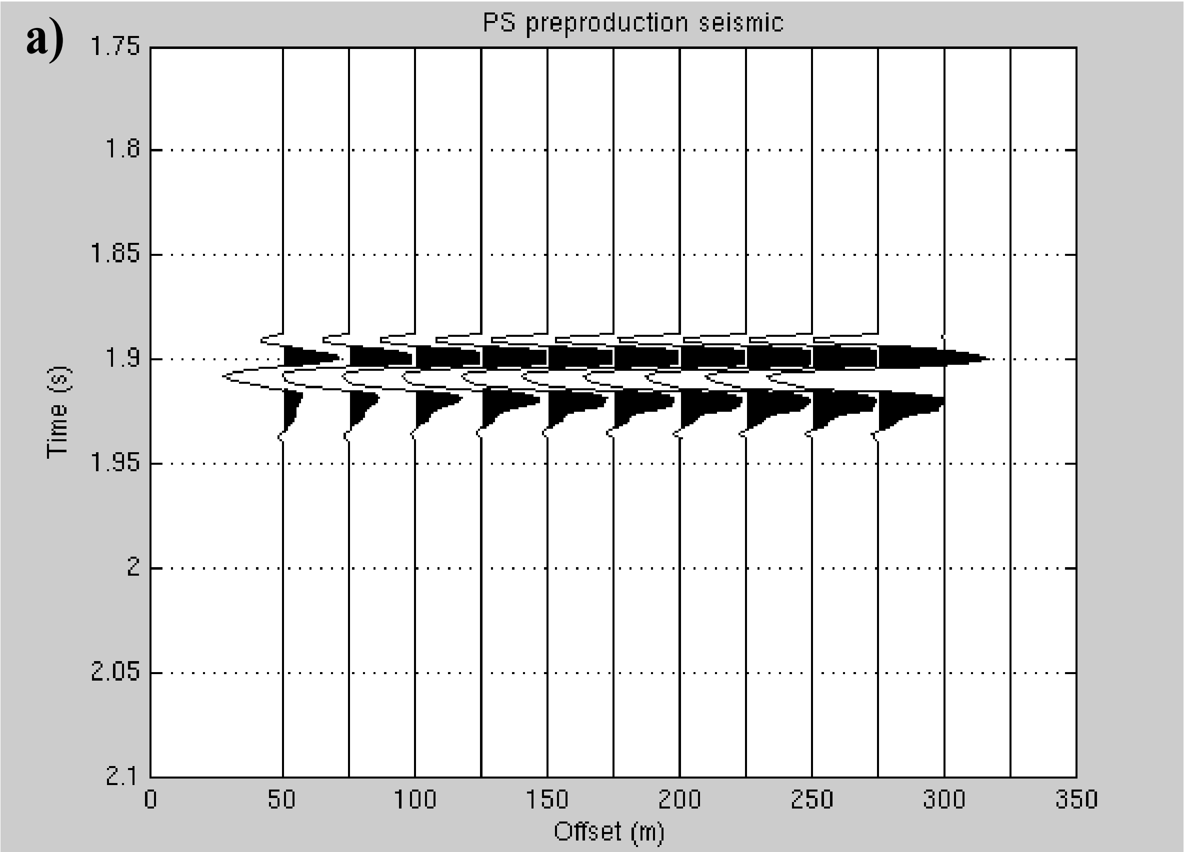

FIGURE 3a. Synthetic PS seismic: a) preproduction with water saturation 10% and initial pressure 2 MPa.

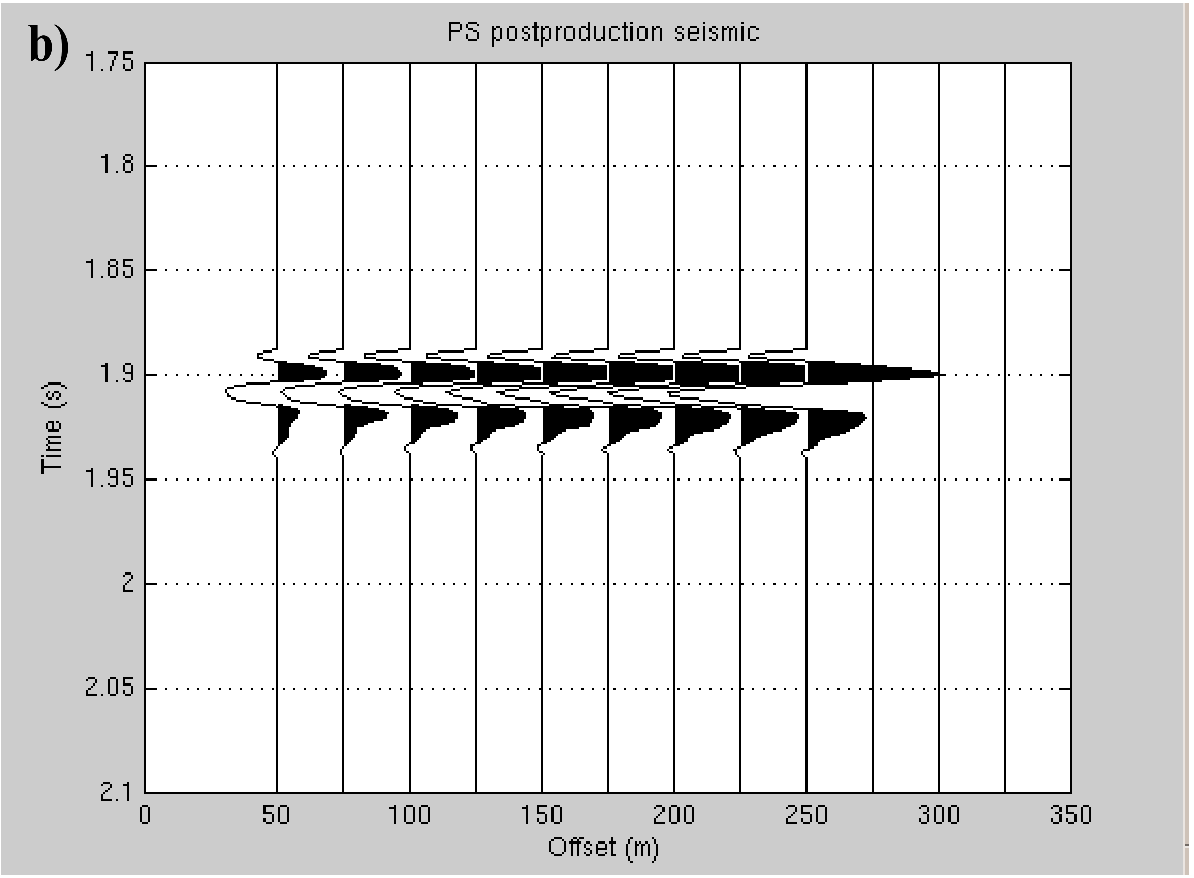

FIGURE 3b. Synthetic PS seismic: b) post production with water saturation 90% and pressure 6MPa.

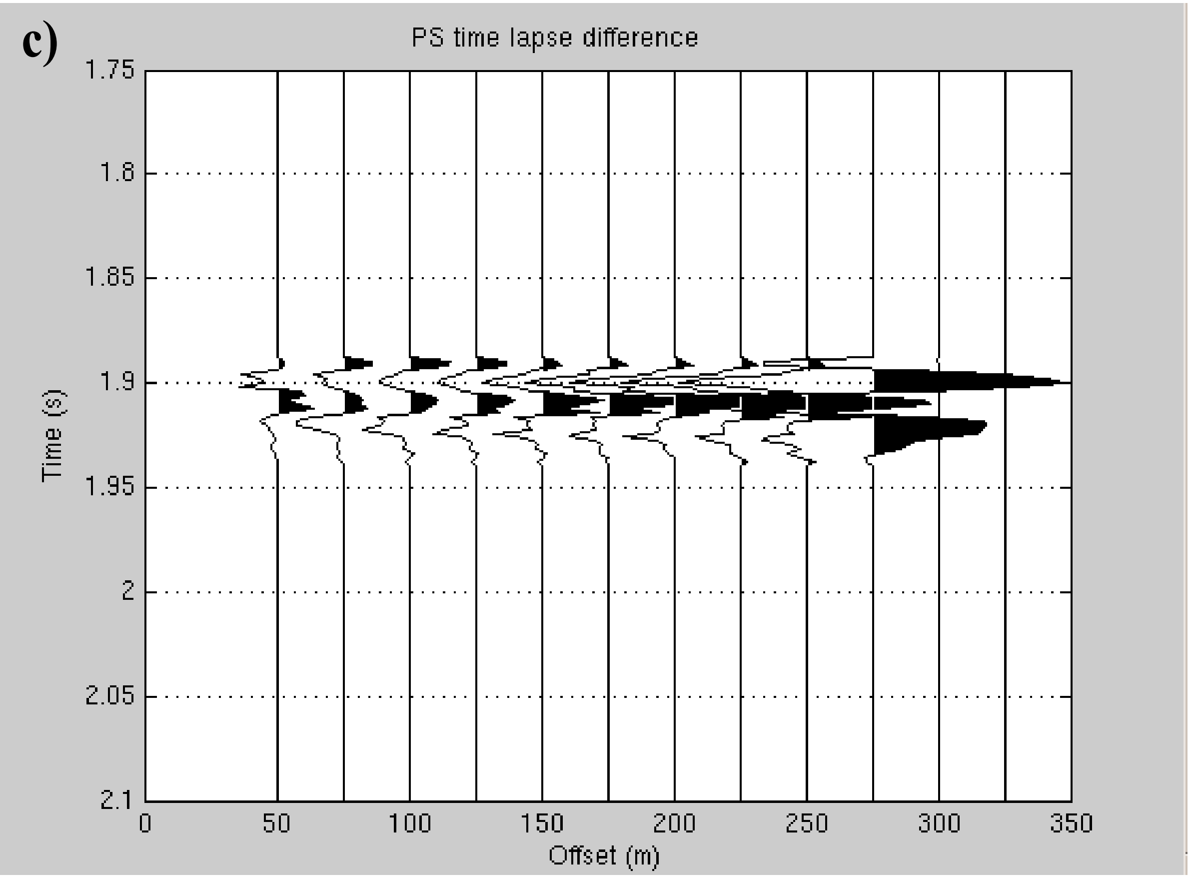

FIGURE 3c. Synthetic PS seismic: c) time-lapse difference.

Pairs of two models representing pre- and post-production scenarios were analyzed together to estimate pressure and saturation changes from seismic data. Parameters for the posterior Gaussian distribution were estimated from measured differences in P-wave zero offset travel time in the reservoir zone and from differences in AVO intercept and gradient along the top reservoir interface for both PP and PS seismic data. The trend model and prior uncertainties for P-wave velocity, S-wave velocity, density, water saturation, and pressure were found by statistical analysis of well-log and core data from the Gullfaks Field, and were set separately for all cases. This makes the correlation matrix for the Gaussian distribution different for all cases. The correlation matrix for the synthetic example described above is given in Table 3. We observe that there are large correlations between relative change in P-wave velocity, density and S-wave velocity. This is valid for all six cases tested. The lowest correlation is found between change in effective pressure and all the other variables. Measured changes in AVO intercept and gradient for both PP and PS seismic data, and changes in P-wave zero offset travel time thickness for the reservoir zone are influencing the expectation vector of the Gaussian distribution. Results from 6 different production scenarios are shown in Table 4. Table 5 shows estimated results for the same synthetic cases using PP AVO data only. In general, stochastic estimation incorporating multicomponent seismic data gives better results than using PP AVO data alone. For all cases, except one, the pressure change estimates are more precise for multicomponent data than for PP data alone. The largest differences between results from PP data alone and results from multicomponent data are found for cases where there is negative or no change in effective pressure. In addition, the standard deviation of pressure changes (i.e. the conditional uncertainty in pressure changes) are lower for multicomponent seismic data. These results are in accordance with the analysis of correlation matrices from PP AVO estimations (Veire et al. 2003), where changes in effective pressure where highly correlated to relative changes in S-wave velocity. This indicates that the additional information about S-waves obtained from converted waves improves the pressure change estimates.

Sw1/Sw2	P1/P2	Sw diff.	P diff.	Est. Sw diff. (St. dev.)	Est. P diff. (st.dev.)	Est./Real α contrast	Est./Real β contrast	Est./Real ρ contrast
0.1/0.9	2/6	0.8	4	0.84 (0.28)	2.49 (1.22)	0.15/0.09	0.05/0.04	0.0004/0.01
0.1/0.5	2/8	0.4	6	0.68 (0.48)	4.40 (1.37)	0.15/0.07	0.13/0.05	-0.0003/0.006
0.1/0.6	2/6	0.5	4	0.63 (0.45)	3.52 (1.45)	0.13/0.07	0.09/0.04	0.01/0.01
0.5/0.9	8/6	0.4	-2	0.24 (0.44)	-1.19 (0.76)	0.02/0.02	-0.06/-0.02	-0.03/0.006
0.6/0.9	6/6	0.3	0	0.24 (0.48)	-0.27 (0.20)	0.04/0.03	-0.03/-0.002	-0.04/0.004
0.5/0.6	8/6	0.1	-2	0.07 (0.48)	-1.77 (1.42)	-0.015/-0.006	-0.023/-0.01	-0.0006/0.002
Mean st. dev.				0.44	1.07			

Table 4: Synthetic results, multicomponent AVO

Sw1/Sw2	P1/P2	Sw diff.	P diff.	Est. Sw diff. (St. dev.)	Est. P diff. (st.dev.)	Est./Real α contrast	Est./Real β contrast	Est./Real ρ contrast
0.1/0.9	2/6	0.8	4	0.85 (0.42)	3.37 (2.40)	0.17/0.04	0.07/0.04	0.02/0.01
0.1/0.5	2/8	0.4	6	0.65 (0.61)	3.91 (4.11)	0.13/0.07	0.06/0.05	0.01/0.006
0.1/0.6	2/6	0.5	4	0.56 (0.45)	2.64 (2.57)	0.13/0.07	0.06/0.04	0.01/0.01
0.5/0.9	8/6	0.4	-2	0.13 (0.59)	0.42 (5.19)	0.02/0.02	0.003/-0.02	0.01/0.006
0.6/0.9	6/6	0.3	0	0.14 (0.45)	0.50 (2.62)	0.03/0.03	0.01/-0.002	0.01/0.004
0.5/0.6	8/6	0.1	-2	-0.06 (0.48)	-0.48 (3.83)	-0.01/-0.006	0.006/-0.01	-0.0001/0.002
Mean st. dev.				0.50	3.45			

Table 5: Synthetic results, PP AVO

Saturation change estimates are of similar quality for multicomponent data and PP AVO data for cases with positive changes in effective pressure, but again, for cases with negative or no change in effective pressure, the multicomponent results are better. The mean value of conditional standard deviations for saturation changes are lower (meaning smaller uncertainty) for multicomponent seismic data than for the results with PP AVO seismic data.

A stochastic travel time model representing uncertainty in travel time interpretation was also tested on the same synthetic data sets (Table 6). For all cases, largest weight and smallest variance was set to the main peak, indicating higher confidence in picking the travel time of the base reservoir at the main peak. Two-way travel time for the base reservoir interface was sampled for pre- and post- production case, using the interpreted travel time as expectation value for the main peak of the multimodal Gaussian distribution. The distance to the two side lobes was determined from the wavelet (Figure 1). Time-lapse travel time differences were calculated from sampled traveltimes, assuming no changes above the reservoir. These travel time differences were used to estimate changes in saturation, pressure, density and velocity. Results presented in Table 6 are the mean value of 500 runs. We observe that the quality of the results using a stochastic travel time model are less precise both for pressure and saturation changes for most cases. The results with the lowest accuracy were produced for cases with a decrease in effective pressure.

Sw1/Sw2	P1/P2	Sw diff.	P diff.	Est. Sw diff.	Est. P diff.	Est./Real α contrast	Est./Real β contrast	Est./Real ρ contrast
0.1/0.9	2/6	0.8	4	0.92	3.77	0.18/0.09	0.09/0.04	0.02/0.01
0.1/0.5	2/8	0.4	6	0.75	3.91	0.15/0.07	0.11/0.05	0.007/0.006
0.1/0.6	2/6	0.5	4	0.63	3.40	0.13/0.07	0.09/0.04	0.013/0.01
0.5/0.9	8/6	0.4	-2	0.29	-0.11	0.04/0.02	-0.01/-0.02	-0.002/0.006
0.6/0.9	6/6	0.3	0	0.29	0.0037	0.05/0.03	0.008/-0.002	-0.002/0.004
0.5/0.6	8/6	0.1	-2	0.035	-1.49	-0.015/-0.006	-0.021/-0.01	0.003/0.002

Table 6: Synthetic results, multicomponent AVO, stochastic traveltime

Discussion

A methodology to perform stochastic estimation of pressure and saturation changes from multicomponent time lapse seismic data have been tested on synthetic seismic data. The results of these tests are promising: the inversion provides in general more precise estimates and have lower uncertainty than inversion based on PP AVO time lapse seismic data alone. However, there are certain limitations in this estimation process that should be discussed.

One of the major limitations is uncertainty in the rock physical relationships used in the prior model. Both the Hertz-Mindlin equation describing the relationship between bulk and shear moduli and pressure, and the basic expression for P-wave velocity make assumptions about isotropy, linearity and elasticity. In addition, the linear relationship between P-wave velocity and saturation may not be valid for a reservoir where the dominant time lapse change is change in pressure. The prior model should be established on a block by block basis, to ensure that the parameters are valid for the area where the estimations are done. The linearized simplifications of Zoeppritz's equations used in the likelihood model also make assumptions about isotropy, in addition to requirements about small velocity- and density contrasts and small incidence angles. However, with the general formulation of the posterior model described in Eqn. 18 and in Appendix B, it should be easy to change both the prior model and the likelihood model to more suitable rock physical and geophysical relationships for the reservoir in question. This is only valid as long as the linearization of the prior and likelihood models are remained. If the prior and likelihood models are not linear, the posterior model will not be Gaussian and the general formulation can not be used. A more fundamental problem is that P-wave velocity might be a lot less receptive to changes in pressure than previously assumed. Holt et al. (2000) showed that the relationship between pressure and P-wave velocity measured on cores changes dramatically in the unloading - reloading process during coring. When changing the pressure on the virgin cores, only small changes in P-wave velocity are observed, making this relationship less suitable in pressure predictions from seismic data.

It is important to be consistent when choosing the time window to calculate AVO attributes and change in P-wave two-way travel time. If this is not done correctly, different reservoir zones with different drainage patterns might be combined, and the estimated saturation and pressure changes will be erroneous. For further details on time lapse changes in seismic travel times we refer to Veire et al. (2003, 2004).

Event correlation of PS seismic data to PP seismic data is a crucial point when combining the two data types. If this is not done properly, non-corresponding events in the two data sets will be combined in the estimation process. The AVO response from these non-corresponding events will provide conflicting information to the likelihood function, and the resulting saturation and pressure change estimates will be wrong. It is not necessary to perform the transformation of PS seismic data to PP traveltimes, but the event correlation step is necessary. In this synthetic example, travel time calibration could be done correctly since seismic velocities were known, but for real seismic data a model of the ratio between S-wave velocity and P-wave velocity is needed to do a proper event correlation. To obtain this velocity model, one possibility is to use stacking velocities for PP- and PS data and transform them to interval velocities using Dix' formula. These interval velocities need to be quality controlled with interval velocities from well logs. Another possibility is to interpret corresponding reflection events in PP- and PS seismic data and calculate the velocity model from these travel times, e.g. Grechka et al., 2002. Interval velocities obtained in the travel time calibration can also be used to perform the necessary calibration of seismic amplitudes from PP and PS seismic data to reflection coefficients. This is needed to calculate AVO intercept and gradients to be used in the likelihood model.

Conclusions

The methodology presented in this paper allows us to estimate pressure and saturation changes from time lapse multicomponent AVO data, giving as additional information conditional uncertainties. The methodology has been tested on synthetic multicomponent seismic data. Results show that pressure and saturation change estimates in general are more precise than estimates from only PP AVO time lapse seismic data. In addition, conditional uncertainties in the inversion are lower for the multicomponent methodology than for the PP AVO methodology. The largest reduction in conditional uncertainty is observed for decreases in effective pressure (increase in pore pressure). The results also confirm the results in Veire et al. (2004), where relative change in S-wave velocity were strongly correlated with change in effective pressure, indicating that information about S-waves should influence the pressure estimates.

Acknowledgements

We acknowledge the VISTA/Statoil research programme for financial support, and Schlumberger for support in this work. We thank Geir Våland Dahl for valuable discussions.

Appendix A - Covariance matrix

The inverse of the covariance matrix for the five-dimensional gaussian distribution is given by

$$\Sigma^{-1} = \begin{bmatrix} q_{11} & q_{12} & q_{13} & q_{14} & q_{15} \\ q_{12} & q_{22} & q_{23} & q_{24} & q_{25} \\ q_{13} & q_{23} & q_{33} & q_{34} & q_{35} \\ q_{14} & q_{24} & q_{34} & q_{44} & q_{45} \\ q_{15} & q_{25} & q_{35} & q_{45} & q_{55} \end{bmatrix}, \tag{A-1}$$

where

$$\begin{aligned}
q_{11} &= -2 \cdot \left[-\frac{s_{11}}{8} - \frac{s_{12}}{8} - \frac{s_{22}}{8} - \frac{1}{2\sigma_\alpha^2} - \frac{1}{8\sigma_{sw}^2(C_1 + C_2)} - \frac{1}{2C_3^2\sigma_p^2} \right] \\
q_{12} &= -\left[-\frac{s_{11}}{4} - \frac{s_{12}}{4} + \frac{s_{13}}{4} - \frac{\gamma^2 s_{14}}{8} + \frac{s_{23}}{4} + \frac{\gamma^2 s_{24}}{8} \right] \\
q_{13} &= -\left[-2\gamma^2 s_{12} + \gamma s_{13} - \gamma\left(\gamma + \frac{1}{2}\right)s_{14} + 2\gamma^2 s_{22} + \gamma s_{23} - \gamma\left(\gamma + \frac{1}{2}\right)s_{24} \right] \\
q_{14} &= -\left[-\frac{1}{2\sigma_{sw}^2(C_1 + C_2)} + \frac{C_4}{C_3\sigma_p^2} \right] \\
q_{15} &= -\frac{1}{C_3\sigma_p^2} \\
q_{22} &= -2 \cdot \left[-\frac{s_{11}}{8} + \frac{s_{13}}{4} + \frac{\gamma^2 s_{14}}{8} - \frac{s_{33}}{8} - \frac{\gamma^2 s_{34}}{8} - \frac{\gamma^4 s_{44}}{32} - \frac{1}{8\sigma_\beta^2} - \frac{1}{2\sigma_\rho^2} \right] \\
q_{23} &= 2 \cdot \left[-\frac{1}{2} \cdot 2\gamma^2 s_{12} + \gamma s_{13} - \gamma\left(\gamma + \frac{1}{2}\right)s_{14} - 2\gamma^2 s_{23} - \gamma^4 s_{24} - \gamma s_{33} + \gamma\left(\gamma + \frac{1}{2}\right)s_{34} \right. \\
&\quad \left. -\gamma^3 s_{34} + \gamma^3\left(\gamma + \frac{1}{2}\right)\frac{s_{44}}{2} - \frac{1}{2\sigma_\beta^2} \right] \\
q_{24} &= -\frac{\phi(\rho_w - \rho_{hc})}{\rho_x\sigma_\rho^2} \\
q_{25} &= -\frac{1}{20P_x\sigma_\beta^2}
\end{aligned} \tag{A-2}$$

$$q_{33} = -2 \cdot \Big[8\gamma^4 s_{22} - 8\gamma^3 s_{23} + 8\gamma^2\left(\gamma + \frac{1}{2}\right)s_{24} + 4\gamma^2\left(\gamma + \frac{1}{2}\right)s_{34} - 2\gamma^2 s_{34}$$

$$-2\gamma^2\left(\gamma + \frac{1}{2}\right)^2 s_{44} - \frac{1}{2\sigma_\beta^2}\Big]$$

$$q_{34} = 0$$

$$q_{35} = -\frac{1}{10P_x\sigma_\beta^2}$$

$$q_{44} = \left[-\frac{1}{\sigma_{sw}^2} - \frac{\phi_x{}^2(\rho_w - \rho_{hc})^2}{\sigma_\rho^2\rho_x{}^2} - \frac{C_4^2}{\sigma_p^2}\right]$$

$$q_{45} = -\frac{C_4}{\sigma_p^2}$$

$$q_{55} = \left[-\frac{1}{100P_x{}^2\sigma_\beta^2} - \frac{1}{\sigma_p^2}\right]$$

Here, s_{ij} are the terms in the covariance matrix of the error, U_D, in the likelihood model.

Appendix B - General matrix description of posterior model

Using general formulas for Gaussian distributions, we use the prior model to derive the joint distribution of the reservoir variables $R = (Y, Z) \sim N(\mu_{YZ}, \Sigma_{YZ})$, the marginal distribution of saturation and pressure changes $Z \sim N(\mu_Z, \Sigma_Z)$, the marginal distribution of velocity and density contrasts $Y \sim N(\mu_Y, \Sigma_Y)$, and the conditional distribution $[Y|Z] \sim N(a_Y + A_Y y, \Sigma_{Y|Z})$ where $a_Y = \mu_Y - \Sigma_{YZ}\Sigma_Z^{-1}\mu_Z$ and $A_Y = \Sigma_{YZ}\Sigma_Z^{-1}$. The posterior model in Eqn. 18 is then given by

$$\begin{aligned}
E[Z|D] &= \mu_Z + \Sigma_Z A_Y^T A_D^T (\Sigma_D + A_D(\Sigma_{Y|Z} + A_Y \Sigma_Z A_Y^T) A_D^T)^{-1} (d - A_D(a_Y + A_Y \mu_Z)) \\
E[Y|D] &= a_Y + A_Y \mu_Z + (\Sigma_{Y|Z} + A_Y \Sigma_Z A_Y^T) A_D^T (\Sigma_D + A_D(\Sigma_{Y|Z} + A_Y \Sigma_Z A_Y^T) A_D^T)^{-1} \\
&\quad \cdot (d - A_D(a_Y + A_Y \mu_Z)) \\
Cov[Z|D] &= \Sigma_Z (I - A_Y^T A_D^T (\Sigma_D + A_D(\Sigma_{Y|Z} + A_Y \Sigma_Z A_Y^T) A_D^T)^{-1} A_D A_Y \Sigma_Z) \\
Cov[Y|D] &= (\Sigma_{Y|Z} + A_Y \Sigma_Z A_Y^T)(I - A_D^T (\Sigma_D + A_D(\Sigma_{Y|Z} + A_Y \Sigma_Z A_Y^T) A_D^T)^{-1} \\
&\quad \cdot A_D(\Sigma_{Y|Z} + A_Y \Sigma_Z A_Y^T)) \\
Cov[Z, Y|D] &= \Sigma_Z A_Y^T (I - A_D^T (\Sigma_D + A_D(\Sigma_{Y|Z} + A_Y \Sigma_Z A_Y^T) A_D^T)^{-1} \\
&\quad \cdot A_D(\Sigma_{Y|Z} + A_Y \Sigma_Z A_Y^T))
\end{aligned} \tag{B-1}$$

Conclusions

In this thesis I have focused on various methods to improve seismic reservoir characterization. Reducing uncertainty in reservoir property estimates from seismic data have potentially large economic impact on the development of a hydrocarbon reservoir. Quantitative reservoir property information can be obtained either through direct estimates of reservoir properties from seismic data or through estimates of elastic properties that later could be related to reservoir properties. I have investigated how to utilize recent advances in seismic technology to improve reservoir property estimates, by analyzing multicomponent seismic data, and time lapse seismic data.

One main topic has been to enhance the estimation of P-wave velocity contrasts, S-wave velocity contrasts and density contrasts by combining PP seismic data with PS seismic data. By adding an additional set of measurements, I have reduced the instability in the system of equations. However, the inversion method requires that the PP and PS seismic data are calibrated to reflection coefficients with the help of well logs. In addition, the PS seismic data needs to be scaled to PP seismic travel times. The methodology has been tested on synthetic seismic data and on multicomponent field seismic data from the North Sea. In the field data study, we have used estimates of P-wave velocity contrast, S-wave velocity contrast, and density contrasts to identify sand layers in a shallow formation. The identified sand layers are consistent with observations from nearby well logs. A possible extension to the joint inversion techniques is to further constrain the inversion by PP travel time information.

I have also performed a deterministic analysis of the uncertainty in the inversion. I find that including empirical relationships between P-wave velocity and density in the inversion reduce the uncertainty for all parameters. This is because the system of equations involve only two unknown variables, P-wave velocity and S-wave velocity, and is less underdetermined than the full system. Furthermore, total uncertainty in joint inversion of PP- and PS seismic data is smaller than total uncertainty in inversion of PP seismic data alone. The largest total uncertainty is seen for the S-wave velocity contrast. From synthetic examples we find that uncertainty in P-wave incidence angles represent the largest contribution to the total uncertainty for velocities and density contrasts.

The least squares inversion methodology was extended to anisotropic inversion. Output of the inversion is relative changes in P-wave velocity, relative changes in S-wave velocity, and relative changes in density. In addition, changes in the anisotropy parameters, ε and δ, across an interface are estimated. Synthetic results show that anisotropic inversion produces better results compared to isotropic inversion for P-wave velocity contrast, S-wave velocity contrast and density contrast for seismic data with anisotropy. However, there are still instabilities in the inversion, in particular in the anisotropy parameters ε and δ. Performing inversion on CCP-sorted seismic data improved the estimated S-wave velocity contrast for the synthetic example presented here.

Next, multicomponent time lapse seismic data were used to estimate changes in pressure and saturation. The method is an extension of existing methodology for surface seismic data. The formulas are explicit expressions related to PP and PS stacks and are therefore well suited for direct implementation in a processing package or a seismic interpretation system. The methodology produced better results than estimation of saturation and pressure changes from time-lapse seismic PP data alone. Necessary input is rock physics models relating changes in seismic parameters to changes in pressure and saturation.

To be able to evaluate uncertainty in the estimations in a better way, stochastic inversion of pressure and saturation changes were implemented first for PP seismic data, then for a combination of PP and PS seismic data. The stochastic methodology incorporates correlation between different variables of the models, as well as spatial dependencies for each of the variables. The stochastic framework is well suited to combine data from different sources (e.g. well logs, seismic data, field analogs) while keeping track of the uncertainties in the data.

The method for PP time-lapse seismic data has been tested on time lapse synthetic seismic data and time lapse seismic AVO data from the Gullfaks Field in the North Sea. Both synthetic and real test show large uncertainties in the estimation of pressure and saturation changes from time lapse PP AVO seismic data. However, results from the Gullfaks Field are consistent both with results from deterministic estimation of pressure and saturation changes from PP AVO data, and with available well log information. The results depend on the quality of the prior trend model, and the estimation should be run in smaller areas, where the prior model is valid for the whole area under investigation. We observe that the correlation between P-wave velocity and S-wave velocity is non-negligible for these data. In the synthetic examples, we observe a coupling between S-wave velocity and change in pressure. In addition, we observe that uncertainty in the estimated change in pressure is larger than uncertainty in the estimated change in saturation; for saturation changes the standard deviation is about 35% of the value range, and for pressure changes the standard deviation is about 75% of the value range.

The methodology was extended to estimate pressure and saturation changes from time lapse multicomponent AVO data. The stochastic estimation has been tested on synthetic multicomponent seismic data. Results show that pressure and saturation change estimates in general are more precise than estimates from only PP AVO time lapse seismic data. In addition, conditional uncertainties in the inversion are lower for the multicomponent methodology than for the PP AVO methodology. The largest reduction in conditional uncertainty is observed for decreases in effective pressure (increase in pore pressure).

References

Aki, K., and Richards, P., 1980, Quantitative seismology: W.H. Freeman & Co.

Alsos, T., Eide, A.L., Hegstad, B.K., Najjar, N.F., Astratti, D., Doyen, P., and Psalia, D., 2002, From qualitative to quantitative 4D seismic analysis of the Gullfaks Field: 64th Ann. Mtg.: Eur. Assn. Geosc. Eng., A-28.

Andorsen, K. and Landrø, M., 2000, Source signature variations versus repeatability - a study based on a zero-offset VSP experiment: Journal of Seismic Exploration, 9, 61-71.

Ata, E. and Michelena, R. J., 1995, Mapping distribution of fractures in a reservoir with P-S converted waves: The Leading Edge, **14**, 664-673.

Bale, R., Leaney, S., Dumitru, G., 2001, Offset-to-angle transformations for PP and PS AVO analysis, 71st Ann. Mtg., Soc. Expl. Geophys., Expanded Abstracts, 235-238.

Barkved, O. I., Mueller, M. C. and Thomsen, L., 1999, Vector interpretation of the Valhall 3D/4C OBS dataset, 61st Mtg.: Eur. Assn. Geosci. Eng., Session:6042.

Barkved, O.I., Kommedal, J., Howe, D., Bærheim, A., 2004, Seismic on demand - First experiences from Valhall: OTC 16929.

Barr, F. J., Paffenholz, J. and Rabson, W., 1996, The dual-sensor ocean-bottom cable method: Comparative geophysical attributes, quantitative geophone coupling analysis and other recent advances, 66th Ann. Mtg., Soc. Expl. Geophys., Expanded Abstracts, 21-23.

Barr, F. J., 1997, Dual-sensor OBC technology: The Leading Edge, **16**, 45-51.

Batzle, M. and Wang, Z., 1992, Seismic properties of pore fluids: Geophysics, Soc. of Expl. Geophys., **57,** 1396-1408.

Beasley, C.J., Chambers, R.E., Workman, R.L., Craft, K.L., and Meister, L.J., 1997, Repeatability of 3-D ocean-bottom cable seismic surveys: The Leading Edge, 16, 1281-1285.

Berg, E., Svenning, B. and Martin, J., 1994, Sumic: Multicomponent sea-bottom seismic surveying in the North Sea - Data interpretation and applications, 64th Ann. Internat. Mtg: Soc. of Expl. Geophys., 477-480.

Berteussen, K. A., Langhammer, J., Andreassen, K., Sognnes, H. I. and Henneberg, K., 1999, Multicomponent sea bottom data in gas hydrate exploration, 61st Mtg.: Eur. Assn. Geosci. Eng., Session:6020.

Bilgeri, D. and Ademeno, E.B., 1982, Predicting abnormally pressured sedimentary rocks: Geophys. Prosp., 30, 608-621.

Bosch, M., 1999, Lithology tomography: From plural geophysical data to lithology estimation: Journal of Geophysical research, **104**, No. B1, 749-766.

Brzostowski, M., Zhu, X., Altan, S., Thomsen, L., Barkved, O. and Rosland, B., 1999, 3D converted - wave processing over the Valhall field, 61st Mtg.: Eur. Assn. Geosci. Eng., Session 6043.

Buland, A., and Omre, H., 2003, Bayesian linearized AVO inversion, Geophysics, **68**, 185-198.

Caldwell, J., Kristiansen, P., Beaudoin, G. J., Tollestrup, A. K., Siddiqui, S. A., Wyatt, K., Camp, W. and Raney, G. B., 1998, Marine 4-component seismic test, Gulf of Mexico: Subsalt Imaging at Mahogany Field, 68th Ann. Internat. Mtg: Soc. of Expl. Geophys., 2091-2092.

Caldwell, J., 1999, Marine multicomponent seismology: The Leading Edge, **18,** 1274-1282.

Cambois, G.,2000, Can P-wave AVO be quantitative?: The Leading Edge, 19, 1246-1251.

Carcuz, J.R., Ikelle, L.T., 2003, Combining PP and PS reflection data - a method for lithology identification: EAGE 65th Conf. & Ex., P126.

Carrillat, A., Nickel, M., Randen, T., Valen, T., Sonneland, L., Fjellanger, J. and Skjerdingstad, A., 2003, Reservoir characterization of the Grane Field with multi-component seismic data, 73rd Ann. Internat. Mtg.: Soc. of Expl. Geophys., 1466-1469.

Castagna, J.P., and Smith, S.W., 1994, Comparison of AVO indicators: A modelling study: Geophysics, 59, 1849-1855.

Castagna, J.P., Swan, H.W., Foster, D.J., 1998, Framework for AVO gradient and intercept interpretation: Geophysics, 63, 948-956.

Cole, S.P., Lumley, D. E. and Meadows, M.A., 2003, 4D Pressure and Saturation Inversion of Schiehallion Field by Rock Physics Modeling, 65th Mtg.: Eur. Assn. Geosci. Eng., A05.

Connolly, P., 1999, Elastic impedance: The Leading Edge, 18, 438-452.

Cooper, M., Christie, P., Thorogood, E., Kristiansen, P. and O'Donovan, A., 1999, Foinaven active reservoir management: The time-lapse signal, 69th Ann. Internat. Mtg: Soc. of Expl. Geophys., 1640-1642.

Davis, T.L., Terrell, M.J., Benson, R.D., Cardona, R., Kendall, R.R., Winarsky, R., 2003, Multicomponent seismic characterization and monitoring of the CO_2 flood at Wayburn Field, Saskatchewan; The Leading Edge, 22, 696-697.

Downton, J.E., Lines, L.R., 2004, Three term AVO waveform inversion, 74th Ann.

Mtg., Soc. Expl. Geophys., Expanded Abstracts, paper 321.

Doyen, P.M., 1988, Porosity from seismic data: A geostatistical approach: Geophysics 53, 1263-1275.

Duffaut, K., Alsos, T., Landrø, M., Rognø, H., Al-Najjar, N., 2000, Shear-wave elastic impedance: The Leading Edge, 19, 1222-1229.

Dutta, N.C., 2002, Geopressure prediction using seismic data: current status and the road ahead: Geophysics, 67, 2021-2041.

Eide, A. L., Ursin, B. and Omre, H., 1997, Stochastic simulation of porosity and acoustic impedance conditioned to seismic data and well data, 67th Ann. Internat. Mtg: Soc. of Expl. Geophys., 1614-1617.

Eidsvik, J., Avseth, P., Omre, H., Mukerji, T., and Mavko, G., 2002, Stochastic reservoir characterization using Bayesian integration of rock physics and Markov random fields: A North Sea example: The Leading Edge, 21, 290-294.

Eidsvik, J., Avseth, P., Omre, H., Mukerji, T., and Mavko, G., 2004, Stochastic reservoir characterization using prestack seismic data: Geophysics, 69, 978-993.

Engelmark, F., 2000, Using converted shear waves to image reservoirs with low-impedance contrast: The Leading Edge, **19,** no. 06, 600-603.

Engelmark, F., 2001, Using 4-C to characterize lithologies and fluids in clastic reservoirs: The Leading Edge, **20,** no. 9, 1053-1055.

Fjellanger, J.P., Skjerdingstad, A-L, Riste, P., Nickel, M. and Carrillat, A., 2003, Improved Imaging in PP and PS, 4C Reservoir Characterization at the Grane Field, 65th Mtg.: Eur. Assn. Geosci. Eng., B26.

Frasier, C., and Winterstein, D., 1990, Analysis of conventional and converted node reflections at Putah Sink, California using three-component data: Geophysics, 55, 646-659.

Fromm, G., Krey, T., and Wiest, B., 1985, Static and dynamic corrections: Seismic Shear Waves, G. Dohr (ed.), 1-86. Handbook of Geophysical Exploration, V. 15a Geophysical Press.

Gabriels, P.W., Horvei, N.A., Koster, J.K., Onstein, A., and Staples, R., 1999, Time lapse seismic monitoring of the Draugen Field: 69th Ann. Internat. Mtg., Soc. Explor., Geophys., Expanded Abstracts, 2035-2037.

Gaiser, J. E., 1996, Multicomponent Vp/Vs correlation analysis: Geophysics, 61, 1137-1149.

Gardner, G.H.F., Gardner, L.W., and Gregory, A.R., 1974, Formation velocity and density – the diagnostic basics for stratigraphic traps: Geophysics, 74, p. 770-780.

Garotta, R., Granger, P.-Y., and Dariu, H., 2002, Combined interpretation of PP and PS data provides direct access to elastic rock properties: The Leading Edge, 21, 532-535.

Gassmann, F., 1951, Elastic waves through a packing of spheres: Geophysics, 16, 673-685.

Greaves, R.J., and Fulp, T.J., 1987, Three-dimensional seismic monitoring of an enhanced oil recovery process: Geophysics, 52, 1175-1187.

Grechka, V., Tsvankin, I., Bakulin, A., Hansen, J. O. and Signer, C., 2002, Joint inversion of PP and PS reflection data for VTI media: A North Sea case study: Geophysics, 67, 1382-1395.

Guilbot, J. and Smith, B., 2002, 4-D constrained depth conversion for reservoir compaction estimation: Application to Ekofisk Field: The Leading Edge, 21, 302-308.

Haas, A. and Dubrule, O., 1994, Geostatistical inversion - A sequential method of stochastic reservoir modelling constrained by seismic data: First Break, **12,** no. 11, 561-569.

Hanson, R., Condon, P., Behrens, R., Groves, S., and MacLeod, M., 2003, Analysis of time-lapse data from the Alba Field 4C/4D seismic survey: Petroleum Geoscience, 9, p. 103 – 111.

Hanssen, P., Ziolkowski, A. and Li, X.-Y., 2003, A quantitative study on the use of converted waves for sub-basalt imaging.: Geophysical Prospecting, **51,** 183-193.

Hastings, W. K., 1970, Monte Carlo sampling methods using Markov chains and their applications, Biometrica, 57, 97-109.

Helgesen, J., and Landrø, M., 1993, Estimation of elastic parameters from AVO effects in the Tau-P domain: Geophysical Prospecting, 41, 341-366.

Holt, R.M., Brignoli, M., and Kenter, C.J., 2000, Core quality: quantification or coring-induced rock alteration: Int. Jour. of Rock Mech. and Mining Sci., 37, 889-907.

Ikelle, L. T., 1996, Amplitude variations with azimuths inversion based on Linearized inversion of common azimuthal sections, in Fjær, E., Holt, R. M. and Rathore, J. S., Ed., Seismic anisotropy: Soc. of Expl. Geophys., 601-644.

Jack, I., 1997, Time-lapse seismic in reservoir management: SEG Distinguished Instructor series, No. 1, Soc. of Expl. Geoph.

Jenkins, S.D., Waite, M.W., and Bee, M.F., 1997, Time-lapse monitoring of the Duri steamflood: A pilot and case study: The Leading Edge, 16, 1267-1274.

Jin, S., 1999, Characterizing reservoir by using jointly P- and S-wave AVO-analysis: 69th Ann. Mtg., Soc. Expl. Geophys., Expanded Abstracts, 687-690.

Jin, S., Cambois, G., and Vuillermoz, C., 2000, Shear-wave velocity and density estimation from PS-wave AVO analysis: Application to an OBS data set from the North Sea: Geophysics, 65, 1446-1454.

Johnston, D.H., McKenny, R.H., Verbeek, J., and Almond, J., 1998, Time-lapse seismic analysis of Fulmar Field: The Leading Edge, 17, 1420-1428.

Johnstad, S., Uden, R., and Dunlop, K., 1993, Seismic reservoir monitoring over the Oseberg Field: First Break, 11, p. 177-185.

Kelly, M.C., and Skidmore, C., 2001, Non-linear AVO equations and their use in 3-parameter inversion: 71st Ann. Mtg., Soc. Expl. Geophys., Expanded abstracts, 255-256.

Koster, K., Gabriels, P., Hartung, M., Verbeek, J., Deinum, G., and Staples, R., 2000, Time-lapse surveys in the North Sea and their business impact: The Leading Edge, 19, 286-293.

Kvam, Ø. and Landrø, M., 2001, Pressure detection from rms velocities - a sensitivity study based on a 4D dataset: 71st Ann. Internat. Mtg., Soc. Explor., Geophys., Expanded Abstracts, 1576-1579.

Landa, J.L., and Horne, R.N., 1997, A procedure to integrate well test data, reservoir performance history, and 4D seismic information into a reservoir description: SPE 38653.

Landrø, M., Duffaut, K., and Rognø, H., 1999a, Well calibration of seabed seismic data: 69th Ann. Mtg., Soc. Expl. Geophys., Expanded abstracts, 860-863.

Landrø, M., Solheim, O. A., Hilde, E., Ekren, B. O. and Strønen, L. K., 1999b, The Gullfaks 4D seismic study: Petroleum Geoscience, 5, 213-226.

Landrø, M., 1999c, Discrimination between pressure and fluid saturation changes from time-lapse seismic data: 69th Ann. Internat. Mtg., Soc.Explor., Geophys., Expanded Abstracts, 1651-1654.

Landrø, M., 2001, Discrimination between pressure and fluid saturation changes from time lapse seismic data: Geophysics 66, 836-844.

Landrø, M., 2002, Uncertainties in quantitative time-lapse seismic analysis: Geophysical Prospecting, 50, 527-538.

Landrø, M., Veire, H.H., Duffaut, K., and Najjar, N., 2003, Discrimination between pressure and fluid saturation changes from marine multicomponent time-lapse seismic data: Geophysics 68, 1592-1599.

Landrø, M., and Stammeijer, J., 2003, Quantitative estimation of compaction and velocity changes using 4D impedance and traveltime changes. 65th Ann. Mtg.: Eur. Assn. Geosc. Eng., A-10.

Li, X.-Y., Dai, H., Mueller, M. C. and Barkved, O. I., 2001, Compensating for the effects of gas clouds on C-wave imaging: A case study from Valhall: The Leading Edge, 20, 1022-1028.

Lumley, D.E., Behrens, R.A., and Wang Z., 1997, Assessing the technical risk of a 4D seismic project: The Leading Edge, 16, 1287-1291.

Lumley, D. E., 2001, The next wave in reservoir monitoring: The instrumented oil field: The Leading Edge, 20, 640-648.

Lumley, D.E., Meadows, M.A., Cole, S.P. and Adams, D. C., 2003, Estimation of Reservoir Pressure and Saturations by Crossplot Inversion of 4D Seismic Attributes, 65th Mtg.: Eur. Assn. Geosci. Eng., A06.

Lygren, M., Fagervik, K., Valen, T.S., Hetlelid, A., Berge, G., Dahl, G.V., Sønneland, L., Lie, H.E., Magnus, I., 2003, A method for performing history matching of reservoir flow models using 4D seismic data: Petroleum Geoscience, 9, 85-90.

Lörtzer, G.J.M., and Berkhout, A.J., 1993, Linearized AVO inversion of multicomponent seismic data, *in* Castagna, J.P., and Backus, M.M., Eds., Offset-dependent Reflectivity - Theory and practice of AVO analysis: Soc. Expl. Geophys., 317-332.

Ma, X-Q., 2001, Global joint inversion for the estimation of acoustic and shear impedances from AVO derived P- and S-wave reflectivity data: First Break, 19, No. 10.

MacLeod, M., Hanson, R. A., Bell, C. R. and McHugo, S., 1999, The Alba Field ocean bottom cable survey: Impact on development: The Leading Edge, 18, 1306-

1312.

Malinverno, A., and Leaney, S., 2000, A Monte Carlo Method to quantify uncertainty in the inversion of zero-offset VSP data: 70th Ann. Internat. Mtg., Soc.Explor., Geophys., Expanded Abstracts, 2393-2396.

Mallick, S., 2001, AVO and elastic impedance: The Leading Edge, 20, 1094-1104.

Margrave, G.F., Stewart, R.R., Larsen, J.A., 2001, Joint PP and PS seismic inversion: The Leading Edge, 20, 978-982.

Martinez, R.D., Schroeder, J.D., and King, G.A., 1991, Formation pressure prediction with seismic data from the Gulf of Mexico: SPE 16621, Formation Evaluation, **3**, 27-32.

Mavko, G., Mukerji, T., and Dvorkin, J., 1998, The rock physics handbook: Cambridge University Press.

Mazzotti, A., and Zamboni, E., 2003, Petrophysical inversion of AVA data: Geophysical Prospecting, **51**, 517-530.

McHugo, S., Probert, A., Hodge, M. C., Kristiansen, P., Painter, D. J. and Hadley, M. J., 1999, Acquisition and processing of a 3D multicomponent seabed data from Alba Field - a case study from the North Sea, 61st Mtg.: Eur. Assn. Geosci. Eng., Session 6026.

Meadows, M., 2001, Enhancements to Landrø's method for separating time-lapse pressure and saturation changes: 71st Ann. Internat. Mtg., Soc.Explor., Geophys., Expanded Abstracts, 1652-1655.

Meunier, J., Huguet, F. and Meynier, P., 2001, Reservoir monitoring using permanent sources and vertical receiver antennae: The Cere-la-Ronde case study: The Leading Edge, 20, no. 6, 622-629.

Mosegaard, K., Tarantola, A., 1995, Monte Carlo sampling of solutions to inverse problems, Journal of Geophysical research, 100, No. B7, 12431-12447.

Najjar, N.F., Strønen, L.K., and Alsos, T., 2003, Time-lapse seismic programme at Gullfaks: value and the road ahead: Petroleum Geoscience, 9, 35-41.

de Nicolao, A., Drufuca, G., and Rocca, F., 1993, Eigenvalues and eigenvectors of linearized elastic inversion: Geophysics, 58, 670-679.

Oldenziel, T., de Groot, P. F. M. and Kvamme, L. B., 2000, Prediction of static and dynamic parameters from time-lapse 3D Seismic, 62nd Mtg.: Eur. Assn. Geosci. Eng., Session X0036.

Okoye, P.N., Zhao, P., and Uren, N.F., 1996, Inversion technique for recovering the elastic constants of transversly isotropic materials: Geophysics, **61**, 1247-1257.

Ostrander, W.J., 1984, Plane-wave reflection coefficients for gas sands at non-normal angles of incidence: Geophysics, 49, 1637-1648.

Plessix, R.-E., and Bork, J., 2000, Quantitative estimate of VTI parameters from AVA responses. Geophysical Prospecting, **48**, 87-108.

Reynolds, E. B., 1970, Predicting overpressured zones with seismic data: World Oil, 171, 78-82.

Rennie, J., Alexandre, R. and Ronen, S., 1997, Sensitivity of repeat 3-D seismic surveys to geometry variations - A controlled experiment, 67th Ann. Internat. Mtg: Soc. of Expl. Geophys., 91-95.

Rickett, J. and Lumley, D. E., 2001, Cross-equalization data processing for time-lapse seismic reservoir monitoring: A case study from the Gulf of Mexico: Geophysics, Soc. of Expl. Geophys., 66, 1015-1025.

Rutherford, S.R., and Williams, R.H., 1989, Amplitude-versus-offset variations in gas sands: Geophysics, 54, 680-688.

Rutledal, H., Ertrevag, E.T. and Berg, J. I., 2001, Oseberg 4 D Study - the Search for Remaining Oil, 63rd Mtg.: Eur. Assn. Geosci. Eng., Session: F-20.

Sheriff, R.E., 1999, Encyclopedic dictionary of exploration geophysics: Soc. Expl. Geophys., 3rd edition.

Sheriff, R.E., and Geldart, L., 1999, Exploration seismology: Cambridge University press, 2nd edition.

Shuey, R.T., 1985, A simplification of the Zoeppritz equations: Geophysics, **50**, 609-614.

Smith, G. C. and Gidlow, P. M., 1987, Weighted stacking for rock property estimation and detection of gas: Geophys. Prosp., 25, 993-1014.

Sollid, A., Ursin, B., 2003, Scattering-angle migration of ocean-bottom seismic data in weakly anisotropic media: Geophysics, **68**, 641-655.

Stewart, R.R., Gaiser, J.E., Brown, R.J., and Lawton, D.C., 2002, Converted-wave seismic exploration: Methods: Geophysics, 67, 1348-1363.

Stewart, R.R., Gaiser, J.E., Brown, R.J., and Lawton, D.C., 2003, Converted-wave seismic exploration: Applications: Geophysics, 68, 40-57.

Stovas, A., Landrø, M. and Arntsen, B., 2003, Use of PP and PS Time-Lapse Stacks for Fluid-Pressure Discrimination, 65th Mtg.: Eur. Assn. Geosci. Eng., A23.

Sønneland, L., and Barkved, O., 1990, Use of seismic attributes in reservoir characterization, in A.T. Buller et al., eds., North Sea oil and Gas reservoirs II, Graham and Trotman, 125-128.

Sønneland, L., Veire, H.H., Raymond, B., Signer, C., Pedersen, L., Ryan, S., and Sayers, C., 1997, Seismic reservoir monitoring on Gullfaks: The Leading Edge, 16, 1247-1252.

Taner, M.T., Koehler, F., and Sheriff, R.E., 1979, Complex seismic trace analysis: Geophysics, 44, 1041-1063.

Tatham, R.H., and McCormack, M.D., 1998, Multicomponent seismology inpetroleum exploration, Soc. Expl. Geophys.

Tessmer, G., and Behle, A., 1988, Common reflection point data stacking technique for converted waves: Geophysical Prospecting, 36, 671-688.

Thompson, M. and Najjar, N.F., 2002, Improved Time-Lapse Seismic Repeatability and Impact on Quantitative Analysis - Statfjord Field, 64th Mtg.: Eur. Assn. Geosci. Eng., P316.

Thomsen, L., 1993, Weak anisotropic reflections, *in* Castagna, J.P., and Backus, M.M., Eds., Offset-dependent Reflectivity - Theory and practice of AVO analysis: Soc. Expl. Geophys., 103-111.

Thomsen, L. A., Barkved, O., Haggard, B., Kommedal, J. and Rosland, B., 1997, Converted-wave imaging of Valhall reservoir, 59th Mtg.: Eur. Assn. Geosci. Eng., Session:B048.B048.

Thomsen, L., 1999, Converted-wave reflection seismology over inhomogeneous anisotropic media: Geophysics, 64, p. 678-690.

Tura, A. and Lumley, D. E., 1998, Subsurface fluid-flow properties form time-lapse elastic-wave reflection data: 43rd SPIE Ann. Mtg., Mathematical Methods in Geophysical Imaging V, 125-138.

Tura, A. and Lumley, D. E., 1999, Estimating pressure and saturation changes from time-lapse AVO data: 69th Ann. Internat. Mtg., Soc.Explor., Geophys., Expanded Abstracts, 1655-1658.

Ursin, B., and Tjåland, E., 1992, Information content of the elastic reflection matrix:

62nd Ann. Mtg., Soc. Expl. Geophys., Expanded Abstracts, 796 - 799.

Veire, H.H., Landrø, M., 2001, Joint Inversion of PP- and PS-seismic data: 71st Ann. Mtg., Soc. Expl. Geophys., Expanded Abstracts, 861-864.

Veire, H.H., Borgos, H.G., Landrø, M., 2003, Stochastic inversion of pressure and saturation changes from time-lapse seismic data; 73rd Ann. Internat. Mtg., Soc.Explor., Geophys., Expanded Abstracts, 1378-1381.

Veire, H.H., Landrø, M., 2004, Exploring the uncertainty in joint inversion of PP- and PS seismic data: Submitted to Geophysical Prospecting.

Veire, H.H., Landrø, M., 2004, Simultaneous inversion of PP- and PS-seismic data: submitted to Geophysics.

Veire, H.H., Borgos, H.G., Landrø, M., 2004, Stochastic inversion of pressure and saturation changes from time-lapse AVO data: Submitted to Geophysics.

VerWest, B., Masters, A. and Sena, A., 2000, Elastic impedance inversion, 70th Ann. Internat. Mtg: Soc. of Expl. Geophys., 1580-1582.

Vidal, S., Huguet, F., and Mechler, P., 2002, Characterizing reservoir parameters by integrating seismic monitoring and geomechanics: The Leading Edge, **21,** 295-301.

De Waal, H., Calvert, R., 2003, Overview of global 4D seismic implementation strategy: Petroleum Geoscience, 9, p. 1-6.

Walton, G.G., 1972, Three-dimensional seismic method: Geophysics, 37, p. 417-430.

Wang, Z., 1997, Feasibility of time-lapse seismic reservoir monitoring: The physical basis: The Leading Edge, 1327-1329.

Watts, G. F. T., Jizba, D., Gawith, D. E., and Gutteridge, P., 1996, Reservoir monitoring of the Magnus Field through 4D time-lapse seismic analysis: Petroleum Geoscience, 2, 361-372.

Whitcombe, D. N., Connolly, P. A., Reagan, R. L. and Redshaw, T. C., 2002, Extended elastic impedance for fluid and lithology prediction: Geophysics, Soc. of Expl. Geophys., 67, 63-67.

Winkler, K. W., 1985, Dispersion analysis of velocity and attenuation in Berea sandstone: J. Geophys. Res., 90, 6793-6800.